UNIVERSITÀ DEGLI STUDI FIRENZE

DOTTORATO DI RICERCA IN
INGEGNERIA INDUSTRIALE

(*Indirizzo in SCIENZA E INGEGNERIA DEI MATERIALI*)

CICLO XXIX

COORDINATORE Prof. Maurizio De Lucia

Anisotropic magnetic properties and relaxation dynamics in molecular magnets

Settore Scientifico Disciplinare ING-IND/22

Dottoranda
Dott. Lucaccini Eva

Tutori
Prof. Caneschi Andrea

Prof. Sorace Lorenzo

Coordinatore
Prof. De Lucia Maurizio

Anni 2013/2016

Anisotropic magnetic properties and relaxation dynamics in molecular magnets

2016, Eva Lucaccini

Dottorato in Ingegneria Industriale, November 2016

Coordinator: prof. Maurizio De Lucia

Tutor: prof. Lorenzo Sorace, prof. Andrea Caneschi

Università degli Studi di Firenze

Piazza San Marco, 4

50121 Firenze

Contents

Glossary

μSR Muon spin relxation.

AC Alternate Current.

CF Crystal Field.

CFP Crystal Field Parameter.

CGS emu Electromagnetic centimetre–gram–second system of units.

CTM Cantilever Torque Magnetometry.

CW Continuous wave.

DC Direct Current.

EDFS Echo detected field-swept.

EPR Electron Paramagnetic Resonance.

FC Field Cooled.

GPS General Purpose Surface - Muon Instrument.

LF Longitudinal field.

NMR Nuclear Magnetic Resonance.

PSI Paul Scherrer Institute.

QTM Quantum Tunneling of Magnetization.

SH Spin Hamiltonian.

SI International System of Units.

SIM Single Ion Magnet.

SMM Single Molecule Magnet.

SQUID Superconducting Quantum Interference Device.

STM Scanning Tunneling Microscopy.

TF Transverse field.

TGA Thermogravimetric analysis.

VSM Vibrating-Sample magnetometer.

XPS X-ray Photoelectron Spectroscopy.

XRPD X-ray Powder diffraction.

ZF Zero field.

ZFC Zero Field Cooled.

Introduction

> There are two possible outcomes: if the result confirms the hypothesis, then you've made a measurement. If the result is contrary to the hypothesis, then you've made a discovery.
>
> *(Enrico Fermi)*

Molecular magnetism is a fascinating research field. The scientist Olivier Kahn, in the preface to his book 'Molecular Magnetism', wrote [1]:

> Molecular magnetism is essentially multidisciplinary. First, it involves synthetic chemistry; one of its challenges is to design molecular systems that exhibit predictable magnetic properties [...] Second, it uses ideas from theoretical chemistry. To design compounds with expected magnetic behavior, it is necessary to use strategies that derive from an understanding of the underlying mechanism of the phenomena...These approaches actually derive directly from the basic concepts of quantum mechanics [...] From a theoretical viewpoint, molecular magnetism is far from being a closed field, where all knowledge is well established. Many questions are still quite controversial [...] Last, molecular magnetism plays an important role in the emerging field of molecular electronics [...] At this stage, it is probably necessary to specify the scope of molecular magnetism. Molecular magnetism deals with the magnetic properties of isolated molecules and assemblies of molecules. These molecules may contain one or more magnetic centers [...].

A year later the publication of the book a report of Sessoli et al. [2] drew further attention on molecular magnetism. A compound containing a magnetic core of twelve manganese ions with a total spin $S = 10$, known as Mn_{12}, showed very interesting properties at cryogenic temperatures: the magnetization was highly anisotropic and had a very long relaxation time below 4 K, causing a pronounced hysteresis. The origin of such a behavior was rooted at the molecular level, meaning that it did not derive from long-range ordering as in ferromagnets. This new class of molecules was then called Single Molecule Magnets SMMs [3].

Starting with Mn_{12}, other compounds were found to exhibit similar features. The first SMMs to be studied were molecules based on exchange-coupled transition metal ions, like Fe_8 [4]. In these systems, the interaction energy among the spins of the

cluster can be expressed using the hamiltonian

$$\mathcal{H} = -J_s \sum_{i,j} \boldsymbol{S}_i \cdot \boldsymbol{S}_j + \sum_i D_i (\boldsymbol{S}_z^i)^2 \tag{0.1}$$

The first term represents the exchange interaction and it is often the dominant one: this allows one to define the total spin S of the ground state of the system. The second term is the magnetic anisotropy of the single centers, which is here assumed to be collinear for all of them, and it results in a preferred orientation of the magnetization. It arises from the symmetry lowering due to interactions of the ions of the magnetic core with their neighboring ligands and from the spin-orbit coupling. The resulting magnetic anisotropy is responsible for the splitting of the $(2S+1)$ levels of the ground state S. Each of them will have an energy $E = DS_z^2$, where D is a linear combination of the D_i. If $D < 0$, the energy will possess a double-well potential shape, with the two minima identified by the S projection $M_S = +S$ and $M_S = -S$. The system has then two distinct states with the same energy and this condition is known as bistability. The energy barrier ΔE that separates the two minima is not infinite, so there is the chance to pass from one well to other. Indeed, for temperature $T \neq 0$, the system can exchange energy with the crystal lattice (phonons), being able to climb the barrier and come down. The distinctive time of such a thermal relaxation, known as Orbach process, follows an Arrhenius law

$$\tau = \tau_0 \mathrm{e}^{\Delta E / k_\mathrm{B} T} \tag{0.2}$$

It is then evident that, as long as the system is stuck in one of the two minima, its magnetization M will be blocked. T_B is thus the maximum T at which the magnetization is frozen, or equivalently, the maximum T at which the system displays hysteresis in plots of M versus magnetic field (H). Another possible way to estimate the blocking temperature is by means of zero field cooled (ZFC) and field cooled (FC) magnetization measurements. Indeed, in this case T_B is defined as the temperature at which ZFC has a maximum and it is not necessarily the same temperature at which the ZFC and FC curves superimpose [3]. Whatever the definition of T_B is, it depends strongly on the experimental conditions. To compare the blocking temperatures of different SMMs T_B has then been proposed as the temperature at which the time (τ) taken for the magnetization to relax is 100 s [3].

The thermal process is not, however, the only way available for the magnetization to relax. SMMs are fascinating systems and they display the coexistence of classical and quantum properties. Indeed, one of the fingerprints of their quantum nature is the observation of quantum tunneling between states on the opposite sides of the barrier [5–8]. This process leads to a temperature independent reversal mechanism that will

be discussed in more detail in section 1.4.

In view of a possible technological exploitation of these systems, the efficiency of SMMs, i.e. the temperature at which bistability is observed, has to be improved. Up until now, liquid helium is still necessary, so a first goal would be to design and synthesize SMMs that work at higher temperatures. In trying to enhance the value of T_B lots of efforts were addressed to increase the value of the total spin of the ground state, in order to have a higher barrier. However, later studies [9] have shown that, for a given molecule, the anisotropy energy of the state of maximum multiplicity is only marginally larger than that of states of lower multiplicity. Given the necessity of controlling both the anisotropy axes of each constituting ion and their coupling, this strategy was not very successful. Indeed, the only polynuclear cluster with improved properties compared to Mn_{12} has only been reported in 2007 [10].

A more appealing possibility is to increase the anisotropy of the single ion and, for this reason, the attention focused on heavier elements of the periodic table: lanthanides and actinides. Unlike transition metal ions, these elements present both a spin and an orbital contribution to the total angular momentum: the spin-orbit coupling in first order leads then to higher values of anisotropy. Indeed, in 2003 a report of Ishikawa et al. [11] showed that a mononuclear lanthanide complex, the so-called terbium double decker $[TbPc_2]^-$, behaved as a SMM. A new branch in the design of SMM was born and in few years further examples of SMMs with a single lanthanide ion were reported [12]. By careful exploitation of synthetic chemistry approach to obtain axial geometries anisotropy energy barrier as large as 1700 K has been recently reported [13] for such systems, often termed Single Ion Magnets (SIMs).

Thanks to these features, since the discovery of the first example of SMM these systems have been proposed as candidates for application in high density storage, molecular spintronic and quantum information processing [14–17]. This requires, as a first step, the comprehension of the different ways a paramagnet can relax. When the relaxation is caused by the energy exchange between the spin system and the phonon bath the corresponding relaxation time is called spin-lattice relaxation time. According to the technique that investigates the magnetization dynamics, this time can be labeled as τ_{SL} (AC susceptometry) or $\mathcal{T}_1$ (Electron Paramagnetic Resonance - EPR). While τ_{SL} represents the relaxation time of the whole magnetization, $\mathcal{T}_1$ is the relaxation time between two energy levels. For a two-level spin system, that is a true $S = 1/2$ with no hyperfine interactions, τ_{SL} and $\mathcal{T}_1$ should describe the same dynamics timescale and therefore they should have comparable values. Any paramagnet possesses, however, another characteristic time, that is known as spin-spin relaxation time (or $\mathcal{T}_2$). This time measures how long the spins behave in a coherent way, that is the time in which the spins lose the memory of the phase of the superposition states in which they have been prepared. For storage application a long $\mathcal{T}_1$ is needed, while for quantum

computing it is $\mathcal{T}_2$ that has to be optimized. This parameter is of crucial importance for single qubit operation, i.e. the simplest operation of a potential quantum computer, for which it should be maximized: an upper limit for it can experimentally be extracted by the phase-memory time $\mathcal{T}_\mathrm{m}$, measured e.g., by pulsed EPR experiment, as it will be shown in chapter 6.

Despite the appeal of potential applications of these systems, we will not deal with them here, since the research activity presented in this dissertation concerns the investigation of the properties of SMMs at a more fundamental level. In particular, since a full comprehension of the mechanisms that are involved in the slow relaxation of the magnetization has not been achieved yet, we focused on the relation between this and the electronic structure of the involved magnetic ion. Apart from quantum tunneling and Orbach process, other mechanisms can be involved in the relaxation: it has been demonstrated that the Orbach process is too often considered responsible for the relaxation, but the overcome of a barrier is not the only way magnetization can relax [18].

The theoretical approach to magnetic relaxation processes dates back to the middle of 20^{th} century [19]: curiously, despite its many approximations and intrinsic limitations, it continues to be used with apparently no caution in the interpretation of data for molecular systems. One of its main assumptions is that only acoustic phonons are considered in the development of simplified expression of field and temperature dependences of the relaxation times pertaining to different processes. However, these SMMs have Debye temperatures of the order of tens of kelvin, at variance with hundreds of kelvin of solid state materials for which the theory has been originally developed [20]. Limiting the phonon spectrum to the acoustic branches in the analysis of the relaxation data of molecular systems seems then a bit restricting. Moreover, according to the same theory, the finding of energy barriers of hundreds of kelvin, when the Debye temperature is so low, contrasts with the hypotheses at the basis of the theory. There is then clearly space for much work here, in trying to correlate the observed dynamic behavior with the electronic structure of the system.

In this respect, an extensive study of a SMM should include an experimental part that correlates results from different techniques, both magnetic and spectroscopic, and a theoretical part that nowadays is embodied by *ab initio* calculations. Indeed, only a virtuous interplay between several experimental approaches and a theoretical modeling of these systems will allow us to obtain a detailed understanding of the relation between the electronic structure and the rich low-temperature magnetization dynamics often observed in these systems [21, 22] .

The main idea of this thesis is to report possible protocols to obtain an as full as possible magnetic characterization, taking into account that, as when we play cards, we may or may not have a lucky hand. Indeed, whatever is the target of our research

we have to deal with the means and data that are available. For instance, the main purpose of a luminescence study could be the determination of the energy splitting of the ground state, that includes several energy levels. Unfortunately, only transitions to excited states are observed, so no direct information on the energy level structure of the ground state is available. Another scenario may include the synthesis of a new sample. If no single crystals are obtained, it may not be possible to get the molecular structure as a first step. Even if the structure is resolved by means of X-ray Powder diffraction spectra (XRPD) we will not be able to perform Cantilever Torque Magnetometry (CTM) or any other anisotropic magnetometry, since these techniques require single crystals.

The thesis is organized in six chapters. In chapter 1 we will present a simple theoretical approach that allows to describe most of the SMMs features. In chapter 2 a summary of the investigation techniques is reported. Together with EPR spectroscopy and static and dynamic magnetic measurement (DC and AC) we will give some basic principles of Muon Spin Relaxation technique (μSR), that is not frequently used in the magnetic characterization of SMMs. In Chapter 3 we will present some results of μSR for two complexes, Er(trensal) and Dy(trensal), that were previously investigated by other techniques [18, 23]. In chapter 4 we will report a comprehensive study of a new Dy(III)-based SIM [22]. In chapter 5 a new series of compounds, the Ln(trenovan) family is reported. They are similar to the Ln(trensal) series but no single crystals nor luminescent data were available. Indeed, their molecular structure was resolved from XRPD. After the experimental characterization, their magnetic properties were simulated by means of a phenomenological approach. Finally, in chapter 6 the magnetic characterization of a vanadyl-based compound is reported. Its long spin-spin relaxation time $\mathcal{T}_2$ makes this kind of molecules suitable to work as potential qubits [24].

1. Electronic structure and magnetic properties of SMMs

> Quelli che s'innamoran di pratica sanza scienzia son come 'l nocchier ch'entra in navilio senza timone o bussola, che mai ha certezza dove si vada.
>
> *(Leonardo da Vinci)*

To understand and model the dynamic behavior of a SMM it is important to obtain a sketch of its energy level structure and of its state composition. In this PhD thesis we focused on the study of SIMs, i.e. systems in which each molecule possesses only one magnetic center (like the well known $[TbPc_2]^-$ [11]). A good description of the energy level structure can be fulfilled by applying the perturbation theory on the energy levels of the free ion. Indeed, a very simple and basic approach starts off with an unperturbed hamiltonian $\mathcal{H}_0$ and then adds up perturbatively the other contributions, which are supposed to be smaller than $\mathcal{H}_0$. We will therefore begin with a brief introduction on the hamiltonian for a free ion, and then describe the effect of the ligands focusing on the Crystal Field approach [25]. The interaction with an external magnetic field and the magnetic anisotropy will be presented in section 1.3, while an overview of the possible mechanisms of relaxation of magnetization and of their phenomenological modeling will be discussed at the end of the chapter.

1.1. The hamiltonian for an isolated ion

If we consider an atom or ion containing a nucleus of charge Ze and N electrons an appropriate hamiltonian for a detailed description of its electronic structure should include:

1. the kinetic energy of the electrons and their potential energy in the electrostatic attractive field of the nucleus (assumed to be point-like and infinitely massive).
2. The electrostatic repulsion between electrons.
3. The magnetic interactions of the electronic spins with their orbital motion (spin-orbit interactions).

4. Several weak effects such as spin-spin interactions between electrons, various relativistic effects, nuclear corrections, etc.

To keep this approach as simple as possible we should ignore all the 'small' effects mentioned in the last point. Thus, neglecting for the moment the spin-orbit interaction, we can write

$$\mathcal{H} = -\frac{\hbar^2}{2m}\sum_{i=1}^{N}\nabla_i^2 - \sum_{i=1}^{N}\frac{Ze^2}{r_i} + \sum_{i<j}^{N}\frac{e^2}{r_{ij}} \tag{1.1}$$

where r_i denotes the relative coordinate of the electron i with respect to the nucleus, $r_{ij} = |\boldsymbol{r}_i - \boldsymbol{r}_j|$ and the last summation is over all pairs of electrons [26]. The presence of the terms $1/r_{ij}$ makes the equation not separable and to solve this problem it is possible to use the *central field approximation*. In this approximation the idea is that each electron moves in an effective potential due to the attraction of the nucleus and the average effect of the repulsive interactions between this electron and the $(N-1)$ other electrons. Since the effect of the other electrons is to partially screen the Coulomb interaction with the nucleus this means that the inter-electron repulsion contains a large spherically symmetric component that will be called $S(r_i)$

$$\sum_i S(r_i) = \left\langle \sum_{i<j}\frac{e^2}{r_{ij}} \right\rangle \tag{1.2}$$

where the braket denotes an average over the distances of the $(N-1)$ other electrons. We can then rewrite equation (1.1) as

$$\mathcal{H} = \mathcal{H}_0 + \mathcal{H}_{\text{er}} \tag{1.3}$$

$$\mathcal{H}_0 = \sum_{i=1}^{N}\left(-\frac{\hbar^2}{2m}\nabla_i^2 - \frac{Ze^2}{r_i} + S(r_i)\right) \tag{1.4}$$

$$\mathcal{H}_{\text{er}} = \sum_{i<j}^{N}\frac{e^2}{r_{ij}} - \left\langle \sum_{i<j}\frac{e^2}{r_{ij}} \right\rangle \tag{1.5}$$

Now $\mathcal{H}_{\text{er}}$ is much smaller than $\sum_{i<j}^{N}\frac{e^2}{r_{ij}}$, which represents the full mutual repulsion between the electrons. We can thus suppose that $\mathcal{H}_{\text{er}} \ll \mathcal{H}_0$ and consider $\mathcal{H}_{\text{er}}$ as a perturbation.

Another important correction to the hamiltonian $\mathcal{H}_0$ is represented by the spin-orbit term that is

$$\mathcal{H}_{LS} = \sum_i \xi(r_i)\boldsymbol{l}_i \cdot \boldsymbol{s}_i \tag{1.6}$$

where $\xi(r_i)$ is a function of r_i and the central potential. It can be shown that the contribution to the sum (1.6) coming from closed subshells vanishes, so that

the summation is only over electrons of partially filled shells. Therefore, the total hamiltonian for a free atom or ion is

$$\mathcal{H}_{\text{tot}} = \mathcal{H}_0 + \mathcal{H}_{\text{er}} + \mathcal{H}_{LS} \tag{1.7}$$

Since $\mathcal{H}_{\text{tot}}$ describes an isolated atom or ion both the total parity and the total angular momentum are constant of the motion. In the present case the total angular momentum is given by:

$$\boldsymbol{J} = \boldsymbol{L} + \boldsymbol{S} \tag{1.8}$$

where $\boldsymbol{L} = \sum_i \boldsymbol{L}_i$ is the total orbital angular momentum of the electrons, $\boldsymbol{S} = \sum_i \boldsymbol{S}_i$ is their total spin angular momentum. In order to discuss the effects of the terms $\mathcal{H}_{\text{er}}$ and $\mathcal{H}_{LS}$ we shall use perturbations theory, starting from the eigenfunctions and eigenvalues of $\mathcal{H}_0$. The calculations is carried out depending on the relative magnitude of the two perturbing terms $\mathcal{H}_{\text{er}}$ and $\mathcal{H}_{LS}$. Generally only two extreme situations are considered: $\mathcal{H}_{\text{er}} \gg \mathcal{H}_{\text{LS}}$ and $\mathcal{H}_{LS} \gg \mathcal{H}_{\text{er}}$. The first one, which is the most frequently encountered, is called *L-S coupling* or *Russell-Saunders coupling*, while the second one is known as the *j-j coupling case*.

In the *L-S coupling* scheme the first perturbation of $\mathcal{H}_0$ to be considered is the inter-electronic repulsion $\mathcal{H}_{\text{er}}$. The possible states of a multi-electron configuration are known as *spectroscopic terms* and are labeled as ${}^{2S+1}L$, with the capital letters $S, P, D, F \ldots$ corresponding to the values of $L = 0, 1, 2, 3 \ldots$ while $(2S+1)$ is called the multiplicity of the term. The configuration of the ground state is usually determined by following the Pauli exclusion principle and the three Hund's rules [26]. As a second step, the spin-orbit perturbation $\mathcal{H}_{LS}$ is included and, since degeneracy is further partially removed, the term ${}^{2S+1}L$ splits into a number of fine structure components, characterized by a value of J. The various components ${}^{2S+1}L_J$ are then called *multiplets* and each of them is still $(2J+1)$-fold degenerate with respect to M_J.

Table 1.1.: Relative magnetudine of the varios contributions in equation (1.9) [27].

First and second transition series	$\mathcal{H}_{\text{LF}} \sim \mathcal{H}_{\text{er}} > \mathcal{H}_{LS}$
Third transition series	$\mathcal{H}_{\text{LF}} \sim \mathcal{H}_{\text{er}} \sim \mathcal{H}_{LS}$
Lanthanides	$\mathcal{H}_{\text{er}} > \mathcal{H}_{LS} > \mathcal{H}_{\text{LF}}$
Actinides	$\mathcal{H}_{\text{er}} \geq \mathcal{H}_{LS} \geq \mathcal{H}_{\text{LF}}$

To complete the picture and account for the physical properties of lanthanide and transition metal complexes we shall consider an ion that interacts with other ions or atoms. The overall hamiltonian will then be

$$\mathcal{H} = \mathcal{H}_0 + \mathcal{H}_{\text{er}} + \mathcal{H}_{LS} + \mathcal{H}_{\text{LF}} \tag{1.9}$$

As regards lanthanide ions in metal complexes, the order of magnitude of different interactions is reported in table 1.1 and in more detail in table 1.2, evidencing that the *L-S coupling* scheme can be employed. For the transition metal ions the situation is more complicated, the *d* orbitals are more diffuse and the ligand field interaction $\mathcal{H}_{\mathrm{LF}}$ is of the same order of magnitude of the interelectronic repulsion $\mathcal{H}_{\mathrm{er}}$. Moreover, the effect of the ligands around the *d* orbitals leads to the 'quenching' of orbital angular momentum, thus reducing the contribution of the spin-orbit coupling $\mathcal{H}_{LS}$. Therefore,

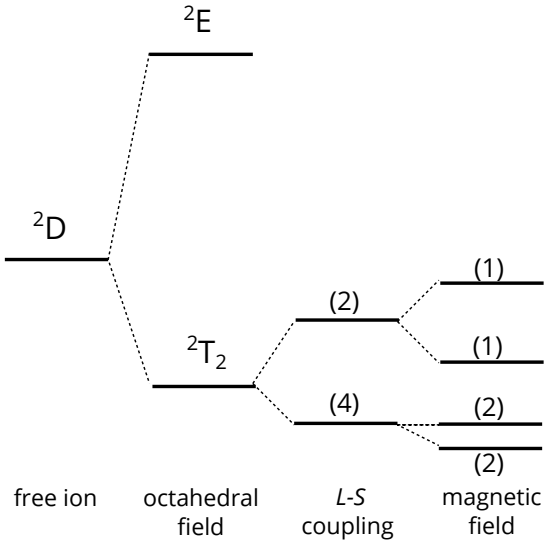

Figure 1.1.: Crystal field, spin-orbit and magnetic field splitting of the ^2D energy level of Ti(III). The figure is adapted from reference [28]. The numbers in parentheses indicate the degeneracy of a particular level (the Jahn-Teller distortion is not considered).

in the case of transition metal ion, the spin value S is a good quantum number and the states can be labeled as $^{2S+1}\Gamma_\gamma$ where Γ_γ are the labels of the irreducible representation, in Bethe's notation, of the point group symmetry of the metal site [3] (see also figure 1.1).

Table 1.2.: Order of magnitude for the energies of lanthanide ions in crystals.

Interaction	Energy (cm^{-1})
Central field hamiltonian	10^4 to 10^5
Interelectronic repulsion	10^4
Spin-orbit interaction	10^3
Crystal field	10^2
Interaction with a magnetic flux density of 10^4 G	1
Hyperfine interactions	10^{-3} to 10^{-1}

1.2. The Crystal Field approach

Among different approaches to model the effect of the ligands the Crystal field theory (CF) is the oldest and the simplest one. It assumes that the metal ion is ionized according to its formal positive oxidation number and the ligands are considered as negative point charges [27].

This theory was initially conceived to explain the spectroscopic characteristics of transition metal ion complexes [25] and it has been quite successfully applied also to lanthanides compounds. In this case, in fact, the $4f$ orbitals are inner compared to the filled orbitals of the xenon configuration and covalence plays a minor role (see figure 1.2).

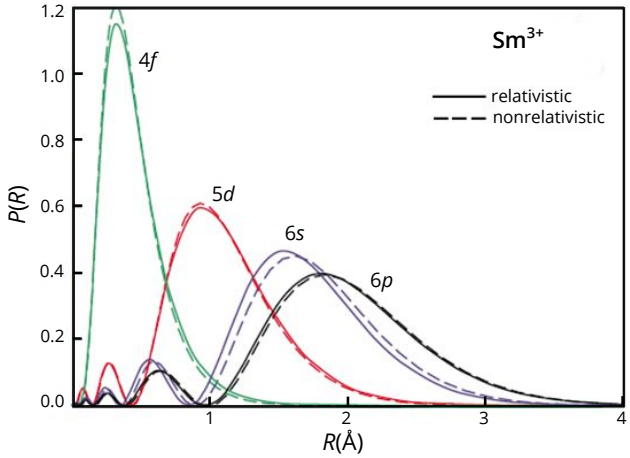

Figure 1.2.: Distribution of the radial charge for Sm(III).

The Crystal field hamiltonian is defined as [29]:

$$\begin{aligned} \mathcal{H}_{\mathrm{CF}} &= -e \sum_i V_{\mathrm{CF}}(\boldsymbol{r}_i) \\ &= -e \sum_{i,L} \frac{(-Ze)_L}{|\boldsymbol{R}_L - \boldsymbol{r}_i|} \end{aligned} \tag{1.10}$$

The summation $\sum_L$ is over the surrounding ions contributing to the crystal field experienced by all the electrons i of the central metal ion. If we expand the potential in equation (1.10), both by using the Legendre polynomials and the spherical harmonic addition theorem [30], we find

$$V_{\mathrm{CF}} = \sum_{i,L} \sum_{k=0}^{\infty} \frac{r_i^k}{R_L^{k+1}} P_k(\cos\omega)$$

$$= \sum_{i,L} \sum_{k=0}^{\infty} \frac{r_i^k}{R_L^{k+1}} \frac{4\pi}{2k+1} \sum_{q=-k}^{k} Y_k^{q*}(\theta,\varphi) Y_k^q(\theta_i,\varphi_i)$$
$$= \sum_{i,L} \sum_{k=0}^{\infty} \frac{r_i^k}{R_L^{k+1}} \frac{4\pi}{2k+1} \sum_{q=-k}^{k} (-1)^q Y_k^{-q}(\theta,\varphi) Y_k^q(\theta_i,\varphi_i) \tag{1.11}$$

The $Y_k^{-q}(\theta,\varphi)$ can be seen as expansion coefficient and the $Y_k^q(\theta_i,\varphi_i)$ as operator. For the sake of clarity $Y_k^{-q}(\theta,\varphi)$ and $Y_k^q(\theta_i,\varphi_i)$ will be shortened to Y_k^{-q} and $Y_k^q(i)$ respectively. It is then possible to rearrange the expression in equation (1.11) in several ways, depending on the system we are studying.

One possible way to deal with equation (1.11) is through the equivalent operator approach, also known as Stevens' formalism [31]. The equivalent operators are based on the result that, by using the Wigner-Eckart theorem, the following matrix elements are proportional and related to each other by a constant factor [32]

$$\langle l,m|x,y \text{ or } z|l,m\rangle \propto \langle l,m|l_x,l_y \text{ or } l_z|l,m\rangle \tag{1.12}$$

Following Abragam and Bleaney [33] it is possible to rearrange equation (1.11) as

$$V_{\mathrm{CF}} = \sum_{k=0}^{\infty} \sum_{q=-k}^{k} a_q^k \boldsymbol{O}_k^q \tag{1.13}$$

Sometimes the same equation is expressed as [34]

$$V_{\mathrm{CF}} = \sum_{k=0}^{\infty} \sum_{q=-k}^{k} \mathcal{A}_q^k \theta_k \boldsymbol{O}_k^q \tag{1.14}$$

where $\boldsymbol{O}_q^k$ are polynomials in the components of angular momentum $\boldsymbol{J}$ (or $\boldsymbol{L}$) and $\mathcal{A}_k^q$ are parameters that can be evaluated from experiment. θ_k are tabulated matrix elements that are easily computed if mixing between different J is neglected, thus the Stevens' formalism is suitable for the description of a single multiplet, speaking in terms of Russel-Saunders coupling.

The explicit form of $\boldsymbol{O}_q^k$ with respect to angular momentum operators and the values of θ_k can be found in the appendices of Abragam and Bleaney textbook [33], while the number of terms required in equation (1.13) depends on the point symmetry of the metal site. The matrix elements of the CF interaction can then be evaluated using the proper basis, that depends on the relative magnitude of the term $\mathcal{H}_{\mathrm{CF}}$ and $\mathcal{H}_{\mathrm{er}}$.

In the case of *transition metal ion* complexes it is worth mentioning that a Spin hamiltonian approach (SH) is quite used too. Indeed, in spectroscopic techniques like Electron Paramagnetic Resonance, EPR, this approach allows to interpret and

classify the obtained spectra without recurring in first instance to fundamental theories. The SH approach eliminates all the orbital coordinates and replaces them with spin coordinates, taking advantage of the symmetry properties of the system. In this view the simplest SH can be written as

$$\mathcal{H}_{\mathrm{SH}} = D\left(\boldsymbol{S}_z^2 - \frac{S(S+1)}{3}\right) + E(\boldsymbol{S}_x^2 - \boldsymbol{S}_y^2) \tag{1.15}$$

where D and E are the axial and rhombic zero field splitting parameters, accounting for the different energies of M_S states in the absence of a magnetic field.

When different multiplets have to be included, as it happens in the analysis of optical spectroscopy data, the equivalent operator approach is not well suited. Wybourne introduced a new formalism [35] and equation (1.11), after some math [29], can be written as

$$V_{\mathrm{CF}} = \sum_i \sum_{k=0}^{\infty} \Bigg[b_0^k \boldsymbol{C}_0^k(i) + \sum_{q=1}^{k} \Big(b_q^k \big(\boldsymbol{C}_{-q}^k(i) + (-1)^q \boldsymbol{C}_q^k(i)\big) + \mathrm{i} b'^k_q \big(\boldsymbol{C}_{-q}^k(i) - (-1)^q \boldsymbol{C}_q^k(i)\big) \Big) \Bigg] \tag{1.16}$$

where

$$b_0^k = \sqrt{\frac{4\pi}{2k+1}} Y_k^0 \sum_L (Ze^2)_L \frac{r^k}{R_L^{k+1}} \tag{1.17}$$

$$b_q^k = \sqrt{\frac{4\pi}{2k+1}} (-1)^q \,\mathrm{Re}\{Y_k^q\} \sum_L (Ze^2)_L \frac{r^k}{R_L^{k+1}} \tag{1.18}$$

$$b'^k_q = \sqrt{\frac{4\pi}{2k+1}} (-1)^q \,\mathrm{Im}\{Y_k^q\} \sum_L (Ze^2)_L \frac{r^k}{R_L^{k+1}} \tag{1.19}$$

$$\boldsymbol{C}_q^k(i) = \left(\frac{4\pi}{2k+1}\right)^{\frac{1}{2}} \boldsymbol{Y}_k^q(i) \tag{1.20}$$

The coefficients b are real number (note that b'^k_q are multiplied by the imaginary unit in equation (1.16)) and contain an angular and a radial part. The radial part dependency is considered to be the same for all states, so instead of r_i^k we have r^k. In the end we will not 'deal' with the radial dependency since everything that concerns non-angular parts will be absorbed by the definition of new coefficients. Indeed, the calculation of CF perturbation pertains matrix elements like

$$\big\langle \tau l L S J M \big| V_{\mathrm{CF}} \big| \tau' l' L' S' J' M' \big\rangle = \left\langle \tau l L S J M \left| \sum_{i,k,q} b_q^k \boldsymbol{C}_q^k(i) \right| \tau' l' L' S' J' M' \right\rangle \tag{1.21}$$

While $\boldsymbol{C}_q^k$ can be evaluated by using group theory methods, the radial part cannot be calculated exactly. It is then more suitable to define new parameters, B_q^k, that will contain both the radial dependency of the b_q^k and the radial part of the wavefunction. As parameters the B_q^k's will be determined semi-empirically, for instance from luminescence data [23].

In the end, after some rearrangements the details of which can be found in literature [29, 35] we obtain

$$\begin{aligned}
&\left\langle \tau LSJM \middle| \sum_i \boldsymbol{C}_q^k(i) \middle| \tau' L'S'J'M' \right\rangle = \\
&(-1)^{2J-M+S+L'+k+l} \left[(2J+1)(2J'+1)\right]^{\frac{1}{2}} \left[(2l+1)(2l'+1)\right]^{\frac{1}{2}} \\
&\times \begin{pmatrix} l & k & l' \\ 0 & 0 & 0 \end{pmatrix} \begin{pmatrix} J & k & J' \\ -M & q & M' \end{pmatrix} \begin{Bmatrix} J & J' & k \\ L' & L & S \end{Bmatrix} \left\langle \tau LS \middle\| \boldsymbol{U}^k \middle\| \tau' L'S' \right\rangle
\end{aligned} \tag{1.22}$$

where the big round and curl brackets represent the $3j$ and $6j$ symbols respectively, while the double reduced matrix element can be calculated by a recursion formula or found tabulated in [36]. Based on the properties for the $3j$ symbols one can deduce some selection rules:

- since for the $4f^n$ configuration $l = 3$ we have

$$\begin{pmatrix} 3 & k & 3 \\ 0 & 0 & 0 \end{pmatrix} = 0$$

  unless $k \leq 6$ and $(k+6)$ is even.

- for the other $3j$ symbol in equation (1.22)

$$\begin{pmatrix} J & k & J' \\ -M & q & M' \end{pmatrix} = 0 \tag{1.23}$$

  unless $-M + q + M' = 0$ and $|J-k| \leq J' \leq (J+k)$. In particular, if $J = J'$ we also have $k \leq 2J$.

The condition $-M + q + M' = 0$ determines which non-diagonal matrix elements will occur in the energy matrix for a given symmetry. The non-diagonal matrix elements are responsible for the fact that M will not remain a good quantum number, while J can be considered as such as long as only one multiplet is considered.

For the sake of clarity it is worth mentioning a couple of things about the B_q^k parameters. First of all they depend on the choice of the reference frame and, among several conventions, one of the most used is due to Prather [29]. According to the latter, the direction of the z axis is along the principal symmetry axis, while y corresponds to

a binary axis (if present). The x axis will be orthogonal both to z and y in order to have a right-handed reference frame. However, when the the symmetry is low the choice of the reference frame could not be straightforward. To overcome this inconvenience Rudowicz proposed to adopt a standardizations of the Crystal Field Parameters (CFP) [37].

As a second point, when dealing with the ground multiplet, the approaches defined in equation (1.22) and (1.14) are interchangeable, provided that $\mathcal{A}_q^k$ are correctly transformed to B_q^k or vice versa. A table with the relations among the parameters can be found in [34].

1.3. Anisotropy and interaction with a magnetic field

The study of magnetic anisotropy is a central topic in Molecular Magnetism, indeed, a necessary but not sufficient condition to observe a SMM behavior is to have magnetic anisotropy, that is a preferred orientation for the direction of magnetization. The origin of magnetic anisotropy resides in the spin-orbit coupling. Indeed, the spin angular momenta do not depend on spatial coordinates: however spins will be coupled to the electronic charge density via spin-orbit coupling, and their energy will therefore depend to some extent on their absolute orientation with respect to the crystal axes.

In lanthanide ions the combined action of the spin-orbit coupling and the crystal field (CF) induced by the ligand(s) donor atoms allows to have anisotropy in first order. On the contrary, in transition metal ion compounds, in particular for the elements with partially filled $3d$ shells, the presence of the ligands leads very often to the quenching of the orbital angular momentum, so that the magnetic properties are reproduced as if the compounds have $J = S$.[1] Anisotropy arises as a second order effect of the spin-orbit coupling with the excited states.

When a magnetic field is applied, the hamiltonian described in equation (1.9) gains a further term, called Zeeman term, that can be expressed as

$$\mathcal{H}_{\text{zmn}} = \mu_{\text{B}} \left(\boldsymbol{L} + g_S \boldsymbol{S} \right) \cdot \boldsymbol{B} \tag{1.24}$$

where μ_{B} is the Bohr's magneton and g_S is the free electron g-factor and, for most purpose, it is set equals to 2.[2] The energy contribution of equation (1.24) can be evaluated by choosing the proper basis. For transition metal ions, as mentioned before, the choice of the basis depends on the relative magnitude of the other interactions in equation (1.9). In the case of lanthanide ions, the Zeeman term can be always considered as a perturbation of the CF eigenstates (see also figure 1.3). Since The

[1] In fact, although the Curie's law is obeyed, the value of the Curie constant can usually be explained only if one assumes that $L = 0$ [20].

[2] In section 2.1 a few words will be spent on units of H and B.

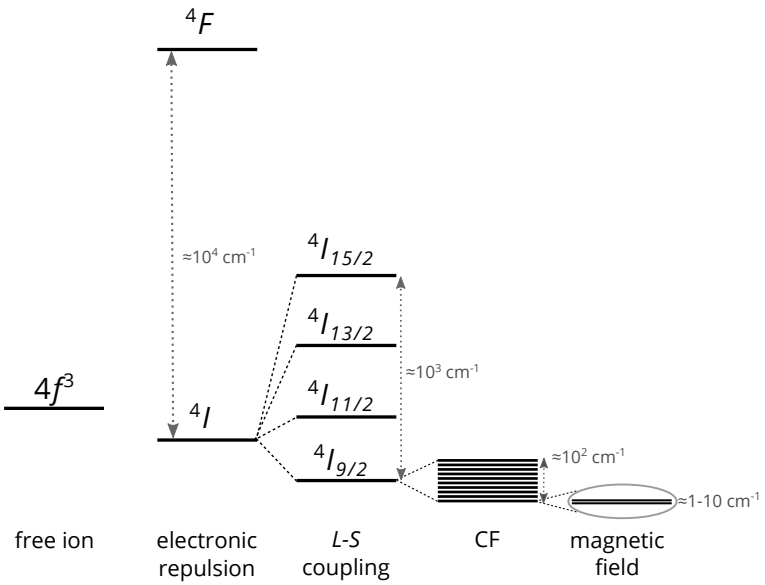

Figure 1.3.: Energy level diagram for Nd(III), considering the interaction described in equation (1.9) and a Zeeman term.

CF eigenstates are linear combinations of $|\tau LSJM\rangle$, to keep the work as simple as possible, we will consider 'pure state' and we will calculate the matrix elements of $\mathcal{H}_{\mathrm{zmn}}$ in the $|\tau LSJM\rangle$ basis (for convenience $|JM\rangle$). If only the ground multiplet is considered, then equation (1.24) can be written as

$$\left\langle JM'\middle|\mathcal{H}_{\mathrm{zmn}}\middle|JM\right\rangle = g_J\mu_{\mathrm{B}}\left\langle JM'\middle|\boldsymbol{B}\cdot\boldsymbol{J}\middle|JM\right\rangle \tag{1.25}$$

where g_J is the Landé factor

$$g_J = \frac{3}{2} - \frac{L(L+1) - S(S+1)}{2J(J+1)} \tag{1.26}$$

The calculation of the matrix elements of equation (1.25) can be performed with the help of the Wigner-Eckart theorem, since $\boldsymbol{J}_z$, $\boldsymbol{J}_x$ and $\boldsymbol{J}_y$ can be rearranged as spherical tensor operator of rank one:

$$\boldsymbol{J}_z = \boldsymbol{J}_0^1 \tag{1.27}$$

$$\boldsymbol{J}_x = \frac{-\boldsymbol{J}_1^1 + \boldsymbol{J}_{-1}^1}{\sqrt{2}} \tag{1.28}$$

$$\boldsymbol{J}_y = \frac{-\boldsymbol{J}_1^1 - \boldsymbol{J}_{-1}^1}{\mathrm{i}\sqrt{2}} \tag{1.29}$$

To understand the behavior of a system under an applied magnetic field it may be

useful to introduce the concept of *effective spin hamiltonian* $\mathcal{H}_{\text{eff}}$

$$\mathcal{H}_{\text{eff}} = g_{\text{eff}}\mu_{\text{B}}\boldsymbol{B}\cdot\tilde{\boldsymbol{S}} \tag{1.30}$$

where $\tilde{\boldsymbol{S}}$ is an effective spin, a fictitious angular momentum such that the degeneracy of the group of levels involved is set equal to $\left(2\tilde{S}+1\right)$. For instance, an isolated Kramers' doublet with two levels can be seen as if it possesses an effective spin $\tilde{S}=\frac{1}{2}$. It is worth noting that $\tilde{S}$ is not necessarily the true angular momentum of the system, in which case g_{eff} does not give the true magnetogyric ratio.

The form of equation (1.30) presupposes that $\mathcal{H}_{\text{eff}}$ depends only on the angle between the field and the effective spin. Actually, what is observed is that the interaction depends also on the angles that the magnetic field $\boldsymbol{B}$ makes with some axes defined by the local symmetry. Therefore a more general form of equation(1.30) will be

$$\mathcal{H}_{\text{eff}} = \mu_{\text{B}}\left(\boldsymbol{B}\cdot\boldsymbol{g}_{\text{eff}}\cdot\tilde{\boldsymbol{S}}\right) \tag{1.31}$$

where $\boldsymbol{g}_{\text{eff}}$ is a 3×3 matrix. If we choose a reference frame that corresponds to the principal axes of $\boldsymbol{g}_{\text{eff}}$,[3] then equation (1.31) reduces to

$$\mathcal{H}_{\text{eff}} = \mu_{\text{B}}\left(g_{xx}B_x\tilde{\boldsymbol{S}}_x + g_{yy}B_y\tilde{\boldsymbol{S}}_y + g_{zz}B_z\tilde{\boldsymbol{S}}_z\right) \tag{1.32}$$

According to the symmetry of the system three possible cases are encountered:

- $g_{xx} = g_{yy} = g_{zz}$, the system is isotropic, meaning that the response to the magnetic field does not depend on the direction along which it is applied;
- $g_{xx} = g_{yy} = g_{\perp}$ and $g_{zz} = g_{\parallel}$, if $g_{\parallel} > g_{\perp}$ the system has an easy axis, otherwise an easy plane;
- $g_{xx} \neq g_{yy} \neq g_{zz}$ the system is fully anisotropic.

In lanthanide ion compounds, an estimate of the upper limit for g_{eff} can be found by writing a state like $\psi = \sum_M c_M \left|JM\right\rangle$ (so without J mixing). If we consider only one value for M (so that $g_{\perp}=0$), supposing $M=J$ we have that

$$g_{\parallel} = g_{\text{eff}} = 2g_J J \tag{1.33}$$

with g_J the Landé factor (see equation (1.26)).

In addition to the interaction with an external magnetic field, also hyperfine coupling between electronic and nuclear spin may play a role. In a way similar to that employed

[3] I.e. the directions that are eigenstates of $\boldsymbol{g}_{\text{eff}}$.

for the magnetic field it can be shown that

$$\mathcal{H}_{\text{hyp}} = \tilde{\boldsymbol{S}} \cdot \boldsymbol{A} \cdot \boldsymbol{I} \tag{1.34}$$

where $\boldsymbol{A}$ is the hyperfine coupling tensor and $\boldsymbol{I}$ represents the nuclear spin. For lanthanide ion compounds hyperfine interaction is usually neglected in computing the energy level structure (see also table 1.2). Indeed, it is rarely detectable in EPR experiments for pure compounds and only high dilution in diamagnetic matrices allows to resolve the hyperfine coupling.

1.4. Magnetic relaxation processes: an overview

The polynuclear cluster Mn_{12} ($Mn_{12}O_{12}(CH_3COO)_{12}(H_2O)_4$) is universally considered the archetypal SMM [2]. Generally, when dealing with a $3d$ polynuclear SMM the overall spin hamiltonian includes terms that describe the exchange coupling interactions between the constituent paramagnetic centers and terms that describe the magnetic anisotropy of each single center. The exchange interaction is often the dominant term, giving rise to a ground state with well defined spin S, energetically well separated from the excited states, which can be much larger than the spin of the single centers. The effect of the anisotropy terms on the ground state, modeled by a spin hamiltonian of the type 1.15 is that of splitting the otherwise degenerate $(2S + 1)$ energy levels. As sketched in the Introduction, this may give rise to an energy barrier between the $\pm M_S$ states. The potential energy, in the simplest view, has then a parabolic dependence on the M_S, since the dominant term in the Spin hamiltonian has the form DS_z^2 (see equation (1.15) and figure 1.4b, with a negative D-value). In this picture, once the system has been magnetized along one direction (say $M_S = S$), the relaxation of the magnetization consists of consecutive transition between M_S states: to invert the magnetic moment the system must climb a number of steps on one side of the energy barrier and descend on the other. The mechanism of the individual steps is of minor importance and the relaxation time has a thermal dependence that is described by an Arrhenius' law:

$$\tau = \tau_0 \mathrm{e}^{\Delta/k_B T} \tag{1.35}$$

For SIMs containing lanthanide ions the magnetic relaxation occurs by means of one or two steps only, therefore the climbing of a single rung becomes important [38]. Indeed, the ground multiplet, split by CF, usually spans hundreds of cm^{-1}, a much larger range compared to $3d$ polynuclear SMMs. The archetype is the $[TbPc_2]^-$, also known as terbium double-decker [11]. The behavior of the relaxation time as a function of temperature was fitted through an Arrhenius' law. The value of the energy barrier, if an energy barrier sketch has a meaning here, was found to be around $200\,\mathrm{cm}^{-1}$, the

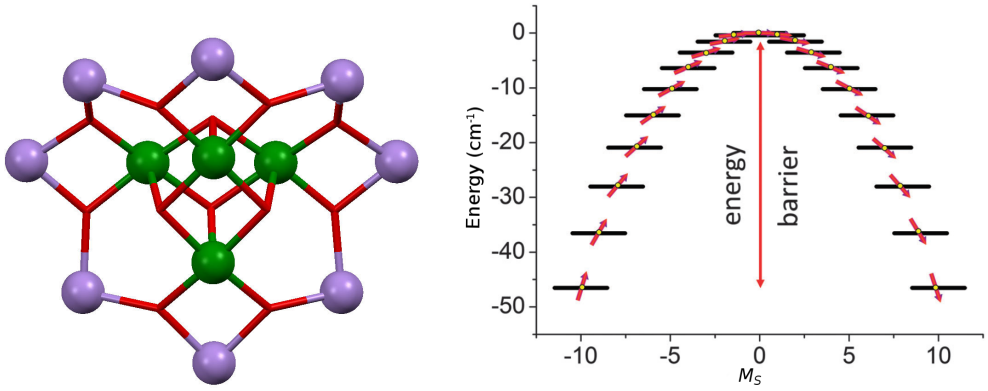

(a) Mn_{12} cluster structure. (b) Scheme for the double potential well for Mn_{12}ac.

Figure 1.4.: In figure 1.4a the magnetic core of Mn_{12} is reported, The violet circles represent the manganese ions with $S = 2$, while the green ones the ions with $S = \frac{3}{2}$. In figure 1.4b the anisotropy energy barrier is shown together with the magnetic relaxation steps [38].

same order of magnitude of the calculated energy of the first excited state [39].

In SMMs another possible way for passing from one side of the energy barrier to the other is through Quantum Tunneling of Magnetization (QTM). This is a temperature independent reversal mechanism which takes place when two levels on the opposite side of the barrier have the same energy but the two states are not orthogonal. For non-Kramers' ions (i.e. ions containing an even number of unpaired electrons) this can occur because of low symmetry CF terms, transverse magnetic fields or hyperfine interactions. For Kramers' ions an important theorem due to Kramers' states that the energy levels will be at least double degenerate (Kramers' doublet), no matter how low is the symmetry [33]. It is then mandatory to break the degeneracy of the resulting doublet for the QTM to occur. QTM, in zero applied magnetic field, can then be induced by hyperfine coupling or dipolar interactions in these systems. In addition, a thermally activated QTM can occur, if the two levels involved are not the lowest one. However, this is only possible if the system is first excited to a higher energy level, which requires a spin-lattice interaction.

It is usually assumed that the transfer of energy in magnetic relaxation takes place between the magnetic spin system and the lattice vibrations. Indeed the *spin-phonon interaction* accounts for various processes that can contribute to relaxation. A theoretical dissertation of such processes usually makes two main assumptions:

- the paramagnetic substances are fairly diluted, thus avoiding the complexities that arise from the interplay of spin-spin and spin-lattice interactions;
- the specific heat of the lattice c_{L} is infinite with respect to that of the spin systems c_{S} and the lattice is in thermal equilibrium with a heat bath of temperature T.

The second condition guarantees that the spin-bath relaxation time τ_{SB}, that is the physical quantity measured in AC magnetometry, is actually the spin-lattice relaxation time τ_{SL}. Indeed, when this request is not fulfilled, the rate of the heat transfer between the phonons and the surrounding heat bath may be so slow that the energy from the spin system will heat up the phonon system. In this case the spin system and the phonons constitute strongly coupled systems. This phenomenon is known as the *phonon bottleneck* [33] and in this case τ_{SB} can be seen as

$$\tau_{SB} = \tau_{SL} + \left(\frac{c_S}{c_L}\right)\tau_{LB} \tag{1.36}$$

where τ_{LB} is the lattice-bath relaxation time [40]. When the term $(c_S/c_L)\tau_{LB}$ is very small then $\tau_{SB} \sim \tau_{SL}$.

The evaluation of τ_{SL} requires to calculate the transition probability between the energy levels of the spin system caused by the interaction with the lattice. Indeed, from the physical point of view, the interaction can be seen as a modulation of the crystal field, through motion of the electrically charged ions under the action of lattice vibrations. There is, therefore, a sort of dynamic orbit-lattice interaction that can indirectly affect the spin levels, causing transition between these levels [33]. A possible approach consists of expanding the crystal field potential V_{CF} in powers of the strain:

$$V_{CF} = V_{CF}^{(0)} + \epsilon V_{CF}^{(1)} + \epsilon^2 V_{CF}^{(2)} + \dots \tag{1.37}$$

where the first term on the right is the static term. If ϵ is a fluctuating strain caused by phonons, then the remaining terms of equation (1.37) give the dynamic part of the spin system-lattice interaction.

To estimate the order of magnitude of the spin-lattice relaxation time τ_{SL} the assumption is usually made that each term $V_{CF}^{(n)}$ is of the same order as $V_{CF}^{(0)}$, though they will contain terms of lower symmetry. We will not enter into detail of the calculation here but we will recall the processes that can be involved in the magnetic relaxation [28] and their temperature and field dependence in Kramers and non-Kramers' ions. Since the calculation of the transition probability implies the evaluation of the matrix element of $V_{CF}^{(n)}$, the result will depend whether a Kramers or a non-Kramers' ion is considered.

To present some quantitative results we will introduce the following notation: the two lowest lying states will be called $|a\rangle$ and $|b\rangle$, separated by an energy difference of δ_{ab}, that can be equal to 0 if the two levels are degenerate in the absence of a magnetic field. For Kramers' ions this is obvious but it can happen also for non-Kramers' ions, when there is accidental degeneracy due to the symmetry of the CF. Then, we will consider an additional energy level $|c\rangle$, that lies at Δ with respect to $|a\rangle$.

The description of the different processes contributing to relaxation dynamics usually follows the traditional paper of Orbach [19], that dates back to the sixties and we will comply with that. A caveat seems however necessary. One of the main assumptions of that model, developed for ionic lattices, is that only acoustic phonons are taken into account, since the maximum phonon energy considered is $\hbar\omega \sim k_B\Theta_D$, where Θ_D is the Debye temperature. The Debye temperature can be seen as a measure of the stiffness of a material and in many solids is around hundreds of kelvin [20]. However, molecular crystals are in general more 'elastic', indeed Θ_D is the order of tenths of kelvin [41, 42]. For this reason, in molecular complexes optical modes lie at lower energy and they may therefore play a significant role in the relaxation of magnetization. Limiting the phonon spectrum to the acoustic branches in the analysis of the relaxation data of molecular systems seems then a bit restricting. Moreover, according to the Orbach's theory, the finding of energy barriers of hundreds of kelvin, when the Debye temperature is so low, contrasts with the hypotheses at the basis of the theory. Therefore, the relations that will be listed below for the different relaxation mechanisms should be taken carefully. Indeed, they are far from complete and the dependencies are simplified. It will be assumed, for instance, that the thermal energy is large compared to the Zeeman energy and that $\Delta \gg k_B T \gg \delta_{ab}$. For a most exhaustive dissertation and to have an idea of the order of magnitude of the several coefficients make reference to [19, 33, 43].

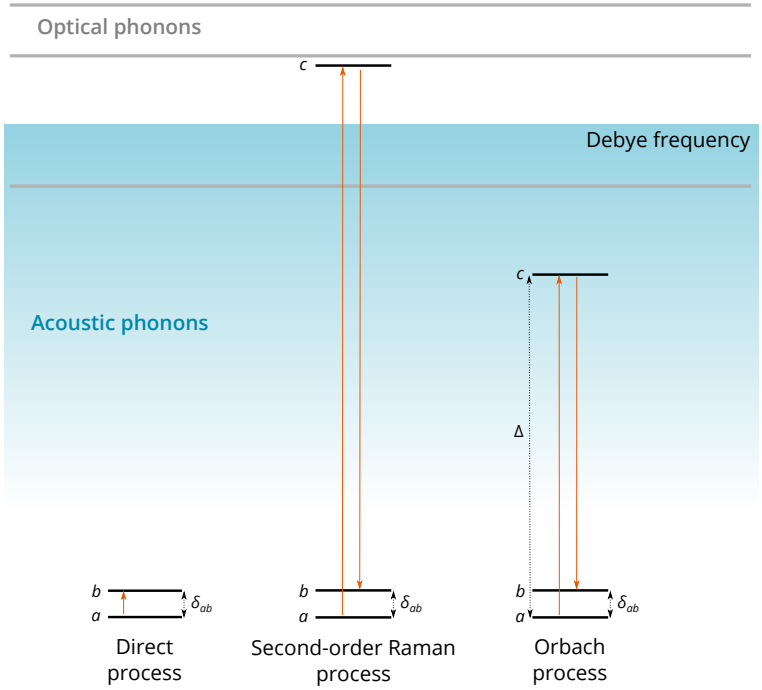

Figure 1.5.: Schematic view of the different processes described in the text, for simplicity it is assumed that potential doublets are split by Zeeman interaction. The figure is adapted from reference [38].

If only terms up to the second order are retained in the expansion of the CF potential, then the following processes are identified:

1. *Direct process.* There is a direct transition from one energy level to another one of the spin system and the energy difference δ_{ab} is taken up by (ore released to) the lattice, meaning that an acoustic phonon of frequency $\delta_{ab}/\hbar$ is absorbed (or emitted), as depicted in figure 1.5. In the absence of magnetic field this one-phonon process is available only for non Kramers' ion with no accidental degeneracy and according to [33] the following dependency on temperature is found:

$$\frac{1}{\tau_{\mathrm{SL}}} \sim aT \tag{1.38}$$

When also a non Kramers' ions experience degeneracy, the application of a magnetic field breaks it ($\delta_{ab} = g\mu_{\mathrm{B}}H$) and we have

$$\frac{1}{\tau_{\mathrm{SL}}} \sim bH^2T \tag{1.39}$$

For Kramers' ions when a magnetic field is applied we find:

$$\frac{1}{\tau_{\mathrm{SL}}} \sim cH^4T \tag{1.40}$$

It is worth mentioning that also hyperfine interaction can break the degeneracy of a Kramers' doublet in zero field, thus allowing a direct process but we will not discuss here the case.

2. *Raman process.* There are actually two types of Raman process. The first one is called first-order Raman process and it arises when the crystal potential $V_{\mathrm{CF}}^{(2)}$ has matrix elements between the two states $|a\rangle$ and $|b\rangle$. It is in principle observable in non-Kramers' ions or in Kramers' ions in the presence of a magnetic field. The second one is called second-order Raman process, in which a phonon of frequency ω_1 causes a virtual transition from one of the lowest states, let's say $|a\rangle$, to an excited one, followed by another virtual transition induced by a second phonon of frequency ω_2, in which the system return to the other ground state ($|b\rangle$). We use the term virtual transition because the energy of the excited state $|c\rangle$ is greater than the upper limit of the phonon spectrum $k_{\mathrm{B}}\Theta_{\mathrm{D}}$ (see figure 1.5). Any two phonons, whose energy difference is equal to δ_{ab}, can take part to the process. Therefore, especially at higher temperatures, there are much more phonons available that satisfy the this condition, compared to the case of the direct process where the single phonon should match δ_{ab} .

For a non-Kramers' ion, considering both type of processes the following approxi-

mate temperature dependency is found:

$$\frac{1}{\tau_{\mathrm{SL}}} \sim eT^7 \tag{1.41}$$

A similar relation can be encountered for Kramers' ion when a magnetic field is applied, $\tau_{\mathrm{SL}}^{-1} \sim H^2T^7$. Otherwise, the behavior in temperature is:

$$\frac{1}{\tau_{\mathrm{SL}}} \sim fT^9 \tag{1.42}$$

3. *Orbach process.* An Orbach process is a two-phonon process that occurs via a real intermediate state $|c\rangle$ of the spin system. The spin system absorbs a phonon and is excited from one of the two lowest states to an upper real state with energy Δ, then it relaxes to the other ground state by emission of another phonon. If the direct process between $|a\rangle$ and $|b\rangle$ is negligible then we find that

$$\frac{1}{\tau_{\mathrm{SL}}} \sim (\Delta)^3 \mathrm{e}^{-\Delta/k_{\mathrm{B}}T} \tag{1.43}$$

2. Experimental techniques

> It doesn't matter how beautiful your theory is, it doesn't matter how smart you are. If it doesn't agree with experiment, it's wrong.
>
> *(Richard P. Feynman)*

In this chapter we will briefly illustrate the experimental techniques used during this PhD. We will begin with the most common experiments of AC and DC magnetometry, that allow to study the static (χ) and dynamic bulk magnetic properties (τ_{SB} and τ_{SL}). Then a digression of EPR investigation, both in continuous wave (g_{eff}) and pulsed methods ($\mathcal{T}_1$ and $\mathcal{T}_2$), will be presented. In section 2.3 we will focus on Muon Spin Relaxation (μSR), a more exotic investigation technique of SMMs, that allows to locally probe the static and dynamic magnetic properties.

2.1. Magnetometers and susceptometers

The physical idea behind a magnetometer is to measure an electromotive force that is proportional to the variation of a magnetic flux (Faraday's law) [3]. This electromotive force is induced in a pick-up coil that collects the flux generated by the magnet itself and by the magnetized sample. The contribution of the magnet is usually eliminated by a proper design of the pick-up coils (the so called first and second order gradiometers), so that the recorded signal is in the end proportional to the magnetization of the sample.

In high sensitivity magnetometers, the induced current is not directly measured but the coils are inductively coupled to a Superconduting QUantum Interference Device (SQUID), a device that consists of a closed superconducting loop including one or two Josephson junctions. A SQUID is in essence a flux-voltage transducer, indeed any change in the magnetic flux in the detection coil induces a proportional change in the persistent current in the detection circuit. SQUIDs are kept in liquid helium bath and are shielded from the magnetic field produced by the superconducting magnet of the magnetometer. For field larger than 80 kOe vibrating samples magnetometers (VSM) are employed, instead of SQUID-based magnetometers, since such field values, even screened, destroy the superconductive state of the SQUID circuit.

During a DC magnetization measurement a static magnetic field H is applied and the

magnetization M[1] of the sample is recorded. As long as M depends linearly on H it is possible to extract the static magnetic susceptibility χ as M/H and the corresponding χT vs T curve, as well as the M vs H behavior. Since

$$\boldsymbol{\chi} = \frac{\partial \boldsymbol{M}}{\partial \boldsymbol{H}} \tag{2.1}$$

$\boldsymbol{\chi}$ is in principle a tensor. However, the magnetic measurement is often performed on a powder sample pressed in a pellet: due to the statistical distribution of grain orientations, the obtained χ value will then be an average, i.e. a scalar value.[2] It should be kept in mind that conventional magnetometers are usually sensitive to the component of magnetization parallel to the applied field. In the case of a single crystal the sample is usually attached on a cube of Teflon and the faces of the cube (XYZ) are indexed with an X-ray diffractometer. This procedure allows to know the orientation of XYZ with respect to the orthogonalized cell frame $ab'c^*$. The magnetization can then be investigated by performing rotations of the crystal around the three orthogonal directions XYZ. The measured values of $\chi = M/H$ are then fitted for each rotation and it is possible to extract the component of the $\boldsymbol{\chi}$ tensor, expressed in the XYZ reference frame. The diagonalization of the tensor leads to the principal values (eigenvalues) and to the principal direction (eigenvectors) of $\boldsymbol{\chi}$ in XYZ but the results can be conveniently translated in the orthogonalized cell frame $ab'c^*$. It must be pointed out that this procedure allows to obtain the $\boldsymbol{\chi}$ tensor of the crystal. This implies that whenever a cell contains molecules that are not iso-oriented the molecular $\boldsymbol{\chi}$ tensor can not be unambiguously determined.

For the sake of clarity few words should be spent at this stage on units. As Olivier Kahn wrote '...The SI is the legal system, but legality is not science...like most of the researchers in this field, we prefer to use the CGS emu system' [1]. In this unit system the magnetic field, H, is measured in oersted (Oe), however it is sometimes expressed also in gauss (G), that is the unit for the magnetic induction B. Indeed, for our purposes, permeability $\mu = \mu_0\mu_\mathrm{r}$ can be assumed to be that of the vacuum, because $\mu_\mathrm{r} = (1 + \chi_V) \sim 1$, where χ_V is the volume magnetic susceptibility (dimensionless). Since $\mu_0 = 1$ in CGS emu H and B have the same numerical value [3]. Molar susceptibility is rigorously expressed in $\mathrm{cm^3\,mol^{-1}}$ but it can be found also in $\mathrm{emu\,mol^{-1}}$.

In an ideal paramagnetic substance the χT vs T curve should be constant, since the energy should be degenerate with respect to M, projection of the angular momentum

[1] The measured magnetization, that is an extensive quantity, is usually rescaled to become a molar magnetization.

[2] To simulate the behavior of powder susceptibility χ it must be kept in mind that, if a non negligible magnetic anisotropy is present, then $\chi \neq \frac{1}{3}(\chi_{xx} + \chi_{yy} + \chi_{zz})$, where χ_{ii} are the calculated values along three orthogonal directions.

J. Indeed, the molar susceptibility according to the Curie's law is

$$\chi = \frac{N_A \mu_B^2 g_J^2 J(J+1)}{3 k_B T} \tag{2.2}$$

where N_A is he Avogadro number, μ_B the Bohr magneton and g_J the Landé's factor. However, in molecular complexes containing lanthanides, the presence of the CF lifts the degeneracy and mixes the M states so that, for low temperatures, a decrease in the χT vs T is observed (see, for instance, figure 2.1). The fitting of the χT vs T curve

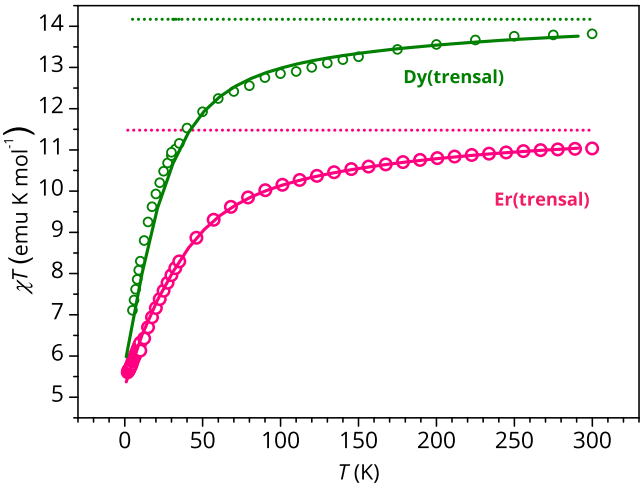

Figure 2.1.: χT vs T curve for Dy(trensal) and Er(trensal). The dotted lines represent the Curie constant for the two ions, while the solid lines are the curves simulated with the CFPs of reference [23].

can then give some information on the low lying levels of the complex. Nevertheless, to have a proper sketch of the energy level diagram a combination of other techniques should be used, such as luminescence, magnetic circular dichroism, multifrequency EPR spectroscopy etc [21].

A susceptometer is a magnetometer that can perform AC measurements. In an AC measurement the sample experiences a small oscillating field $h\cos(\omega t)$, usually with an amplitude not larger than 15 Oe. The pick-up coils are a first order gradiometer so that the detected signal is only due to the sample. Together with the oscillating field h a static magnetic field H_0 can be applied. The advantage of this kind of measurement is twofold: first, since the amplitude of the oscillating field is weak, the quantity actually measured is much closer to the real susceptibility $\partial M/\partial H$ without loosing in sensitivity, even at very low applied external DC field (see figure 2.2). As a second and more specific feature, this technique allows to investigate the dynamics of magnetization, by varying the frequency ω of the oscillating field. The complex

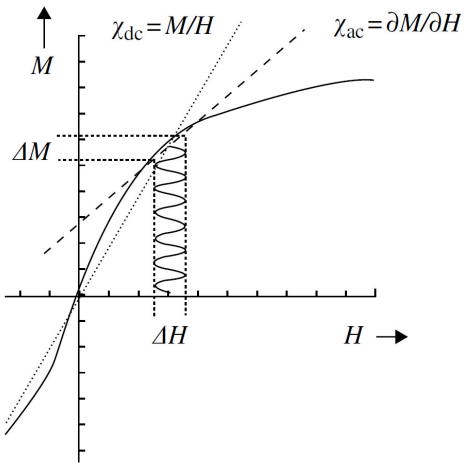

Figure 2.2.: The figure highlights the differences between M/H and $\frac{\partial M}{\partial H}$ [3].

susceptibility can be seen as:

$$M(t) = M_0 + \mathrm{Re}\{[(\chi' - \mathrm{i}\chi'')h\mathrm{e}^{\mathrm{i}\omega t}]\} = M_0 + (\chi' \cos(\omega t) + \chi'' \sin(\omega t))h \tag{2.3}$$

If $\chi'' \neq 0$, then the magnetic moment of the sample is not able to follow the oscillating field and we observe a relaxation of the magnetization. The real and imaginary components of the susceptibility are fitted according to [44]

$$\chi'(\omega) = \chi_S + (\chi_T - \chi_S)\frac{1 + (\omega\tau)^{1-\alpha}\sin(\pi\alpha/2)}{1 + 2(\omega\tau)^{1-\alpha}\sin(\pi\alpha/2) + (\omega\tau)^{2-2\alpha}} \tag{2.4}$$

$$\chi''(\omega) = (\chi_T - \chi_S)\frac{(\omega\tau)^{1-\alpha}\cos(\pi\alpha/2)}{1 + 2(\omega\tau)^{1-\alpha}\sin(\pi\alpha/2) + (\omega\tau)^{2-2\alpha}} \tag{2.5}$$

where τ is the relaxation time, α represents the distribution in relaxation times, χ_T and χ_S are the thermal and adiabatic susceptibility (for the possible mechanisms of relaxation see section 1.4).

DC magnetic measurements that will be presented in this dissertation were performed by using a Quantum Design MPMS SQUID magnetometer on powders pressed in a pellet. AC susceptibility was measured using a Quantum Design PPMS in AC mode for the frequency range 10 Hz to 10^4 Hz. The Quantum Design MPMS SQUID magnetometer was used for low frequencies (0.02 Hz to 10^3 Hz).

2.2. Electron Paramagnetic Resonance

EPR is a spectroscopic technique that allows to study molecules or atoms with at least one paramagnetic center, indeed it is largely employed for the characterization of molecular materials, organic radicals, metalloproteins, etc. Starting from the first

observation of an EPR spectrum by Zavoisky in 1944 [45], for a long period EPR used continuous-wave (CW) methods, in contrast with NMR spectroscopy, where they have been superseded by a multiplicity of pulse methods [46]. Lately, thanks to availability of less expensive commercial instrumentation, pulsed EPR has become an emerging research field and several variety of pulsed EPR techniques have been developed [47].

EPR can be a useful tool in the characterization of SMMs. Indeed, CW experiments can give information on the g-tensor anisotropy (see section 1.3), while pulsed EPR has been more recently employed to investigate the spin-lattice relaxation and the coherence time [24, 48].

2.2.1. Continuous wave EPR

EPR experiment on SMMs are usually performed at low temperature, especially for lanthanide-based complexes. Indeed, their unquenched orbital angular momentum implicates fast spin-lattice relaxation times and an EPR signal detectable only at cryogenics temperatures (see below). The splitting due to CF is such that only the lowest energy levels will be populated at low temperatures. The features of an EPR spectrum are then usually interpreted considering an effective spin $\tilde{S}$ that, for Kramers' ions, is often taken as 1/2. For non Kramers' ions the situation is more problematic, since the condition to observe the resonance may be not fulfilled at all, as we will explain in the following.

The interaction between a paramagnetic center and an external static field can be modeled through the concept of effective hamiltonian

$$\mathcal{H}_{\text{eff}} = \mu_{\text{B}} \left(\boldsymbol{B}_0 \cdot \boldsymbol{g}_{\text{eff}} \cdot \tilde{\boldsymbol{S}} \right) \tag{2.6}$$

Let's firstly suppose to have a $\tilde{S} = 1/2$ and an isotropic g_{eff}. When an external field is applied the degeneracy is broken and there is an energy splitting ΔE between the two levels $\approx B_0(\text{G})10^{-4}\,\text{cm}^{-1}$. If an oscillating magnetic field B_1 with frequency ν is applied it is possible to induce a magnetic transition between two energy levels if

$$h\nu = g_{\text{eff}}\mu_{\text{B}}B_0 \tag{2.7}$$

Since the Zeeman interaction is of order of few cm^{-1} the frequency ν will be in the range of the microwaves (1 GHz to 1000 GHz). The observation of a transition does not depend, however, only on the frequency employed. It must indeed satisfy the selection rules for the magnetic dipole transition: if the oscillating field is perpendicular to B_0 then $\Delta M_S = \pm 1$, while if it is parallel $\Delta M_S = 0$. The transition probability is higher the higher is the value of the matrix elements of the interaction between the two states.

In addition to that, the EPR signal is detectable if its linewidth Δ_B is not too broad

and this depends on the spin-lattice relaxation time $\mathcal{T}_1$ and on the spin-spin relaxation time $\mathcal{T}_2$. Indeed

$$\Delta_B \propto \frac{1}{\mathcal{T}_1} + \frac{1}{\mathcal{T}_2} \tag{2.8}$$

$\mathcal{T}_1$ can be increased by cooling the sample, and this is the reason why most EPR experiments, on systems containing $3d$ or $4f$ magnetic centers, are performed at liquid nitrogen or liquid helium temperature. As regards $\mathcal{T}_2$, it becomes longer by lowering the concentration of the spins in the sample, for instance lanthanide complexes are often diluted using an isostructural complex containing Y(III), La(III) or Lu(III)), which are diamagnetic. We will discuss further $\mathcal{T}_1$ and $\mathcal{T}_2$ in section 2.2.2

For Kramers' ions the hypothesis of having a $\tilde{S} = 1/2$ is often very reasonable. Indeed, at low temperature it is legitimate to suppose that only the lowest doublet is effectively populated. The experimentalist is then quite confident that the condition (2.7) is likely satisfied.[3] For non-Kramers' ion the situation is more delicate because they have integer values of angular momentum and it is less trivial to satisfy (2.7). This can happen, for instance, if the lowest state is a doublet due to an accidental CF degeneracy. Otherwise, if the lowest state is a singlet but the first excited state is low enough in energy that is populated at low temperature and it is a doublet, then the latter can satisfy (2.7). Eventually, there can be also an inter-state transition, maybe between two singlets if they are very close in energy. Anyhow, after that the requirement (2.7) is satisfied, then selection rule on M_S must hold and the matrix elements of the transitions should not be negligible.

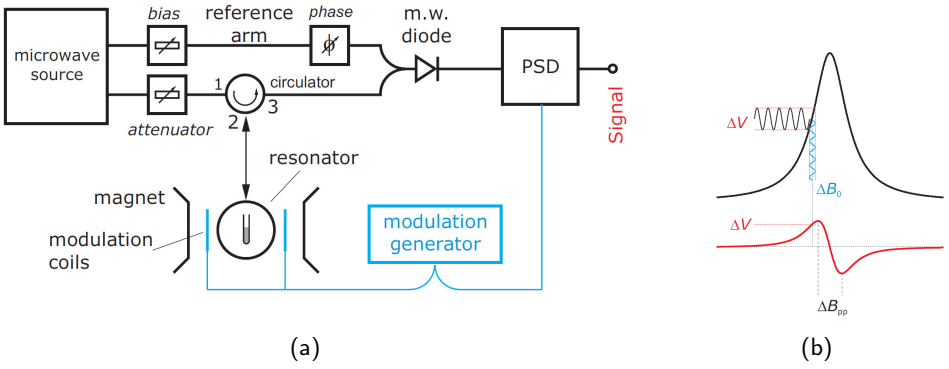

Figure 2.3.: The left panel (a) shows a schematic view of a CW EPR spectrometer. The right side (b) reports the absorption and the first derivative spectrum.

In CW experiment the spectrometer is built to work at a given frequency and the field B_0 varies. The EPR spectrum are then labeled according to the frequency employed,

[3] Of course also the selection rule must hold and in some cases this does not occur. Let's take for instance a Dy(III)-based complex: if the lowest doublet is a pure $|\pm 15/2\rangle$ then there will be no transitions, since the transition matrix elements are zero.

following the nomenclature developed in radar technology: X-band if $\nu = 9.5\,\text{GHz}$, Q-band if $\nu = 35\,\text{GHz}$, W-band if $\nu = 95\,\text{GHz}$. The higher is the frequency the better a given transition is resolved, since the corresponding g_{eff} is more clearly identified. Moreover, in the case of SMMs with non-Kramers' ions, if the frequency is higher there are more chances to fulfill condition (2.7). The use of higher frequencies requires to have higher static fields, which are usually generated by an electromagnet for X or Q-band frequencies while for W-band and beyond a superconductive magnet is necessary. In figure 2.3a a sketch of a standard EPR spectrometer is reported. Its main components are: the microwave source that generates B_1, the magnets that proceduce B_0, the resonator, the modulation coils that generate a small field parallel to B_0 and the signal detection system. We will briefly mention the role of the modulation coils while for a comprehensive description of the other components make reference to [49]. In figure 2.3b the absorption spectrum and the corresponding first derivative spectrum are displayed. Indeed, to minimize the noise contribution a phase-sensitive detection technique is used. This means that a a modulating field B_2, usually with a frequency of 100 kHz and amplitude 0.1 G to 10 G is superimposed to B_0. If the modulation amplitude is much less than the width of the signal then a derivative signal with respect to the original one is obtained.

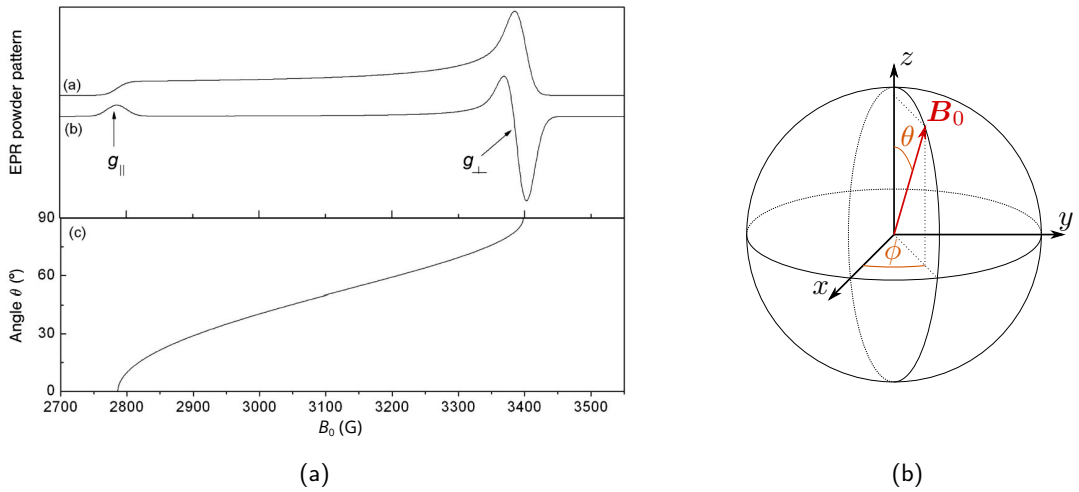

Figure 2.4.: In figure 2.4a a comparison between the absorption (a) and first derivative (b) EPR lineshape for $S = 1/2$ spin system with axial symmetry randomly oriented is reported. The angular dependence curve (θ vs B_0) is shown as (c) and it can be obtained from equation (2.9). The figure is adapted from reference [47]. In figure 2.4b the reference frame xyz is collinear to the principal axes of g_{eff}. The pair of angles (θ, ϕ) identifies the direction of B_0.

Coming back to condition (2.7), if the tensor g_{eff} is not isotropic the field B_0 will not be in general parallel to one of the principal axes of g_{eff} (see section 1.3 and figure

2.4b). Its orientation with respect to the principal axes will be identified by a pair of angles (θ, ϕ) and the resonance condition becomes

$$h\nu = g_{\text{eff}}(\theta, \phi)\mu_{\text{B}}B_0 \tag{2.9}$$

where

$$g_{\text{eff}}(\theta, \phi) = \sqrt{\sin^2(\theta)\cos^2(\phi)g_1 + \sin^2(\theta)\sin^2(\phi)g_2 + \cos^2(\theta)g_3} \tag{2.10}$$

and g_1, g_2, g_3 are the principal values of the tensor. As an example, in figure 2.4a a spectrum of an axial system is reported.

Both a crystal or powder samples can be measured through EPR. For a single crystal it is possible to perform an EPR experiment by rotating the sample along three orthogonal directions. The modus operandi is therefore similar to the determination of $\boldsymbol{\chi}$ tensor case mentioned in section 2.1. The principal values of g_{eff} and the corresponding orientation of principal axes with respect to the molecule can then be extrapolated.[4] On the contrary, in a powder spectrum only the principal values of g_{eff} can be extracted: it is then more correct to label the observed value as g_1, g_2 and g_3 than of g_{xx}, g_{yy} and g_{zz}, since no information is obtained about the orientation of the magnetic axes.

The CW EPR spectra that will be presented in this thesis were recorded with a E500 Bruker spectrometer for the X band and a E600 Bruker spectrometer for the W band. The high field-high frequency EPR spectra were recorded on a home-made instrument at LNCMI – Grenoble [50, 51].

2.2.2. Pulsed EPR

The principal advantage of pulsed EPR is the opportunity to change the type of EPR experiment according to the kind of information we want to extract. For instance, if we are interested in the spin relaxation then a spin echo or an inversion recovery measurement are a good approach, while if the main concern is to resolve hyperfine interactions then an ENDOR (Electron Nuclear Double Resonance), a HYSCORE (Hyperfine Sublevel Correlation Spectroscopy) or ESEEM (Electron Spin Echo Envelope Modulation) measurement would be more effective [52]. We will not give a complete description of pulsed EPR and its applications because it is beyond the scope of this thesis. In the following, we will focus on spin echo experiments, in particular how to measure the spin lattice relaxation time $\mathcal{T}_1$ and the spin-spin relaxation time $\mathcal{T}_2$, since these have been applied in chapter 6. The treatment will be kept to a base level: for a rigorous introduction make reference to [53].

In a pulsed EPR experiment the electron spins are excited by a series of microwave pulses and the signal induced by these pulses is measured while there are no microwaves

[4] If the crystal cell contains molecules that are not iso-oriented the determination of the orientation of the magnetic tensors may not be univocal.

applied. Since spins are quantum entities the correct picture would require a quantum treatment. Anyway, if we deal with an ensemble of non interacting electron spins (each of them having $S = 1/2$), we may consider the sum of the electron spin moments, that is a magnetization, and call it $\boldsymbol{M}$. $\boldsymbol{M}$ is a macroscopic quantity that follows the laws of classical mechanics. This fact allows us to introduce the basic concept of pulsed EPR in a more intuitive way. This classical vector $\boldsymbol{M}$ is a depiction of the quantum density matrix that describes a single unpaired electron [52]. For systems containing atoms or molecules with $S > 1/2$ the full quantum treatment by means of the density matrix formalism is required [53].

Let's imagine to have the magnetization of a spin ensemble represented by a vector $\boldsymbol{M}$. We neglect for the moment the interaction of $\boldsymbol{M}$ with the surrounding apart from external applied fields. A static magnetic field $\boldsymbol{B}_0$ identifies the z_{L}-direction of the laboratory frame. Since

$$\frac{\mathrm{d}\boldsymbol{M}}{\mathrm{d}t} = -\frac{g_e \mu_{\mathrm{B}}}{\hbar} \boldsymbol{M} \times \boldsymbol{B}_0 \tag{2.11}$$

the magnetization is invariant if it lies along $\boldsymbol{B}_0$, otherwise it will precess around the z_{L} axis with an angular frequency

$$\omega_S = \frac{g_e \mu_{\mathrm{B}} B_0}{\hbar} \tag{2.12}$$

that is also called Larmor frequency. We then introduce a second magnetic field $\boldsymbol{B}_1$ in the picture. $\boldsymbol{B}_1$ is a time dependent, linearly polarized magnetic field and it can be seen as the sum of two magnetic fields rotating in opposite directions with frequency ω_{mw} in the $x_{\mathrm{L}}y_{\mathrm{L}}$ plane. We now move the description of the motion of $\boldsymbol{M}$ in a reference frame xyz that rotate counterclockwise in $x_{\mathrm{L}}y_{\mathrm{L}}$ plane with frequency ω_{mw}. In this reference frame one of the rotating components of $\boldsymbol{B}_1$ will be stationary, while the other one will rotate with a frequency $2\omega_{\mathrm{mw}}$ and will be neglected in the following. Let the direction of B_1 be along along x in the new reference frame. We will keep ignoring for the moment any relaxation processes for the magnetization components. We introduce the quantity $\Omega_S = \omega_S - \omega_{\mathrm{mw}}$ and $\omega_1 = g_e \mu_{\mathrm{B}} B_1/\hbar$ and we write down the equation for the motion of $\boldsymbol{M}$

$$\frac{\mathrm{d}M_x}{\mathrm{d}t} = -\Omega_S M_y \tag{2.13}$$

$$\frac{\mathrm{d}M_y}{\mathrm{d}t} = \Omega_S M_x - \omega_1 M_z \tag{2.14}$$

$$\frac{\mathrm{d}M_z}{\mathrm{d}t} = \omega_1 M_y \tag{2.15}$$

If $\omega_{\mathrm{mw}} = \omega_S$, that is the resonant radiation case, then $\Omega_S = 0$ and $\boldsymbol{M}$ will precess around x. Otherwise, there will be a superposition of precession (along z and x) that

leads to a nutation about an effective field B_{eff} which is vector sum of the off-resonance contribution Ω_S and the microwave field ω_1. The axis of the effective field is inclined of $\theta = \arctan(\omega_1/\Omega_S)$ and the nutation frequency is $\omega_{\text{eff}} = \sqrt{\Omega_S^2 + \omega_1^2}$.

The magnetic field B_1 is actually on for a short time, meaning that it is a pulse of length t_{p}. In the resonant case $\theta = \pi/2$ and there will be a precession about the x axis. If at $t = 0$ $\boldsymbol{M}$ is along z, it will be rotated, after the pulse, by an angle $\beta = \omega_1 t_{\text{p}}$. For instance, if $\beta = \pi/2$ the magnetization, parallel to z at $t = 0$, will be along y at the time t_{p} and it remain constant since we are ignoring relaxation. This is a so called $\pi/2$ pulse along x.

When we are out of resonance, $\Omega_S \neq 0$, there are few considerations to be done. If $\Omega_S \ll \omega_1$ then B_0 may be neglected during the pulses and it will be considered in the time intervals where B_1 is absent, the so-called intervals of free precession. Indeed, the magnetization after the pulse will be along y and it will have a precession in the rotating reference frame xyz with a frequency Ω_S. However, if $\Omega_S \ll \omega_1$ does not hold, the actual angle flip will be $\beta_{\text{eff}} = \omega_{\text{eff}} t_{\text{p}}$ and the axis of rotation lies no longer in the xy plane. It is then important to maximize ω_1/Ω_S so that $\theta \to \pi/2$. This means to have a larger B_1 (or equivalently a shorter pulse) [54].

If we now recall that the magnetization can relax, there are additional terms that must be considered in the equation system defined in (2.13). Indeed, if the electron spins interact with the surrounding there must be some processes that restore the equilibrium. When an external static field B_0 parallel to z is present and a pulse is applied the magnetization will tend to re-align with the z axis after a time $\mathcal{T}_1$, the so called spin-relaxation time. The transverse relaxation time $\mathcal{T}_2$ describes how fast the magnetization in the xy plane disappears. Including this terms we find the rotating-frame Bloch's equations

$$\frac{\mathrm{d}M_x}{\mathrm{d}t} = -\Omega_S M_y - \frac{M_x}{\mathcal{T}_2} \tag{2.16}$$

$$\frac{\mathrm{d}M_y}{\mathrm{d}t} = \Omega_S M_x - \omega_1 M_z - \frac{M_y}{\mathcal{T}_2} \tag{2.17}$$

$$\frac{\mathrm{d}M_z}{\mathrm{d}t} = \omega_1 M_y - \frac{M_z - M_0}{\mathcal{T}_1} \tag{2.18}$$

For instance, after a $\pi/2$ pulse that rotates M_z along M_y, if $\Omega_S \neq 0$, the signal will actually precess about the z axis with frequency Ω_S and an observer along y will now see an oscillating signal that decays because of transverse relaxation ($\mathcal{T}_2$).

We will now briefly mention how to measure the spin-lattice relaxation time $\mathcal{T}_1$ and the transverse relaxation time $\mathcal{T}_2$. Actually, in the latter case the experiment provides $\mathcal{T}_{\text{m}}$, the phase-memory time, a lower limit of $\mathcal{T}_2$. Indeed, $\mathcal{T}_{\text{m}}$ is influenced also by non resonant processes that contribute to the loss of signal, making $\mathcal{T}_{\text{m}}$ shorter than $\mathcal{T}_2$.

The most direct way of measuring relaxation time relies on spin echo methods.

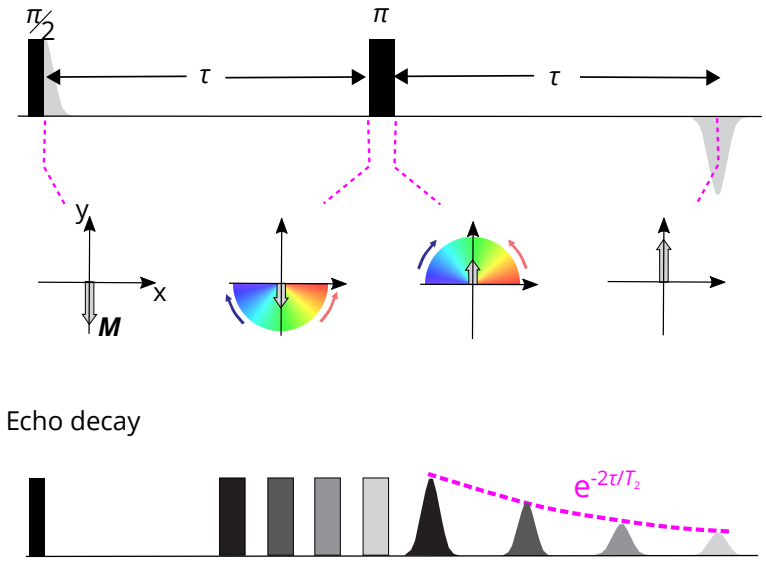

Figure 2.5.: Top: sequence pulses with the $\pi/2$ followed by the π pulse that refocuses the various transverse vectors. Bottom: Intensity of the echo signal by varying the value of τ. Figure adapted from [55].

As regards $\mathcal{T}_{\mathrm{m}}$ this is measured by means of a two-pulse echo as a function of the pulse interval (Hanh echo). Firstly a $\pi/2$ along x is applied,[5] and the magnetization is rotated along y. However, the ensemble of spin has actually different Larmor frequencies ω_S and the condition $\Omega_S = 0$ cannot be satisfied for all of them at the same time. We have then a precession of the various magnetization vectors, with individual frequencies $(\omega_{S,i} - \omega_{\mathrm{mw}})$. After a time τ a π pulse along x is applied, the magnetization vectors refocus and an echo signal is detected (see figure 2.5). By varying the time interval between the two pulses it is possible to reconstruct the decay of the transverse magnetization as a function of time and $\mathcal{T}_{\mathrm{m}}$ is then extracted by fitting the decay curve.

There are several sequences that can be used to measure $\mathcal{T}_1$: the most common one, known as inversion recovery, uses a π pulse to invert the magnetization, from z to $-z$. The magnetization will then start to relax and, after a time t_I, called inversion time, a two pulse sequence like the one described above is applied. By varying t_I a recovery curve as function of time is obtained and it is possible to extract $\mathcal{T}_1$.

One of the advantages of pulsed EPR with respect to AC susceptometry is that EPR is a resonant technique. Moreover, it gives access to faster time scale and the experiment can be performed at higher temperatures. $\mathcal{T}_1$ is a measure of the relaxation time between two levels and its value can be in principle different from AC τ_{SL}. In the case of a two-level system ($S = 1/2$) $\mathcal{T}_1$ and τ_{SL} should have comparable values. Indeed, the two techniques should probe the same dynamics only in the case of a true $S = 1/2$ with ho hyperfine splitting.

[5] We assume an ideal pulse, infinitesimally short.

2.3. Muon Spin relaxation

Muon Spin Relaxation spectroscopy, μSR, is a technique that can be employed to investigate several phenomena in condensed matter physics. In particular, it can be used for probing local static and dynamic magnetic properties [56].

μSR makes use of beams of spin-polarized muons, elementary particle with $S = 1/2$ and with a mass intermediate between that of the electron and the proton. In principle, μSR can be performed both with positive or negative muons but, since the latter behave like heavy electrons they are easily captured by the atoms in the sample material. Positive muons are then employed most of the times, they can be implanted in a sample and the detection of their precession and relaxation gives information on the local magnetic properties of the sample.

One of the advantages of using μSR technique is that it can be performed in zero applied field. It also gives access to a time window of the dynamics that bridges the gap between neutron scattering (1×10^{-8} s to 1×10^{-13} s) on one side, and bulk magnetic measurements on the other (1×10^{-4} s to 1×10^{2} s). However, since muon beams imply the presence of particle accelerator, μSR is available only in large scale facilities. In Europe there are two main centers, ISIS at the Rutherford Appleton Laboratory of the Science and Technology Facilities Council in England and Paul Scherrer Institute (PSI), near Villigen in Switzerland.

Muon beams used in μSR can be identified by their time structure (pulsed vs. continuous) and by the muon momentum or energy (surface vs. decay-channel beam lines). The measurement reported in this dissertation were collected in three different stages at PSI with continuous surface muon beams, in particular on GPS (General Purpose Surface-Muon Instrument) and DOLLY beamlines.

2.3.1. Muon production and spectrometer

The production of fully polarized muon beams relies on the parity violation of weak interaction. A high energy proton beam[6] collides on a carbon or beryllium target and this produces positive pions π^+, as it can be see in figure 2.6a. The positive pion then decays in a positive muon μ^+ and in a muon neutrino ν_μ[7]

$$\pi^+ \rightarrow \mu^+ + \nu_\mu \tag{2.19}$$

[6] It can be shown that the threshold for the pion production implies that the kinetic energy of the proton beam in the laboratory frame must be at least 281.5 MeV. In practice, a beam energy of 500 MeV is usually employed [57].

[7] For the sake of simplicity we will use the symbol μ^+ instead of $\bar{\mu}^+$ because the charge distinguishes between the particle and the anti-particle. In the case of neutrino we will keep the barred notation.

In the rest frame of the pion the outgoing muon and neutrino have opposite linear momentum equal to 29.79 MeV/c an the kinetic energy of the muon is 4.1 MeV.

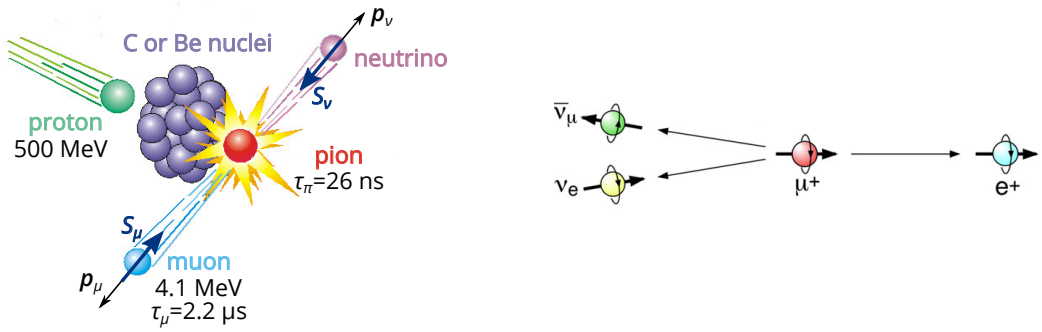

(a) Pion production and decay.

(b) Decay of a positive muon.

Figure 2.6.: On the left side (a) of the panel the pion production and its decay is shown. On the right side (b) of the panel the three body decay for a positive muon is represented.

Since the pion is a spinless particle and neutrino has negative helicity, meaning that its spin is aligned antiparallel with its momentum, muon and neutrino spin must be opposite to fulfill the angular momentum conservation (see figure 2.6b). Therefore, to obtain fully polarized muons one possibility is to select only muons that originate from motionless pions. This is achievable if the rest frame of the pion coincides with the laboratory frame, meaning that the pion decays on the surface of the production target (surface muon beams).[8]

The muons itself decays with a lifetime of 2.2 µs, to a positron, an electron neutrino and a muon antineutrino

$$\mu^+ \rightarrow e^+ + \bar{\nu}_\mu + \nu_e \tag{2.20}$$

In this case the situation is more complicated, since there are three particles. The only detectable particle is the positron and the phenomenon of non parity conservation implies that the positron has an anisotropic spatial distribution. Indeed, it is preferably emitted along the direction of the muon spin and the angular distribution function of the positron can be expressed as

$$W(E, \theta) = 1 + a_0(E) \cos\theta \tag{2.21}$$

where θ is the angle between the positron direction and the muon spin, the factor a_0 is called initial asymmetry and it depends on the positron energy, for instance $a_0(E_{\max}) = 1$. Since the positron detectors used in μSR are not sensitive to the energy

[8] In decay-channel beam high-momentum pion are allowed to decay in flight and the beam line geometry collects only forward or backward muon with respect to the direction of pion momentum. In this case the muon energy is one order of magnitude greater than a surface muon.

of the particle detected the average over all energy of the function $a_0(E)$ gives $a_0 = 1/3$. In practice, a smaller value of a_0 around 0.2 is usually found due to experimental conditions.

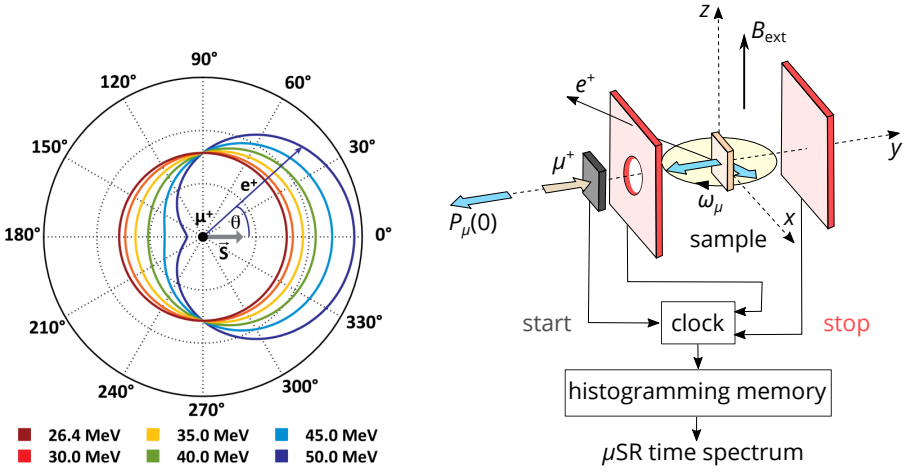

(a) Positron angular distribution. (b) μSR spectrometer.

Figure 2.7.: On the left side (a) of the panel the spatial distribution of the positron for different energies is shown. On the right side (b) a schematic view of μSR spectrometer is presented.

In figure 2.7b the basic layout of a μSR spectrometer is shown. When a muon trigger passes through a scintillation detector (dark grey in figure) the detector delivers a signal which establishes zero time (t_0) and starts a digital clock. When the forward or the backward detector (red in figure) register a decay event, that is a positron, a stop signal is sent to the clock, which stores the elapsed time span ($t - t_0$) as a digital number. The procedure is repeated for a large number of incoming muons and to obtain a time histogram the number of registered events is typically of order of $\sim 10^6$. An additional logical circuit, called muon gate, prevents that a second muon triggers the counter while the stop signal has not been recorded.

The data collected by the forward detector should be least-square fitted using

$$N_{\mathrm{F}}(t) = N_{\mathrm{F}}(0)\mathrm{e}^{-t/\tau_\mu}(1 - a_0 G(t)) \tag{2.22}$$

where $G(t)$ denotes the spin relaxation function and it allows for possible loss of degree of polarization with time. For the backward detector the equation is analogue but, because of the shift of 180°, it is $\propto (1 + a_0 G(t))$.

Usually, it is the backward-forward ratio, called asymmetry $\mathcal{A}(t)$ that is fitted. Ideally it is defined as [56]

$$\mathcal{A}(t) = \frac{N_{\mathrm{B}}(t) - N_{\mathrm{F}}(t)}{N_{\mathrm{B}}(t) + N_{\mathrm{F}}(t)} \tag{2.23}$$

However, since from the experimental point of view the forward and backward detector have different counting efficiencies, one defines a parameter α

$$\alpha = \frac{N_{\mathrm{F}}(0)}{N_{\mathrm{B}}(0)} \tag{2.24}$$

and, combining equation (2.22) and (2.24), the asymmetry $\mathcal{A}(t)$ becomes

$$\mathcal{A}(t) = \frac{(1-\alpha) + (1+\alpha)a_0 G(t)}{(1+\alpha) + (1-\alpha)a_0 G(t)} \tag{2.25}$$

if $\alpha = 1$ equation (2.23) is recovered and $\mathcal{A}(t) = a_0 G(t)$. The α parameter causes a shift of the baseline for $\mathcal{A}(t) \to \infty$ and its value is usually determined by performing low transverse field measurements.

The muon can implant in different sites and the total asymmetry $\mathcal{A}(t)$ of the muon ensemble is divided into the partial asymmetries of the n distinct muon sites, according to

$$\mathcal{A}(t) = \sum_{i}^{N} \mathcal{A}_i(t) \tag{2.26}$$

The initial partial asymmetry, $\mathcal{A}_i(0)$ may be written as $\mathcal{A}_i(0) = \mathcal{A}p_i$, where p_i is the stopping probability at the ith site.

2.3.2. Transverse, zero and longitudinal field measurements

In a μSR experiment the projection of the polarization $G(t)$ along a direction is measured, that is the direction of the positron detector. In transverse field (TF) geometry, supposing that the z axis is the axis of the magnetic field, $G_x(t)$ is measured. In zero field (ZF) and longitudinal field (LF) $G_z(t)$ is measured.

Transverse field means that the applied magnetic field is oriented perpendicular to the initial muon spin polarization. Sensing a TF the muon spin precesses in the plane perpendicular to the field axis (z axis) and the asymmetry $\mathcal{A}(t)$ has the form

$$\mathcal{A}(t) = a_0 G_x(t) \cos(2\pi f_\mu t) \tag{2.27}$$

where the spin precession frequency f_μ is directly proportional to the magnitude of the field $\boldsymbol{B}_\mu$

$$f_\mu = \frac{\gamma_\mu}{2\pi} B_\mu \tag{2.28}$$

where γ_μ is the muon magnetogyric factor and its value is $85.1\,\mathrm{kHz\,G^{-1}}$. The field B_μ is the overall field experienced by the muon, i.e. the sum of the applied field and of the average of internal fields of the sample. According to the internal field distribution, that can be Gaussian or Lorentzian, the function $G_x(t)$ will have a different time

dependence. It is beyond the scope of this dissertation to deepen this point and we make reference to [56] for further details.

TF measurements are usually performed because they allow to fit the α parameter that accounts for the different counting efficiencies of the two detectors. The correct α value, in fact, will give oscillation centered around zero.

To perform measurement in longitudinal geometry (ZF or LF) it is mandatory to have a true perpendicular field condition because a low frequency spin precession induced by a weak external field is difficult to distinguish from slow relaxation.

In zero field (ZF) measurements, for a true paramagnet, the local fields of the sample are randomly oriented. This means that the mean value of $\boldsymbol{B}_\mu$, $\langle \boldsymbol{B}_\mu \rangle$, vanishes and we will not observe a precession. However, the second central moment of the field distribution, $\langle B_\mu^2 \rangle$, will be in general different from zero. If the the distribution of internal field is stationary and Gaussian the muon spin relaxation can be described by the (Gaussian) Kubo-Toyabe function [56]

$$G_z(t) = \frac{1}{3} + \frac{2}{3}(1 - \Delta^2 t^2)\mathrm{e}^{-\frac{1}{2}\Delta^2 t^2} \tag{2.29}$$

In this case, as it can be seen in figure 2.8, not all the muons precess since some of them (1/3 of the ensemble) reside in sites where the local magnetic field is parallel or antiparallel to their initial spin direction. These muons will have a constant polarization unless the field changes with time.

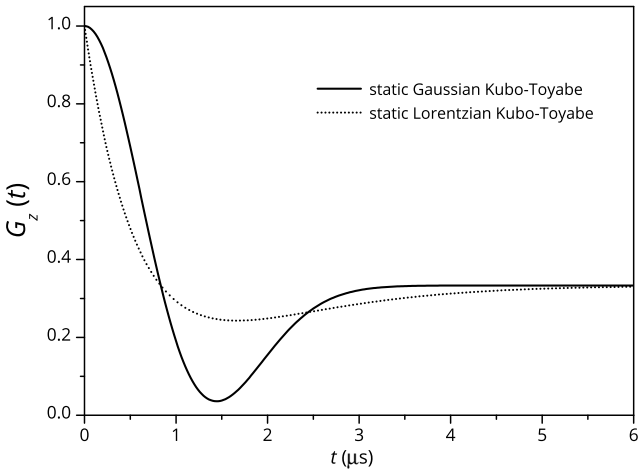

Figure 2.8.: Static Kubo-Toyabe function in ZF for a Gaussian field distribution (solid line) and for a Lorentzian field distribution (dotted line).

In the case of diluted spin systems, when less than 10 % of the surroundings atoms have a moment, it is more appropriate a Lorentzian distribution of the field and the corresponding polarization is described by the Lorentzian Kubo Toyabe function (see

figure 2.8)

$$G_z = \frac{1}{3} + \frac{2}{3}(1 - at)\mathrm{e}^{-at} \tag{2.30}$$

The application of longitudinal field B_L, parallel to the initial direction of the muon spin, can be useful when a Kubo-Toyabe relaxation is observed in ZF. Indeed, the applied field competes with the internal field distribution and, under certain conditions, the muon senses only the parallel-oriented B_L. The main effect, in this case, is the suppression of the spin depolarization (longitudinal field decoupling), that means that 1/3 of the ensemble of muons with spin parallel or antiparallel to the local field is increased in B_L.

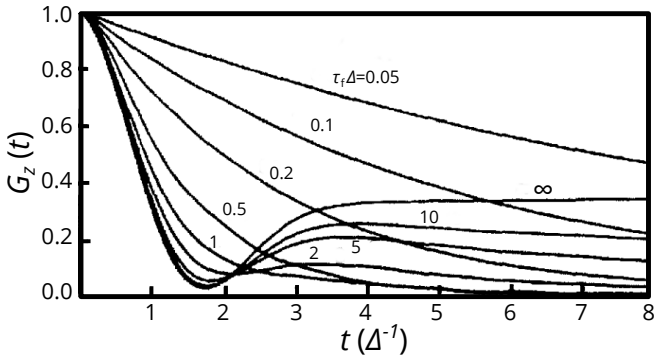

Figure 2.9.: Zero-field dynamic Gaussian Kubo-Toyabe function for different field fluctuations. Each curve is labeled by the value $\tau_f\Delta$. The static case (see also figure 2.8)is recovered when $\tau_f\Delta \to \infty$. The figure is adapted from reference [56].

So far we dealt with a static case, for which the internal field of the sample can be considered stationary. Kubo treated also the dynamic case [58], when the muon sees a local field that fluctuates randomly with an average rate $1/\tau_f$. This can be due to the muon that hops from site to site (muon diffusional motion) or from internal fields themselves that fluctuate. The dynamics can be taken into account by making two hypothesis:

- the local field changes direction at a time t according to a probability distribution $p(t) = \mathrm{e}^{-t/\tau_f}$;
- the field after a 'collision' is chosen randomly from the distribution of the internal fiels and it is uncorrelated with the field before the collision.

However, even in ZF there is not an analytic solution but only numerical. Nevertheless there are some considerations that can be done. If $\tau_f\Delta > 1$, where Δ/γ_μ is the width of the field distribution,[9] we have the slow-fluctuation limit and the main effect is that the 1/3 tail decays (see figure 2.9). The application of a longitudinal field B_L, in this

[9]We suppose $\Delta \neq 0$, which is necessary for having depolarization, otherwise $G_z(t) = 1$.

limit, can still get to a partial decoupling. This means that the information on the field distribution width (Δ/γ_μ) and on the fluctuation time τ_f can be obtained separately.

Unfortunately, if $\tau_\mathrm{f}\Delta < 1$ the minimum vanishes and the spin relaxation function tends to

$$G_z(t) = \mathrm{e}^{-\lambda t} \tag{2.31}$$

where $\lambda = \tau_\mathrm{f}\Delta^2$ and it contains information both on the fluctuation rate and on the width of the field distribution. In ZF it is not possible to separate the two contributions. The application of a longitudinal field turns to be useful only if B_L can be large enough so that the corresponding Larmor frequency is comparable to the fluctuation rate.

The study of λ as a function of temperature and of the applied field gives information on the local dynamics felt by the muon and, in some cases, it is also possible to extract separately both τ_f and Δ.

3. μSR investigation of Er(trensal) and Dy(trensal)

> Nothing in life is to be feared, it is only to be understood. Now is the time to understand more, so that we may fear less.
>
> *(Maria Skłodowska Curie)*

In this chapter we will present some results of a μSR study on two lanthanide SIMs containing Er(III) and Dy(III). We will start by summarizing the structural features of these complexes and by reporting the main outcomes obtained in previous experimental investigations [18, 23]. In section 3.2 we will analyze and discuss the μSR results.

3.1. Main features of Ln(trensal) complexes

The Ln(trensal) (H_3trensal = 2,2′,2″−Tris(salicylideneimino)triethylamine) compounds were initially studied because the trensal ligand is a rare example of heptadentate coordination agent and more than one synthetic strategy is available in literature [59, 60]. The complexes feature a crystallographically imposed trigonal symmetry (see figure 3.1a), with the Ln site on the C_3 axis. The different synthetic procedures result in the molecule crystallizing in two different spatial groups, $P\bar{3}$ and $P\bar{3}c1$. All the results that we will present refer to samples crystallized in $P\bar{3}c1$.

An overall characterization of the luminescence properties of the series was carried out by Flanagan et al. [23] in 2002. The investigation was focused on the ligand-field analysis of the trensal ligand. The luminescence measurements allowed to determine the splitting of energy levels of the lanthanide ion in the presence of the CF produced by the ligand. A CFP set was extracted for all the compound of the series, with the obvious exceptions of Ce, Pm, Gd and Yb and the parameters' values were rationalized on the basis of a simple Angular Overlap Model [23].

Some years later, while more and more lanthanide-based complexes were investigated as potential SMMs in the field of Molecular Magnetism, the Ln(trensal) family made a comeback. Indeed, in trying to model and rationalize the features of a SMM it is of great advantage to know, or at least to be able to calculate, its energy levels and eigenfunctions. In less than two years several studies appear on the magnetic

behavior of some of the complexes of the Ln(trensal) family, in an attempt to exploit the extremly detailed knowledge of their electronic structure gained by luminescence measurements [18, 61–63].

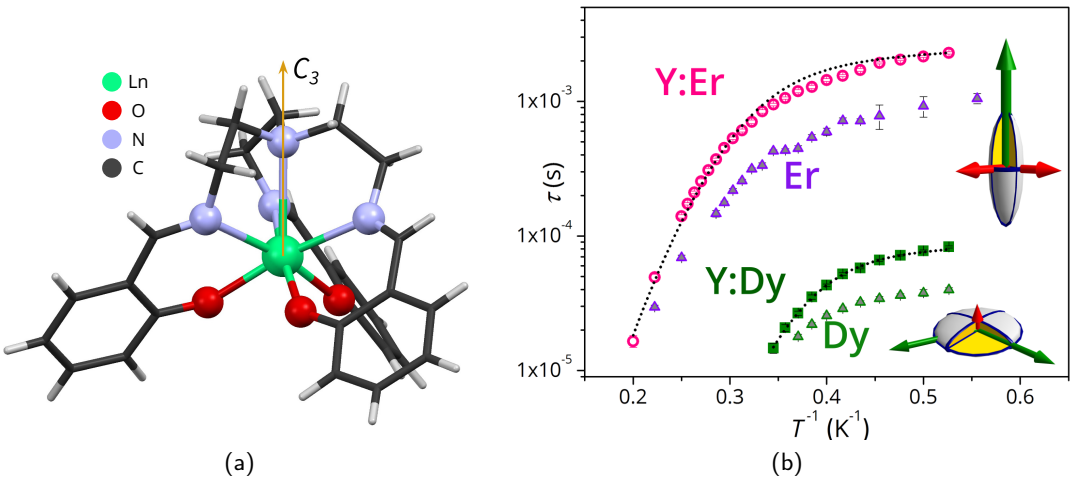

Figure 3.1.: Figure 3.1a: molecular structure of the Ln(trensal) complex. Figure 3.1b: relaxation time τ for Er(trensal) and Dy(trensal) together with their derivative diluted in Y(trensal). The dotted line are the best fit curves obtained by using equation (3.2) and parameters reported in table 3.1. A graphical visualization of g^2_{eff} for the ground doublet of the two complexes is reported.

We will briefly recall the most important features that concern Er(trensal) and Dy(trensal), from here on **Er** and **Dy**. The ground multiplets are ${}^4I_{15/2}$ for **Er** and ${}^6H_{15/2}$ for **Dy**, the two lanthanide ions have indeed half integer spins and are therefore Kramers' ions. This means that the energy levels due to CF will be doubly degenerate and, in both cases, the ground multiplet is split in 8 doublets. Their molecular symmetry reduced the overall numbers of CFP to nine (eight with a proper choice of the orientation of the xy plane). The CF interaction, following Wybourne's formalism, can be written as

$$V_{\text{CF}}(C_3) = B^2_0\boldsymbol{C}^2_0 + B^4_0\boldsymbol{C}^4_0 + B^4_3(\boldsymbol{C}^4_{-3} - \boldsymbol{C}^4_3) + \mathrm{i}B'^4_3(\boldsymbol{C}^4_{-3} + \boldsymbol{C}^4_3) + B^6_0\boldsymbol{C}^6_0 + B^6_3(\boldsymbol{C}^6_{-3} - \boldsymbol{C}^6_3) + \mathrm{i}B'^6_3(\boldsymbol{C}^6_{-3} + \boldsymbol{C}^6_3) + B^6_6(\boldsymbol{C}^6_{-6} + \boldsymbol{C}^6_6) + \mathrm{i}B'^6_6(\boldsymbol{C}^6_{-6} - \boldsymbol{C}^6_6) \tag{3.1}$$

A set of CFPs, derived from luminescence measurements, can be found in [23]. For **Dy** none of the levels of the ground multiplet was observed during the luminescence investigation [23], while, for **Er**, all the energies of the 8 doublets were identified [64]. These CFPs were then employed to simulate the χT curve, reported in figure 2.1: as previously mentioned, the observed temperature dependence can be attributed to the progressive depopulation of the excited sublevels of the ground multiplet.

The CFPs allowed to evaluate the g_{eff} factor, investigated by continuous wave EPR. The estimate was in agreement with the experimental results, since it predicted the correct type of magnetic anisotropy: **Er** presented an easy axis magnetic anisotropy while **Dy** was easy-plane (see inset in figure 3.1b), as confirmed by EPR results. The different kind of magnetic anisotropies can be explained by following the work on the aspherical electron density distributions carried out by Sievers [65] and more recently made popular by Rinehart and Long [66]. The latter study suggests that it is possible to rationalize the design of new lanthanide-based SIMs by exploiting their single-ion anisotropy combined with the proper choice of the ligand(s). The electronic density of Dy(III) has an oblate shape when $M_J = J$, therefore, by choosing a ligand whose electron density has an axially distributed electron density can lead to a highly anisotropic and bistable ground state (i.e. to easy axis magnetic anisotropy). For prolate ions, such as Er(III) $M_J = J$ is obtained when the ligand has a mainly equatorial electron density. In the case of the H_3trensal ligand the results from the magnetic anisotropy investigation would suggest an equatorial geometry rather than an axial one, since **Er** showed an easy axis magnetic anisotropy while **Dy** was easy-plane. However, the calculations of the ground doublet composition by means of the CFPs derived in the paper of Riley and coworkers [23] evidenced different M_J contributions to the ground doublet wavefunction both for **Er** and **Dy**. Indeed, while for **Er** the ground doublet had a large contribution from the $|\pm 13/2\rangle$, **Dy** was higlhy mixed, with the major contributions from $|\pm 1/2\rangle$, $|\pm 7/2\rangle$ and $|\mp 5/2\rangle$(see also appendix A). Therefore, when the ground doublet is not a pure $|\pm M_J\rangle$, the description of the electronic density shape as prolate or oblate is not completely correct: this indicates the limits of this model, as it was already pointed out in the study of magnetic anisotropy of the Ln(DOTA) complexes [67].

A more detailed study of the magnetic anisotropy by means of Cantilever Torque Magnetometry (CTM) [63] evidenced that the CFPs of **Dy** did not correctly reproduce the angular and field dependence of the magnetic anisotropy at low temperature, while for **Er** the accord was good. This discrepancy was attributed to having obtained the electronic structure of the ground-state multiplet of **Dy** indirectly by the set of CFPs needed to reproduce transitions to upper-lying multiplets: this results in an incorrect prediction of magnetic properties at low temperature.

Despite the two different magnetic anisotropies [18], AC susceptometry measurements highlighted that both compounds, in the presence of an applied magnetic field, showed slow relaxation of magnetization. This feature was proved to be of molecular origin, since their derivatives diluted in Y(III) exhibited the same behavior (**YDy** and **YEr** - doped with the 3.1 % and 5.8 % of Dy(III) and Er(III) respectively). This result indicates that slow relaxation of magnetization can take place also in compunds with easy plane anisotropy: up until recently the appearance of a magnetic bistability was

retained possible only when an easy axis anisotropy was present [3]. Indeed, as we will see in a moment the relaxation can not be ascribed to the overcome of a magnetic anisotropy barrier.

The temperature dependence of the relaxation time τ for the the diluted complexes was modeled according to

$$\tau^{-1} = \frac{B_1}{1 + B_2 H^2} + A_1 H^4 T + A_2 B^2 T + C T^n + \tau_0^{-1} \mathrm{e}^{-\Delta / k_\mathrm{B} T} \tag{3.2}$$

where the first term represents a phenomenological modelization of QTM in the presence of an applied field ($H = 800\,\mathrm{Oe}$ for **YEr** and $H = 900\,\mathrm{Oe}$ for **YDy**). The second and

	YDy	**YEr**
B_1 (s^{-1})	$(158 \pm 2) \times 10^2$	$(71 \pm 4) \times 10^1$
B_2 (Oe^{-2})	$(9.2 \pm 0.7) \times 10^{-7}$	$(2.7 \pm 0.4) \times 10^{-6}$
A_1 ($\mathrm{s}^{-1}\,\mathrm{K}^{-1}\,\mathrm{Oe}^{-4}$)	$(3 \pm 2) \times 10^{-11}$	$(2.0 \pm 1.8) \times 10^{-12}$
A_2 ($\mathrm{s}^{-1}\,\mathrm{K}^{-1}\,\mathrm{Oe}^{-2}$)	$(2.0 \pm 0.1) \times 10^{-3}$	$(1.4 \pm 0.1) \times 10^{-4}$
C ($\mathrm{s}^{-1}\,\mathrm{K}^{-\mathrm{n}}$)	0.3 ± 0.1	0.027 ± 0.001
n	11	9

Table 3.1.: Best fit parameters for relaxation time τ.

the third terms are simplified relations that take into account the direct process for Kramers' ions with and without, respectively, hyperfine interactions [33]. The fourth term, CT^n, represents the Raman process and the last one is the Orbach contribution. The latter was actually excluded from being involved in the relaxation dynamics, at least in the temperature range investigated (2 K to 5 K). This should be seen as a caveat, since the Orbach mechanism is too often called up as responsible for the relaxation. Indeed, in the case of **Er**, a hypothetical energy barrier evaluated from a semilog-plot of the relaxation time would be lower than the first excited state, that was observed directly in luminescence measurement (see reference [18], also available in appendix A).

To avoid overparametrization, the values of B_1, B_2, A_1 and A_2 were extracted from the dependence of τ on the applied field H. They were then kept fixed while fitting the temperature dependence of τ with equation (3.2) (see table 3.1). The best fit curves are reported also in figure 3.1b.

3.2. μSR data analysis

The μSR investigation was performed on powder samples of **Dy** and **Er** at the PSI facility. The aim of these measurements was to probe the capability of μSR for investigating details of the low temperature dynamics of Ln based SMMs by using a

technique which is potentially applicable also to nanostructured materials [68]. Indeed, a few reports indicate that Ln(trensal) family might be deposited on different surfaces using UHV techniques [61, 69]

A first set of measurements was collected at the end of 2013, but the analysis revealed some problems in the data, probably due to an underestimation of possible thermo-magnetic effects. Indeed, when these samples were first measured through μSR the only available information on dynamics derived from AC measurements. Since AC relaxation was too fast above 5 K, no particular care was used in deciding the order of μSR measurements for $T > 5$ K. However, muons are sensitive to faster dynamics, therefore, they can see a sort of magnetic memory of the system for a wider range of temperatures. For this reason, the problems evidenced in this first set of measurements could be attributed to an induced thermo-magnetic history.

Another aspect that was pointed out was that the muon spin polarization relaxed because of dynamical field fluctuations. Indeed, as it was explained in section 2.3.2, if the distribution of the internal fields were static, ZF should have evidenced a recovery of 1/3 of the polarization but this was not the case. Therefore, in planning a new investigation we decided not to perform ZF measurements, but to study the temperature dependence of the Asymmetry for several value of LF.

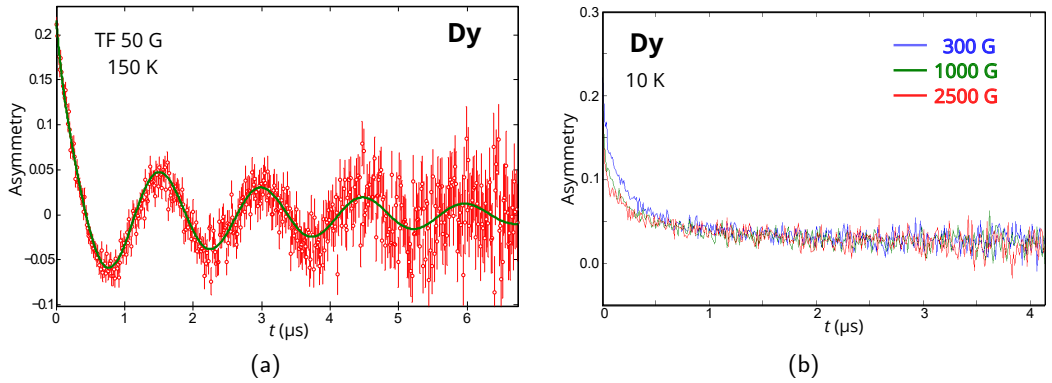

Figure 3.2.: Left panel (a): experimental data for TF Asymmetry of **Dy** (symbols), the solid curve is the best fit curve that allows to determine α. For the sake of clarity a binning factor of 50 was employed. Right panel (b): overlay of the Asymmetries of **Dy** for three different values of LF at 10 K (binning factor 30).

Dy was measured at the GPS (General Purpose Surface) Muon Instrument in November 2015 using a time windows of 7 µs and a time resolution of 0.3 ns. **Er** was measured at the DOLLY instrument, a clone of GPS, in July 2016 with a a time windows of 7 µs and a time resolution of 0.58 ns. The magnetic investigation began by applying a TF field of 50 G to determine α, the parameter that accounts for the different counting efficiencies of the forward and backward detectors (see section 2.3.2).

The fitting procedure returned an α value of 1.21 for **Dy** (GPS) and 1.09 for **Er** (DOLLY). In the GPS instrument, in contrast to DOLLY [70], the α parameter is

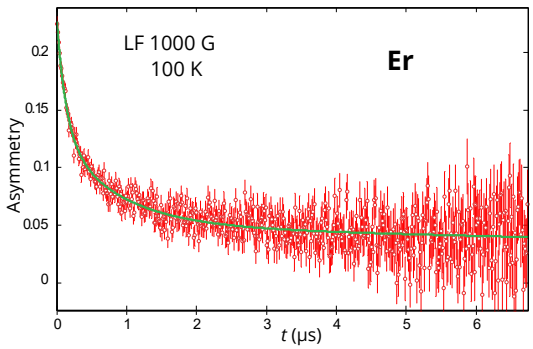

Figure 3.3.: Experimental data for LF Asymmetry of **Er** (symbols), measured with an applied field of 1000 G at 100 K (binning factor 20). The solid curve is the best fit curve using equation (3.3) (see text).

sensitive to the magnitude of the longitudinal applied field. After the estimation of α through TF measurements, its value was interpolated by following the longitudinal field dependence reported in [71]. In figure 3.2a an example of TF measurement for the **Dy** sample is reported.

Afterwards, LF measurements as a function of temperature were performed for three values of applied magnetic field: 300 G, 1000 G and 2500 G (see for instance figure 3.2b and 3.3). A field scan, from 0 G to 5000 G, was performed at 2 K and 10 K for both complexes. The analysis of the data was not straightforward,[1] and the Asymmetry was eventually fitted by means of three simple exponential decays. Although in case of fast fluctuations the Asymmetry is often modeled by means of a stretched exponential or of two simple exponenentials, there are also few examples of a three decay behavior, see for instance [73]. As it was mentioned at the end of section 2.3.1, the muon can implant in different site and the three contributions indicate that there should be three main collections of stopping sites. The Asymmetry for **Dy** and **Er** was modeled according to:

$$\mathcal{A}(t) = A_{\text{fast}}\mathrm{e}^{-\lambda_{\text{fast}}t} + A_{\text{int}}\mathrm{e}^{-\lambda_{\text{int}}t} + A_{\text{slow}}\mathrm{e}^{-\lambda_{\text{slow}}t} + C_{\text{bk}} \tag{3.3}$$

where C_{bk} takes into account the contribution of a constant background and the subscripts fast, intermediate and slow highlight the relative value of the relaxation rates λ. The values of the A_{fast}, A_{int} and A_{slow} were estimated from high temperature measurements and were kept constant for all the fits. Moreover, since **Dy** and **Er** are isostructural samples they should have the same weights for the three components (since the muon should implant at the same sites in the two samples). This means that,

[1] The data analysis was performed with Mulab, a Matlab toolbox developed by the University of Parma [72].

once the value of the initial Asymmetry is identified, each component should represent the same percentage of the total Asymmetry in both compounds. As an example, if the slow component represents the 20 % of the total Asymmetry for **Dy**, then it should be the same for **Er**. The theoretical value of the initial Asymmetry is 1/3, as mentioned in section 2.3.1, but it is usually smaller than that due to experimental conditions. In the case of **Er** and **Dy** the initial Asymmetry is 0.23. In table 3.2 we report the amplitudes A_{fast}, A_{int}, A_{slow} and C_{bk} used for the fits of the experimental data.

	Dy	**Er**
A_{fast}	0.10	0.10
A_{int}	0.08	0.08
A_{slow}	0.05	0.05
C_{bk}	0.02	0

Table 3.2.: Amplitudes of the three exponential contributions of equation (3.3).

The fitting of the Asymmetry allowed to obtain, for each value of the applied field, the behavior of λ_{fast}, λ_{int}, λ_{slow}, as a function of temperature T. In figures 3.4, 3.5 and 3.6 the slow and intermediate components are reported. We do not display the behavior of the fast component because it shows the same kind of dependence of the other ones but the uncertainty on its value is much larger. Indeed, the fast component accounts for a very rapid relaxation that has to be considered to model the Asymmetry curve at early times. However, the value of λ_{fast} is of the order of $10^2\,\mu\text{s}^{-1}$, which correspond to a dynamics of the order of the ns. This is a value outside the time window investigated by muons, thus λ_{fast} does not have a physical meaning.

For both complexes λ_{slow} and λ_{int} display a broad peak around 10 K, that is narrower in the case of **Er**. Interestingly, a similar feature was observed also in NMR measurements performed at the University of Pavia (see figure 3.7). Besides, the different magnetic anisotropies of the two complexes do not seem to be be relevant for the dynamics, as in the case of AC measurements.

The behavior of λ as a function of the longitudinal applied field is reported in figure 3.8 but its trend is not very helpful in trying to model the temperature dependence of λ_{slow} and λ_{int}. Indeed, the interpretation of the relaxation rate extracted from μSR is not very obvious. Even the application of longitudinal field of the order of 10^3 G seems not to cause decoupling. If we compare the absolute value of the peaks we notice that it increases if the applied magnetic field is increased. This is an anomalous behavior with respect to other SMMs investigated with the same technique [74–76], since the peak usually decreases when the field is increased. It is however worth noting that also NMR measurements show an atypical behavior. Indeed, the ratio between the peaks of two datasets, collected at different applied field, should usually scale as the ratio

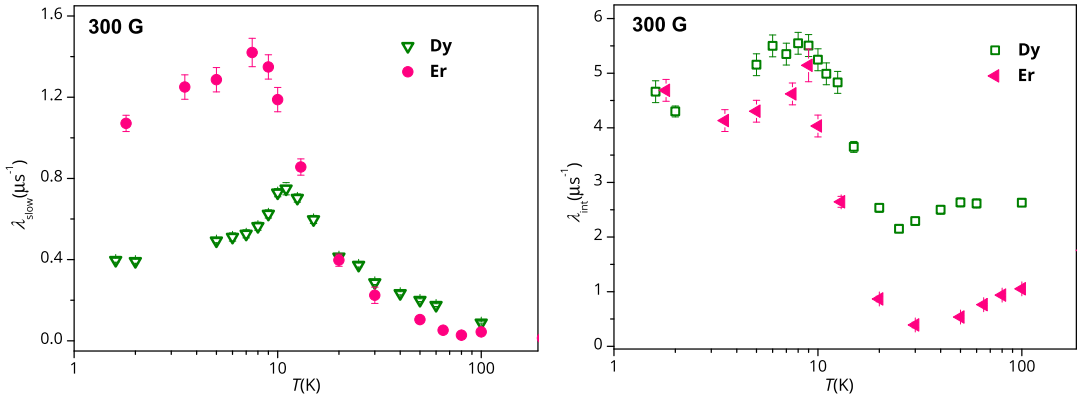

Figure 3.4.: Left panel (a): T dependence of the slow component of the muon longitudinal relaxation rate for **Dy** (triangles) and **Er** (full circles), in the presence of an applied magnetic field of 300 G. Right panel (b): intermediate component of the relaxation rate for **Dy** (empty squares) and **Er** (full triangles).

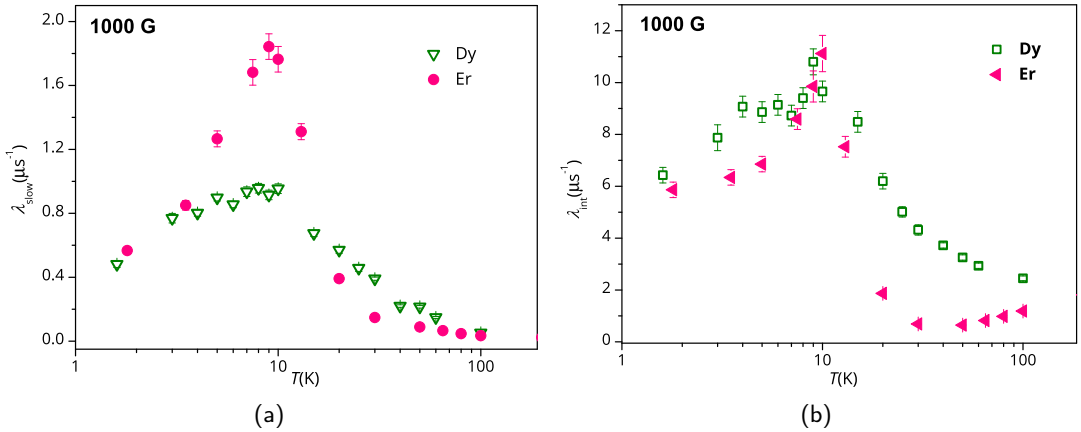

Figure 3.5.: Left panel (a): T dependence of the slow component of the muon longitudinal relaxation rate for **Dy** (triangles) and **Er** (full circles), in the presence of an applied magnetic field of 1000 G. Right panel (b): intermediate component of the relaxation rate for **Dy** (empty squares) and **Er** (full triangles).

between the fields. If we look at figure 3.7a we see that the peak of the data collected at 6 T is lower than the peak of 0.5 T, but they are not in a 1 : 12 ratio.

The investigation of the relaxation dynamics of the muon spin for **Dy** and **Er** presents then some new and unusual features compared to previous reports on SMMs, both polynuclear 3*d* and lanthanide-based SIMs. Few remarks should be made. First of all, the so-called standard behavior of other SMMs (peak decreases when the field increases) descends from the hypotheses of the BPP theory (Bloembergen, Purcell, Pund) [77]. BPP theory was developed to explain the phenomenological relaxation time T_1 in NMR spectroscopy and it is widely employed also in μSR. BPP theory makes the assumption that the autocorrelation function of the microscopic fluctuations causing the relaxation is proportional to e^{-t/τ_c}, where τ_c is the correlation time. This leads to the following dependence of the relaxation rate λ on τ_c and on longitudinal field H:

$$\lambda \propto \frac{\tau_c}{1 + (\gamma_\mu H)^2 \tau_c^2} \tag{3.4}$$

where $\gamma_\mu = 85\,000\,\mathrm{Hz\,G^{-1}}$, is the muon gyromagnetic ratio. Looking at equation (3.4) it is evident that for higher magnetic field we get a lower value of λ. As a second point, the SMMs that follow this standard behavior present also a significant contribution to AC relaxation from the Orbach process [74, 76]. In those cases, then, μSR and AC seemed to probe the same relaxation dynamics. As regards **Dy** and **Er** the AC relaxation time did not involve an Orbach process but, since muons are sensitive to local fluctuations it is expected that they probe a different dynamics with respect to AC measurements.

In conclusion, the results of the μSR investigation for the two complexes do not follow the theoretical models employed for other SMMs. The anomalous behavior, confirmed also by NMR measurements, demands to re-examine the overall assumptions that leads to 3.4 and check their validity, in order to be able to reproduce the experimental features of **Dy** and **Er**. Indeed, to our knowledge, there are not other examples of molecular compounds that exhibit these characteristics.

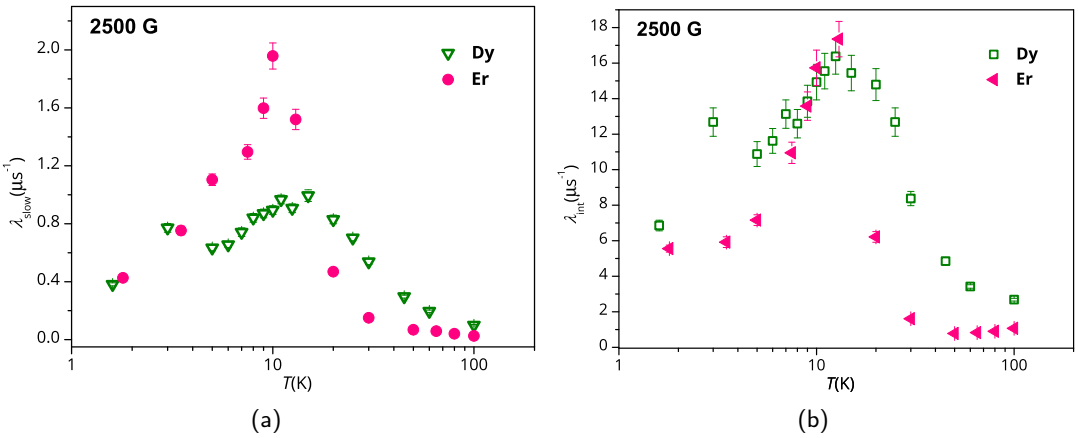

Figure 3.6.: Left panel (a): T dependence of the slow component of the muon longitudinal relaxation rate for **Dy** (triangles) and **Er** (full circles), in the presence of an applied magnetic field of 2500 G. Right panel (b): intermediate component of the relaxation rate for **Dy** (empty squares) and **Er** (full triangles).

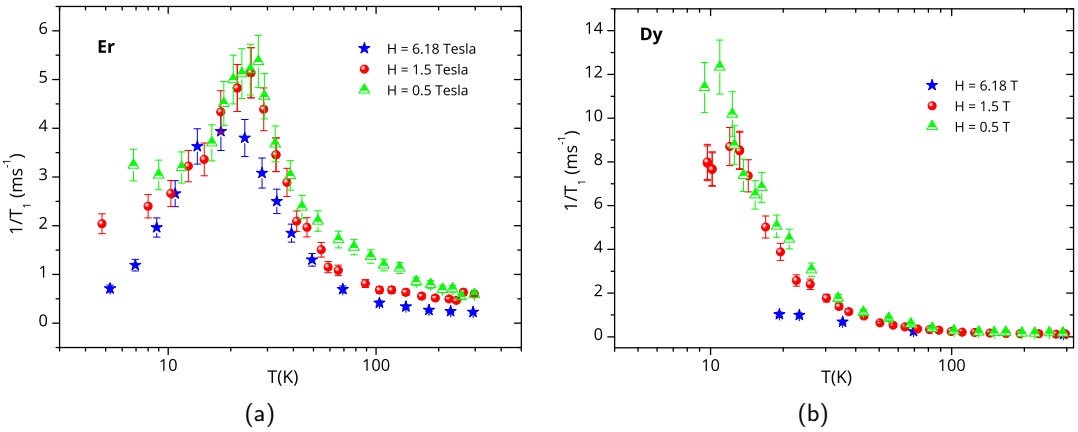

Figure 3.7.: Left panel (a): NMR spin-lattice relaxation rate of **Er** as a function of temperature for different applied field. Right panel (b): NMR spin-lattice relaxation rate of **Dy** as a function of temperature for different applied field. The measurements were performed at the University of Pavia by Dr. Fatemeh Adelnia.

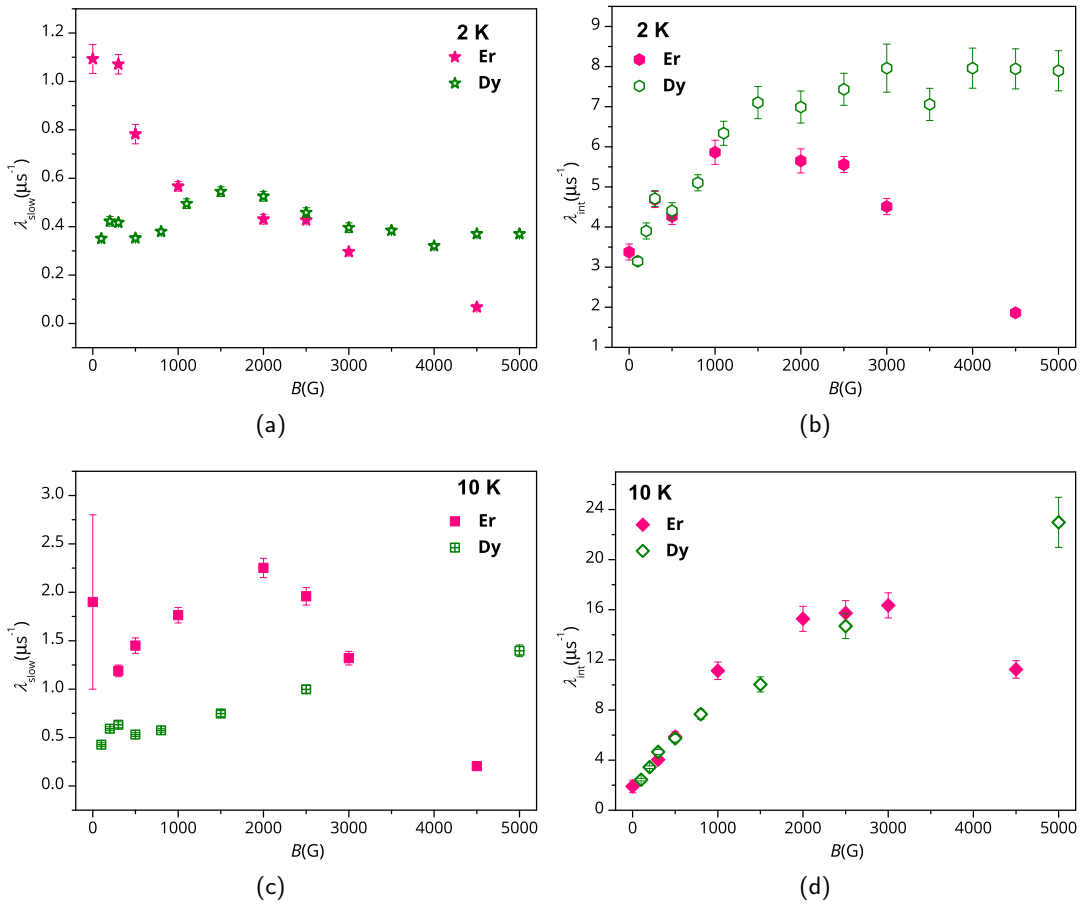

Figure 3.8.: Slow and intermediate components as a function of the applied magnetic field, measured at 2 K (a)-(b) and 10 K (c)-(d).

4. A synergistic study of a new Dy(III) complex

> The hardest problems of pure and applied science can only be solved by the open collaboration of the world-wide scientific community.
>
> *(Kenneth G. Wilson)*

The understanding of the behavior of a SMM needs to collect as much information as possible about their electronic structure and the resulting magnetic properties. It is then important to combine and compare several investigation techniques in order to have a coherent interpretation of the outcomes. In the previous chapter we showed the results of a magnetic investigation of two lanthanide complexes: the available spectroscopic information proved to be supportive in providing a reading key of the AC magnetization dynamics. In this chapter we will present a new mononuclear Dy(III) complex behaving as SIM in zero field for which no luminescence data or other spectroscopic techniques results were ready to hand. We then decided to perform a complete experimental characterization, obtained by X-ray diffractometry, EPR spectroscopy, single crystal CTM, AC and DC susceptibility flanked by theoretical analysis based on *ab initio* methods. This work is the result of the collaboration of several people: Prof. Jean-Pierre Costes, who synthesized the complex, Dr. Mauro Perfetti, who performed the CTM measurements and analysis, and of Mr. Matteo Briganti, who dealt with *ab initio* calculations.

We will begin the dissertation by recalling the most important structural features of the compound, we will then present and discuss the magnetic investigation. The *ab initio* results will be progressively introduced along with the experimental results. The theoretical calculations employed the quantum chemistry package MOLCAS 8.0 [78].

4.1. Structural features

An exhaustive description of the synthesis, crystallographic data collection and structure determination is reported in [22], also available in appendix B. Here, we will summon up the main features of the complex, in view of the presentation and discussion of the magnetic investigation.

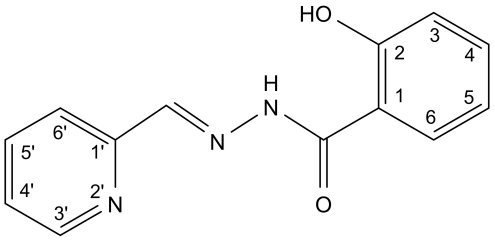

(a) LH_2 ligand.

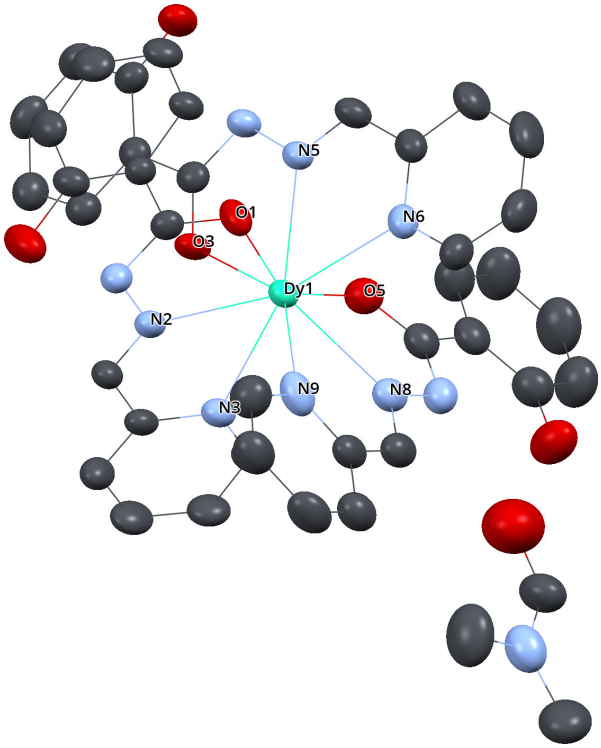

(b) $Dy(LH)_3 \cdot dmf$.

Figure 4.1.: Upper panel (a): the LH_2 ligand. Lower panel (b): view of the asymmetric unit of **Dy**, including one molecule of the complex and one dmf molecule. Hydrogen atoms are not shown for the sake of clarity. Ellipsoids are drawn at the 55 % probability level.

Chemical formula	$C_{42}H_{37}DyN_{10}O_7$
Formula mass ($g\,mol^{-1}$)	956.32
Crystal system	monoclinic, $P2_1/n$
Z	4
a, b, c (Å)	9.8585(3),22.1870(6),19.1215(4)
α, β, γ (°)	90, 94.160(3), 90
Volume (Å^3)	4171.3(2)

Table 4.1.: Structural information of the compound: the asymmetric unit of $Dy(LH)_3 \cdot dmf$ is made up of one $Dy(LH)_3$ neutral molecule and one dmf molecule. Each cell contains 4 asymmetric units.

The LH_2 ligand (2-hydroxy-N'-[(*E*)-(2-hydroxy-3-methoxyphenyl)methylidene]benzhydrazide) is reported in figure 4.1a. It is a potentially pentadentate ligand, however, only three of its binding sites are used to bind to the Dy(III) ion, which results in a neutral molecule that is, in principle, sublimable [79]. When dissolved in dimethylformamide (dmf), this LH_2 ligand reacts with $Dy(NO_3)_3$ in the presence of piperidine to give a yellow complex, which was found to be neutral, with the Dy(III) ion being coordinated to three monodeprotonated ligands. The molecular structure obtained by single-crystal X-ray diffactometry indicates that the $Dy(LH)_3 \cdot dmf$, from here on **Dy**, crystallizes in the monoclinic $P2_1/n$ space group. Its asymmetric unit is composed of one mononuclear $Dy(LH)_3$ neutral molecule and one dmf molecule (see figure 4.1b). A summary of the main structural information can be found in table 4.1.

In AC, DC and EPR investigations we performed measurements on powder samples of both **Dy** and of its derivative diluted in Y(III) (**YDy**, 10 %), while the for CTM study we employed a single crystal sample of **YDy**.

4.2. Magnetic anisotropy and static properties

DC measurements investigated the magnetization of **Dy** both as a function of field H and temperature T. The χT vs T curve is reported in figure 4.2a: a smooth decrease is observed on lowering temperature, which is attributed to the depopulation of excited levels of the $^6H_{15/2}$ multiplet, split by the CF. The Y(III) diluted analogue, **YDy**, showed the same behavior, apart for the saturation value at high temperature, that is lower than the **Dy** sample. The small discrepancy is probably due to the presence of small amount of diamagnetic impurities, not detectable from X-ray diffraction patterns. The little step around 40 K in the χT curve is attributed to saturation effects, since the applied magnetic field was changed from 1000 Oe to 10 000 Oe. The figure 4.2a shows, together with experimental data, the simulated χT curve, calculated with the software EVALUCF [80] using the CFP derived from *ab initio* calculations. The simulation is

in good agreement with the experimental behavior and it also reproduces the little jump at 40 K. The field dependence of the magnetization M is reported in figure 4.2b for $T = 2$ K: the concentration of Dy in Y was estimated by superimposing the magnetization curve of **Dy** and of diluted sample **YDy**, resulting in a 10 % of dilution, in agreement with the estimate expected by the synthetic procedure. The saturation value of M is $5\mu_B$, as already observed for other molecular complexes containing Dy(III) [81, 82].

Both EPR and CTM techniques were employed to study the magnetic anisotropy of the system. Unfortunately, the EPR investigation through a X-band spectrometer revealed that the complex was silent (both **Dy** and **YDy**). This could be attributed to either fast relaxation or to a low intra-doublet transition probability due to the ground-state composition, with the excited levels too high in energy for the observation of a inter-doublet transition (see section 2.2.1 of the experimental chapter). The latter explanation is a mark of a large axiality of the ground state that was then investigated by CTM, which proved to be very useful in determining anisotropic features of lanthanide-based SMMs [63, 83, 84]. This technique measures the magnetic torque of a molecule immersed in a homogeneous magnetic field by detecting the variation in the capacitance of a capacitor: the sample is glued over one of the two capacitor plates and the deflection of the cantilever is proportional to the magnetic torque experienced by the sample.

The CTM technique would deserve an extensive introduction which is beyond the scope of this thesis. For a CTM investigation focused on SMMs the reader can refer to [85]. Since the analysis and the simulation of the torque data requires to employ different reference frames, we will list them here for the sake of clarity: the XYZ reference frame or laboratory frame where the torque is actually measured, the orthogonal cell frame $ab'c^*$ (here abc^*) and the molecular reference frame xyz, identified by the principal axes of the g-tensor.

The torque $\boldsymbol{T}$ is defined as the vector product between the magnetization $\boldsymbol{M}$ and the magnetic field $\boldsymbol{B}$. Experimentally, only the $\mathcal{T}_Y$ component of the torque is detectable (XYZ - laboratory frame). In a CTM measurement for any given T and B a rotation around a chosen axis is performed and θ defines the rotation angle, that is the angle between the cantilever plane and the magnetic field direction. When the magnetic field B is increased so that the limit $g\mu_B S_{\text{eff}} B \ll k_B T$ is not more valid, the torque curves assume a different shape if B is parallel or perpendicular to the easy direction of anisotropy, making possible the disentanglement of non collinear contributions.

The measurements were performed on a single crystal of **YDy** to reduce the effect of intermolecular interactions. Considering that the compound crystallizes in the space group $P2_1/n$ and the molecules do not sit on any symmetry element, the crystal anisotropy will be in general different from the molecular one. Since the crystallographic

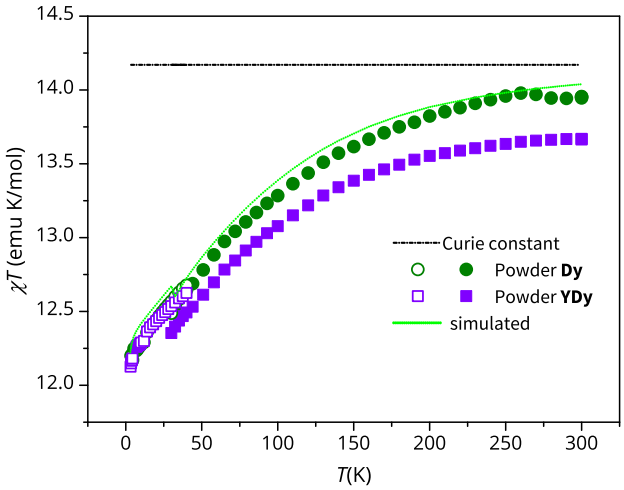

(a)

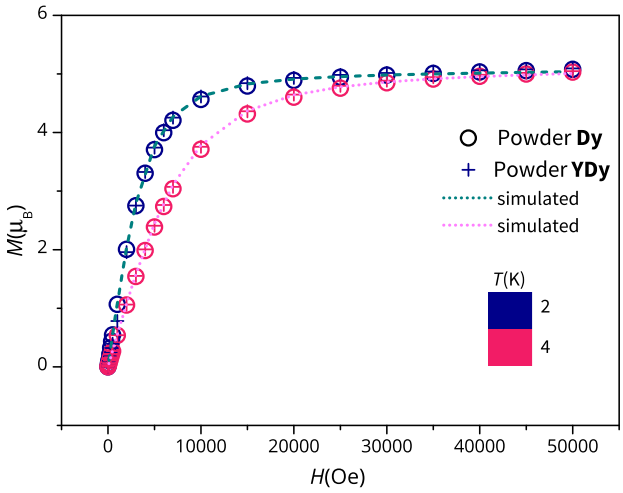

(b)

Figure 4.2.: Upper panel (a): Temperature dependence of χT of **Dy** (circles)and **YDy** (squares) along with theoretical curves (dotted line) calculated by using CFPs derived from *ab initio* calculations. The dashed line corresponds to the expected free-ion χT value ($14.17\,\mathrm{emu\,K\,mol^{-1}}$). The empty circles and squares correspond to an applied static field H of 1000 Oe while the full ones to a field of 10 000 Oe. Lower panel (b): behavior of magnetization versus field at 2 K for **Dy** (empty circles) and **YDy** (cross), the dotted lines are the simulations calculated with the CFPs extracted from *ab initio* calculations (see also table 4.3).

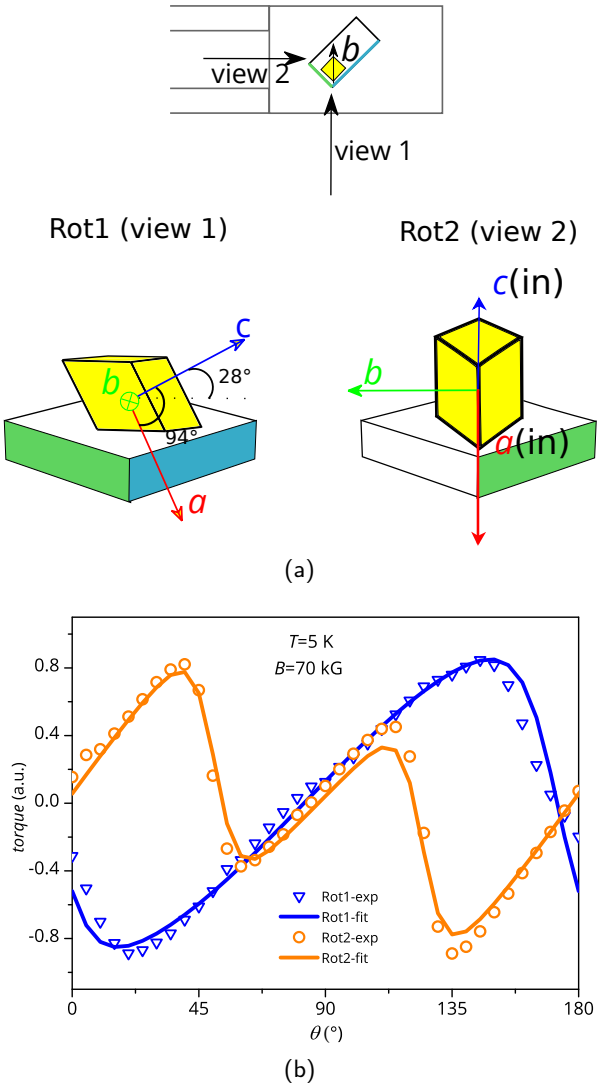

Figure 4.3.: Figure 4.3a: position of crystal on the cantilever for the two rotations. The orientation for view 1 and view 2 is for the rotation angle $\theta = 270°$. Figure 4.3b: torque curves for the two rotations in a magnetic field of 70 kG and at 5 K. The solid lines represent the best fit of the magnetic torque by using the parameters reported in the text.

axis b is a C_2 axis and the ac plane is a glide plane there will be only two non collinear contributions in the cell structure. To try to disentangle the two contributions, after having indexed the crystal, the investigation consisted of two sets of rotations: the first rotation (Rot1) had b as a rotation axis while in the second rotation (Rot2) the rotation axis was in the ac plane (see figure 4.3a). The first rotation turned out to be useful, since all molecules in the unit cell provided the same contribution, being related by the twofold axis that lies along b, whereas two families of differently oriented molecules were detected in the second rotation. Both for Rot1 and Rot2 the torque signal was measured at $T = 5\,\mathrm{K}$ and $T = 10\,\mathrm{K}$, with B ranging from 30 kG to 70 kG. An effective spin hamiltonian was employed to model the electronic structure

$$\mathcal{H}_{\mathrm{eff}} = \mu_{\mathrm{B}} \boldsymbol{S}_{\mathrm{eff}} \cdot \boldsymbol{g}_{\mathrm{eff}} \cdot \boldsymbol{B} \tag{4.1}$$

where $\boldsymbol{g}$ is the g-tensor and $\boldsymbol{S}_{\mathrm{eff}}$ is an effective $S = 1/2$ spin operator. To correctly reproduce the torque shape, three further parameters have to be taken into account: a scale factor (F_{SC}, that must be the same for all rotations) and two Euler angles, namely ρ and ξ (using the extrinsic $x-$convention), which describe the orientation of the molecular reference frame with respect to the crystallographic one. Indeed in the case of uniaxial anisotropy the third Euler angle is irrelevant. The fitting procedure for the parameters gave: $g_x = g_y = 0.010 \pm 0.005$, $g_z = 16 \pm 1$, $\rho = (212 \pm 1)^\circ$, $\xi = (71 \pm 1)^\circ$ and $F_{\mathrm{SC}} = (2.6 \pm 0.3) \times 10^{-2}$ (see for instance figure 4.3b to compare experimental data and calculated curves). The components of $\boldsymbol{g}$ indicates that the complex is strongly axial and this explains why no EPR signal was detected. The

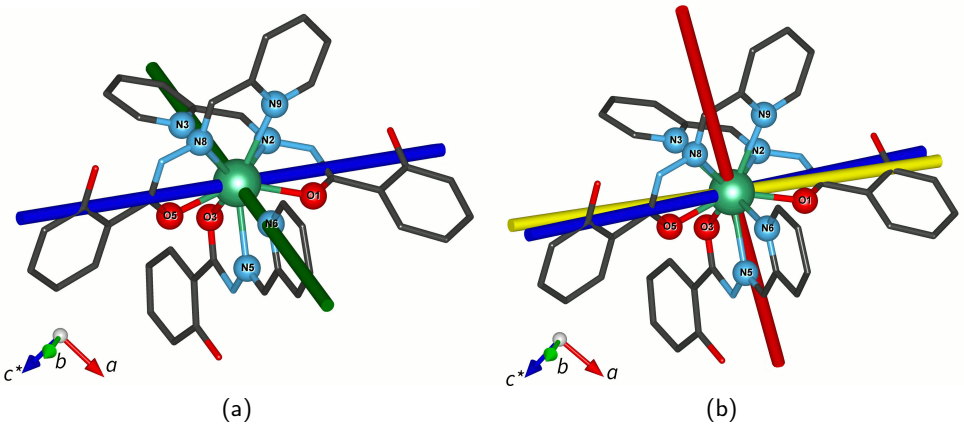

Figure 4.4.: Left panel (a): two possible directions of the easy axis of magnetic anisotropy as determined by CTM: the blue one is substantially coincident with the calculated one (compare with figure4.4b). Right panel (b): direction of the easy axis anisotropy for the first three energy doublets: ground (blue), first excited (yellow), second excited (red) computed direction.

resulting director cosines of the easy axis (z in molecular reference frame), with respect to abc^* are: $\cos\alpha_1 = -0.501$, $\cos\alpha_2 = 0.801$, $\cos\alpha_3 = 0.326$ ($\alpha_1 = 120°$, $\alpha_2 = 37°$ and $\alpha_3 = 71°$). However, since there are two non collinear molecules in the unit cell, the director cosines can identify two possible orientations for the magnetic anisotropy axis with respect to the molecular structure (see figure 4.4a). The support given by *ab initio* calculations allowed to cast light on this point. Indeed, the calculated ground Kramers' doublet showed an almost pure Ising character with a principal value of $g_z = 19.8$ and contribution from $M_J = \pm 15/2$ only. The computed easy axis orientation for the ground doublet (see figure 4.4b) had director cosines : $\cos\alpha_1 = -0.531454$, $\cos\alpha_2 = 0.788731$, $\cos\alpha_3 = 0.308967$ $\alpha_1 = 122°$, $\alpha_2 = 38°$ and $\alpha_3 = 72°$). It is palpable that the calculated easy axis orientation almost coincides with one of the two possible choices provided by the CTM analysis (compare figure 4.4b with figure 4.4a). The interplay between the experimental characterization and the *ab initio* calculations is then evident: the calculations allowed to unravel the knot about the molecular orientation of the easy axis, and, at the same time, they were supported by the good prediction of the χT vs T and M vs H data (see figure 4.2). The energy of the first excited doublet was calculated to be at $195\,\mathrm{cm}^{-1}$, while the second one should lie at $237\,\mathrm{cm}^{-1}$. In table 4.2 the energies for the eight doublets of the ground multiplet are reported, along with the value of the corresponding principal values of the g-tensor.

	Energy Levels	(cm^{-1})	g_x	g_y	g_z
$^6H_{\frac{15}{2}}$	E_0	0	0.0	0.0	19.8
	E_1	195	0.5	1.8	14.9
	E_2	237	0.1	2.2	14.3
	E_3	289	1.5	3.7	12.1
	E_4	324	0.6	2.8	13.8
	E_5	371	2.6	4.5	8.8
	E_6	430	3.4	4.1	7.4
	E_7	478	1.1	4.7	15.9

Table 4.2.: Results of the calculations with RCC basis sets for **Dy**: energy splitting of the ground $^6H_{\frac{15}{2}}$ multiplet and principal values of the corresponding g tensor for each Kramers' doublet.

4.3. Magnetization dynamics

The dynamic properties of **Dy** were extensively studied by AC susceptometry. The measurements were performed as a function of frequency (0.02 Hz to 10 000 Hz) for several temperatures and applied fields and the investigation revealed a composite dynamic magnetic behavior between 2 and 10 K. **Dy** showed two different relaxation

Wybourne's parameter					
	cm^{-1}		cm^{-1}		cm^{-1}
B_0^2	628.3	B_0^4	458.4	B_0^6	−346.8
B_1^2	24.9	B_1^4	−239.1	B_1^6	−251.8
B'^2_1	23.4	B'^4_1	−156.9	B'^6_1	−185.9
B_2^2	−103.0	B_2^4	86.3	B_2^6	9.6
B'^2_2	45.1	B'^4_2	−103.5	B'^6_2	−199.7
		B_3^4	−54.2	B_3^6	−271.1
		B'^4_3	20.6	B'^6_3	−221.7
		B_4^4	−98.2	B_4^6	−65.2
		B'^4_4	−90.8	B'^6_4	−185.7
				B_5^6	−17.5
				B'^6_5	−110.6
				B_6^6	−129.3
				B'^6_6	−258.3

Table 4.3.: Crystal field parameters of the Crystal field Hamiltonian in the Wybourne's notation (see section 1.2). B_q^k represent the real parameters while B'^k_q are the imaginary ones. The output of the MOLCAS 8.0 [78] provided the parameters in the extended Stevens' operator notation.

channels in zero and non-zero magnetic static field: the application of an external field allows to suppress one channel and activate the other one (see figure4.5). The study

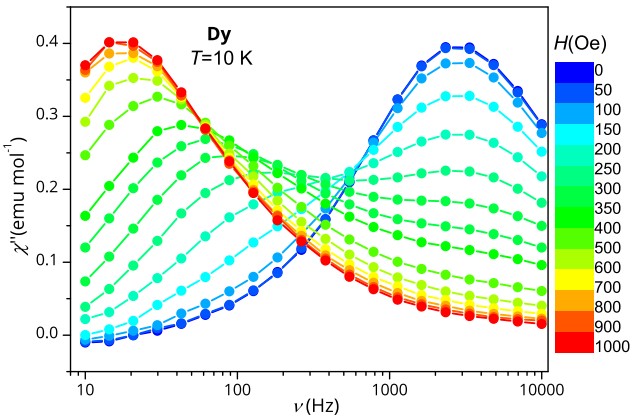

Figure 4.5.: Imaginary susceptibility of **Dy** at 10 K as a function of the applied field.

of the field dependence of the relaxation was performed at 2 K and it evidenced that the relaxation rate had a minimum for $H = 1000$ Oe, so we chose this field for the measurements under external field. A similar feature was already been observed in the Dy(DOTA) derivative as well as in other SMMs [81, 86–89].

The magnetization dynamics of **Dy** presented then interesting features and we decided to investigate the magnetically diluted **YDy** sample, in order to clarify if the

interaction between magnetic centres played any role in this peculiar behavior. Even in the diluted sample, two different relaxation channels were found to contribute to relaxation in zero and applied field.

The imaginary susceptibility curves χ'' in zero and applied field were fitted according to a Debye model [3, 90] and the corresponding relaxation times versus T^{-1} are reported in figure 4.6 for the zero and applied field measurements. Comparing figure 4.6a and 4.6b it is evident that the relaxation rate of both channels (zero and non zero field) is slower in the **YDy** sample than in the pure sample **Dy**. Accordingly, at 2 K the diluted sample exhibited a butterfly shaped hysteresis (see figure 4.7), that was no longer visible above 4 K. A sweep-rate dependent hysteresis was observed at µK temperatures using a Micro-Squid (see figure 4.8). The channel dominating in zero field has a relaxation rate that is almost temperature independent up to 10 K for both samples. In the case of the **YDy** the rate, two order of magnitude slower than that of **Dy**, starts to increase from $T = 10$ K reaching values close to that of the pure sample **Dy** around 20 K. On the other hand, the rate observed for the relaxation channel activated by applying a magnetic field is clearly temperature dependent even at lower temperatures (see figure 4.6). For **Dy** the relaxation rate reaches a plateau at very low temperature, while this was not observed for **YDy**, since below 4 K the rate was so slow that it could not be investigated with our instrumentation.

As a whole, this behavior suggests that the dominant process in zero field is directly related to QTM, whereas the slower one, occurring in applied field, is dominated by thermally activated relaxation.

The observed temperature dependence of the relaxation rate of **YDy** for both relaxation channel was reproduced by including three contributions, a Raman and an Orbach process and a temperature independent process [21, 91–93]:

$$\tau^{-1} = CT^n + \tau_0^{-1} \exp(-\Delta/T) + B \tag{4.2}$$

We performed a simultaneous fit of the relaxation time in field and in zero field (the corresponding parameters being indicated by *f* and *zf*, respectively, in the following), using the same set of parameters for Orbach process (τ_0 and Δ), while the Raman contribution was left free to vary for the two situations. This was intended to account for the possible contribution of direct process in the case of in-field measurements, which may affect the best fit value obtained for the Raman relaxation. A first attempt was made by fixing the value for the energy barrier Δ at 270 K $\sim 195\,\mathrm{cm}^{-1}$, that is the energy of the first excited doublet computed by *ab initio* calculations. We obtained the following values for the best-fit parameters: $\tau_0 = (1.3 \pm 0.2) \times 10^{-10}$ s, $n_f = 6.19 \pm 0.04$, $C_f = (5.0 \pm 0.5) \times 10^{-5}\,\mathrm{s}^{-1}\mathrm{K}^{-\mathrm{n}}$, $B_f = 0$ (fixed), $n_{zf} = 5.5 \pm 0.2$, $C_{zf} = (6 \pm 4) \times 10^{-4}\,\mathrm{s}^{-1}\mathrm{K}^{-\mathrm{n}}$, $B_{zf} = (53 \pm 2)\,\mathrm{s}^{-1}$. In a second step the Δ parameter was

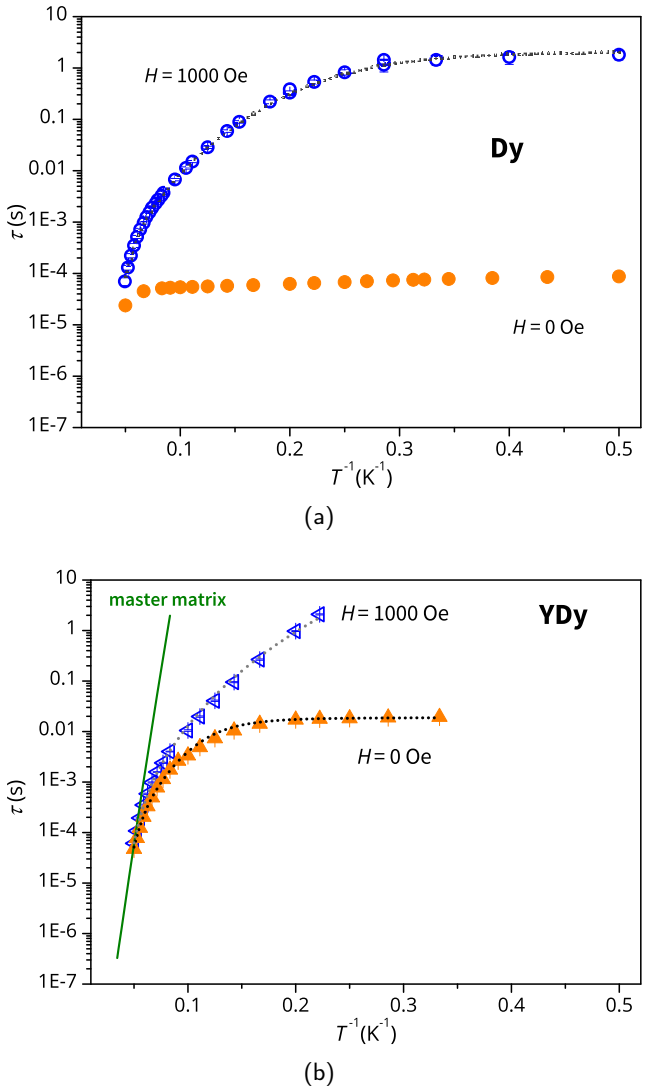

Figure 4.6.: Figure 4.6a: relaxation times versus T^{-1} for compound **Dy**, in zero (full circles) and applied static field (empty ones). The relaxation in zero field is almost temperature independent up to 12 K. The grey dotted line represents the best fit curve with $\Delta = 270$ K. Figure 4.6b: relaxation times versus T^{-1} for compound **YDy**, in zero (full triangles) and applied static field (empty triangles). The dotted lines represent the fit of the relaxation time (see equation 4.2) with $\Delta = 270$ K, the solid line is the relaxation time simulated using the master matrix equation (see text).

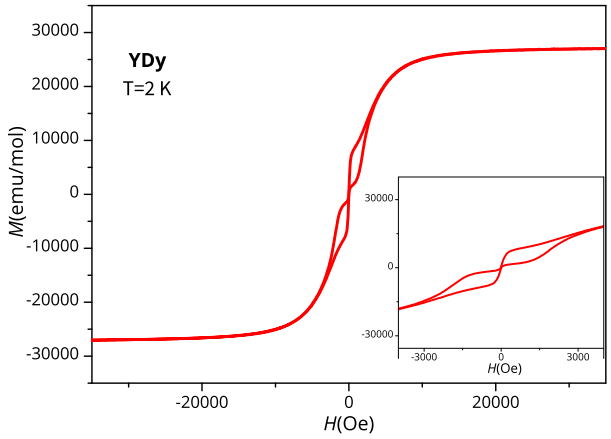

Figure 4.7.: The compound **YDy** exhibited a butterfly shaped hysteresis at 2 K that was not longer visible above 4 K. The hysteresis loop closes around 3000 Oe, indeed AC measurements evidenced that an applied field greater than 1000 Oe increased again the relaxation rate.

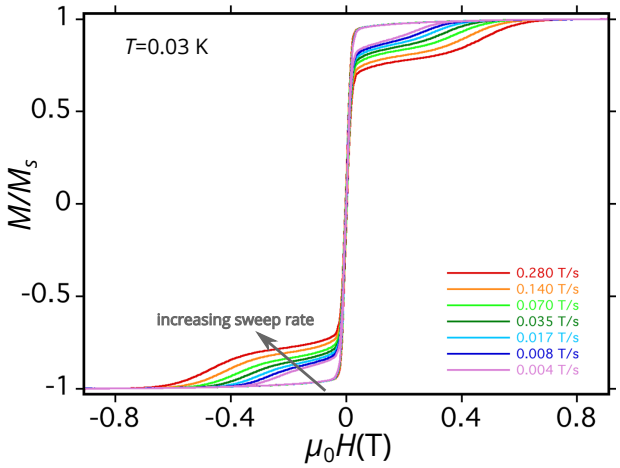

Figure 4.8.: Butterfly shaped hysteresis of **Dy** at 0.03 K for several sweep rates of the magnetic field. The measurements were performed in Grenoble by the research group of professor Wolfgang Wernsdorfer.

left free to vary, providing as best fit values $\tau_0 = (1 \pm 2) \times 10^{-11}\,\mathrm{s}$, $\Delta = (318 \pm 44)\,\mathrm{K}$ (ca. $230\,\mathrm{cm}^{-1}$), $n_f = 6.22 \pm 0.04$, $C_f = (4.7 \pm 0.5) \times 10^{-5}\,\mathrm{s}^{-1}\mathrm{K}^{-\mathrm{n}}$, $B_f = 0$ (fixed), $n_{zf} = 5.6 \pm 0.2$, $C_{zf} = (5 \pm 3) \times 10^{-4}\,\mathrm{s}^{-1}\mathrm{K}^{-\mathrm{n}}$, $B_{zf} = (53 \pm 2)\,\mathrm{s}^{-1}$. It is clear from these results that, while at low temperature Raman and QTM dominate the relaxation, the Orbach process is active in promoting the relaxation in the high temperature regime. It is however not completely clear whether the latter process occurs via the first or the second excited doublet. The differences in τ_0 values are qualitatively consistent with expectations, τ_0 being smaller in the case of larger Δ.

As a comparison, we performed also the fit of the relaxation time of the pure sample **Dy** with $H = 1000\,\mathrm{Oe}$. Fixing the energy barrier at $\Delta = 270\,\mathrm{K}$ we obtained the following values: $\tau_0 = (1.9 \pm 0.2) \times 10^{-10}\,\mathrm{s}$, $n_f = 5.35 \pm 0.03$, $C_f = (4.90 \pm 0.03) \times 10^{-5}\,\mathrm{pers/K^n}$, $B_f = (0.45 \pm 0.04)\,\mathrm{s}^{-1}$ (fixed). If the energy barrier was left free to vary we got: $\tau_0 = (1.6 \pm 0.2) \times 10^{-11}\,\mathrm{s}$, $\Delta = (316 \pm 21)\,\mathrm{K}$. The other parameters were found to be consistent with the ones obtained with the fixed energy barrier.

4.3.1. Relaxation time through a Master Matrix approach

A physical interpretation of the phenomenological fit of the relaxation time included *ab initio* calculations of the transition moments between the states [94, 95] and a master matrix approach based on the system eigenstates computed by *ab initio* [3].

On the basis of these transition moments (see figure 4.9) no efficient QTM relaxation is expected for the ground Kramers' doublet: the underestimation of the probability of QT relaxation by transition moments with respect to the experimental results is clearly due to the fact that this method does not take into account residual dipolar interactions and hyperfine coupling (in the present case the magnetic nuclei are Dy(^{161}Dy, relative abundance= 18.9 % and ^{163}Dy, relative abundance = 24.9 %, both with $I = 5/2$) [96]. The *ab initio* results pointed out that the most probable processes occurring from the first excited state are both Orbach and thermally assisted QTM mechanisms: the former provides access to the second excited state while the latter would allow a reversal of the magnetization. On the basis of the above considerations a relaxation via the second excited state ($E_2 = 237\,\mathrm{cm}^{-1}$) seems to be more likely, in fairly good agreement with the phenomenological value of the above reported value of the energy barrier of $230\,\mathrm{cm}^{-1}$.

Although the transition magnetic moments are increasingly used in rationalizing the spin dynamics, they still provide only semi-quantitative indications [97, 98]. Therefore, a master matrix approach, based on the electronic structure derived by *ab initio* calculations, can furnish a more quantitative reproduction of the observed dynamics. This approach assumes a series of steps of the direct process type promoted by a

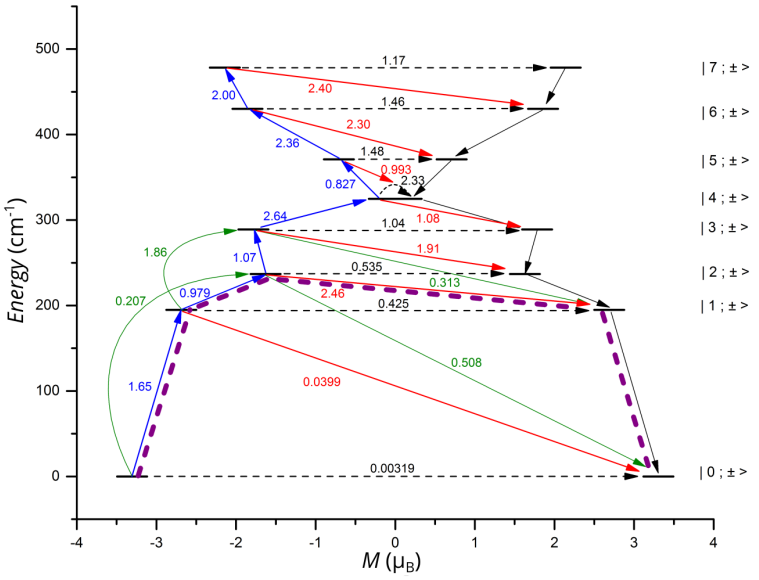

Figure 4.9.: The *ab initio* computed magnetization blocking barrier for **Dy**. The red arrows show the possible pathways of the Orbach process. The dotted black arrows represent the presence of (thermal assisted) quantum tunneling. The numbers are the mean absolute values for the corresponding matrix elements of transition magnetic moment. The dotted purple lines show the most probable relaxation pathways for the reversal of magnetization.

suitable spin phonon coupling Hamiltonian, assumed here of the Villain type[3] for the sake of simplicity. Indeed, the employment of a dynamic spin phonon coupling Hamiltonian proposed in Abragam and Bleaney textbook [33] did not seem to be feasible, because the low symmetry of the systems implied a huge number of CFP following different distortions [99]. Despite being simple, our approach allowed to extract the relaxation time by calculating the relaxation rate γ_q^p from a state $|q\rangle$ (eigenstate of the Hamiltonian that describes the system) to another state $|p\rangle$:

$$\gamma_q^p = \frac{3v}{\pi\hbar^4 m c_s^5} \frac{(E_p - E_q)^3}{\exp\{[\beta(E_p - E_q)]\} - 1} \left\{ |\tilde{D}_a|^2 \left[|\langle p|\boldsymbol{J}_+^2|q\rangle|^2 + |\langle p|\boldsymbol{J}_-^2|q\rangle|^2 \right] + |\tilde{D}_b|^2 \left[|\langle p|\{\boldsymbol{J}_+, \boldsymbol{J}_z\}|q\rangle|^2 + |\langle p|\{\boldsymbol{J}_-, \boldsymbol{J}_z\}|q\rangle|^2 \right] \right\} \tag{4.3}$$

where β is $1/k_B T$, v and m are the volume and the mass of the unit cell, $\tilde{D}_a$ and $\tilde{D}_b$ are the spin-phonon coupling parameters.

The CF eigenfunctions of the ground J multiplet and the corresponding eigenvalues in zero applied field obtained by the *ab initio* calculations were used to obtain the Crystal Field matrix as $\mathcal{H}_{\mathrm{CF}} = \boldsymbol{R}^T \boldsymbol{V} \boldsymbol{R}$ (where $\boldsymbol{R}$ is the eigenfunction matrix and $\boldsymbol{V}$

the diagonal matrix of the corresponding eigenvalues). Therefore the only parameters that need to be adjusted in (4.3) are the spin-phonon coupling parameters and $v/(mc_s^5)$. The diagonalization of the complete hamiltonian including the CF and the Zeeman interaction, $\mathcal{H}_{\mathrm{CF}} + \mathcal{H}_{\mathrm{zmn}}$, provided new eigenvalues and eigenfunctions by which it was possible to calculate the master matrix $\mathbf{\Gamma}$ for all the investigated temperatures. Diagonalization of the master matrix allowed to extract the relaxation time as

$$\tau = -1/\lambda_1 \tag{4.4}$$

where λ_1 is the first non vanishing eigenvalue of the master matrix. If the spin-phonon coupling parameter are set to 0.05 and the pre-factor $(3v/\pi\hbar^4 mc_s^5)$ to 3000, we obtained the solid green curve shown in figure 4.6b. This approach reproduces well the high temperature region above 15 K but it overestimate the relaxation time at lower temperatures. Indeed, this kind of calculation is not intrinsically able to take into account a Raman-like contribution to relaxation, that was phenomenologically employed in equation (4.2). Speaking of which it must be pointed out that, despite the contribtion of a T^n term, we cannot even be sure that this is associated to a real Raman process. Indeed, interactions which are not taken into account by the model, such as hyperfine and residual dipolar intermolecular interactions, may open the possibility of relaxation via quantum tunneling, and might also change the expected field and temperature dependence of direct processes [100].

To conclude, we have presented a comprehensive experimental and theoretical investigation of the anisotropy and dynamic behaviour of a novel mononuclear lanthanide-based SMM. The several approaches proved to be complementary and mutual supportive. Indeed, CTM could provide independent confirmation of the results of *ab initio* calculations in the absence of further spectroscopic information. In turn this allowed to analyze the observed dynamics of the magnetization on the basis of the calculated electronic structure of the lanthanide center. The observed behaviour could be qualitatively rationalized via the commonly used transition probabilities provided by the *ab initio* suite [94, 95]. In addition to this we showed that the relaxation behaviour in the higher temperature range can be correctly reproduced assuming the *ab initio* computed electronic structure in a statistical analysis based on the master matrix approach. On the other hand, further processes are clearly contributing at low temperature, resulting in an experimental relaxation rate which is much faster than predicted by this approach. This might be due either to a true Raman process or to the unaccounted hyperfine and dipolar intermolecular interactions, the latter reduced but not completely quenched by the doping level used here.

5. The Ln(trenovan) series: finding Ariadne's thread

> Above all, don't fear difficult moments. The best comes from them.
>
> *(Rita Levi Montalcini)*

In the introductive chapter to this dissertation we mentioned that the goal of any study aimed at investigating the correlation between electronic structure and magnetization dynamics has to be adapted according to the means at our disposal. This point is clearly evidenced by the investigation we performed on a new series of mononuclear lanthanide compounds, Ln(trenovan) (where H_3trenovan=tris(((3 - methoxysalicylidene)amino)ethyl)amine), which we report in this chapter.

This study required the setup of a different strategy, since we could not use a multitechnique approach like the one described in chapter 4. Indeed, the lack of single crystal samples made more difficult to obtain the molecular structure, that was eventually solved for three derivatives of the series starting from X-ray powder patterns. This fact prevented from performing an investigation of the magnetic anisotropy through single crystal magnetometric techniques such as CTM and it impeded also to conduct high quality luminescence measurements and obtain direct information on the electronic structure. A theoretical approach, like the *ab initio* method employed in the case of $Dy(LH)_3$, was also not very suitable here for two main reasons. First of all, despite that the Ln(trenovan) are all isomorphous, only for three of them was possible to obtain the refinement of the molecular structure. In performing such kind of theoretical calculations it is mandatory to use the exact structure for every sample, so this type of approach would have been feasible only for three complexes. Moreover, as we will show in the next section, the molecular structure of the Ln(trenovan) compounds is very similar to that of the Ln(trensal) series, therefore the calculations would have been demanding from the computational point of view. We therefore decided to follow a different protocol, that combined the magnetic investigation and a phenomenological modeling of the magnetic properties starting from the available information on the Ln(trensal) series.

For this aim we focused the attention only on some of the derivatives of the Ln(trenovan) series, that is the complexes containing Nd, Tb, Dy, Ho, Er and Tm. We

conducted in parallel a magnetic investigation of the corresponding compounds of the Ln(trensal) series, by performing DC magnetometry and CW-EPR experiments and, in the case of Er(trensal) and Dy(trensal), we exploited the results obtained in the magnetic characterization already reported in chapter 3 [18]. After having collected this extra magnetic information for the Ln(trensal) series, in collaboration with Dr. José Jaime Baldoví, we performed a refinement of the trensal CFPs derived from luminescence, including in the physical properties to be fitted the static magnetic susceptibility and all the energies of the observed luminescence transitions [23]. The fitting procedure was performed with the CONDON computational package [101] and it allowed to obtain new sets of CFPs. In order to have a feedback on this method, we calculated the effective g-factor for the complexes containing Kramers' ions and compared the results with the values measured in CW-EPR experiments. Once that the CFPs obtained for the trensal complexes were satisfactory we used them as an input in the program CONCORD.f to fit the magnetic susceptibility of the related family Ln(trenovan) for which only powder susceptibility data and EPR data were available.

In the following, we will first of all introduce the structural features of the Ln(trenovan) series, by briefly reporting how the molecular structure was refined. Then, we will discuss the results of the fitting procedure for the Ln(trensal) family, comparing the experimental and calculated χT vs T curves and the g_{eff} factors. In the second part of the chapter we will present the whole magnetic characterization of the Ln(trenovan) series and we will show some results obtained by preliminary fits of the magnetic susceptibilities.

5.1. Structural features of the Ln(trenovan) series

The synthesis of the Ln(trenovan) series, where H_3trenovan=tris(((3 - methoxysalicylidene) amino)ethyl)amine, was completed by Dr. Jean-Pierre Costes following two different experimental pathways. The H_3trenovan ligand was obtained as previously described from reaction of tris(2-aminoethyl)amine with orthovanillin. The lighter Ln complexes (Ln= Ce, Pr, Nd, Sm) were prepared according to the previously published two-steps process [102] in which the first step corresponds to complexation of Ln ions to the outer O_3O_3 coordination site of the tripodal ligand, with nitrato anions as counter-ions. The resulting complex is isolated and deprotonated in the second step by addition of triethylamine, with a concomitant change of coordination site from the outer O_3O_3 site to the inner N_4O_3 site. The heavier Ln complexes (Ln=Eu-Yb) and the corresponding Y-doped derivatives were prepared in a single step procedure, with triethylamine added to a mixture of the corresponding nitrate salt and H_3L in dimethylformamide.

Chemical formula	$C_{30}H_{33}N_4O_6Pr$	$C_{30}H_{33}N_4O_6Gd$	$C_{30}H_{33}N_4O_6Tm$
Formula mass ($g\,mol^{-1}$)	686.15	702.49	714.17
Crystal system	trigonal	trigonal	trigonal
Space group	*P*-3	*P*-3	*P*-3
Z	2	2	2
a (Å)	14.456(1)	14.240(1)	14.001(1)
b (Å)	14.456(1)	14.240(1)	14.001(1)
c (Å)	7.887(1)	8.121(1)	8.347(1)
α	90	90	90
β	90	90	90
γ	120	120	120
Volume ($Å^3$)	1427.34(1)	1426.25(1)	1417.11(1)

Table 5.1.: Crystal structure data for Pr(trenovan), Gd(trenovan) and Tm(trenovan).

Only microcrystalline samples were obtained from the synthesis and this hampered the determination of the molecular structure by means of single-crystal X-ray diffraction. However, the XRPD diffraction patterns were of good quality and showed that all the samples were isomorphous. In collaboration with Dr. Laura Chelazzi, we determined the structure by means of XRPD, taking advantage that, according to the followed synthetic procedure, Ln(trenovan) compounds should have a molecular structure similar to the one of the Ln(trensal) series. Therefore, for structure solution and refinement

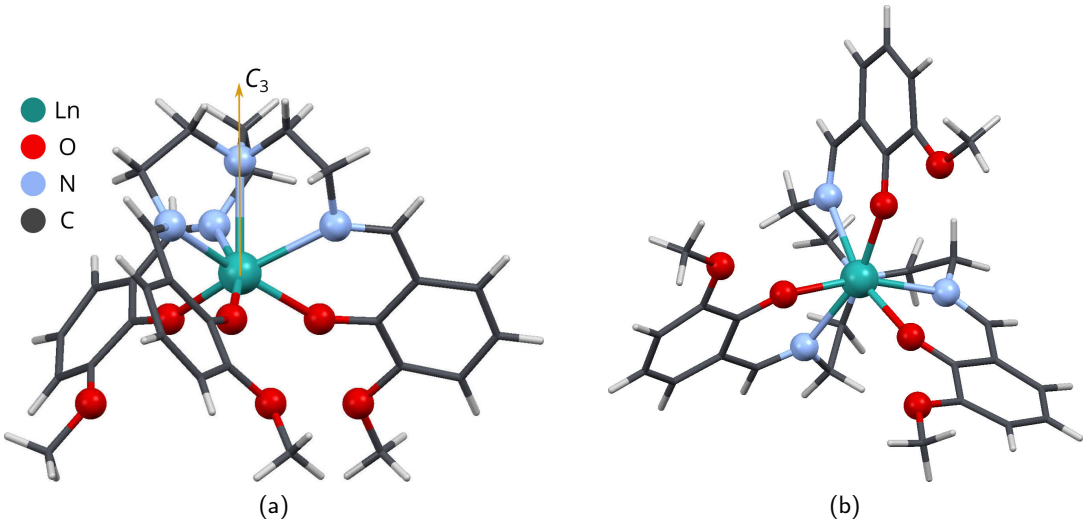

Figure 5.1.: Right panel (a): view along the crystallographic axis a of a molecule of Pr(trenovan) : the Ln ion is coordinated to 3 oxygens and 4 nitrogens. Left panel (b): view along the c axis.

data polycrystalline samples of Pr(trenovan), Gd(trenovan) and Tm(trenovan) were sealed in a 0.5 mm capillary, and an X-ray powder diffractogram in the 2θ range 3°

to 60° (step size 0.01°, time/step 2 s, $V = 40\,\mathrm{kV}$, $I = 40\,\mathrm{mA}$) was collected on a D8 Bruker diffractometer equipped with a primary Ge monochromator for Cu $K_{\alpha 1}$ and a Sol-X solid state detector in Debye-Scherrer geometry.

The structure of Tm(trenovan) was solved by simulated annealing performed using EXPO2013 [103]. The crystal structure data obtained both for Tm(trenovan), Gd(trenovan) and Pr(trenovan) are reported in table 5.1, while in figure 5.1 the molecular structure is displayed. The space group is P-3, there are two molecules per cell and both the lanthanide ion and the aminic nitrogen of the ligand lie on the C_3 axis. The asymmetric unit is then one third of the Ln(trenovan) molecule, the structure of which is closely resembling, both in term of ligand environment and symmetry, that of Ln(trensal) described in chapter 3.

The powder diffraction data for the 9 remaining Ln(trenovan) structures were analyzed with the software Highscore plus, 15 peaks were chosen in the 2θ range 3° to 40° and unit cell parameters were found thanks to the algorithm DICVOL. Pawley refinements were performed for all the 9 unit cell parameters and results are shown in table 5.2.

5.2. Validation of the protocol: the Ln(trensal) series

The Ln(trensal) compounds (Ln=Nd, Tb, Dy, Ho, Er, Tm) were synthesized as previously described [60] and the X-ray powder diffraction patterns of the selected complexes were collected, resulting superimposable to the ones obtained from the crystallographic information file of the corresponding solved molecular structures.

The magnetizations of powder samples pressed in pellets were then measured in a temperature range 2 to 300 K: for $T < 40\,\mathrm{K}$ a static field $H = 1000\,\mathrm{Oe}$ was applied, while for higher temperatures the magnitude of the field was increased, using $H = 10\,000\,\mathrm{Oe}$. We extracted the static magnetic susceptibility χ as M/H and the corresponding χT vs T curves are reported in figure 5.2. The decrease of χT observed on lowering temperature is attributed to the depopulation of the excited levels of the ground multiplet, as it was also briefly discussed for Er(trensal) and Dy(trensal) in section 3.1.

The electronic structures of this family were determined using the CONDON package [101]. This program permits to describe the spectroscopic and magnetic properties in d and f systems with high local symmetry using the full basis of microstates. For the Ln(trensal) complexes, we used as an input the parameters of the Ligand-Field Hamiltonian determined by Flanagan et al.[23]: electron repulsion parameters (F^k, $k = 2, 4, 6$), spin-orbit coupling constant (ξ_{SO}) and crystal field parameters (B_q^k). A total of 12 parameters have been varied (8 CFPs and the 4 free-ion ones) in order to fit all the spectroscopic information as well as the magnetic susceptibility of the complexes.

	Ce	**Nd**	**Sm**	**Eu**	**Tb**	**Dy**	**Ho**	**Er**	**Yb**
Z	2	2	2	2	2	2	2	2	2
Crystal system	trigonal	trigonal	trigonal	trigonal	trigonal	trigonal	trigonal	trigonal	trigonal
Space group	P-3	P-3	P-3	P-3	P-3	P-3	P-3	P-3	P-3
a (Å)	14.514(1)	14.430(1)	14.314(1)	14.281(1)	14.188(1)	14.147(1)	14.101(1)	14.081(1)	13.977(1)
b (Å)	14.514(1)	14.430(1)	14.314(1)	14.281(1)	14.188(1)	14.147(1)	14.101(1)	14.081(1)	13.977(1)
c (Å)	7.831(1)	7.924(1)	8.048(1)	8.071(1)	8.146(1)	8.208(1)	8.272(1)	8.287(1)	8.363(1)
α	90	90	90	90	90	90	90	90	90
β	90	90	90	90	90	90	90	90	90
γ	120	120	120	120	120	120	120	120	120
Volume (Å^3)	1427.34	1429.00	1428	1425.49	1420.00	1422.47	1423.16	1421.06	1414.11

Table 5.2.: Crystal cell parameters for the Ln(trenovan) series, see text for details.

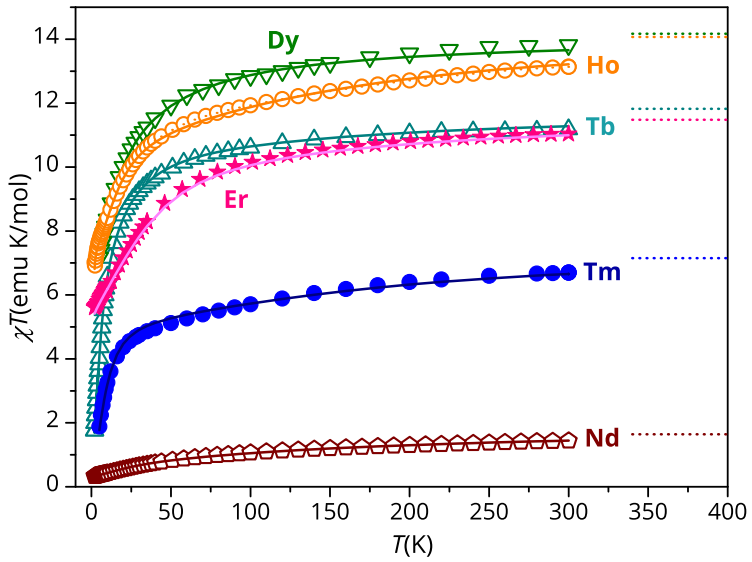

Figure 5.2.: Experimental values (symbols) and theoretical fits (solid lines) of the χT curves for the Ln(trensal) series from 2 to 300 K: Nd (wine empty pentagons), Tb (dark cyan empty triangles), Dy (green empty triangles), Ho (orange empty circles), Er (pink stars), Tm (blue full circles). The dotted lines represent the value of the Curie's constant for the corresponding free ion.

	Nd	**Tb**	**Dy**	**Ho**	**Er**	**Tm**
	(cm^{-1})	(cm^{-1})	(cm^{-1})	(cm^{-1})	(cm^{-1})	(cm^{-1})
B_0^2	−770(518)	−426(122)	−847(1081)	−921(37)	−761(40)	−940(9)
B_0^4	−55(98)	263(17)	−780(297)	−395(87)	−118(24)	−365(49)
B_3^4	−2414(244)	−2326(12)	−2267(238)	−1624(104)	−1855(54)	−1481(2)
B_0^6	1647(49)	−417(73)	−356(436)	565(120)	1032(17)	1301(631)
B_3^6	484(35)	1337(664)	803(494)	432(74)	466(43)	31(388)
B_6^6	1049(51)	74(65)	843(273)	297(47)	706(71)	378(5)
B'^6_3	−226(95)	−182(1544)	−377(1473)	−749(29)	8(417)	−737(5)
B'^6_6	97(107)	327(805)	−169(892)	1194(10)	17(355)	38(16)
ξ_{SO}	888(41)	1705	1866(119)	2122(46)	2368(53)	2612(156)
F^2	71 502(1800)	89 540	95 039(6256)	92 746(1269)	95 400(2133)	102 027(7184)
F^4	52 604(1120)	63 485	62 755(3299)	73 317(1787)	74 491(954)	73 661(7433)
F^6	32 365(2737)	43 345	53 145(3775)	53 794(2361)	49 956(4105)	53 041(3576)
SQX	1.53 %	2.21 %	0.62 %	0.54 %	0.46 %	1.11 %

Table 5.3.: Parameters of the Ligand-Field Hamiltonian extracted by fitting both the spectroscopic energy levels and the magnetic susceptibilities. The CFPs are in Wybourne's notation (see section 1.2): B_q^k represent the real parameters while B'^k_q are the imaginary ones.

A total of 23 (Tb), 45 (Dy), 88 (Ho), 56 (Er), 41 (Tm) and 63 (Nd) energy levels or Kramers doublets have been fitted together with the magnetic susceptibility data. An order of magnitude of priority has been given to the ground J energy levels when determined. This is the first time in which a systematic study combining spectroscopic and magnetic data is performed for a family of compounds. The resulting CFPs, the F^ks and the ξ_{SO} are reported in table 5.3, together with the total relative error of the fits (SQX).

In the case of Er(trensal) we took advantage of the work of Pedersen et al. [61] where the magnetic susceptibility and the magnetization along the easy axis direction were experimentally determined. Furthermore, the determination of $g_{\parallel}$ by EPR permitted to simulate the evolution of the ground doublet under an applied magnetic field. All these experimental data have been fitted resulting in a more accurate picture with a total relative error of 0.46 %. As in the work of Flanagan et al. [23], in the case of Tb(trensal), the electron repulsion parameters and the spin-orbit constant were not varied in the fitting, due to the smaller number of energy levels spectroscopically determined: this explains the larger discrepancy (2.21 %) obtained for this complex.

Nd $^4I_{9/2}$	**Tb** $^7F_6$	**Dy** $^6H_{15/2}$	**Ho** $^5I_8$	**Er** $^4I_{15/2}$	**Tm** $^3H_6$
(cm^{-1})	(cm^{-1})	(cm^{-1})	(cm^{-1})	(cm^{-1})	(cm^{-1})
0	0	0	0	0	0
66	15	36	3	54	20
243	15	107	3	101	371
426	55	214	41	110	371
816	55	295	41	300	425
	109	673	215	560	425
	197	747	315	614	473
	440	786	315	647	548
	440		363		782
	520		421		782
	520		421		872
	535		641		872
	579		673		933
			673		
			726		
			726		
			737		

Table 5.4.: Energy levels of the ground multiplet for the investigated derivatives of the Ln(trensal) series. For Kramers' ions (Nd, Dy, Er) the energies of the doublets were reported.

In the fitting procedure we considered all the spectroscopic transitions observed in the paper of Flanagan et al. (0 cm^{-1} to 20 000 cm^{-1}), thus calculating all the energy

	composition
Nd	82 % $\|\pm 5/2\rangle$, 5 % $\|\mp 1/2\rangle$, 12 % $\|\mp 7/2\rangle$
Tb	47 % $\|0\rangle$, 21 % $\|3\rangle$, 21 % $\|-3\rangle$, 5 % $\|6\rangle$, 5 % $\|-6\rangle$
Dy	34 % $\|\mp 7/2\rangle$, 32 % $\|\pm 5/2\rangle$,23 % $\|\mp 1/2\rangle$, 6 % $\|\mp 13/2\rangle$, 5 % $\|\pm 11/2\rangle$
Ho	38 % $\|3\rangle$, 38 % $\|-3\rangle$, 16 % $\|0\rangle$
Er	77 % $\|\pm 13/2\rangle$, 20 % $\|\pm 1/2\rangle$
Tm	46 % $\|6\rangle$, 46 % $\|-6\rangle$, 9 % $\|-3\rangle$, 9 % $\|3\rangle$

Table 5.5.: Composition of the ground doublets and ground states for the Ln(trensal) family.

levels up to 20 000 cm^{-1}. Since magnetic properties are influenced mainly by the lowest energy levels, in table 5.4 we reported only the energy splittings of the ground multiplets while in table 5.5 the composition of the ground doublet or of the ground state can be found. A direct comparison of the experimental [64] and calculated energy levels of the ground multiplet is only possible for Er(trensal) complex and the agreement is very good.

As an additional feedback to the procedure, we calculated the g_{eff} factor of Nd, Dy and Er, using the CFPs reported in table 5.3 and the home-developed software EVALUCF [80]. The results are displayed in table 5.6 evidencing a good qualitative agreement with the experimental values. The magnetic anisotropy of Er and Dy was previously investigated in other works [18, 61, 63] (see also chapter 3), while this is the first time that the anisotropy of Nd(trensal) complex is reported. As it can be seen from table 5.6, the ground doublet of the complex is characterized by an easy-axis magnetic anisotropy.

	Nd		**Dy**		**Er**	
	exp	calc	exp	calc	exp	calc
$g_{\parallel}$	2.65(1)	2.79	1.8(1)	1.4	11.8(4)	11.1
$g_{\perp}$	0.71(1)	1.07	9.4(5)	9.9	3.6(1)	4.3

Table 5.6.: Experimental values of g_{eff} and calculated ones, using the CFPs reported in table 5.3. The EPR investigation of the pure Nd(trensal) complex was conducted with a X-band spectrometer at 5 K, while the values of the g_{eff} for Er(trensal) and Dy(trensal) originate from a previous EPR W-band experiment on Y(III) diluted samples (3.1 % and 5.8 % of Dy(III) and Er(III) respectively) [18].

The fitting procedure of the spectroscopic and magnetic data for Ln(trensal) complexes aimed both to validate the working method and to obtain CFPs that could be used as starting guesses for the fitting of the Ln(trenovan) χT curves: the set of CFP reported in table 5.3 were introduced as an input in the program CONCORD.f in order

to fit the magnetic susceptibility of the Ln(trenovan) compounds.

5.3. Magnetic characterization of the Ln(trenovan) series

The modeling of the magnetic susceptibilities of the Ln(trenovan) (Ln=Nd, Tb, Dy, Ho, Er, Tm) was not straightforward. The room temperature values of the χT vs T curves were far below the Curie's constant and this could not be attributed only to CF effects. Since the XRPD patterns did not evidence the presence of other crystalline phase, in collaboration with Dr. Giuliano Giambastiani, we performed a Thermogravimetric analysis (TGA) on the selected samples: the results indicated the presence of a variable residual of solvent used for washing (dimethylformammide or diethylether). In particular for Nd the amount was quite large, around 22 % of the weight, while for the others the percentage was lower (Tb 12 %, Dy 8.5 %, Ho 7 %, Er 6 % and Tm 3 %).

Nd $^4I_{9/2}$	**Tb** $^7F_6$	**Dy** $^6H_{15/2}$	**Ho** $^5I_8$	**Er** $^4I_{15/2}$	**Tm** $^3H_6$
(cm^{-1})	(cm^{-1})	(cm^{-1})	(cm^{-1})	(cm^{-1})	(cm^{-1})
0	0	0	0	0	0
50	12	37	3	58	11
188	12	100	3	110	219
380	35	258	28	119	219
876	35	276	28	457	301
	80	723	66	648	301
	109	798	108	669	349
	255	826	108	692	468
	255		274		497
	271		274		497
	300		314		573
	300		568		573
	358		574		617
			574		
			593		
			593		
			601		

Table 5.7.: Energy levels of the ground multiplet for the investigated derivatives of the Ln(trenovan) series. For Kramers' ions (Nd, Dy, Er) the energies of the doublets were reported.

The values of the molar susceptibility extracted from DC measurements were then rescaled for each sample, according to the different amount of solvent estimated by TGA. The magnetic susceptibility of Nd, Tb, Dy, Ho, Er and Tm complexes were then fitted with the CONDON package. The resulting energy levels and CFPs are reported in table 5.7 and 5.9, while the composition of the wavefunctions can be found

	composition
Nd	72 % $\|\pm5/2\rangle$, 19 % $\|\mp1/2\rangle$, 9 % $\|\mp7/2\rangle$
Tb	32 % $\|3\rangle$, 32 % $\|-3\rangle$, 19 % $\|0\rangle$, 9 % $\|6\rangle$, 9 % $\|-6\rangle$
Dy	69 % $\|\pm1/2\rangle$, 17 % $\|\pm7/2\rangle$, 12 % $\|\mp5/2\rangle$
Ho	43 % $\|3\rangle$, 43 % $\|-3\rangle$, 8 % $\|0\rangle$
Er	92 % $\|\pm13/2\rangle$
Tm	46 % $\|6\rangle$, 46 % $\|-6\rangle$

Table 5.8.: Composition of the ground doublets and ground states for the Ln(trenovan) family.

in table 5.8. Since no information on the energies of excited multiplets was available, the electron repulsion parameters (F^k, $k = 2, 4, 6$) and spin-orbit coupling constant (ξ_{SO}) were not fitted but fixed to the values found for the Ln(trensal) series.

The temperature dependence of the experimental χT curves, together with the calculated ones, is displayed in figure 5.3, showing features analogue to the one of the Ln(trensal). There are, however, small differences, in particular for Er(trenovan) and Tm(trenovan) compared to their homologue trensal derivatives. In the case of Er(trenovan) we notice that the experimental χT value at low temperature (5 K) is larger than the corresponding one for Er(trensal), being 7.62 emu K mol^{-1} for the former and 5.86 emu K mol^{-1} for the latter. This may suggest that the ground doublet of Er(trenovan) is more magnetic than that of Er(trensal). This hypothesis is indeed confirmed by EPR data (*vide infra*).

As regards Tm(trenovan), the χT curve shows a very rapid increase in temperature compared to that of Tm(trensal). This can be ascribed to a different energy level structure of the two complexes. Indeed the fitting of the magnetic susceptibility suggests the presence of excited states lying at lower energy compared to those reported in table 5.4 for Tm(trensal). This hypothesis is partially confirmed by the information extracted from the high-field high-frequency EPR spectra collected for this sample (*vide infra*). More generally, the energy levels reported in table 5.7 seem to indicate that, in the case of Tb, Ho and Tm, the energy splittings due to the CF result to be lesser than the corresponding Ln(trensal) complexes, while for the half-integer spin complexes the energy spanning is comparable.

As a partial feedback to the fitting procedure we employed the CFP obtained by CONDON to calculate the g_{eff} factor of Nd, Dy and Er derivatives. The comparison between the calculated g_{eff} factor and the experimental values is reported in table 5.10. The correct kind of magnetic anisotropy is predicted and a qualitative agreement is confirmed for all the three complexes. Moreover, the calculated g_{eff} corroborates the higher value of axiality for Er(trenovan) compared to Er(trensal).

Although the results obtained from this fitting procedure do not embody the ultimate

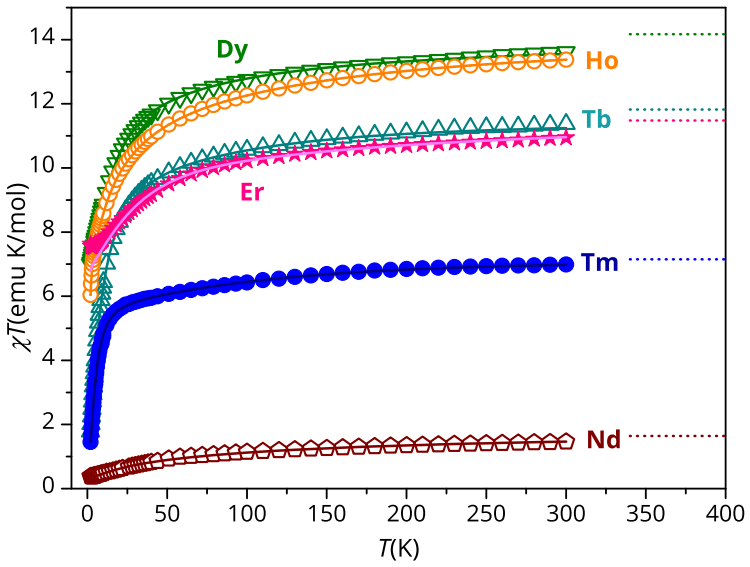

Figure 5.3.: Experimental values (symbols) and theoretical fits (solid lines) of the χT curves for the Ln(trenovan) series from 2 to 300 K: Nd (wine empty pentagons), Tb (dark cyan empty triangles), Dy (green empty triangles), Ho (orange empty circles), Er (pink stars), Tm (blue full circles). The dotted lines represent the value of the Curie's constant for the corresponding free ion.

	Nd	**Tb**	**Dy**	**Ho**	**Er**	**Tm**
	(cm^{-1})	(cm^{-1})	(cm^{-1})	(cm^{-1})	(cm^{-1})	(cm^{-1})
B_0^2	−558(847)	−234(116)	−780(42)	733(18)	−793(492)	−936(3)
B_0^4	497(169)	360(22)	1686(69)	1100(19)	1163(209)	−25(2)
B_3^4	−2965(52)	−898(10)	−2055(566)	256(11)	−2273(848)	−111(1695)
B_0^6	1483(36)	−1267(8)	114(167)	161(22)	1067(218)	198(143)
B_3^6	653(42)	736(106)	772(64)	64(13)	503(133)	−90(37)
B_6^6	1005(52)	−1668(142)	1211(41)	−876(43)	625(329)	298(5)
B'^6_3	−246(104)	1803(5)	−1395(46)	−196(6)	44(2135)	−587(12)
B'^6_6	249(44)	2520(21)	−246(225)	1265(12)	−114(2578)	254(21)

Table 5.9.: Parameters of the CF Hamiltonian extracted by fitting the magnetic susceptibilities and using as starting guesses the best-fit parameters of the Ln(trensal) complexes. The CFPs are in Wybourne's notation (see section 1.2): B_q^k represent the real parameters while B'^k_q are the imaginary ones.

	Nd		**Dy**		**Er**	
	exp	calc	exp	calc	exp	calc
$g_{\parallel}$	2.62(1)	2.24	1.63(1)	1.88	13.54(1)	14.33
$g_{\perp}$	0.68(1)	1.57	8.7(2)	10.36	2.37(1)	2.38

Table 5.10.: Experimental values of g_{eff} and calculated ones using the CFPs reported in table 5.9. The EPR investigation of the pure Nd(trenovan) and Y(III) diluted Dy(trenovan) ((9.2 % of Dy(III)) was conducted with a X-band spectrometer at 5 K, while the values of the g_{eff} for Er(trenovan) derive from high-field high-frequency EPR spectra at frequency $\nu = 331.2$ GHz (see also figure 5.4a).

picture of the electronic structure of the Ln(trenovan) complexes, they are however supportive and can be used as guesses to explain some of the magnetic features observed in this series.

5.3.1. Investigation of the magnetic anisotropy

We will now discuss the magnetic anisotropy of all the complexes of the series, that was investigated by means of CW- EPR spectroscopy (X-band and W-Band in the Laboratory of Molecular Magnetism, Florence) and also by high field- high frequency EPR at the LNCMI (Grenoble) in collaboration with Dr. Anne-Laure Barra. All the samples were undiluted except Gd(trenovan) and Dy(trenovan), for which the isostructural complexes YGd(trenovan)and YDy(trenovan) were studied (5.6 % and 8.2 % of Gd(III) and Dy(III) respectively).[1]

The crystal symmetry of the series of isostructural complexes Ln(trenovan) is strictly trigonal, with the Ln ion lying on the C_3 axis. Therefore, the preferred orientations for the magnetization will be along the C_3 axis or in a plane perpendicular to it. The

	Ce	**Yb**
	exp	exp
$g_{\parallel}$	-	4.92(1)
$g_{\perp}$	1.94(1)	2.643(6)

Table 5.11.: Experimental values of g_{eff} of pure Ce(trenovan) and Yb(trenovan). The Ce(trenovan) EPR investigation was performed at X-band spectrometer (ca. 9.4 GHz) and at 10 K, while the values of the g_{eff} for Yb(trenovan) were obtained by high-field high-frequency EPR spectra at frequency $\nu = 220.8$ GHz and $T = 5$ K (see also figure 5.4b).

Ln(trenovan) complexes exhibited both kind of magnetic anisotropy: Ce, Dy and Gd

[1] The concentration of Gd and Dy dopants in Y phase was estimated by the scaling factor necessary to superimpose superimposing the magnetization curves of pure and diluted sample.

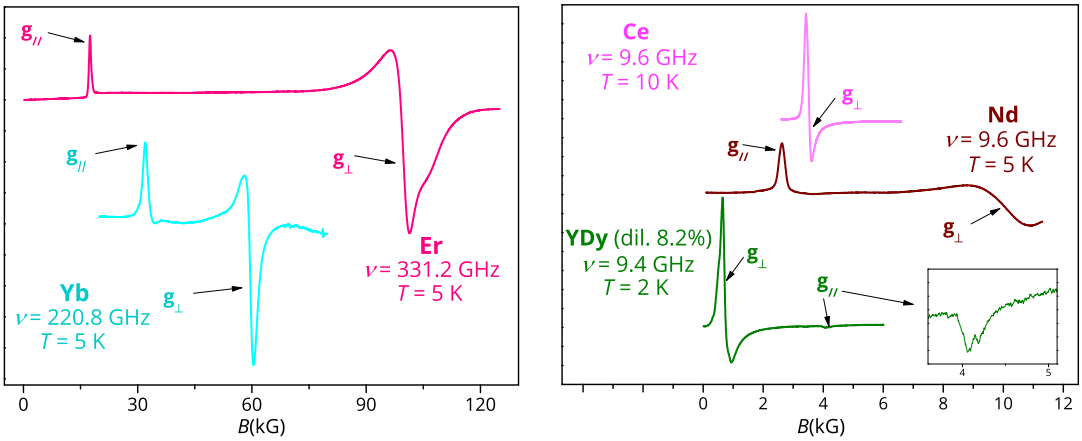

Figure 5.4.: Right panel (a): high-frequency EPR spectra for pure Er(trenovan) and Yb(trenovan) samples measured at LNMCI-Grenoble. Left panel (b): X-band EPR spectra for pure Ce(trenovan), diluted YDy(trenovan) and pure Nd(trenovan).

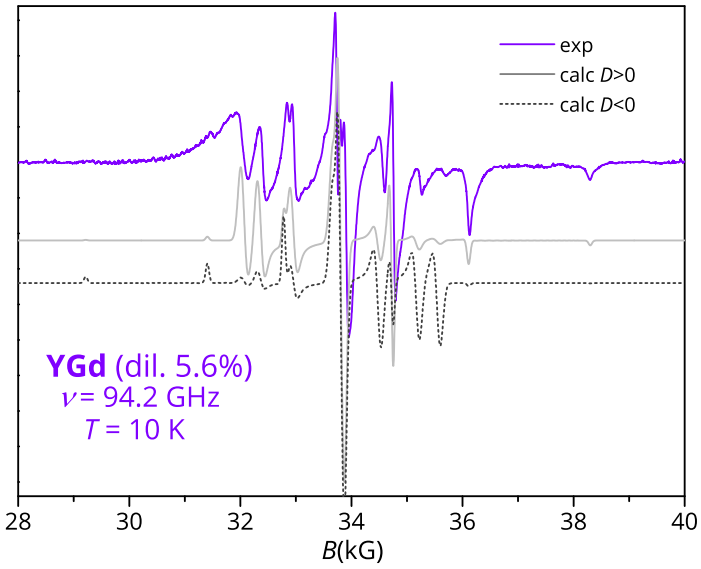

Figure 5.5.: W-band EPR spectrum for YGd(trenovan), along with its simulation obtained with Easyspin. See text for the values of the simulation parameters.

derivatives have an easy plane magnetic anisotropy, while Nd, Er and Yb derivatives have an easy axis anisotropy (see figure 5.4 and tables 5.10 5.11). In the case of Ce derivative the EPR investigation did not detect any signal corresponding to a parallel transition. Since Ce(III) has a ground multiplet with $J = 5/2$, the trigonal symmetry of the CF mixes state with $M_J = \pm 5/2$ and $M_J = \mp 1/2$. A simple estimate of the $g_{\parallel}$ value suggests that, to be consistent with the observed $g_{\perp}$, its value should be around 0.40 and it is thus beyond the instrumental limit of the X-band spectrometer.

As regards Sm(trenovan) the sample turned out to contain some Gd(III) impurity: indeed its EPR spectrum features a striking similarity to the one of Gd(trenovan) diluted in the Y(III) diamagnetic matrix (see figure 5.6). We attributed this behaviour

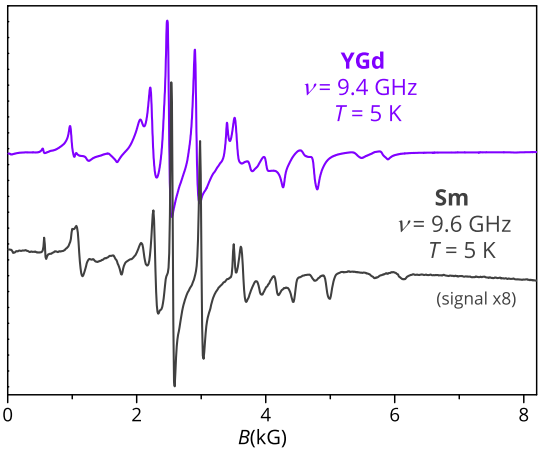

Figure 5.6.: Comparison of the X-band EPR spectra of YGd(trenovan) and Sm(trenovan). For the sake of clarity the spectrum of Sm was amplified by a factor 8.

to the very low magnetic moment of Sm(trenovan) at low temperature, which then acts as an effective 'quasi-diamagnetic' matrix for the Gd(III) impurity dopants. The simulation of the W-band EPR spectrum of YGd(trenovan) is reported in figure 5.5 and it was obtained through the Matlab toolbox Easyspin [104], on the basis of the following spin hamiltonian in Stevens'notation:

$$\mathcal{H} = b_2^0 \boldsymbol{O}_2^0 + b_4^0 \boldsymbol{O}_4^0 + \mu_B \boldsymbol{S} \cdot \boldsymbol{g} \cdot \boldsymbol{B} \tag{5.1}$$

with $S = 7/2$ and $b_2^0 = D/3$, where D is the zero-field splitting parameter. The best simulation of the EPR spectrum gave $D = (0.0615 \pm 0.0005)\,\mathrm{cm}^{-1}$, that implies an energy splitting of the ground multiplet around 1 K ($D(S^2 - 1/4)$), and $b_4^0 = 4.5 \times 10^{-5}\,\mathrm{cm}^{-1}$ and $g = 1.995$. The values of the D and g parameters are consistent with those of other Gd(III)-based complexes [105, 106]: these complexes are indeed quite isotropic since Gd(III) has the $4f$ shell half filled and the orbital contribution to the angular momentum cancels.

A few words should be spent on the positive D parameter we have just reported. An accurate determination of the sign of D would have required to study the variation of the YGd EPR spectrum as a function of temperature, in order to observe a change in the intensity of the outermost transitions, either parallel or perpendicular. However, this was not feasible because only the spectrum collected at 10 K had a signal to noise ratio good enough to evidence clearly these transitions, which were further of quite weak intensity. Nevertheless, the analysis of the relative intensity of the parallel transitions, simulated both by using $D = 0.0615$ and $D = -0.0615$ and the same fourth-order term, strongly supports the hypothesis of a $D > 0$ (see also figure 5.5) Finally, the spectra were not resolved enough to obtain reasonable estimates of trigonal anisotropy parameters (b_4^3, b_6^3, b_6^6).

The EPR investigation of complexes with integer spin is usually less straightforward, because it is common not to detect a signal, for the reasons discussed previously in section 2.2.1. The Ln(trenovan) complexes with integer spin do not make an exception, indeed we were able to identify a signal in the EPR spectrum of Tm(trenovan) and Tb(trenovan) only, while the spectra of Pr(trenovan) and Ho(trenovan) could not be safely assigned. The complexes containing Tb and Tm were measured both in X-band and at high-field high-frequency. The X-band EPR spectrum of Tm(trenovan) was completely uninformative, while the high frequency EPR spectra were more simple to analyze by plotting the resonance field as a function of microwave frequency (see figure 5.7). If we assume that the observed transitions are parallel ones we can interpret the EPR spectra according to an effective doublet hamiltonian

$$\mathcal{H} = g_{\parallel}\mu_{\mathrm{B}} B \boldsymbol{S}_z + \Delta \boldsymbol{S}_x + \Delta \boldsymbol{S}_y \tag{5.2}$$

where Δ is the energy gap in zero field between the two levels for which the transition is observed [33] and the $\boldsymbol{S}_x$ and $\boldsymbol{S}_y$ terms arise as a consequence of the transverse terms of the CF. By studying the dependence of the microwave frequency on the resonance field it is possible to get a lower estimate of this energy gap Δ, that is evidenced by the y-intercepts of the linear fits in figure 5.7 (red dotted lines). Since for low fields the linearity does not hold, the estimated energy gap is a lower limit of the real one.

The linear dependence of the microwave frequency on the resonance field (see figure 5.7) suggests that Tm could have an energy separation between the ground state and the first excited one of about 9 cm^{-1}. This deduction is in quite good agreement with the energy levels extracted from the fitting of its χT curve (see table 5.7), thus lending support to the obtained set of CFPs. However, the linear dependence of the resonance field, with an estimated effective g value of 8.9, is completely at odds with the results of magnetic characterization, which indicated two low lying singlets with extremely small effective g values. Further, one has to consider that to get a reasonable transition

probability, either the polarization of the microwave should be parallel to the applied field, or the local symmetry at low temperature should be lower than trigonal, allowing for further mixing of different M_J states.

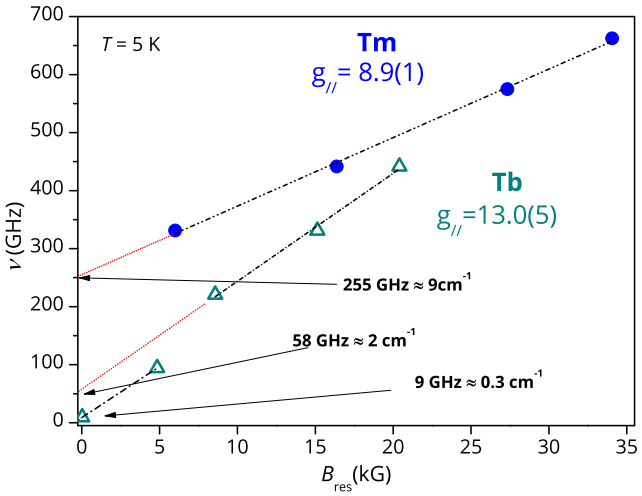

Figure 5.7.: Frequency vs resonance field for Tm(trenovan) and Tb(trenovan).

For Tb(trenovan) the interpretation of the spectra turned out to be more complex: the measurements in X-band evidenced a transition in zero field with four lines, that are attributable to the hyperfine interactions with a $I = 3/2$ nucleus. Since the transition is observed in zero field the two energy levels should be separated by $0.3\,\mathrm{cm}^{-1}$. On the other hand, the analysis of high frequency data suggests an energy gap of $2\,\mathrm{cm}^{-1}$. A possible explanation to this discrepancy could be that different paramagnetic species are involved, meaning that the observed transitions are due to Tb(III) ions that experience different electrostatic environment. The sample, checked with powder X-ray, resulted to be isostructural with the other samples of the series with a tolerance of about 5 %. EPR spectroscopy is, however, a very sensitive technique so it is likely that even small amount of a different paramagnetic species could be detected. Actually, the same explanation had to be invoked to explain the observation of a similar EPR spectrum in Tb(trensal) [63].

The behavior of the magnetic anisotropy for the Ln(trenovan) series can be explained considering the aspherical electron density distributions of the lanthanide ions, previously outlined in chapter 3. Indeed the anisotropies of Ce and Dy derivatives have easy plane anisotropy while Er and Yb derivatives are easy axis. However, as already observed for Ln(trensal), the EPR investigation evidenced that all the complexes are characterized by highly mixed ground states and this is particularly true for Nd for which a weak easy axis anisotropy is observed, whereas a weak easy plane one could be expected if one assumed a behavior similar to Dy [66].

5.3.2. Magnetization dynamics

The investigation of the magnetization dynamics for the Ln(trenovan) series evidenced that only compounds that contains Kramers' ions exhibit a non-zero imaginary susceptibility and only in presence of an applied magnetic field. Moreover, the magnetic relaxation seems to be independent from the magnetic anisotropy of the complexes, since compounds with both easy axis and easy plane anisotropy showed a non-zero out of phase susceptibility. An analogue behavior was already observed for Er(trensal) and Dy(trensal) in chapter 3.

The magnetic relaxation was firstly studied as a function of the applied magnetic field at 2 K: the field, which provided the maximum of the imaginary susceptibility, was chosen as optimum field and was employed to perform the measurements in function of temperature. The scan in field at 2 K also evidenced a secondary maximum in the imaginary susceptibility for applied fields greater than 2000 Oe: its intensity however decreases very rapidly with temperature and it is no longer visible above 5 K. Moreover, this peak is completely absent in the diluted samples YGd(trenovan) and YDy(trenovan). This behavior suggests that the presence of this secondary peak in χ'' may be due to dipolar interactions between different paramagnetic centers. Indeed, a similar feature was observed also in pure Er(trensal) and Dy(trensal) samples.

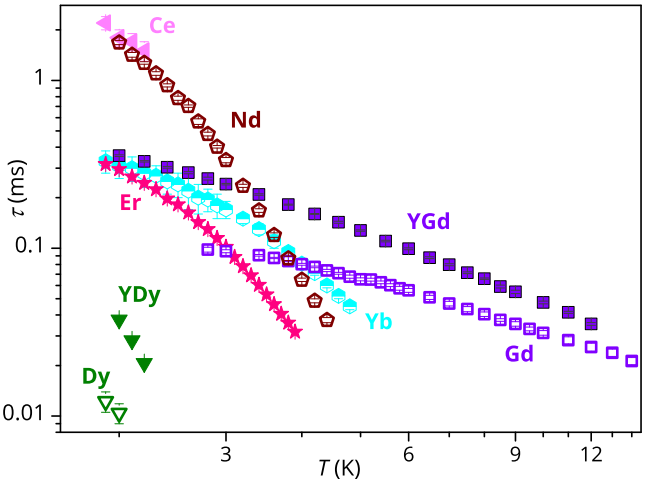

Figure 5.8.: Temperature dependence of the magnetic relaxation time for the Ln(trenovan) complexes with half-integer spins.

The temperature dependence of the relaxation time for the compounds of the series is reported in figure 5.8. Although the Sm(trenovan) complex showed a non-zero imaginary susceptibility, we did not report its relaxation time in the figure. Indeed, on the basis of the above reported EPR characterization, we could not exclude that the observation of a slow dynamics might be traced back to the Gd impurity. This stresses once more the importance of an integrated approach to the characterization of slow

relaxing lanthanide complexes, where AC susceptibility results are complemented by spectroscopic outcomes.

A quantitative study of the mechanisms involved in the magnetic relaxation was not feasible, since it would have required to investigate the diluted analogues of the samples and they were not available. However, it is evident from the *log-log* plot in figure 5.8 that the relaxation time of the investigated pure complexes presents two type of regimes that can be attributable to a Raman-like mechanism (at higher temperatures) and a direct process (at lower temperature). The lack of the corresponding diluted sample prevented any further in-depth analysis.

As regards YDy(trenovan), above 2.2 K its dynamics was too fast to be measured with our AC susceptometer: indeed, the corresponding relaxation time, extracted by fitting the χ'' curves with the Casimir Dupré equation [90], is available only for three temperatures and it is not thus suitable for discussion (see figure 5.8). In the case of YGd(trenovan), it is possible to affirm that the relaxation is not promoted by an Orbach process, since EPR results showed that the whole $S = 7/2$ multiplet spans only 1 K and D value is positive. Indeed, a simple check of the YGd(trenovan) relaxation time above 7 K by means of the Arrhenius' law would give an energy barrier of $10\,\mathrm{cm}^{-1}$, that, in this case, has no physical meaning.

As a whole, these results indicate once more that this type of complexes does not behave as 'real' SMM, if we denote with this term systems for which relaxation can be engineered by varying the anisotropy. The crucial parameter is rather the number of unpaired electrons, only Kramers' ions showing in-field slow relaxation. In this respect, the analysis of a quite complete series such as that of Ln(trenovan) can be of help even in the absence of detailed spectroscopic or *ab initio* characterization.

6. Molecular spin qubits: relaxation dynamics of a vanadyl-based complex

Misura ciò che è misurabile, e rendi misurabile ciò che non lo è.

(Galileo Galilei)

Quantum bits, or qubits, are at the basis of quantum computation and different strategies to realize them are currently explored [107], since this would result in a tremendous improvement of our computing capabilities. Any two-level system can be used as a qubit, but this does not necessarily mean that the system must possess only two states: indeed if a system possesses two levels well separated in energy from the excited ones, they can fit for the purpose. There are several physical systems that are currently studied as potential qubits: ionic traps [108], photons [109], quantum dots in semiconductors [110] and of course nuclear [111–113] and electronic spins [16, 114–117]. The advantage of using spin-systems relies on the fact that spins can be initialized and read-out by performing magnetic resonance techniques. The parameters that need to be optimized in the design of these qubits are: i) the spin-lattice relaxation time $\mathcal{T}_1$, that measures the loss of energy from the system because of the interaction with the environment (lattice); ii) the characteristic time, $\mathcal{T}_2$, in which the spin loses the memory of the phase of the superposition state in which it has been prepared. This parameter is of crucial importance for single qubit operation and, as it was stated in section 2.2.2, a lower estimation of this decoherence time can be extracted by the phase-memory time $\mathcal{T}_\mathrm{m}$, measured, e.g., by pulsed EPR experiments.

Transition metal complexes offer tremendous potential as tunable qubits, indeed reported $\mathcal{T}_\mathrm{m}$ are typically around a few microseconds at cryogenic temperatures [118]. These long coherence times are partially due to the quenching of orbital angular momentum featured by these systems. Indeed, especially for light transition metals, the spin-orbit coupling, which mediates the spin-phonon coupling, is significantly lower than, e.g. that of lanthanide-ions. Thus, in the rational design of systems exploitable as qubits it is important to understand that any process causing a $\mathcal{T}_1$ relaxation also results in a $\mathcal{T}_2$ relaxation. Indeed, if the spin exchange energy with its external environment

both the transverse and longitudinal components of its angular momentum would be randomly changed and it would immediately lose phase relations with other spins. Up until few years ago the quest for systems behaving as spin-qubits was concentrated on polynuclear transition metal complexes [16] and one of the most known example is the Cr_7Ni ring [119]. However, the main disadvantage of these systems is that, despite having a ground state with $S = 1/2$, the presence of relatively low-lying excited states add additional paths for a spin-lattice relaxation. More recently, the research in this field then focused back on simplest spins $S = 1/2$, that can be embodied either by organic radicals [120] or by $3d$ transition metal ions[121]. Since the valence electrons for $3d$ transition metal locate in outer d orbitals, the ligands coordinating to the transition metal influence significantly the property of quantum coherence. Indeed, the interaction of the electronic spin with the nuclear spins of the ligand is often the most relevant source of decoherence. In recent times it has been evidenced that compounds containing V(IV) ions assembled with nuclear spin-free ligands show outstanding results as regards the value of $\mathcal{T}_m$ [122, 123] (see also figure 6.7 at the end of the chapter).

In this chapter we will present the results of the investigation of a vanadyl-based complex, $VO(dpm)_2$, with a special focus on the study of its magnetic relaxation dynamics. Indeed, we combined pulsed EPR spectroscopy and AC susceptometry to obtain the spin-lattice relaxation time $\mathcal{T}_1$ and the AC relaxation time τ_{SL} of pure powder, diluted and concentrated solutions. The high volatility of the complex was also exploited to obtain thick films (150 nm), that were studied through X-ray photoelectron spectroscopy (XPS) and low temperature scanning tunneling microscopy (STM). The results of these investigations indicated that $VO(dpm)_2$ molecules can be deposited intact on the surfaces and feature a weak interaction with the gold substrate. It is therefore reasonable to envisage that $VO(dpm)_2$ molecules retain their paramagnetic nature when in contact with the gold substrate. In this chapter we will not discuss further the results of the deposition on surface, since the PhD research activity focused on the study of static and dynamic magnetic properties of bulk compounds (for the full paper see appendix C). Anyway, it is important to stress that both the investigation of the relaxation dynamics and the study of the deposition on surfaces pointed out that this complex possesses very promising features for potential applications as molecular spin-qubit.

This work resulted in the cooperation of several people, in particular Mr. Lorenzo Tesi, who synthesized the sample and dealt with the AC susceptometry and the AC data analysis, Prof. Mario Chiesa and Dr. Elena Morra, who performed the pulsed EPR experiments and prof. Lorenzo Sorace who performed the CW EPR experiment. The surface investigations were accomplished by Miss Irene Cimatti and Dr. Matteo Mannini.

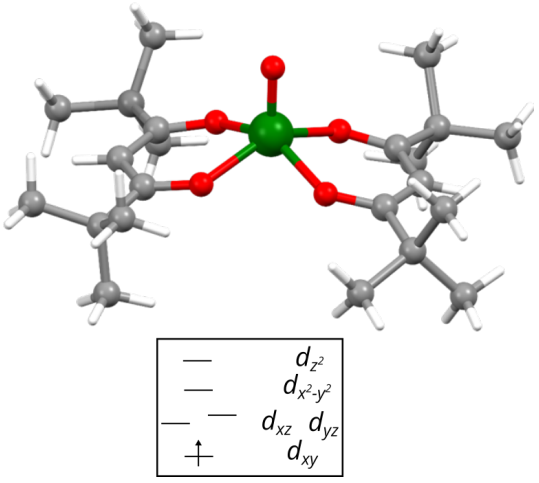

(a)

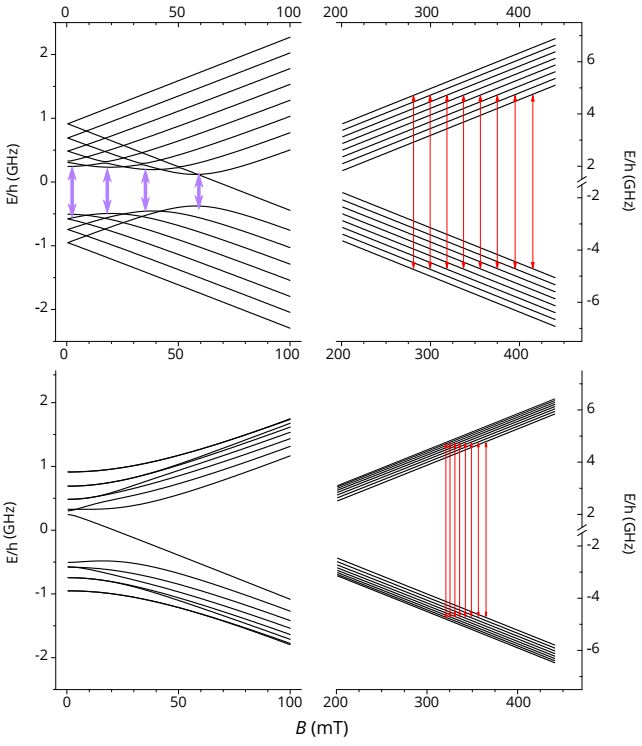

(b)

Figure 6.1.: Figure 6.1a: Molecular structure of $VO(dpm)_2$ and energy splitting of the d orbitals in a distorted tetragonal symmetry. Figure 6.1b: Zeeman splitting of the $S = 1/2$, $I = 7/2$ manifold calculated with the field applied along the largest hyperfine coupling component (upper) and along the smallest (lower) (parameters in the text). Red lines correspond to the observed X-band ($\nu = 9.4\,\mathrm{GHz}$) EPR transitions while in violet are drawn the potential low frequency transitions at the avoided level crossings.

6.1. Structural features

The complex, $VO(dpm)_2$, where dpm^- is the anion of dipivaloylmethane, was synthesized according to a previous reported procedure [124] and its molecular structure is shown in figure 6.1a. The first coordination sphere possesses a distorted tetragonal symmetry and the system crystallizes in the monoclinic space group $P2_1$, with two molecules per cell. The strongly axial ligand field produced by the short V=O bond removes orbital degeneracy, the d_{xy} orbital is the lowest in energy and the only one to be half occupied. Since only one electron is present in the external shell, vanadyl systems are therefore well described by a spin $S = 1/2$ with slightly anisotropic $\boldsymbol{g}$ tensor. The most abundant isotopes of vanadium is ^{51}V (99.75 %) that possesses a nuclear spin $I = 7/2$, hence the $S = 1/2$ doublet is splits in 16 states, as it is shown in figure 6.1b.

6.2. Magnetic relaxation dynamics

AC susceptometry was initially performed on a polycrystalline sample of $VO(dpm)_2$. As expected, the complex did not show any imaginary components of the susceptibility in zero static field, however the application of a weak field induced slow relaxation of the magnetization. The study of relaxation as a function of temperature was then performed with an applied field of 2000 Oe: the maxima of the imaginary component χ'' were studied in a frequency range 10 Hz to 10 000 Hz up to 80 K (see figure 6.2a). Such a high temperature slow relaxation is usually observed in molecules exhibiting strong magnetic anisotropy, for instance in double-decker $Tb(Pc)_2$ complexes [11], but here it has evidently a different origin. The corresponding relaxation time, extracted by fitting the χ'' curves with the Casimir Dupré equation [90], is reported in figure 6.2b. Since the complex is a system with spin 1/2 there is no barrier to be overcome and no excited states that can be thermally populated, so an Orbach contribution to the relaxation is excluded. The relaxation time was thus modeled according to

$$\tau^{-1} = aT + bT^n \tag{6.1}$$

where the first term corresponds to the direct mechanism, dominating at low temperature, and the second one to a Raman-like, i.e. a multi-phonon process involving virtual excited states. The best fit values are: $a = (59 \pm 2)\,s^{-1}\,K^{-1}$, $a = 0.052\,s^{-1}\,K^{-n}$ and $n = 3.22 \pm 0.02$. The exponent of the Raman contribution approaches the value of 3 predicted in the case that both acoustic (lattice) and optical (molecular) vibrations are involved in the process [43]. To have more hints on the mechanisms that take part to the magnetic relaxation we performed AC measurements as a function of the applied field from 0.2 kOe to 90 kOe and for three different temperatures: 5 K, 10 K, 15 K. The

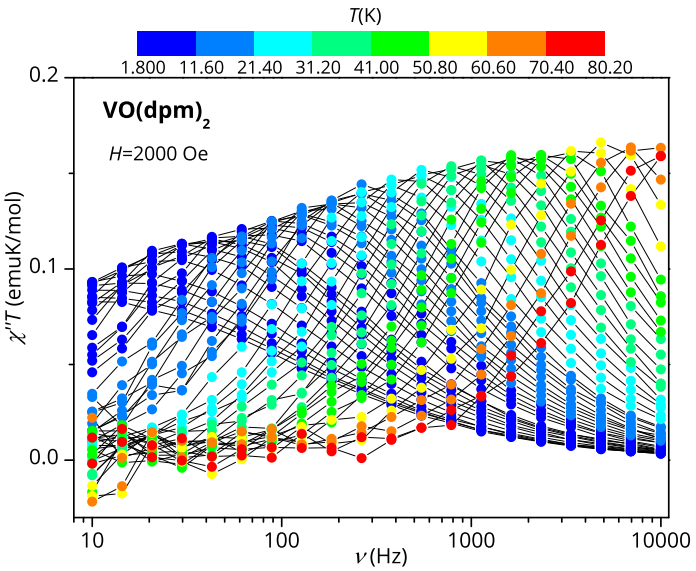

Figure 6.2.: Upper panel (a): frequency dependence of the imaginary component of the AC susceptibility of $VO(dpm)_2$ bulk in $H = 2000\,\mathrm{Oe}$ multiplied by temperature to be readable in 2 K to 80 K temperature range. Lower panel (b): temperature dependence of the relaxation time of the magnetic susceptibility measured in $H = 2000\,\mathrm{Oe}$ for the pure and the diluted samples of $VO(dpm)_2$: two dispersions in polystyrene with $1:5$ and $1:10$ mass ratio and a 200 mM CH_2Cl_2 : toluene frozen solution.

relaxation time, as a function of the applied field, is shown in figure 6.3. The initial increase of τ for weak applied field is followed by an almost flat region that extends up to ca. 40 kOe, followed by a rapid decrease at higher fields. Two contributions to the relaxation rate can be considered: a direct process is responsible for the decrease of the relaxation time at higher field, while a second mechanism is accountable for the initial increase. The latter causes the efficient relaxation in zero field and presents a field dependence that is similar to the Brons-van Vleck formula developed to describe the Raman process in concentrated system [125]

$$\tau^{-1} = cH^4 + d\frac{1+eH^2}{1+fH^2} \tag{6.2}$$

where the first term presents the typical dependence of a direct process for a Kramers' system. The parameters of the second term need a short explanation: the d term represents the zero field relaxation rate, similar to the tunnelling rate in SMMs, the f parameter takes into account the ability of the external field to suppress these mechanisms, while the e parameter, strongly dependent on the concentration of the spin centres, takes into account the field effects on the relaxation of interacting spins. All the best-fit values are reported in table 6.1, for each of the three temperatures investigated.

The long spin-lattice relaxation measured by AC susceptometry was a hint of a possible long coherence time, that is a long $\mathcal{T}_2$. The spin-spin relaxation time is however accesible only with pulsed EPR experiment, and as it was mentioned in chapter 2 the more the system is diluted the longer is $\mathcal{T}_2$. Unfortunately, extensive efforts to prepare the titanyl-based diamagnetic analogue failed due to the instability of the mononuclear species $TiO(dpm)_2$ in favour of the dimeric one $[TiO(dpm)_2]_2$ [126], thus precluding the preparation of isomorphous crystalline solid solutions. As an alternative, in view of pulsed EPR measurements, two dispersions of $VO(dpm)_2$ in polystyrene with mass ratio 1 : 5, $\mathbf{PS}_{1:5}$, and 1 : 10, $\mathbf{PS}_{1:10}$, as well as a frozen 200 mM solution of $VO(dpm)_2$ in a 2 : 3 CH_2Cl_2 : toluene mixture ($\mathbf{sol}_{200\,\mathrm{mM}}$), were prepared and investigated by AC susceptometry. The AC investigation was intended to measure the relaxation time τ in a sample with a concentration comparable with those of the polymeric dispersion and to compare its value with the $\mathcal{T}_1$ extracted from the consecutive pulsed EPR experiments.

The diluted samples showed slow relaxation of the magnetization and the corresponding relaxation times are reported in figure 6.2b, together with the one of the polycrystalline sample of $VO(dpm)_2$. As it can be noticed, polymeric dispersions are characterized by a relaxation rate which is ca. 20 times faster than bulk sample, with minor difference between the two concentrations, suggesting that matrix effects to the relaxation dominate over those induced by dilution. The reason for such effect

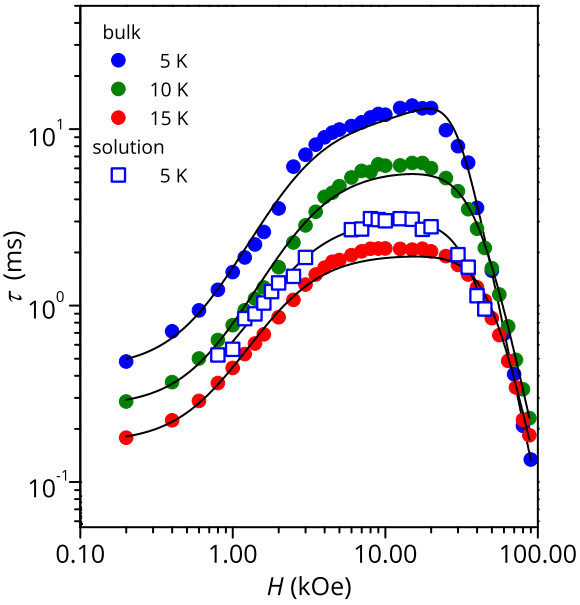

Figure 6.3.: Field dependence of the relaxation time of the magnetic susceptibility of $VO(dpm)_2$ and $\mathbf{sol}_{200\,\mathrm{mM}}$ frozen solution sample (see legend). The solid lines represent the best fit obtained with equation (6.2). Best fit parameters are reported in Table 6.1.

T (K)	c ($s^{-1}\,kOe^{-4}$)	d (s^{-1})	e (kOe^{-2})	f (kOe^{-2})
5	$(0.96 \pm 0.04) \times 10^{-4}$	2060 ± 180	$(7.6 \pm 0.7) \times 10^{-2}$	$(240 \pm 30) \times 10^{-2}$
10	$(0.73 \pm 0.01) \times 10^{-4}$	3460 ± 150	$(7.6 \pm 0.4) \times 10^{-2}$	$(179 \pm 12) \times 10^{-2}$
15	$(0.97 \pm 0.03) \times 10^{-4}$	5740 ± 270	$(15.1 \pm 0.9) \times 10^{-2}$	$(190 \pm 16) \times 10^{-2}$
5	$(2.00 \pm 0.11) \times 10^{-4}$	3600 ± 550	$(13.7 \pm 1.4) \times 10^{-2}$	$(160 \pm 40) \times 10^{-2}$

Table 6.1.: Best-fit parameters of equation (6.2) used to reproduce the field dependence of the magnetization relaxation rate of $VO(dpm)_2$ measured at the three investigated temperatures and of $\mathbf{sol}_{200\,\mathrm{mM}}$ at 5 K (last row).

can be ascribed to the more elastic nature of the polymeric matrix compared to the frozen solution, leading to a more efficient spin-lattice relaxation in the former case. The *log-log* plot evidences that the relaxation time of the diluted samples presents a linear dependence: $\tau^{-1} \propto T^n$, with $n = 1.49 \pm 0.04$ for $\mathbf{PS}_{1:5}$ and $n = 1.86 \pm 0.04$ for $\mathbf{sol}_{200\,\mathrm{mM}}$. Exponents larger than one for the direct mechanism are generally attributed to spin–phonon bottleneck effects [43], which are expected to be more relevant for these samples that have a small contact-surface with the helium bath than the ground microcrystalline powder of the bulk sample. Indeed, a more recent work of Tesi et. al [127] evidenced a giant spin-phonon bottleneck effects both in $VO(dpm)_2$ and in other two vanadyl-based molecules. As a comparison, in figure 6.3 the field dependence of the $\mathbf{sol}_{200\,\mathrm{mM}}$ is reported: its behavior indicates that, despite some matrix effects, the peculiar dependence of τ is an intrinsic property of the structure of the molecule.

6.3. CW and pulsed EPR

CW-EPR X-band experiments were performed at low temperature on a microcrystalline powder of $VO(dpm)_2$, on $\mathbf{PS}_{1:10}$, $\mathbf{PS}_{1:5}$ and on the solution $\mathbf{sol}_{200\,\mathrm{mM}}$ (see figure 6.4a). We also measured a frozen 1 mM solution of $VO(dpm)_2$ ($\mathbf{sol}_{1\,\mathrm{mM}}$), since pulsed EPR requires quite diluted systems to investigate the phase-memory time $\mathcal{T}_\mathrm{m}$. Both the EPR spectrum of $\mathbf{sol}_{1\,\mathrm{mM}}$, and the spectra $\mathbf{PS}_{1:10}$ and $\mathbf{PS}_{1:5}$ showed narrower lines compared to the bulk compound. The position of the lines is not varying, and this is comforting since it indicates that the spin Hamiltonian parameters, and the electronic structure, are maintained in different environments. As mentioned in section 6.1, the spectra evidenced the anisotropic hyperfine coupling of the electron $S = 1/2$ and the nuclear spin $I = 7/2$, more clearly in the frozen solution $\mathbf{sol}_{1\,\mathrm{mM}}$: in the high and low field extreme regions, peaks due to the parallel components of the hyperfine structure are observed, whereas in the center the closely spaced perpendicular ones are evident.

The simulations of the EPR spectra reported in figure 6.4b were obtained with the Matlab toolbox Easyspin [104], on the basis of the following SH:

$$\mathcal{H} = \boldsymbol{I} \cdot \boldsymbol{A} \cdot \boldsymbol{S} + \mu_\mathrm{B} \boldsymbol{S} \cdot \boldsymbol{g} \cdot \boldsymbol{B} \tag{6.3}$$

the best-fit parameters are reported in table 6.2 and are consistent with the slight structural rhombicity observed by X-ray diffractometry.

An Echo detected field-swept EPR spectrum (EDFS) was recorded using the standard Hahn sequence (see section 2.2.2) for $\mathbf{sol}_{200\,\mathrm{mM}}$, $\mathbf{sol}_{1\,\mathrm{mM}}$ (see figure 6.4b), and $\mathbf{PS}_{1:10}$ diluted samples at 5 K. The observation of a spin-echo is a first indication that quantum coherence is observed in these samples. The same spin Hamiltonian parameters used for the simulation of the CW spectrum yielded good simulations of the EDFS spectrum,

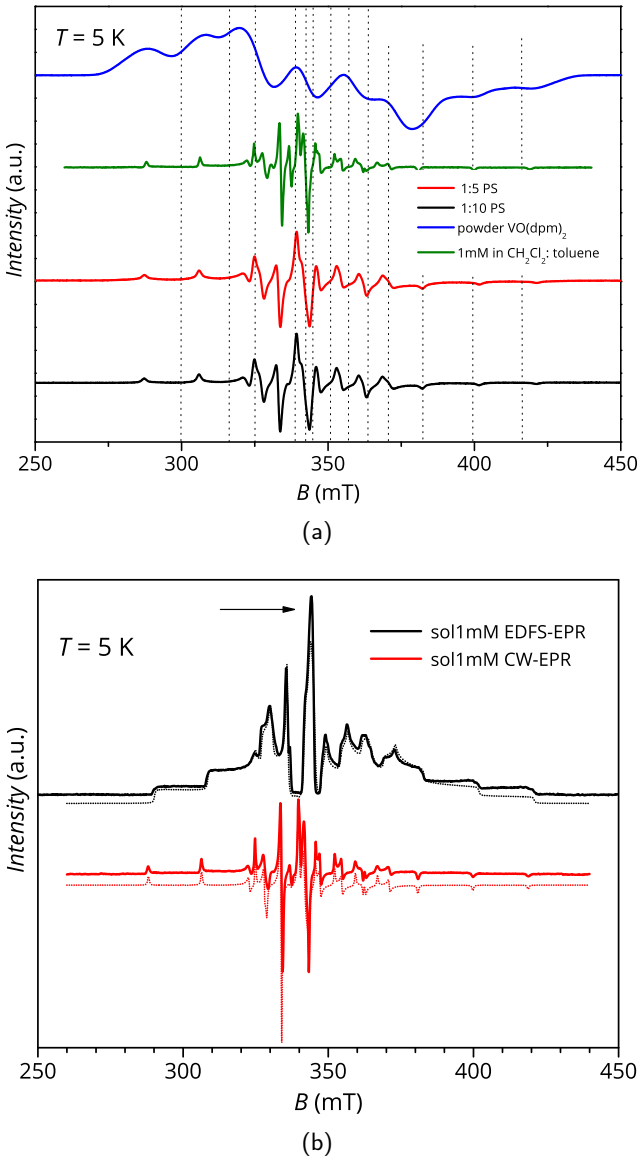

Figure 6.4.: Upper panel (a): CW-EPR X-band spectra at 5 K for the $VO(dpm)_2$, the PS dispersion ($\mathbf{PS}_{1:10}$ and $\mathbf{PS}_{1:5}$) and the frozen 1 mM solution ($\mathbf{sol}_{1\,\mathrm{mM}}$) . The dotted lines evidence the coincidence of the resonant fields in the different samples. Lower panel (b): Echo detected (black trace) and CW (red trace) experimental EPR spectra of $\mathbf{sol}_{1\,\mathrm{mM}}$, measured at 5 K, and best simulations (dotted traces - parameters in table 6.2). The arrow marks the field position of $\mathcal{T}_1$ and $\mathcal{T}_\mathrm{m}$ determination.

g_x	g_y	g_z
1.9880 ± 0.0002	1.9815 ± 0.0003	1.9490 ± 0.0002
A_x (cm^{-1})	A_y (cm^{-1})	A_z (cm^{-1})
0.0056 ± 0.0001	0.0063 ± 0.0003	0.0170 ± 0.0002

Table 6.2.: Best-fit parameters of equation (6.3) that were employed to simulated the curves of figure 6.4b and to draw the Zeeman diagrams of figure 6.1b.

confirming that the entire $VO(dpm)_2$ sample is experiencing the detected coherence.

The coherence time $\mathcal{T}_\mathrm{m}$ was measured, using a standard Hahn-echo sequence, as a function of temperature and field position for $\mathbf{sol}_{1\,\mathrm{mM}}$ to reduce spin–spin interactions. In figure 6.5a the echo decay traces are reported. The curves were fitted according to

$$y = y_0 + k_m \mathrm{e}^{-(2t/\mathcal{T}_\mathrm{m})^{\beta_m}} \tag{6.4}$$

In figure 6.5b the temperature dependence of $\mathcal{T}_\mathrm{m}$, recorded at 343 mT, is displayed. This points out that, between 4 and 80 K, the coherence time is almost temperature independent (varying from 2.7 to 2.1 µs). Above 80 K the less rigid environment opens new relaxation pathways leading to the loss of echo above 110 K, a phenomenon widely reported in literature. At the same time, β_m varies from 1.3 at low temperature to 1.1 around 100 K, thus approaching a mono-exponential decay at high temperatures. This trend suggests that the dynamics of magnetic nuclei plays a role in the decoherence.

In correspondence with this long coherence time, Rabi-oscillations of the $\mathbf{sol}_{1\,\mathrm{mM}}$ sample were observed in a nutation experiment (see figure 6.6). This fact highlights the possibility to generate arbitrary coherent superposition of states, fulfilling one of the two main requirements for creating universal quantum gates [128].

The $\mathcal{T}_\mathrm{m}$ is actually influenced by the spin-lattice relaxation time $\mathcal{T}_1$, so we performed a further investigation of the $\mathbf{sol}_{1\,\mathrm{mM}}$ sample to measure $\mathcal{T}_1$. We employed two different experimental procedures: at low temperature (5 K to 60 K) the echo saturation by fast repetition, suitable for long relaxation times was used [53], whereas at higher temperature the standard inversion recovery procedure was applied (see section 2.2.2). The value of the spin-lattice relaxation time was extracted by fitting the recovery curves with the following equation

$$y = y_0 + k_1 \mathrm{e}^{-(t/\mathcal{T}_1)^{\beta_1}} \tag{6.5}$$

with the best-fit stretched parameter β_1 is in the range 0.6 to 0.9. The temperature dependence of $\mathcal{T}_1$ was reported in figure 6.5b. As it can be noticed, above 40 K the relaxation time $\mathcal{T}_1$ features a T^{-n} dependence with $n = 3.2 \pm 0.2$. A direct comparison

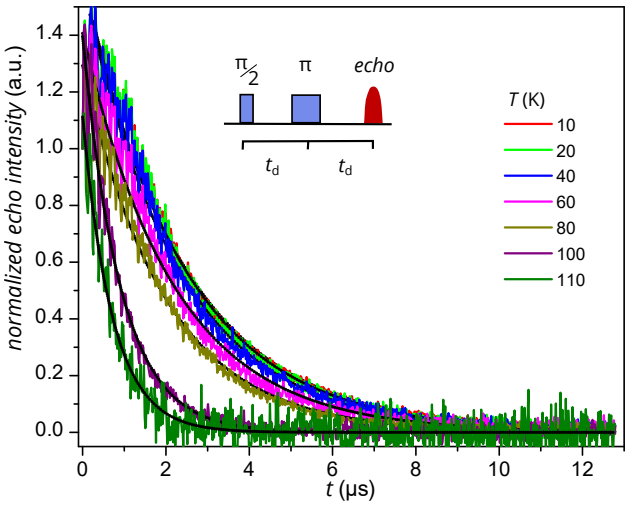

(a)

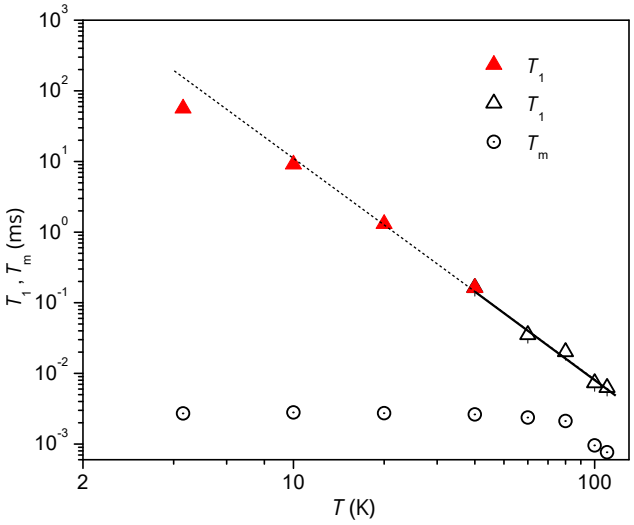

(b)

Figure 6.5.: Figure 6.5a: pulsed EPR Hahn echo decay traces for $\mathbf{sol}_{1\,\mathrm{mM}}$ at different temperatures recorded at 343 mT. In the inset the employed pulse sequence. Figure 6.5b: temperature dependence of of $\mathcal{T}_1$ and $\mathcal{T}_\mathrm{m}$ for $\mathbf{sol}_{1\,\mathrm{mM}}$. Full symbols refer to experiments of echo saturation by fast repetition, empty ones to inversion recovery experiments. The solid line corresponds to the best-fit of the high temperature data with $\mathcal{T}_1 \propto T^{-n}$.

with AC results was not possible, since we did not investigate $\mathbf{sol}_{1\,\mathrm{mM}}$ sample because the signal was below the AC instrumentation sensitivity. However, we were able to perform a quantitative comparison of the spin-lattice relaxation times for the $\mathbf{sol}_{200\,\mathrm{mM}}$: the results are consistent with those obtained by AC susceptibility (see figure 6.2b), confirming that the two techniques are actually probing the same process. As a last

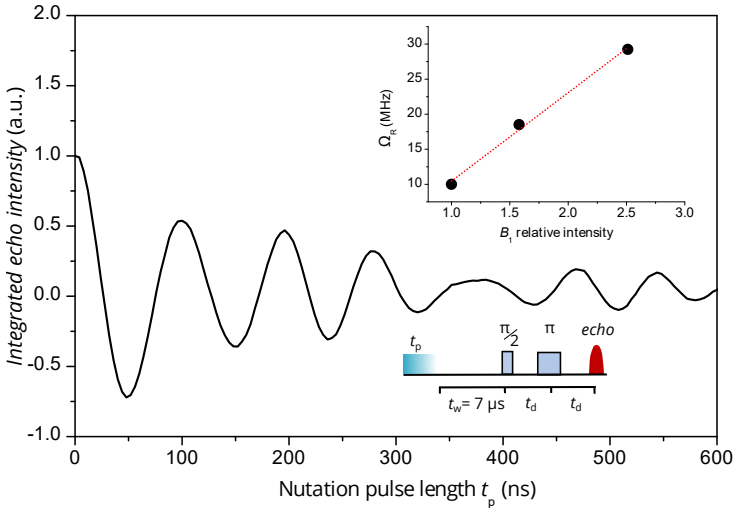

Figure 6.6.: Rabi oscillations for $\mathbf{sol}_{1\,\mathrm{mM}}$ recorded at 4.3 K at 10 dB microwave attenuation. In the inset the Rabi frequency (Ω_R) vs. oscillating field intensity superimposed to the linear best-fit.

check we also measured the temperature dependence of relaxation times for $\mathbf{PS}_{1:10}$, to establish whether this molecule maintains its long decoherence time in a solid matrix (for $\mathcal{T}_1$ see figure 6.2b). Even in this case, an echo was detected and $\mathcal{T}_\mathrm{m}$ was measured up to 220 K. Compared to the frozen solution the values of $\mathcal{T}_\mathrm{m}$ measured at the same field position are one order of magnitude faster.

In conclusion, the results obtained by the combination of AC susceptibility and pulsed EPR investigation evidenced that this multi-technique approach has a particular relevance in the perspective of the search for molecular spin-qubits. Indeed, a long coherence time depends on the value of the spin-lattice relaxation time $\mathcal{T}_1$, whose field dependence can be easily studied with AC susceptometry. On the contrary, EPR relies on the resonance condition but it gives access to faster time scale and the experiment can be performed at higher temperatures. The magnetic dynamics probed by the two technique revealed to be the same, though $\mathcal{T}_1$ and τ extracted with the two techniques are exactly equal only in the case of a $S = 1/2$ with no hyperfine splitting.

In figure 6.7 the measured $\mathcal{T}_\mathrm{m}$ of different systems is reported. The coherence time of $VO(dpm)_2$ in diluted solution is longer than the $\mathcal{T}_\mathrm{m}$ measured for polynuclear transition metal ion complexes, as Cr_7Ni or Fe_8: this depends on the fact that the excited states of the polynuclear systems can play a role in speeding up the spin-lattice relaxation

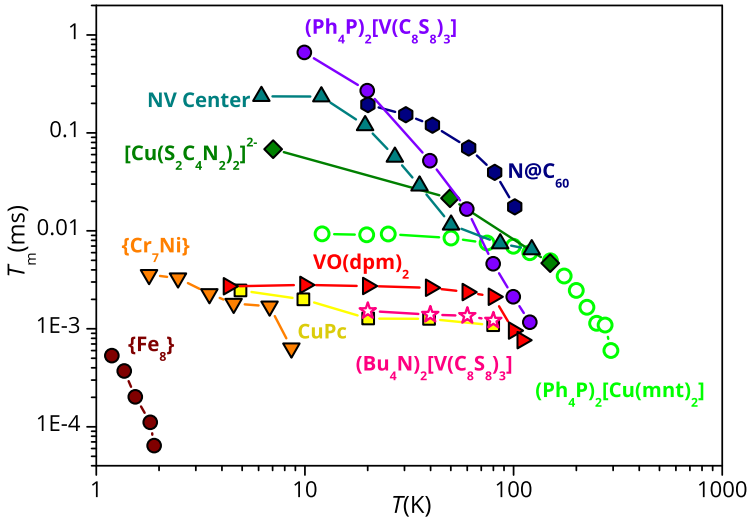

Figure 6.7.: Comparison of the $\mathcal{T}_m$ values for several notable molecular and solid state electronic spin qubits. The figure is adapted from reference [123]. The results reported in this work and the ones of references [129] and [122] have been added.

time. This results in $\mathcal{T}_m$ being limited by $\mathcal{T}_1$ even at relatively low temperature, and remarks that $\mathcal{T}_1$ is a crucial variable that must be taken into account to improve $\mathcal{T}_m$.

In addition, to select a system with $\mathcal{T}_1$ long enough not to limit $\mathcal{T}_m$, the latter can be increased, and coherence observed at higher temperature, by reducing as much as possible the number of nuclear spins in the material. This was pointed out in the paper of Bader et al. [129] (see empty green circles in figure 6.7) and by a recent work of Freedman and coworkers [123], who evidenced a considerable step forward in the design of single-qubit complexes with transition metal center. Indeed, a 0.01 mM frozen solution of deuterated $(Ph_4)_2[V(C_8S_8)_3]$ in CS_2 (violet circles in figure 6.7) displays, around 10 K, a coherence time near 1 ms. As the temperature increases, however, $\mathcal{T}_m$ becomes faster, reaching values comparable to that of $VO(dpm)_2$ and CuPc at 80 K due to $\mathcal{T}_1$ limitation of $\mathcal{T}_m$ and to the frozen solution environment used for this study. The results we obtained on $VO(dpm)_2$ evidence that VO-based complexes can be considered as a useful starting points in the quest for a molecular based spin qubits. It is clear that there is still a long way to go to reach the goal of a functional quantum computer, anyway every single step forwards counts. Moreover, the interest in the subject from the scientific community is very high, as it is evident from the fact that all the studies reported in figure 6.7 were performed in recent years.

Conclusions

The scientific work presented in this dissertation focused on the magnetic characterization of molecular complexes showing slow relaxation of the magnetization. In particular, one of the focal points of the research activity was the study of the relaxation dynamics of lanthanide-based compounds, with the addition of the vanadyl-based complex reported in chapter 6. The investigation of the dynamic properties of these complexes was carried out by means of different techniques, that aimed to evidence different aspects of the observed relaxation dynamics. In chapter 3 we illustrated the results of the investigation of Er(trensal) and Dy(trensal) by means of μSR spectroscopy, also partially corroborated by preliminary NMR measurements. Although not conclusive, the outcomes provided by μSR pointed out that the local dynamics probed by muons can be quite different from the one investigated by AC susceptometry. Furthermore, the μSR results evidenced that molecular complexes behaving as SMMs can be a source of inspiration to trigger new theoretical analysis of the relaxation. Indeed, the model commonly employed for rationalizing the μSR data in systems for which the Orbach relaxation process is the only relevant one is clearly failing here, and no appropriate models are currently at hand in this field.

AC susceptibility confirmed to be a fundamental tool to investigate the spin-lattice relaxation time (τ) and, therefore, to gain insights on relaxation mechanisms that require an energy exchange with phonons. Pulsed EPR, on the other hand, has the advantage to study, in the proper experimental conditions, how the spin-spin interactions affects the magnetic dynamics and therefore the coherence time $\mathcal{T}_{\mathrm{m}}$, that is a crucial ingredient to potentially exploit this molecular system for quantum information processing. In wider terms, it has been asserted that the combination of AC susceptibility and pulsed EPR investigation has a particular relevance in view of the search for molecular spin-qubits [24], since the two techniques complement each other in terms of timescales and sensitivity in samples of different spin concentrations.

The rationalization of the relaxation dynamics is another important aspect that was in depth-analyzed. Indeed, the behavior of the relaxation time as a function of temperature should be modeled coherently with the electronic structure of these systems. This point was firstly stressed in the study of Er(trensal) and Dy(trensal) [18], for which the information derived from previous luminescence measurements [23] allowed to correctly interpret the behavior of the relaxation time by identifying the

mechanisms involved. On the other hand, the study of the $Dy(LH)_3$ complex reported in chapter 4 evidenced that, in the absence of further spectroscopic information, *ab initio* calculations allow to analyze the observed dynamics of the magnetization on the basis of the calculated electronic structure. The observed behavior could be then qualitatively rationalized via the commonly used transition probabilities [94, 95] and, in addition, a statistical analysis based on the master matrix approach was performed by employing the *ab initio* results of the electronic structure of the system. The case of $Dy(LH_3)$ complex is indeed emblematic, because it included a comprehensive experimental and theoretical investigation of the anisotropy and dynamic behaviour. The several approaches, such as CTM, DC and AC magnetometry and *ab initio* calculations, proved to be complementary and mutually supportive.

However, as it was mentioned in the introductive chapter to this dissertation, the goal of any study aimed at investigating the correlation between electronic structure and magnetization dynamics has to be adapted according to the available means. Indeed, even in the less lucky cases, it is possible to find a strategy to obtain an as full as possible magnetic characterization. As regards this point, the study of the Ln(trenovan) revealed to be quite challenging. Nevertheless, we were able to partially unravel the knot, finding a protocol to partially simulate the magnetic properties of the complex of the series, by means of a phenomenological approach. In this instance, the CW EPR investigation proved to be fundamental for several reasons. First of all, it provided a benchmark to test the goodness of the phenomenological description of the electronic structure of some of the complexes. Then, it was also helpful as alarm bell, since its great sensitivity allowed to detect even small amount of paramagnetic species different from the one expected.

The study of the molecular complexes reported in this dissertation outlined some useful guidelines, that can be constructive to plan future improvements in the field of Molecular Magnetism. Indeed, as regards possible synthetic strategies, both the Ln(trensal) and Ln(trenovan) complexes taught us that even a relatively high molecular symmetry may not lead to SMMs with competitive performances, since in the case of the C_3 symmetry the three transverse terms of the CF hamiltonian are responsible for the mixed wavefunctions reported in chapter 5, which are detrimental for the observation of SMM behavior. These families of complexes also remind us that the dynamics of magnetic relaxations can be quite composite and the mechanisms involved are less understood than the well studied Orbach process. In this respect this thesis points out that, for meaningful comparison among the behavior of different complexes in term of dynamic properties, the simple report of an effective barrier might be misleading. More useful structure/properties correlation can be gained by considering the different terms contributing to the slow dynamics.

To conclude, by paraphrasing the well known motto ‘United we stand divided we

fall' we can state that the success of a scientific investigation is based on a virtuous interplay between various techniques, that allow to have different and complementary perspective on the studied system and, least but not last, on collaboration among the scientists involved.

A. Er(trensal) and Dy(trensal) paper

ChemComm

COMMUNICATION

View Article Online
View Journal | View Issue

Cite this: *Chem. Commun.*, 2014, **50**, 1648

Received 20th November 2013,
Accepted 5th December 2013

DOI: 10.1039/c3cc48866g

www.rsc.org/chemcomm

Beyond the anisotropy barrier: slow relaxation of the magnetization in both easy-axis and easy-plane Ln(trensal) complexes†

Eva Lucaccini,[a] Lorenzo Sorace,*[a] Mauro Perfetti,[a] Jean-Pierre Costes[b] and Roberta Sessoli[a]

We present a spectroscopic and magnetic (both static and dynamic) characterization of two isostructural Dy and Er complexes evidencing that, despite the different types of magnetic anisotropy, the two molecules show similar slow relaxation of the magnetization in a static magnetic field.

The number of mononuclear lanthanide complexes reported to show slow relaxation of the magnetization at low temperature has increased very rapidly after the seminal report of Ishikawa on terbium-phthalocyaninate,[1] making this one of the most studied subjects in molecular magnetism.[2] Despite the efforts and the achievements obtained to date, many open questions remain on the behaviour of these molecules, which need to be rationalized if one wishes to improve their properties in term of the blocking temperature. In particular, the relaxation processes characterizing these systems are often more complex than assumed. With the exception of few reports,[3,4] the slow relaxation of the magnetization is usually attributed to an Orbach mechanism[5] even if further experimental or theoretical confirmation is not available. However, the clarification of the different dynamics reported so far and the exploration of the different pathways for magnetic relaxation require a detailed picture of the electronic structure of these systems. Experimentally, this can only be obtained by using a combined spectroscopic and magnetic characterization of structurally simple systems.[6]

Following this approach, we present here the results obtained by a combined magnetic, Electron Paramagnetic Resonance (EPR) and Crystal Field (CF) analysis, on mononuclear lanthanide complexes having the formula Ln(trensal) (where H_3trensal = 2,2′,2″-Tris-(salicylideneimino)triethylamine) which feature crystallographically imposed trigonal symmetry (Fig. 1, inset and Fig. S1 and S2, ESI†).[7]

This series represents an ideal system for correlating the magnetization dynamics with the magnetic anisotropy because C_3 symmetry, preserved at liquid helium temperature,[7b] reduces the number of CF parameters to be determined to describe their electronic structure. These are known with great accuracy thanks to the high quality luminescence spectra which were previously analysed and reproduced for most of the derivatives in the series.[7b] In the following we will focus on Er^{III} (**1**) and Dy^{III} (**2**) derivatives, since both these ions show a ground $J = 15/2$ state but, according to phenomenological approach popularized by Long, should behave differently in terms of the low temperature dynamics.[2b]

We first analyzed the χT *vs.* T curves (Fig. 1): the room temperature values are in agreement with those expected for the $^4I_{15/2}$ and $^6H_{15/2}$ multiplets of Er^{III} and Dy^{III}, while the observed temperature dependence can be attributed to the progressive depopulation of the excited sublevels. To evaluate if this behaviour is in agreement with the CF parameters reported in ref. 7*b* (Table S1, ESI†) we used the home-developed software EVALUCF.[8] Here the effect of the CF over the different multiplets, arising from the spin–orbit splitting of the ground term of each rare-earth, is calculated

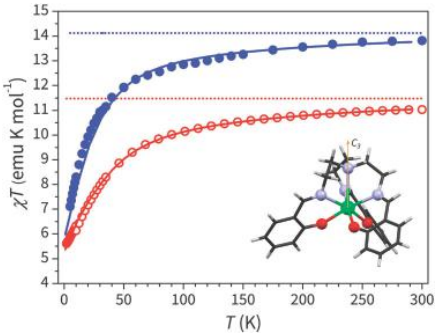

Fig. 1 Temperature dependence of the χT product for **1** (empty circles) and **2** (full circles), along with theoretical curves calculated by using the CF parameters reported in ref. 7*b*. Dashed lines correspond to the expected free-ion χT values. In the inset the molecular structure of Ln(trensal) is sketched, evidencing the trigonal symmetry.

[a] *Dipartimento di Chimica "U. Schiff" and UdR INSTM, Universitá di Firenze, Via della Lastruccia 3-13, Sesto Fiorentino(FI), Italy. E-mail: lorenzo.sorace@unifi.it; Fax: +39 0554573372; Tel: +39 0554573336*

[b] *Laboratoire de Chimie de Coordination 205, route de Narbonne 31077 Toulouse, Cedex 4, France*

† Electronic supplementary information (ESI) available: Synthetic procedure; experimental setup; Powder X-ray diffractograms; EPR spectra; isothermal magnetization curves, original *ac* susceptibility data. See DOI: 10.1039/c3cc48866g

using the appropriate Hamiltonian in the Wybourne formalism,[9] which for C_3 symmetry is:†

$$\hat{H}_{CF} = B_0^2\boldsymbol{C}_0^2 + B_0^4\boldsymbol{C}_0^4 + B_3^4(\boldsymbol{C}_{-3}^4 - \boldsymbol{C}_3^4) + B_0^6\boldsymbol{C}_0^6 + B_3^6(\boldsymbol{C}_{-3}^6 - \boldsymbol{C}_3^6) + iB_3'^6(\boldsymbol{C}_{-3}^6 + \boldsymbol{C}_3^6) + B_6^6(\boldsymbol{C}_{-6}^6 + \boldsymbol{C}_6^6) + iB_6'^6(\boldsymbol{C}_{-6}^6 - \boldsymbol{C}_6^6) \quad (1)$$

The energy difference between the different multiplets was phenomenologically adjusted to correctly reproduce the results reported in ref. 7*b*, and the final diagonalization provided the eigenvalues and eigenvectors in terms of the $|J, M_J\rangle$ components. The effect of a magnetic field was then evaluated over a 55 point grid to obtain the powder average susceptibility at different temperatures.[8] This approach, without any free parameters, reproduced very well the experimental curves for both derivatives, lending further support to the correctness of the parameter set.

The resulting energy patterns for the two ground multiplets are reported in Table 1: a gap of 54 and 50 cm^{-1} is calculated between the ground and first excited doublets for **1** and **2**, respectively. The corresponding ground state wavefunctions are characterized in both cases by large mixing of different $|M_J\rangle$ (Table 1 and Fig. S3, ESI†). By calculating the effect of the magnetic field over the energy levels of the two complexes we could calculate the effective *g* values for the ground doublets of the two derivatives as $g_\perp^{eff} = 1.2$, $g_\parallel^{eff} = 13$ for **1** and $g_\perp^{eff} = 9.6$, $g_\parallel^{eff} = 2.6$ for **2**. Experimental confirmation of this estimate could be obtained by EPR spectroscopy on microcrystalline powder samples, both at X- and W- band (Fig. 2 and Fig. S4, ESI†), which confirmed the expected trend, with **1** being the easy axis ($g_\parallel = 11.8 \pm 0.4 > g_\perp = 3.6 \pm 0.1$) and **2** the easy plane ($g_\perp = 9.4 \pm 0.5 > g_\parallel = 1.8 \pm 0.1$). The observed *g* values for **1** are also in agreement with the saturation value of the *M vs. H* curve, slightly higher than the calculated one (Fig. S5, ESI†). At any rate, the combined luminescence, EPR and *dc* magnetic analysis provided a sound quantitative description of the electronic structure of these systems, evidencing the different character of the magnetic anisotropy of the two derivatives, as expected on the basis of the prolate and oblate charge distribution of the two ions.[2b,10] Since **1** is an easy axis system with a non-negligible gap between the ground and the first excited doublet, it may be expected to show slow relaxation of the magnetization at low temperature with an Arrhenius like dependence of the relaxation rate, while **2** should not.

Table 1 Energies of the 8 doublets of the $J = 15/2$ multiplets calculated with the CF parameters reported in ref. 7*b*, and corresponding composition of ground doublets. Contributions lower than 5% are not reported. See ESI for more details

Energies (cm^{-1})								
1	0	54	102	109	321	568	619	651
2	0	50	98	172	414	577	645	787

Amplitude of $\|M_J\rangle$ contributing to ground doublets	
1	$68.4\%\left\|\pm\frac{13}{2}\right\rangle, 5\%\left\|\pm\frac{7}{2}\right\rangle, 10.4\%\left\|\pm\frac{1}{2}\right\rangle, 11.6\%\left\|\mp\frac{13}{2}\right\rangle$
2	$8.7\%\left\|\pm\frac{13}{2}\right\rangle, 24.3\%\left\|\pm\frac{7}{2}\right\rangle, 33.1\%\left\|\pm\frac{1}{2}\right\rangle, 20.2\%\left\|\mp\frac{5}{2}\right\rangle, 5.3\%\left\|\mp\frac{11}{2}\right\rangle$

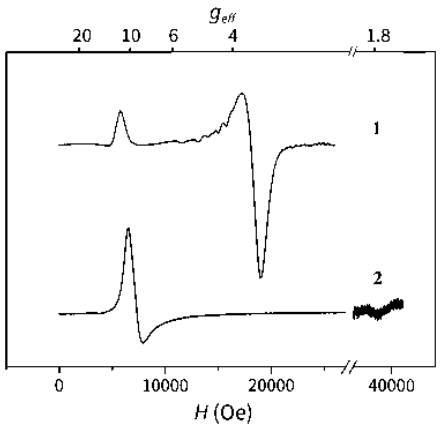

Fig. 2 W-band (94.3 GHz) spectra of microcrystalline powder samples of **1** and **2**, recorded at 5 K.

To investigate this point, variable frequency *ac* magnetic susceptibility experiments were performed for complexes **1** and **2** as a function of temperature, with and without applied *dc* field. In the absence of the *dc* field, none of the two complexes showed out-of phase magnetic susceptibility, χ''. This is not surprising, since quantum tunneling (QT) of magnetization[11] is expected to play a relevant role due to the mixture of different $|J, M_J\rangle$ characterizing the ground doublets of the two derivatives. However, when applying *dc* fields in the range of 200–2400 Oe at 1.9 K, a clear slow relaxation process is unexpectedly observed for both complexes, the maximum of the relaxation time being observed at an applied field of about 800 Oe and 900 Oe for **1** and **2**, respectively (Fig. S6, ESI†).

The Arrhenius plot of the temperature dependence of the relaxation times, obtained by fitting the χ'' *vs.* ν curves to a Debye model (Fig. S7 and S8, ESI†),[12] evidences quite a similar trend for the two derivatives, with large deviation from linear behaviour at lower temperatures. A tentative fit of the high temperature region results in the following parameters: $\tau_0 = (2.7 \pm 0.5) \times 10^{-8}$ s, $\Delta = 22 \pm 1$ cm^{-1} for **1**, and $\tau_0 = (5 \pm 2) \times 10^{-7}$ s, $\Delta = 7 \pm 1$ cm^{-1} for **2**. The two estimated barriers are clearly in contrast to the energy difference between the ground and the first excited doublet obtained by the luminescence data, indicating that the outcome of the phenomenological fit to the Arrhenius law has no physical meaning in this case, thus excluding that the observed barrier is connected to an Orbach process. Since both the easy axis **1** and the easy-plane **2** complexes show slow relaxation of the magnetization, it is quite clear that other mechanisms should account for the observed slow relaxation.

To analyse this issue in more detail we performed experiments on a isomorphous Y(trensal) complex doped with 5.8% and 3.1% of Er^{III} and Dy^{III}, respectively (see ESI†) to rule out the possibility of effects due to intermolecular interactions. These are indeed known to play a relevant role in the magnetic relaxation of single-molecule magnets, especially in mononuclear and f-element systems.[13]

Both systems showed field and temperature dependences of the dynamic susceptibility which are largely similar to those of the pure samples (Fig. S9 and S10, ESI†). The analysis of the relaxation rate as a function of the field at low temperature ($T = 1.8$ K) is reported in the upper panel of Fig. 3 and points to a competition between

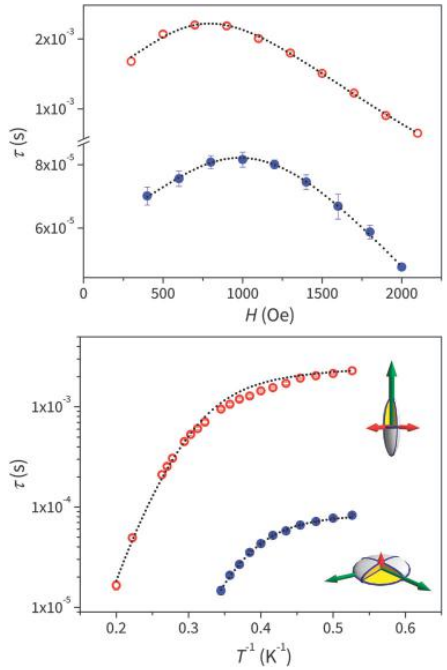

Fig. 3 Field (upper) and temperature (lower) dependence of the relaxation times of Y:Er(trensal) (empty circles) and Y:Dy(trensal) (full circles) and best fit curves obtained by using eqn (2) and (3). The ellipsoids in lower panel graphically represent the anisotropy of the susceptibility tensors of the ground doublet of the two derivatives.

two different field dependent relaxation processes. The increase in relaxation time observed in lower fields indicates that, on applying the field, QT processes are reduced, while the decrease observed at higher fields should be attributed to the increased relevance of the direct process. On these grounds, we tentatively analyzed the observed behaviour using eqn (2):

$$\tau^{-1} = \frac{B_1}{1 + B_2 H^2} + A_1 H^4 T + A_2 H^2 T \qquad (2)$$

where the first term represents the field dependence of QT process,[14] the second one the direct process for a Kramers ion without hyperfine interactions, and the third one is the direct process for a Kramers ion in the presence of hyperfine interaction.[15] Indeed, both samples contain magnetic and non-magnetic nuclei. The best fit curves provided in both cases very small values for the direct process not involving hyperfine interaction (parameters: $A_1 = (2.0 \pm 1.8) \times 10^{-12}$ s^{-1} K^{-1} Oe^{-4}, $A_2 = (1.4 \pm 0.1) \times 10^{-4}$ s^{-1} K^{-1} Oe^{-2}, $B_1 = (71 \pm 4) \times 10$ s^{-1}, $B_2 = (2.7 \pm 0.4) \times 10^{-6}$ Oe^{-2} for **1**; $A_1 = (3 \pm 2) \times 10^{-11}$ s^{-1} K^{-1} Oe^{-4}, $A_2 = (2.0 \pm 0.1) \times 10^{-3}$, s^{-1} K^{-1} Oe^{-2} $B_1 = (158 \pm 2) \times 10^2$ s^{-1}, $B_2 = (9.2 \pm 0.7) \times 10^{-7}$ Oe^{-2} for **2**). The temperature dependence of the relaxation time for the diluted systems are reported in the lower panel of Fig. 3: the weak temperature dependence of τ observed at low temperature suggests a contribution by the QT process, whereas the temperature dependence observed at higher T indicates that relaxation proceeds by exchange of energy with lattice vibrations. The observed curvature of the Arrhenius plot indicates a non-negligible influence of direct and/or Raman processes in determining the relaxation rate,[15,16] the former having been confirmed using the field dependent measurements. On these grounds we analysed the temperature dependence of the relaxation rates for diluted samples by using eqn (3):

$$\tau^{-1} = \frac{B_1}{1 + B_2 H^2} + A_1 H^4 T + A_2 H^2 T + C T^n + \tau_0^{-1} \exp(-\Delta/kT) \qquad (3)$$

where the first three terms are the same as in eqn (2), the fourth is the Raman one, and the fifth is the Orbach one. Due to the large number of parameters involved we fixed the first three to the values obtained by the analysis of the field dependent relaxation rate. For none of the two derivatives reasonable fits could be obtained by including Orbach processes in addition to the direct and QT ones, while a Raman process, with variable exponent n, provided reasonable reproduction of the data (best fit values $n = 9$ for **1** and $n = 11$ for **2**). Therefore it is evident that the relaxation is not occurring *via* the first excited doublet in any of the two derivatives.

In summary we conclude that, despite Er(trensal) being an easy axis type complex and Dy(trensal) an easy plane one, the two molecules show slow relaxation of the magnetization, both as a function of temperature and of the field. This observation invalidates the general assumption that the slow dynamics of magnetization is associated with the magnetic anisotropy in lanthanide complexes, and stresses the absolute importance of complementing the magnetic characterization of these systems with spectroscopic techniques.[17] It is clear that only a multitechnique approach allows us to understand the factors affecting the magnetization dynamics and relaxation mechanisms in these systems and can provide a valuable feedback to develop new synthetic strategies.

We acknowledge the financial support of MIUR through the project Futuro in Ricerca 2012 (RBFR12RPD1) and of EC through ERC-AdG MolNanoMas (267746).

Notes and references

1 N. Ishikawa, M. Sugita, T. Ishikawa, S. Koshihara and Y. Kaizu, *J. Am. Chem. Soc.*, 2003, **125**, 8694.
2 (*a*) D. N. Woodruff, R. E. P. Winpenny and R. A. Layfield, *Chem. Rev.*, 2013, **113**, 5110; (*b*) J. D. Rinehart and J. C. Long, *Chem. Sci.*, 2011, **2**, 2078; (*c*) L. Sorace, C. Benelli and D. Gatteschi, *Chem. Soc. Rev.*, 2011, **40**, 3092; (*d*) M. A. AlDamen, S. Cardona-Serra, J. M. Clemente-Juan, E. Coronado, C. Martí-Gastaldo, A. Gaita-Arino, F. Luis and O. Montero, *Inorg. Chem.*, 2009, **48**, 3467.
3 (*a*) G. Cucinotta, M. Perfetti, J. Luzon, M. Etienne, P. E. Car, A. Caneschi, G. Calvez, K. Bernot and R. Sessoli, *Angew. Chem., Int. Ed.*, 2012, **51**, 1606; (*b*) M.-E. Boulon, G. Cucinotta, J. Luzon, C. Degl'Innocenti, M. Perfetti, K. Bernot, G. Calvez, A. Caneschi and R. Sessoli, *Angew. Chem., Int. Ed.*, 2013, **52**, 350.
4 (*a*) R. J. Blagg, L. Ungur, F. Tuna, J. Speak, P. Comar, D. Collison, W. Wernsdorfer, E. J. L. McInnes, L. F. Chibotaru and R. E. P. Winpenny, *Nat. Chem.*, 2013, **5**, 673; (*b*) K. Bernot, J. Luzon, L. Bogani, M. Etienne, C. Sangregorio, M. Shanmugam, A. Caneschi, R. Sessoli and D. Gatteschi, *J. Am. Chem. Soc.*, 2009, **131**, 5573; (*c*) H. L. C. Feltham, Y. Lan, F. Klöwer, L. Ungur, L. F. Chibotaru, S. Brooker and A.K. Powell, *Chem.–Eur. J.*, 2011, **17**, 4362.
5 R. Orbach, *Proc. R. Soc. London, Ser. A*, 1961, **264**, 458.
6 (*a*) J. D. Rinehart and J. R: Long, *Dalton Trans.*, 2012, **41**, 13572; (*b*) N. Magnani, R. Caciuffo, E. Colineau, F. Wastin, A. Baraldi, E. Buffagni, R. Capelletti, S. Carretta, M. Mazzera, D. T. Adroja, M. Watanabe and A. Nakamura, *Phys. Rev. B*, 2009, **79**, 104407.

7 (*a*) P. V. Bernhardt, B. M. Flanagan and M. J. Riley, *Aust. J. Chem.*, 2000, **53**, 229; (*b*) B. M. Flanagan, P. V. Bernhardt, E. R. Krausz, S. R. Lüthi and M. J. Riley, *Inorg. Chem.*, 2002, **41**, 5024.
8 E. Lucaccini, Master thesis, Univ. of Florence, 2013.
9 C. Görller-Walrand and K. Binnemans, in *Handbook on the Physics and Chemistry of Rare Earths*, ed. K. A. Gschneidner Jr and L. Eyring, 1996, vol. 23, p. 121.
10 J. Sievers, *Z. Phys. B: Condens. Matter Quanta*, 1982, **45**, 289.
11 D. Gatteschi, R. Sessoli and J. Villain, *Molecular nanomagnets*, Oxford University Press, Oxford, 2006.
12 H. B. J. Casimir and F. K. Du Pré, *Physica*, 1938, **5**, 507.
13 K. Meihaus, J. Rinehart and J. R. Long, *Inorg. Chem.*, 2011, **50**, 8484.
14 A. Fort, A. Rettori, J. Villain, D. Gatteschi and R. Sessoli, *Phys. Rev. Lett.*, 1998, **80**, 612.
15 A. Abragam and B. Bleaney, *Electron Paramagnetic Resonance of Transition Ions*, Dover, New York, 1986.
16 (*a*) J. M. Zadrozny, M. Atanasov, A. M. Bryan, C.-Y. Lin, B. D. Rekken, P. P. Power, F. Neese and J. R. Long, *Chem. Sci.*, 2013, **4**, 125; (*b*) J.-L. Liu, K. Yuan, J.-D. Leng, L. Ungur, W. Wernsdorfer, F.-S. Guo, L. F. Chibotaru and M.-L. Tong, *Inorg. Chem.*, 2012, **51**, 8538.
17 During the submission of this manuscript we were informed that another group is currently working on the magnetic characterization of Er(trensal): J. Dreiser, private communication.

Electronic Supplementary Material (ESI) for Chemical Communications

ELECTRONIC SUPPLEMENTARY INFORMATION

Beyond anisotropy barrier: slow relaxation of the magnetization in both easy-axis and easy-plane Ln(trensal) complexes

Eva Lucaccini,[a] Lorenzo Sorace,[a*] Mauro Perfetti,[a] Jean-Pierre Costes,[b] and Roberta Sessoli[a]

[a] *Department of Chemistry "Ugo Schiff" and INSTM Research Unit, University of Florence, Via della Lastruccia 3, 50019 Sesto Fiorentino, Italy. E-mail:* lorenzo.sorace@unifi.it

[b] *Laboratoire de Chimie de Coordination du CNRS, 205, route de Narbonne, BP 44099, 31077 Touluse Cedex 4, France.*

1 Synthesis

Powder microcrystalline samples of Er(trensal) and Dy(trensal) were obtained by the synthetic procedure reported in ref. (*1*). Yttrium diluted samples were obtained by adding the desired molar ratio of Y(trensal) and Er(trensal) or Dy(trensal) in MeOH, refluxing for 30 min and cooling at room temperature. After filtration under vacuum the solid was washed with MeOH and dried under nitrogen flux. The obtainment of the correct $P\bar{3}c1$ phase was checked by powder X-ray diffractograms (figure S1). All the patterns are superimposable to the one obtained from the crystallographic information file (.cif) of the solved molecular structure (Er derivative) (*2*).
Extremely diluted samples (0.5 %) were obtained for Dy derivative, but this did not result in any detectable change of the magnetic properties, except an increased signal-to-noise ratio due to the lower amount of material probed, so we chose the few percent dilution.

2 Experimental setup

X-ray powder diffraction patterns of both pure and Y-diluted samples were measured with a Bruker D8 Advance powder diffractometer equipped with a Cu source (K_α, $\lambda = 1.54$ Å).
Dc magnetic measurements were performed by using a Quantum Design MPMS SQUID magnetometer on powders pressed in a pellet to avoid field induced orientation of the crystallites. The concentration of Dy and Er in Y diluted samples was estimated by treating the corresponding magnetic data as if the samples contained only Y and then comparing the residual room temperature χT with that of the pure sample from Curie law (14.17 emu K mol^{-1} for Dy and 11.48 emu K mol^{-1} for Er).
Ac susceptibility was measured using Quantum Design PPMS in *ac* mode for the frequency range $1 \div 10^4$ Hz. The Quantum Design MPMS SQUID magnetometer was used for low frequencies ($0.1 \div 10^3$ Hz).
EPR spectra were recorded at 5 K and 10 K with a E500 Bruker spectrometer for the X band ($\nu \sim 9.4$ GHz) and a E600 Bruker spectrometer for the W band ($\nu \sim 94$ GHz).

3 Computation

The CF hamiltonian for a C_3 point symmetry is:

$$\begin{aligned} V_c(C_3) = {} & B_0^2\mathbf{C}_0^2 + B_0^4\mathbf{C}_0^4 + B_3^4(\mathbf{C}_{-3}^4 - \mathbf{C}_3^4) + \mathrm{i}B'^4_3(\mathbf{C}_{-3}^4 + \mathbf{C}_3^4) + B_0^6\mathbf{C}_0^6 \\ & + B_3^6(\mathbf{C}_{-3}^6 - \mathbf{C}_3^6) + \mathrm{i}B'^6_3(\mathbf{C}_{-3}^6 + \mathbf{C}_3^6) + B_6^6(\mathbf{C}_{-6}^6 + \mathbf{C}_6^6) + \mathrm{i}B'^6_6(\mathbf{C}_{-6}^6 - \mathbf{C}_6^6) \end{aligned} \quad (1)$$

In this symmetry one can always choose an orientation of xy axes such that $B'^4_3 = 0$ so to minimize the number of CF parameters (see table S1). The energy levels, the wavefunction composition and the corresponding g_{eff} expected on the basis of the reported CF parameters (table S1) were calculated using a home-developed software which allowed to include the effect of mixing of the higher lying multiplets arising form the same spectroscopic term of the ground one. The composition of the

ground multiplet of Dy(trensal) was calculated including $J = \frac{13}{2}$ and $J = \frac{11}{2}$ but no major effects were noticed on considering the two excited multiplets. On the contrary for Er(trensal) inclusion of excited multiplets ($J = \frac{13}{2}, \frac{11}{2}, \frac{9}{2}$) results in an increased admixing of $|JM_J\rangle$ components contributing to the ground state wavefunction.

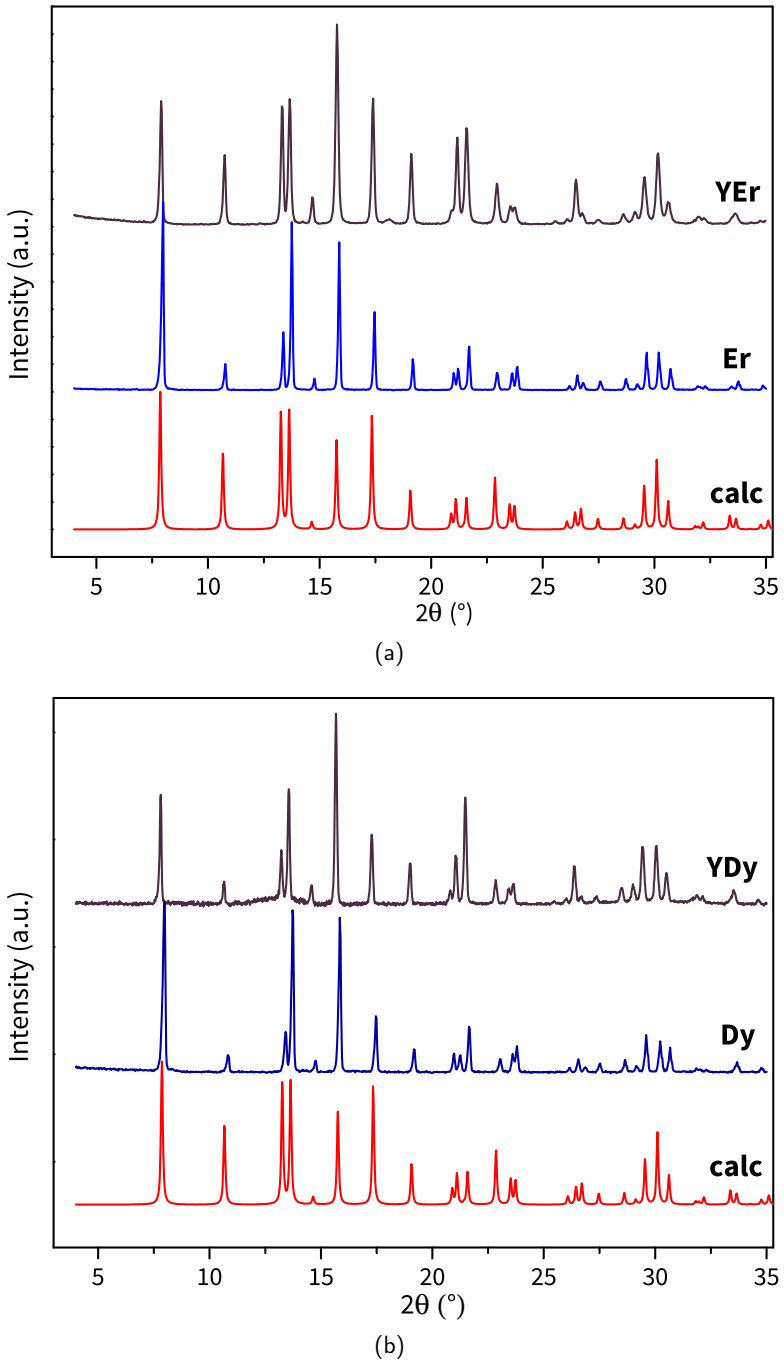

Figure S1: X-ray diffraction spectra of Er(trensal) and Dy(trensal) and of their Y-diluted samples. The red lines represent the calculated diffraction pattern for reported molecular structure (*2*).

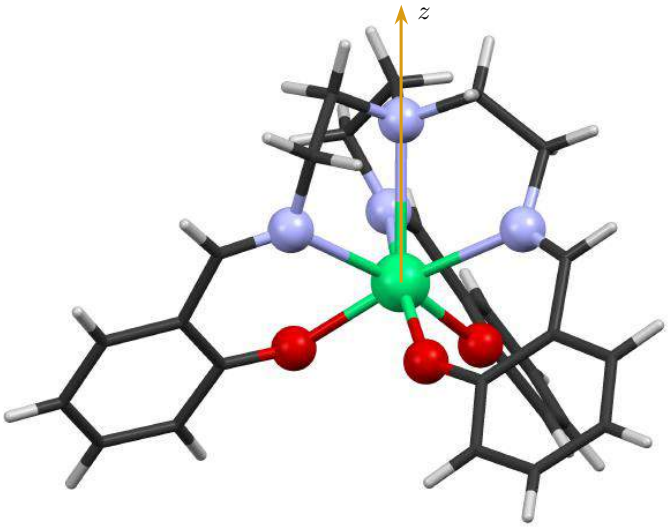

(a)

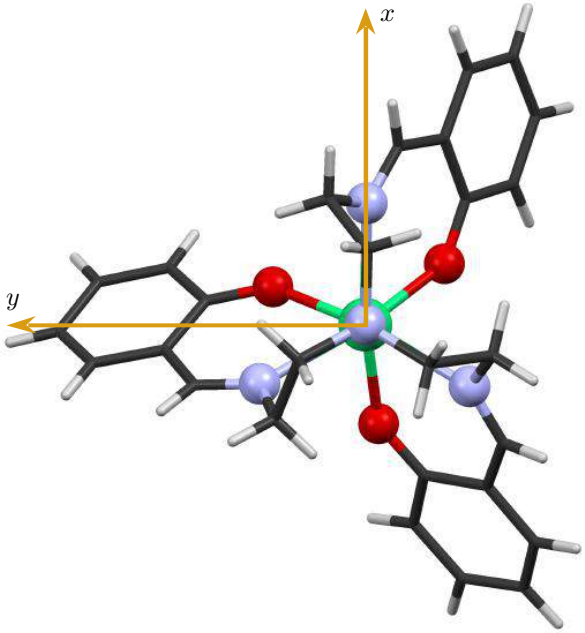

(b)

Figure S2: Molecular structure of Ln(trensal). The orientation of x and y axes is not defined *a priori* but it has been chosen in order to have a minimal set of CF parameters (*2*). The green colour identifies Ln, the red the oxygen, the light blue the nitrogen, the grey the carbon and the white the hydrogen.

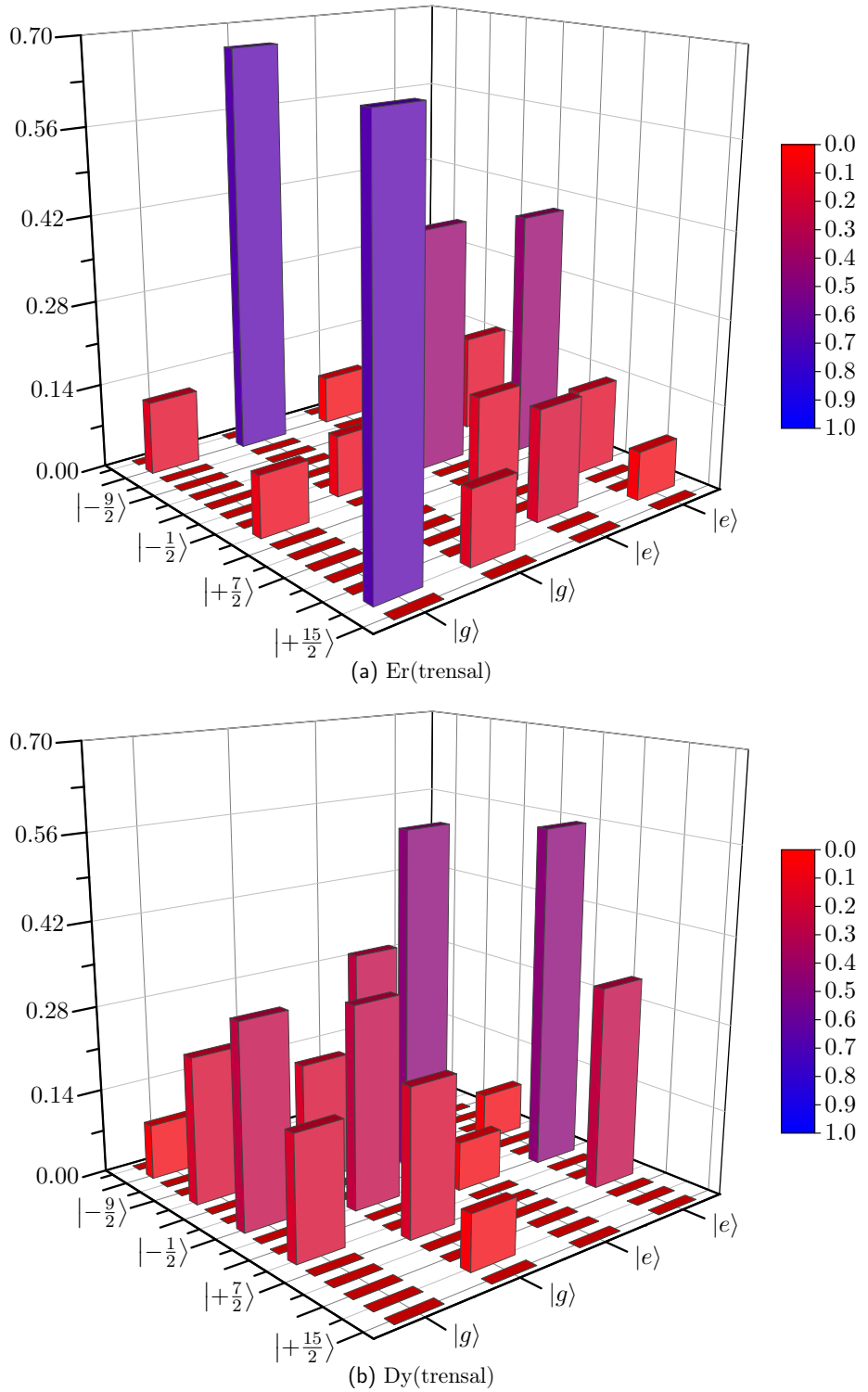

(a) Er(trensal)

(b) Dy(trensal)

Figure S3: Composition of the ground doublet and of the first excited doublet for Er(trensal)(figure a) and Dy(trensal) (figure b). For clarity reasons contribution of M_J states less than 8 % are not included. More details can be found in tables S2 and S3.

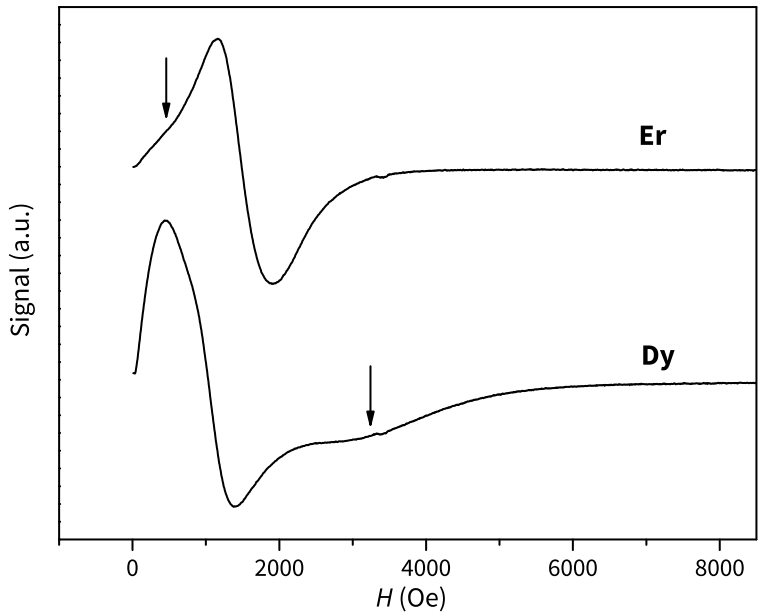

Figure S4: X band spectrum (9.4 GHz) of microcrystalline powder of Er(trensal) and Dy(trensal). The arrows evidence the parallel component of g_{eff} for the two compounds.

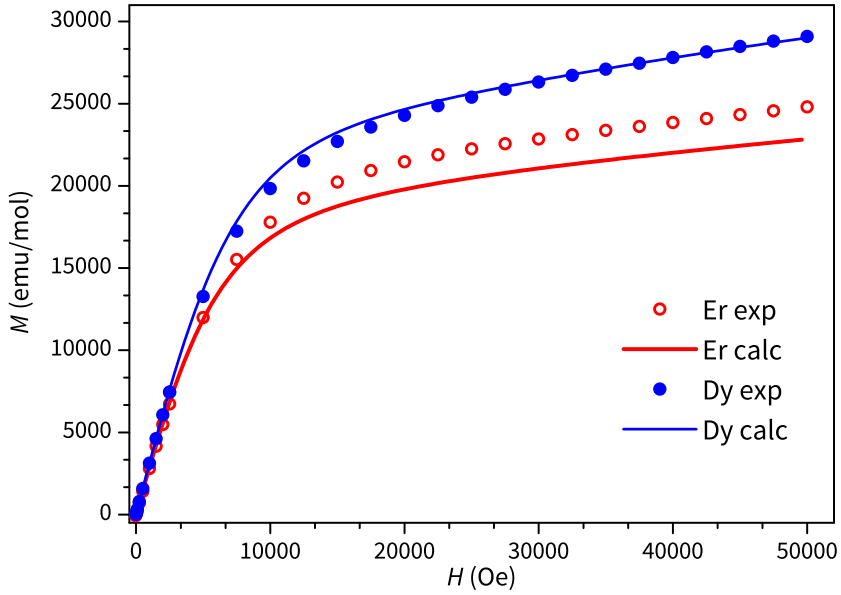

Figure S5: M vs H curves ($T = 1.9$ K): the circles represent the experimental data for Er(trensal) (empty) and for Dy(trensal) (full). The solid lines are the powder average magnetizations calculated using the CF parameters of reference (*2*) and a 55 points grid.

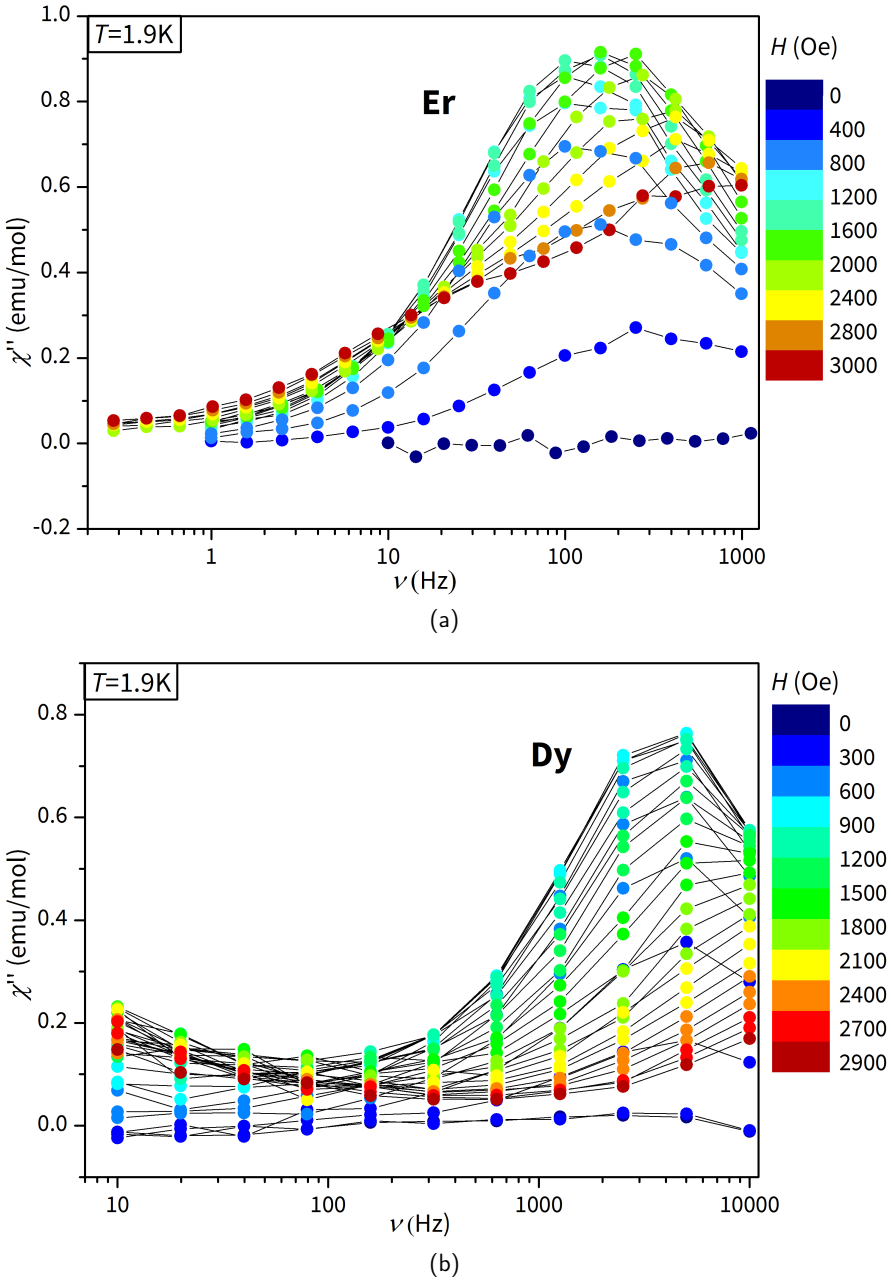

Figure S6: Imaginary susceptibility χ'' for different values of static dc field ($T = 1.9\,\mathrm{K}$).

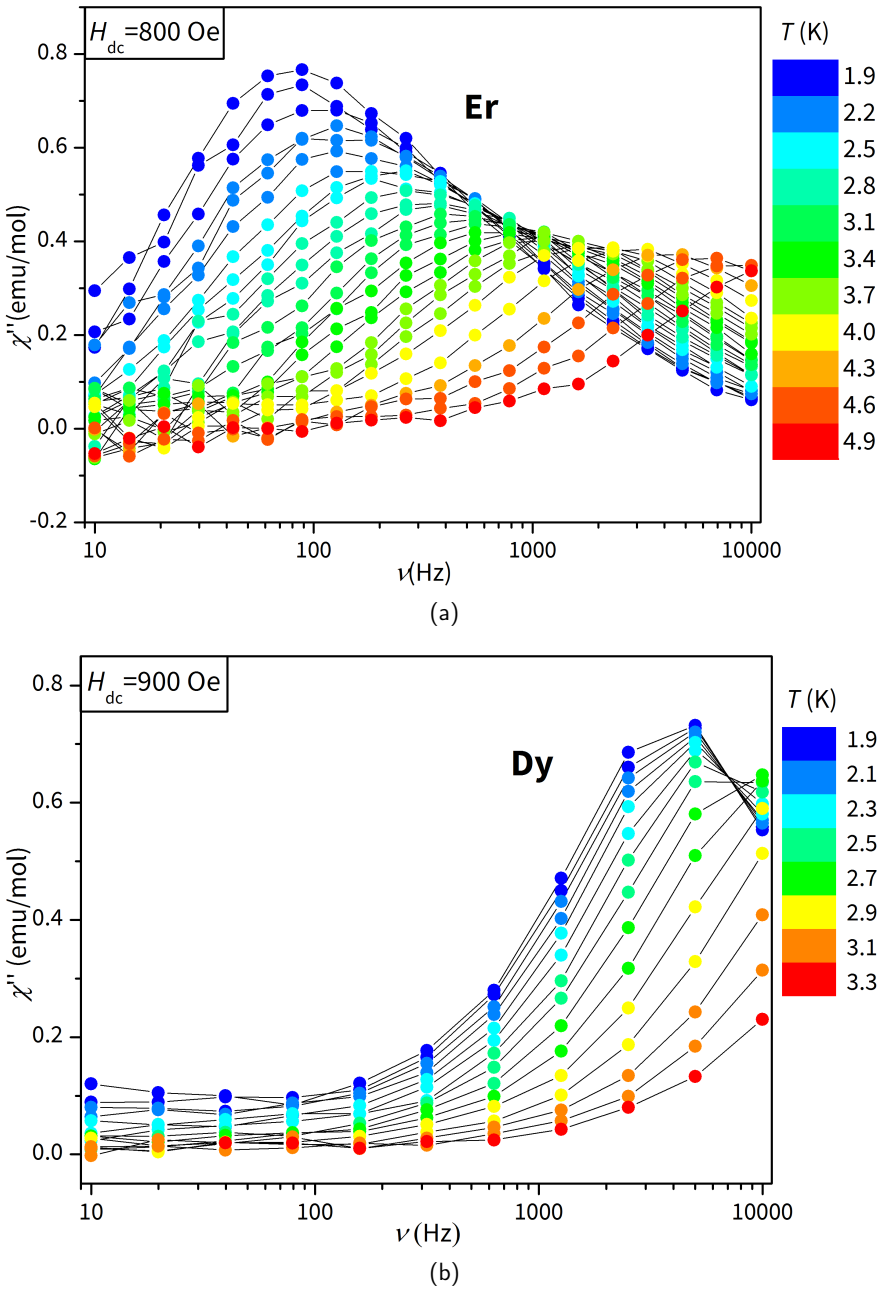

Figure S7: Imaginary susceptibility χ'' for different values of temperature T at the indicated static field.

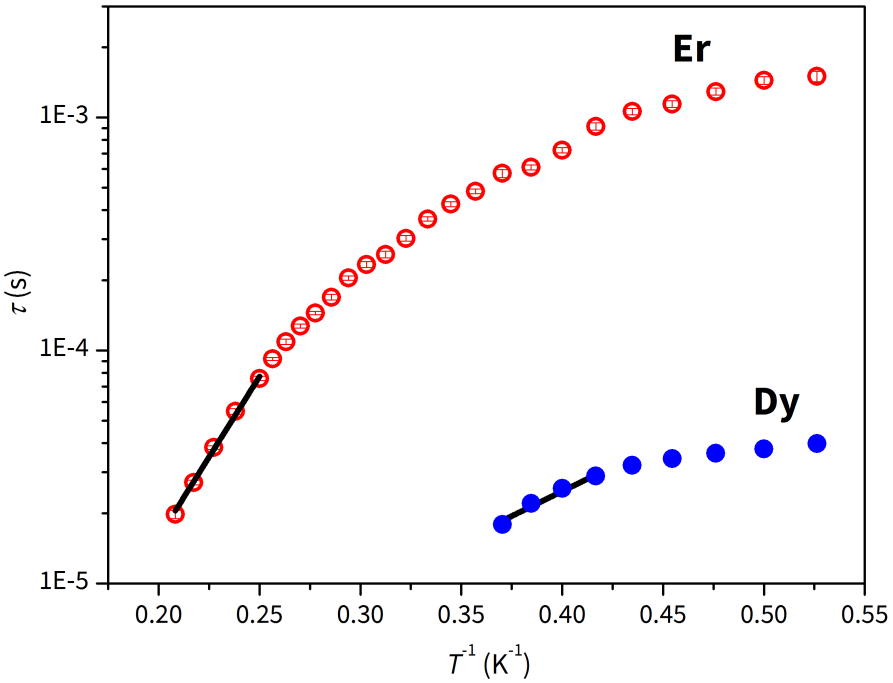

Figure S8: Arrhenius plot of temperature dependence of the relaxation rates of pure samples of Er(trensal) and Dy(trensal). Solid lines represent the best fit of the high temperature region using the Arrhenius formula $\tau = \tau_0 e^{\Delta E/k_B T}$ (see text for details).

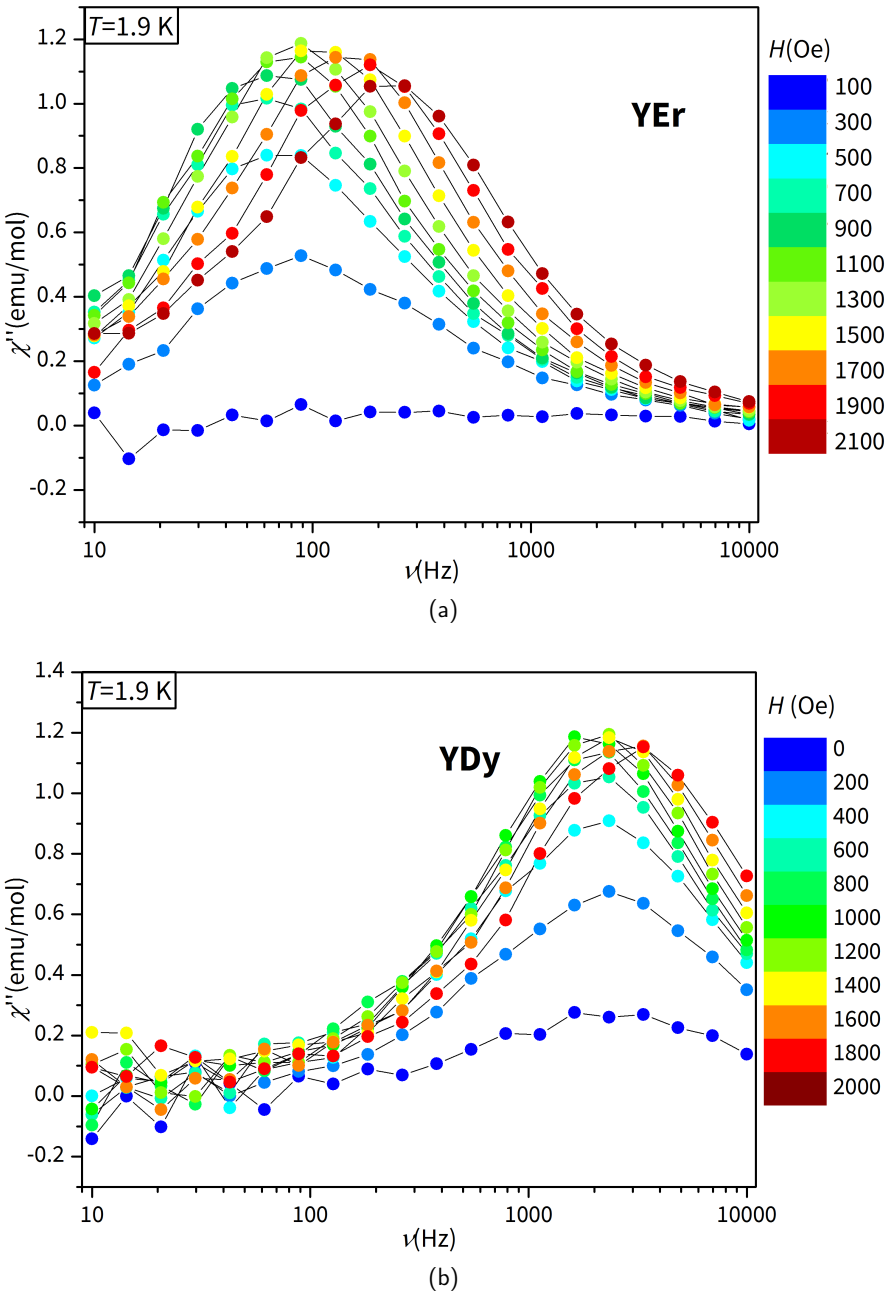

Figure S9: Imaginary susceptibility χ'' for Y-diluted samples at different values of static *dc* field. The dilutions are 5.8 % for Y:Er(trensal) and 3.1 % forY:Dy(trensal).

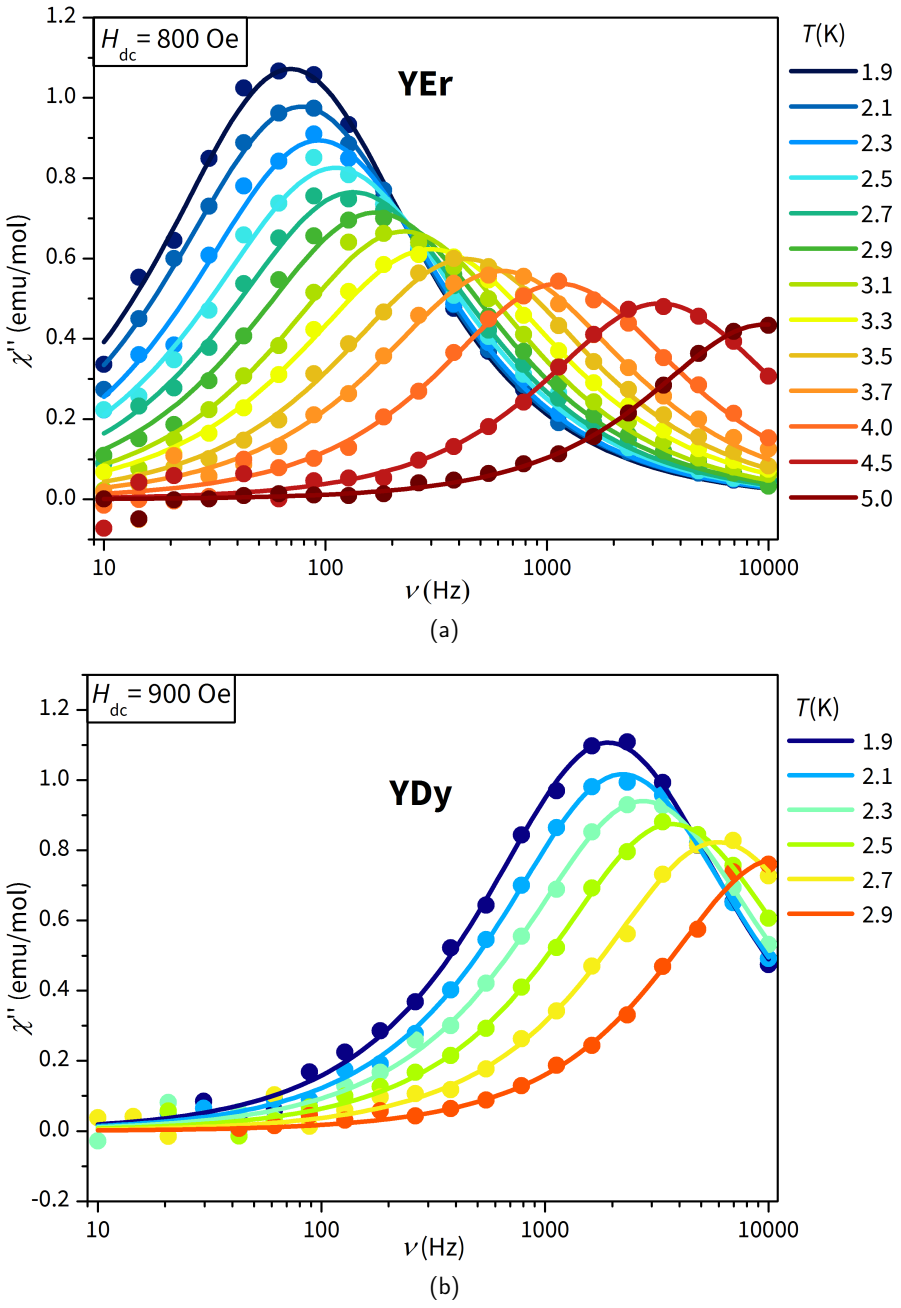

Figure S10: Imaginary susceptibility χ'' for Y-diluted samples at different values of temperature T. The solid lines are fits of the curves using the Debye formula (*3*).

Table S1: Crystal field parameters B_q^k for Dy(trensal) and Er(trensal). The values are expressed in cm^{-1} and the uncertainties are in brackets (*2*).

	Dy	Er
B_0^2	−671(39)	−720(59)
B_0^4	−186(77)	−44(106)
B_3^4	−2153(34)	−2121(83)
B'^4_3	0	0
B_0^6	1241(57)	988(36)
B_3^6	439(41)	353(49)
B'^6_3	−284(83)	92(53)
B_6^6	660(49)	545(34)
B'^6_6	145(137)	311(36)

Table S2: Composition of the ground doublet and of the first excited doublet for Er(trensal).

state	composition
ground state	68.4 % $\left\vert\pm\frac{13}{2}\right\rangle$, 11.6 % $\left\vert\mp\frac{13}{2}\right\rangle$, 10.4 % $\left\vert\pm\frac{1}{2}\right\rangle$, 5 % $\left\vert\pm\frac{7}{2}\right\rangle$
1° excited state	40 % $\left\vert\mp\frac{1}{2}\right\rangle$, 18 % $\left\vert\pm\frac{11}{2}\right\rangle$, 16 % $\left\vert\pm\frac{5}{2}\right\rangle$, 14 % $\left\vert\mp\frac{7}{2}\right\rangle$, 8 % $\left\vert\mp\frac{13}{2}\right\rangle$

Table S3: Composition of the ground doublet and of the first excited doublet for Dy(trensal).

state	composition
ground state	33.1 % $\left\vert\mp\frac{1}{2}\right\rangle$, 24.3 % $\left\vert\mp\frac{7}{2}\right\rangle$, 20.2 % $\left\vert\pm\frac{5}{2}\right\rangle$, 8.7 % $\left\vert\mp\frac{13}{2}\right\rangle$, 5.3 % $\left\vert\mp\frac{11}{2}\right\rangle$
1° excited state	56 % $\left\vert\mp\frac{3}{2}\right\rangle$, 33 % $\left\vert\mp\frac{9}{2}\right\rangle$, 8 % $\left\vert\pm\frac{3}{2}\right\rangle$

References

1. P. V Bernhardt *et al.*, *Australian Journal of Chemistry* **53**, 229–231 (2000).
2. B. M. Flanagan *et al.*, *Inorganic Chemistry* **41**, 5024–5033 (2002).
3. D. Gatteschi *et al.*, *Molecular Nanomagnets* (Oxford University Press, 2006).

B. $Dy(LH)_3$ paper

ChemPubSoc Europe

DOI: 10.1002/chem.201505211

CHEMISTRY
A European Journal
Full Paper

Single-Molecule Magnets |*Hot Paper*|

Relaxation Dynamics and Magnetic Anisotropy in a Low-Symmetry Dy^{III} Complex

Eva Lucaccini,[a] Matteo Briganti,[a, b] Mauro Perfetti,[a, c] Laure Vendier,[d] Jean-Pierre Costes,[d] Federico Totti,*[a] Roberta Sessoli,[a] and Lorenzo Sorace*[a]

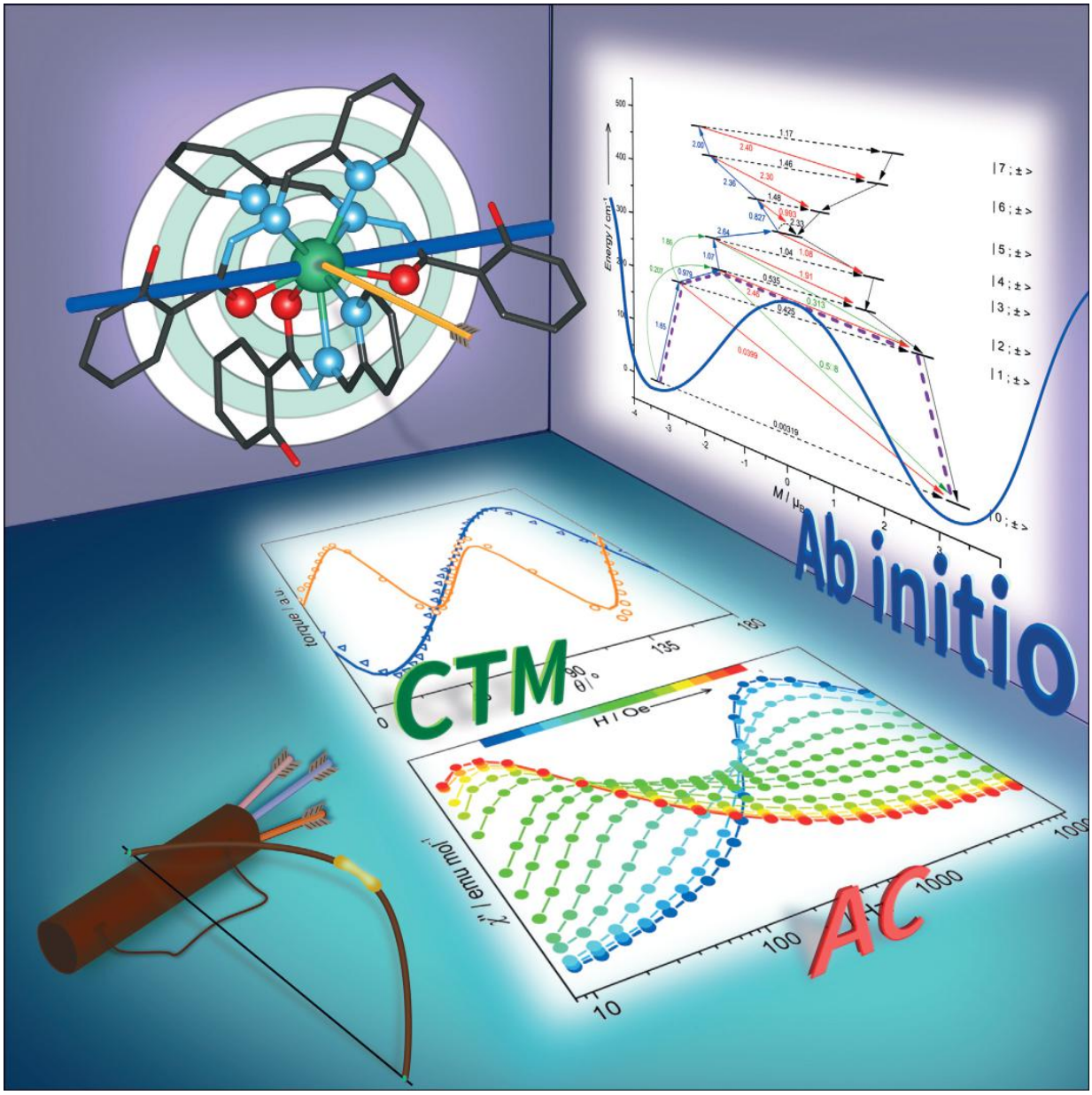

Abstract: The magnetic behaviour of a $Dy(LH)_3$ complex (LH^- is the anion of 2-hydroxy-*N*′-[(*E*)-(2-hydroxy-3-methoxyphenyl)methylidene]benzhydrazide) was analysed in depth from both theoretical and experimental points of view. Cantilever torque magnetometry indicated that the complex has Ising-type anisotropy, and provided two possible directions for the easy axis of anisotropy due to the presence of two magnetically non-equivalent molecules in the crystal. Ab initio calculations confirmed the strong Ising-type anisotropy and disentangled the two possible orientations. The computed results obtained by using ab initio calculations were then used to rationalise the composite dynamic behaviour observed for both pure Dy^{III} phase and Y^{III} diluted phase, which showed two different relaxation channels in zero and non-zero static magnetic fields. In particular, we showed that the relaxation behaviour at the higher temperature range can be correctly reproduced by using a master matrix approach, which suggests that Orbach relaxation is occurring through a second excited doublet.

Introduction

The discovery by Ishikawa and co-workers,[1] that a lanthanide bisphthalocyaninato molecule shows slow relaxation of magnetisation at low temperature, has ignited considerable interest in the dynamics of the magnetisation of lanthanide-based complexes.[2,3] Following that seminal report, these systems (referred to as single-ion magnets) have been proposed as candidates for applications in high-density data storage, molecular spintronics and quantum information processing.[4–7] The origin of the peculiar magnetic behaviour of lanthanide ions lies in their strong magnetic anisotropy, which stems from the combined action of the spin-orbit coupling and the crystal field (CF) induced by the donor atoms of the ligand(s), and by the large total angular momentum *J* (for the second half of the 4f series).[8]

When the two states with the largest projection of *J* are the ground state, this results in an anisotropy energy barrier for the reversal of the magnetisation. In the absence of other efficient relaxation paths, it is then possible to observe slow relaxation of the magnetisation through an Orbach process, with the thermal dependence of the relaxation rate following an Arrhenius-like behaviour. This result requires both a highly symmetric axial disposition of the ligands around the lanthanide centre, which reduces the mixing between states with different M_J values, and a resulting ground state characterised by an M_J value that is as large as possible.[9] Although it has been shown that complexes with low symmetries can also possess axial eigenstates,[10–12] in these situations it is not possible to predict a priori the composition of the ground state because several different $|M_J\rangle$ values can in principle contribute to it. It has further been noted that the relaxation of the magnetisation can be due to different mechanisms.[13–15] For example, at low temperature and for small values of applied magnetic field, quantum tunnelling of magnetisation (QT) can be strongly effective in accelerating the relaxation. In this regard, molecules that contain Kramers' ions are clearly preferred because in the absence of further interactions QT is forbidden for semi-integer spins. However, this process can be mediated by dipolar and hyperfine interactions, so fast relaxation of the magnetisation is often observed under a zero field. Suppression of QT is then achieved by diluting paramagnetic complexes within an isostructural diamagnetic matrix, which reduces dipolar interactions, and/or by applying a static magnetic field. However, on increasing the magnetic field, the direct process gains importance due to the larger number of available phonons of correct energy and can become the dominant contribution.[16] Finally, relaxation may occur through a Raman process that gives a more marked temperature dependence of the magnetic relaxation time (τ) because an interaction with phonons from the thermal bath and virtual energy states is involved.[17] It is quite clear that to correctly describe the relaxation processes in these systems, a detailed picture of the electronic structure of the lanthanide ion and its relation to the molecular structure is needed. An approach that combines spectroscopic characterisation (electron paramagnetic resonance, luminescence, inelastic neutron scattering) and ab initio theoretical studies is now becoming the standard procedure for this scope.[10,18–22] Single-crystal magnetic measurements are still not very widespread,[23,24] even though they can cast light on magnetic anisotropy by providing access to the preferred orientations of magnetisation and to the degree of axiality of the low-lying levels of the *J* multiplet.[25–27] However, most crystal structures are comprised of symmetry-related but magnetically non-equivalent sites. In these cases, single-crystal magnetometry provides an averaged response and deconvolution of the different contributions to anisotropy is often impossible.[28,29] Cantilever torque magnetometry (CTM), which only probes the anisotropic part of the magnetisation, is less affected by this

[a] *E. Lucaccini, M. Briganti, Dr. M. Perfetti, Dr. F. Totti, Prof. Dr. R. Sessoli, Prof. Dr. L. Sorace*
Dipartimento di Chimica "U.Schiff" and UdR INSTM
Università degli Studi di Firenze
Via della Lastruccia 3-13, 50019 Sesto Fiorentino (Italy)
E-mail: federico.totti@unifi.it
lorenzo.sorace@unifi.it

[b] *M. Briganti*
Current address: Instituto de Química, Universidade Federal Fluminense
Outeiro de São João Batista, 24020-141 Niterói, Rio de Janeiro (Brazil)

[c] *Dr. M. Perfetti*
Current address: Institut für Physikalische Chemie
Universität Stuttgart, Pfaffenwaldring 55, 70569 Stuttgart (Germany)

[d] *Dr. L. Vendier, Dr. J.-P. Costes*
Laboratoire de Chimie de Coordination CNRS
205 Route de Narbonne, Toulouse F-31077 (France)

Supporting information for this article can be found under http://dx.doi.org/10.1002/chem.201505211.

problem.[29] Furthermore, its high sensitivity and ability to measure the magnetic anisotropy up to relatively high temperatures allow one to get an independent estimate of the gap between the ground and first excited doublet in lanthanide complexes.[29,30] The outcome of this experimental characterisation can then be used to validate the results of ab initio calculations that, in their turn, help to unravel the knot and to avoid misinterpretation of the observed dynamic behaviour by providing information on the composition of the eigenstates and the corresponding energy gaps. Following this strategy, we present herein a complete experimental characterisation, obtained by using X-ray diffractometry, electron paramagnetic resonance (EPR) spectroscopy, single-crystal CTM and ac and dc susceptibility, alongside a theoretical analysis based on ab initio methods, of a new mononuclear Dy^{III} complex that behaves as a single-ion magnet in zero field. The complex has been synthesised by using a potentially pentadentate ligand; however, only three of its binding sites are used to bind to the Dy^{III} ion, which results in a neutral molecule that is, in principle, sublimable.[31]

Results and Discussion

Synthesis and structure determination

The 2-hydroxy-*N*′-[(*E*)-(2-hydroxy-3-methoxyphenyl)methylidene]benzhydrazide ligand, LH_2 (Scheme 1), was obtained by

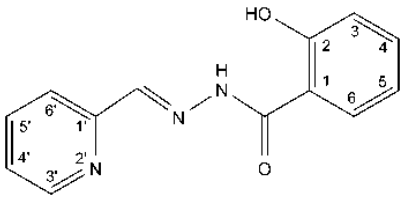

Scheme 1. LH_2 ligand with the numbering scheme used in the NMR spectroscopy data (^1H and ^{13}C).

treating 2-hydroxybenzohydrazide with pyridine carboxaldehyde, in accordance with the procedure reported in the Experimental Section. This is a potentially pentadentate ligand that possesses two functional groups that can be deprotonated; its coordination chemistry has, until now, only been investigated with regard to nickel or cobalt complexes.[32] Its complete characterisation, including assignment of 1D and 2D ^1H and ^{13}C NMR spectra and chemical analysis are also reported in the Experimental Section, and partially differ from those previously reported.[32] When dissolved in dimethylformamide (DMF), this LH_2 ligand reacts with $Dy(NO_3)_3$ in the presence of piperidine to give a yellow complex, which from analytical data and X-ray analysis (see below) was found to be neutral, with the Dy^{III} ion being coordinated to three monodeprotonated ligands.

The molecular structure obtained by using single-crystal X-ray diffractometry indicates that $Dy(LH)_3$·DMF (**Dy**) crystallises in the monoclinic $P2_1/n$ space group. Its asymmetric unit

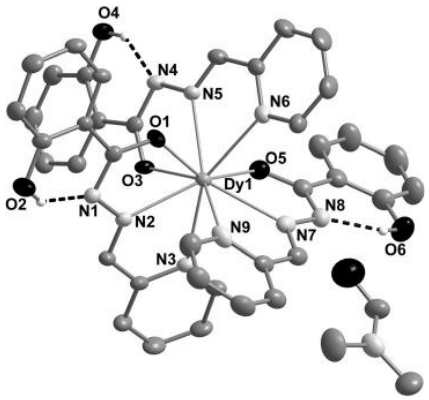

Figure 1. View of the asymmetric unit of **Dy**, including one molecule of the complex and one DMF molecule. The dashed lines indicate the three intramolecular hydrogen bonds that stabilise the structure. The remaining hydrogen atoms are not shown for the sake of clarity. Ellipsoids are drawn at the 40% probability level, with the exception of the three hydrogen atoms, for which a ball-and-stick representation is used.

(Figure 1) is composed of one mononuclear $[Dy(LH)_3]$ neutral molecule and one DMF molecule. The Dy^{III} ion is surrounded by a N_6O_3 coordination environment provided by three tris-chelating LH^- ligands. The hydrazide function is deprotonated whereas the phenol function remains protonated and not involved in coordination with the Dy^{III} ion. Each ligand remains essentially planar, with the exception of the phenolic residues, due to the presence of an intramolecular hydrogen bond that involves the non-deprotonated phenol function and the hydrazide nitrogen atom of each ligand. The Dy–N(pyridine) bond lengths (2.574(3)–2.696(4) Å) are slightly longer than the Dy–N(hydrazide) bond lengths (2.496(3)–2.538(4) Å) and the shorter bonds that involve the Dy–O of the hydrazone part of the ligand (2.322(3)–2.368(3) Å; selected bonds and angles are reported in Table S1 in the Supporting Information). Analysis of the nine-coordinate Dy-centred N_6O_3 polyhedron by using the SHAPE program[33] (see Table S2 in the Supporting Information) suggests that the coordination polyhedron is intermediate between the different possible choices for a nine-coordinate arrangement, with a slight preference for a spherical capped-square antiprism. For this option, the capping atom is the N8 hydrazide nitrogen and the two square faces of the antiprism have at their vertices the N9-N3-O5-N6 and O1-N2-O3-N5 atoms (Figure S1 in the Supporting Information). The packing of the molecules in the lattice is such that the closest Dy–Dy intermolecular separation is 10.73 Å. Phenoxo- rings on molecules related by the inversion centre are parallel; however, the corresponding centroids are separated by 6.75 Å so the corresponding π–π stacking interactions are expected to be very weak.[34]

Static magnetic properties

The static magnetic properties of a microcrystalline powder sample of **Dy** were investigated by using dc measurements and the behaviour of the magnetisation was studied both as

a function of field (H) and temperature (T). The χT versus T curve is reported in Figure S2 in the Supporting Information; the room-temperature experimental value ($\chi T = 13.97$ emu K mol^{-1}) is consistent with the free ion expectation for Dy^{III} ($^6H_{15/2}$, $g_J = 4/3$, $\chi T = 14.17$ emu K mol^{-1}). A smooth decrease was observed on lowering the temperature, which is attributed to the depopulation of excited levels of the $^6H_{15/2}$ multiplet, split by the CF. The magnetisation versus field was measured at 2 and 4 K and is reported in Figure S3 in the Supporting Information. The saturation value was 5 μ_B, as already observed for other molecular complexes that contain Dy^{III}.[35,36]

Study of the magnetic anisotropy

EPR spectroscopy is widely used to investigate the magnetic anisotropy of Kramers' systems, however, in our case the complex was revealed to be silent. This can, in principle, be attributed to either fast relaxation or a low intra-doublet transition probability due to the ground-state composition, whereas the excited doublets are too high in energy to observe inter-doublet transitions. The latter explanation points to a large axiality of the ground state, which was then investigated by using CTM. This technique exploits the magnetic torque of a molecule immersed in a homogenous magnetic field and has already proven to be extremely useful to determine the anisotropic features of lanthanide-based single-molecule magnets.[29,30,37] In this experimental setup, the variation in the capacitance of the capacitor due to the deflection of the cantilever is proportional to the magnetic torque experienced by the sample. This torque T is defined as the vector product between the magnetisation (M) and the magnetic field (B). Experimentally, only the T_y component of the torque that lies on the rotation axis (chosen as the y axis of the XYZ laboratory reference frame) is detectable, thus we can write Equation (1):

$$T_Y = M_Z B_X - M_X B_Z = B^2 \sin\varphi\cos\varphi(\chi_{ZZ} - \chi_{XX}) \quad (1)$$

in which an additional $B^2(2sin^2\varphi - 1)\chi_{XZ}$ term was omitted because it is always possible to set it to zero by using a proper shift in the rotation. In Equation (1), which is only valid for $g\mu_B S_{eff} B \ll k_B T$, χ_{IJ} are the components of the magnetic susceptibility tensor and φ is the angle between the magnetic field B and the projection of the easy axis (z axis in the xyz molecular reference frame) on the rotation plane. This should not be confused with the rotation angle (the angle between the cantilever plane and the magnetic-field direction), hereafter denoted as θ. If B is increased enough, Equation (1) breaks down and the torque curves assume a different shape if B is parallel or perpendicular to the easy direction of anisotropy, which makes it possible to disentangle non-collinear contributions. To reduce the effect of intermolecular interactions and demagnetising fields due to shape anisotropy, we chose to use a sample of the isostructural Y^{III} derivative doped with approximately 10% Dy^{III}, hereafter denoted **YDy**. Because the compound crystallises in the monoclinic space group $P2_1/n$ and the molecules do not sit on any symmetry element, the crystal anisotropy will be in general different from the molecular one. The orthogonal crystallographic reference frame in a monoclinic space group is abc^* and rotations in two orthogonal planes have been performed: in the first one (Rot1) the rotation is performed around b, whereas in the second one (Rot2) the rotation axis lies in the ac^* plane (see Figure S4 in the Supporting Information for details of the reference frames and rotation geometries). Interestingly, in the first rotation all molecules in the unit cell provide the same contribution, being related by the twofold axis that lies along b, whereas two families of differently oriented molecules are detected in the second rotation. We measured the torque signal at $T = 5$ and 10 K with B ranging from 30 to 70 kG. The resulting torque data were fitted by modelling the electronic structure of the **Dy** complex by using an effective spin-Hamiltonian:

$$\mathcal{H}_s = \mu_B \mathbf{S}_{eff} \cdot \boldsymbol{g} \cdot \mathbf{B} \quad (2)$$

in which $\boldsymbol{g}$ is the g tensor, diagonal in the molecular reference frame, μ_B is the Bohr magneton and $\mathbf{S}_{eff}$ is an effective $S = 1/2$ spin operator. To correctly reproduce the torque shape, three further parameters have to be taken into account: a scale factor (F_{sc}, which must be the same for all rotations) and two Euler angles, namely ρ and ξ (by using the extrinsic x-convention), which describe the orientation of the molecular reference frame with respect to the crystallographic one. Indeed, in the case of uniaxial anisotropy the third Euler angle is irrelevant. In Figure 2 we report two torque curves measured at the same applied magnetic field and temperature for the two rotations with corresponding fits (the complete set of experimental data and the corresponding fits are reported in Figure S5 in the Supporting Information). The fitting procedure gave the following best fit parameters: $g_x = g_y = 0.010(5)$, $g_z = 16(1)$, $\rho = 212(1)^\circ$, $\xi = 71(1)^\circ$ and $F_{sc} = 2.6(3) \times 10^{-2}$, which indicates the strong Ising character of the ground doublet. The resulting director cosines of the easy axis (z in the molecular reference frame), with respect to abc^* are $\cos\alpha_1 = -0.501$, $\cos\alpha_2 = 0.801$, $\cos\alpha_3 = 0.326$ ($\alpha_1 = 120^\circ$, $\alpha_2 = 37^\circ$, $\alpha_3 = 71^\circ$). Due to the presence of two magnetically non-equivalent mole-

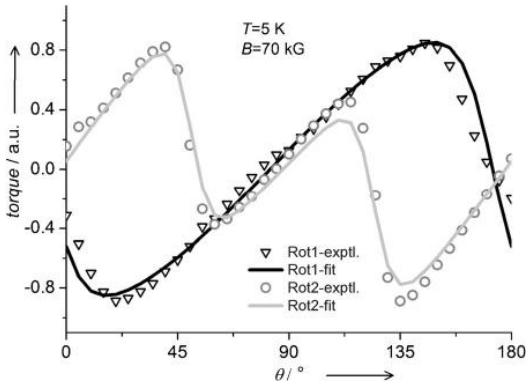

Figure 2. Torque curves for the two rotations in a magnetic field of 70 kG and at 5 K. The solid lines represent the best fit of the magnetic torque by using the parameters reported in the text; the symbols are the experimental data for Rot1 (▽) and Rot2 (○).

cules in the unit cell, these direction cosines can identify two possible orientations for the magnetic anisotropy axis with respect to the molecular structure, see Figure 3a. It is interesting to note that neither of the two possibilities correlate to the highest symmetry axis (C_4 or C_3) of the best fit coordination polyhedra, capped-square antiprism or tricapped-trigonal prism (see Figure S1 in the Supporting Information). This is in agreement with the fact that the idealised structural geometry does not take into account the heterolepticity of the complex, which results in a CF symmetry completely different from the structural one. A simple electrostatic model[38] has been used to calculate the orientation of the easy axis of magnetisation: the angle between experimental (drawn as a black rod in Figure 3a) and the calculated direction resulted in a value of about 13° (see Tables S3–S4 and Figure S7 in the Supporting Information). Because the error of a visual crystal alignment can be estimated to be about 5° (see the Experimental Section), we can consider the calculated orientation to be in fair agreement with the experimental one. This confirms that the coordination environment of Dy^{III} in the complex can provide a strong Ising character, but an accurate prediction of the orientation of the anisotropy axis, as well as an estimation of the low-symmetry components of the CF, requires a more detailed approach.

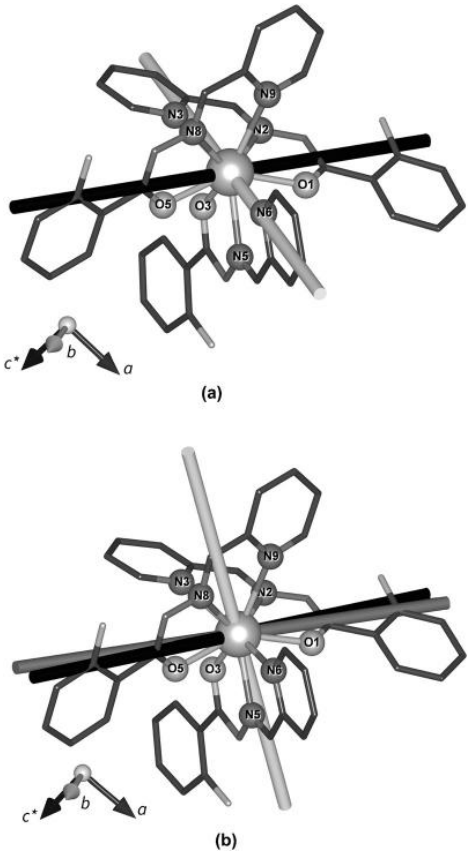

Figure 3. a) The two possible directions of the easy axis of magnetic anisotropy of **Dy** as determined by using CTM: the one identified by the black rod is substantially coincident with the calculated direction (compare with Figure 3b). b) The computed direction of the magnetic easy axis for the first three energy doublets: ground (black), first excited (grey), second excited (light grey).

Ab initio calculations

Since we had indications of the strong Ising character of the complex, we chose to perform an accurate ab initio characterisation to get more detailed insights into the Dy^{III} electronic structure. A first relevant test of the correct reproduction of experimental properties concerns calculation of the orientation and magnitude of the magnetic anisotropy compared with the results of CTM. In agreement with the latter, the calculated ground Kramers' doublet shows an almost-pure Ising character with a principal value of $g_z = 19.8$ (see Table 1) and a contribution from $M_J = \pm 15/2$ only.

Table 1. Results of the calculations by using the RCC basis sets for **Dy**: energy splitting of the ground $^6H_{15/2}$ multiplet and principal values of the corresponding g tensor for each Kramers' doublet. See Table S6 in the Supporting Information for the calculated splitting of the first excited multiplet ($^6H_{13/2}$).

	Energy level	[cm^{-1}]	g_x	g_y	g_z
$^6H_{15/2}$	E_0	0	0.0	0.0	19.8
	E_1	195	0.5	1.8	14.9
	E_2	237	0.1	2.2	14.3
	E_3	289	1.5	3.7	12.1
	E_4	324	0.6	2.8	13.8
	E_5	371	2.6	4.5	8.8
	E_6	430	3.4	4.1	7.4
	E_7	478	1.1	4.7	15.9

The computed easy axis orientation for the ground doublet (Figure 3b) lies approximately on the line that connects two carbonyl groups of two LH^- ligands ($\cos\alpha_1 = -0.531454$, $\cos\alpha_2 = 0.788731$, $\cos\alpha_3 = 0.308967$). It is evident that the calculated direction is almost coincident with one of the two possible choices provided by the CTM analysis (see above and Figure 3a), with an angle of 2.9° formed by the calculated and experimental orientations, well below the estimated experimental uncertainty (5°). Interestingly, the quality of the fit of the torque data is not very sensitive to the actual magnitude of the g_z value, as long as the system has strong Ising character (i.e., $g_z > 15$, $g_x,\ g_y < 1$), whereas it depends strongly on the Euler angles. As a consequence, if the torque fit is performed with the g values fixed to the computed ones ($g_z \approx 20$), the Euler angles are not affected (see Figure S6 in the Supporting Information). The calculated ab initio anisotropic properties are then perfectly consistent with the results of the CTM investigation.

With this proof of the reliability of ab initio calculations, we used the set of calculated Stevens' spin-Hamiltonian parameters[39] (see Table S5 in the Supporting Information) that pertain to the ground $J = 15/2$ state to simulate the static magnetic properties of the complex by using the home-developed soft-

ware EVALUCF.[13] In particular, the correct simulation of the *M* versus *H* curves at low temperature confirms that the ground doublet properties are well reproduced by ab initio calculations, whereas an indication of the correct evaluation of energy splitting and eigenstates of the ground $J = 15/2$ state can be provided by the simulation of the χT versus *T* curve. For this quantity, the agreement between experimental and calculated curves (see Figure S2 in the Supporting Information), except for a small scaling factor within experimental error (< 5%), lends further support to the electronic structure obtained by using ab initio calculations. This is reported in term of computed energy splitting[39] between the Kramers' doublets and their composition ($|M_J\rangle$ contributions larger than 0.1) in Figure S8 in the Supporting Information. The calculated energy separations between ground doublet and the first and second excited doublets are 195 and 237 cm^{-1}, respectively. The first excited doublet shows a prominent contribution from the $|M_J\rangle = \pm 13/2$ components with only $|M_J\rangle = \pm 11/2$ and $|M_J\rangle = \pm 7/2$ ones as minor contributions, which are nevertheless enough to induce appreciable deviations from the axiality of the ***g*** tensor. A much larger mixing between different $|M_J\rangle$ components is observed for the third excited doublet, whereas for the fifth excited doublet the axiality is completely lost.

It is to be stressed that in addition to the increased rhombicity, the non-collinearity of the easy axis with respect to that of the ground state also increases with the energy of the doublets (see Table S7 in the Supporting Information and Figure 3b). Indeed, the easy axis of the ground doublet forms an angle of 6° with the easy axis of the first excited doublet and an angle of about 60° with that of the second excited doublet. In this framework, the calculations suggest that if magnetic relaxation occurs only through an Orbach two-phonon mechanism, this should likely involve the second excited state. In such a case the energy barrier to be overcome would be of the order of 330 K, which indicates the possible observation of an overall slow relaxation rate at relatively high temperatures.

Dynamic magnetic properties

To gain more insights into this important point, the dynamic magnetic properties of **Dy** were investigated by performing ac magnetic susceptibility experiments in a broad range of frequency (0.02–10 000 Hz), temperature and dc applied field (see Figures S9–S12 in the Supporting Information). This investigation revealed a composite dynamic magnetic behaviour between 2 and 20 K. The pure complex showed two different relaxation channels in zero and non-zero magnetic static fields; the application of an external field allows the suppression of one channel and the activation of the other (see Figure 4). Further, field-dependent measurements indicated that the slow relaxation process reaches a minimum rate for $H_{dc} =$ 1000 Oe, whereas at higher fields the rate starts to increase again. This led us to choose this field for the measurements under an

external field. This behaviour is reminiscent of that previously reported by some of our group for the Dy(DOTA) derivative and other SMMs.[35,40–43] The imaginary susceptibility curves χ''

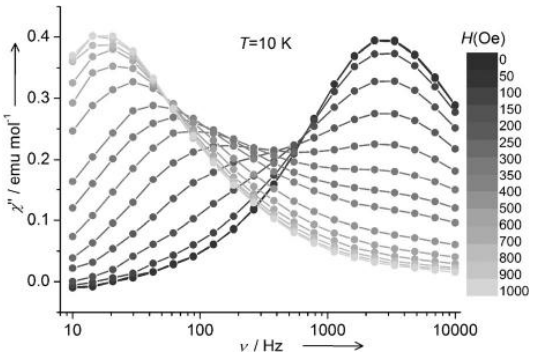

Figure 4. Imaginary susceptibility of Dy at 10 K as a function of the applied field.

in zero and applied field were fitted according to a Debye model[44,45] and the corresponding relaxation times are reported in Figure 5a as Arrhenius plots. We note that the relaxation rate of the channel that dominates in zero field is almost temperature-independent up to 12 K. Above this temperature, it starts to increase with temperature similarly to the behaviour observed for the relaxation channel activated with an applied

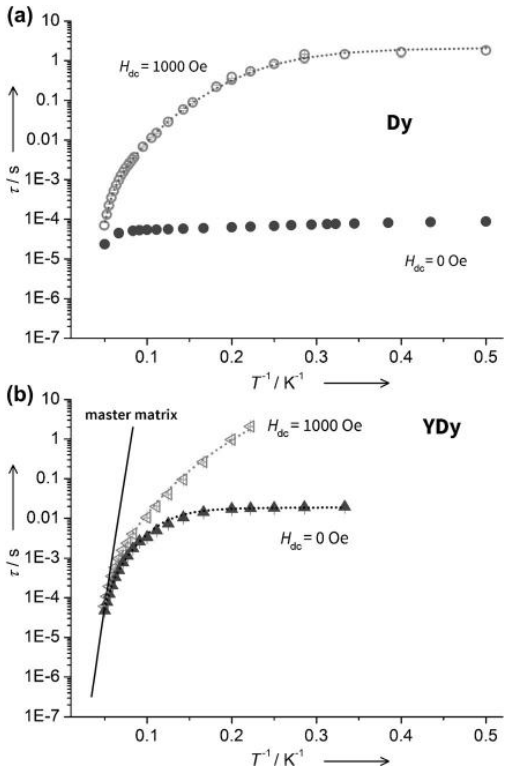

Figure 5. a) Relaxation times vs. T^{-1} for **Dy**, in zero (●) and applied static field (○). The relaxation in zero field is almost temperature independent up to 12 K. The grey dotted line represents the best fit curve with $\Delta = 270$ K. b) Relaxation times vs. T^{-1} for **YDy** in zero (▲) and applied static field (◁). The dotted lines represent the fit of the relaxation time; see Equation (3) with $\Delta = 270$ K, the solid line is the relaxation time simulated by using the master matrix equation.

magnetic field. This trend is present up to 20 K, at which they become too fast to be measured. Conversely, the rate observed for the relaxation channel activated by applying a magnetic field is clearly temperature-dependent even at lower temperatures (see Figure 5a and Figures S11 and S12 in the Supporting Information). As a whole, this behaviour suggests that the dominant process in zero field is directly related to the QT of magnetisation, whereas the slower process, which occurs in an applied field, is dominated by thermally activated relaxation. The curved nature of the Arrhenius plot for the relaxation time in a field, however, clearly points to a combination of processes that contribute to the relaxation, which include the persistence of a temperature-independent process at the lowest temperatures.[13]

To clarify whether the intermolecular (dipolar) interactions between magnetic centres play any role in this behaviour, we have repeated the investigation of the dynamics on the magnetically diluted **YDy** sample (Dy^{III} concentration of 10.5%; see Figure S3 in the Supporting Information). Its χT versus T curve is reported in Figure S2 in the Supporting Information, and shows the same temperature behaviour as the pure compound. Even in the diluted sample, two different relaxation channels were found to contribute to relaxation in zero and applied fields (see Figures S13–S16 in the Supporting Information). However, for **YDy** the relaxation of magnetisation is characterised by a much longer relaxation time τ, which reaches a few seconds at 4.5 K. Accordingly, at 2 K the diluted sample exhibited a butterfly-shaped hysteresis (see Figure S17 in the Supporting Information) that is not visible above 4 K. The observed temperature dependence of the relaxation rate of **YDy** for both relaxation channels was reproduced by including three contributions; Raman and Orbach processes and a temperature-independent process:[19,46–48]

$$\tau^{-1} = CT^{n} + \tau_0^{-1}\exp(-\Delta/T) + B \qquad (3)$$

We performed a simultaneous fit of the relaxation time in a field and in zero field (the corresponding parameters are indicated by *f* and *zf*, respectively, below), by using the same set of parameters for the Orbach process (τ_0 and Δ), whereas the Raman contribution was left free to vary for the two situations. This was intended to account for the possible contribution of a direct process in the case of in-field measurements, which may affect the best-fit value obtained for the Raman relaxation. A first attempt was made by fixing the value for the energy barrier Δ at 270 K to be approximately 195 cm^{-1}, which is the energy of the first excited doublet computed by ab initio calculations. With this pre-condition, we obtained the following values for the best-fit parameters: $\tau_0 = 1.3(2) \times 10^{-10}$ s, $n_f = 6.19(4)$, $C_f = 5.0(5) \times 10^{-5}$ $s^{-1}K^{-n}$, $B_f = 0$ (fixed), $n_{zf} = 5.5(2)$, $C_{zf} = 6(4) \times 10^{-4}$ $s^{-1}K^{-n}$, $B_{zf} = 53(2)$ s^{-1}. In a second step, the Δ parameter was left free to vary, to give the following best-fit values: $\tau_0 = 1(2) \times 10^{-11}$ s, $\Delta = 318(44)$K ($\approx$230 cm^{-1}), $n_f = 6.22(4)$, $C_f = 4.7(5) \times 10^{-5}$ $s^{-1}K^{-n}$, $B_f = 0$ (fixed), $n_{zf} = 5.6(2)$, $C_{zf} = 5(3) \times 10^{-4}s^{-1}K^{-n}$, $B_{zf} = 53(2)$ s^{-1} (see also Figure S18 in the Supporting Information). It is clear from these results that, although at low temperature Raman and QT dominate the relaxation, the Orbach process is active in promoting the relaxation in the high-temperature regime. It is, however, not completely clear whether the latter process occurs via the first or the second excited doublet. For the obtained τ_0 values, it is known that, for an Orbach process, τ_0 should be $(10^{-3} \div 10^{-5})\Delta^{-3}$ (Δ expressed in K);[49] substitution of the two different values for Δ gives a value of τ_0 in line with the findings. Moreover, the differences in τ_0 values are qualitatively consistent with expectations, τ_0 being smaller in the case of larger Δ.

Quantitative rationalisation of magnetisation dynamics

To obtain some more hints on the mechanism of the single-ion relaxation, transition moments between the states were computed[9,50] (see Figure 6). Based on these transition moments, no efficient QT relaxation is expected for the ground Kramers' doublet. The underestimation of the probability of QT relaxation by transition moments with respect to the experimental results is clearly due to the fact that this method takes into account only purely electronic, single-molecular properties, whereas zero-field QT in Kramers' systems needs residual dipolar interactions and hyperfine coupling to occur (in the present case the magnetic nuclei are Dy (^{161}Dy, rel. ab. = 18.9% and ^{163}Dy rel. ab. = 24.9%, both with $I = 5/2$).[51] On the basis of the ab initio results, a thermally assisted QT is likely to occur already for the first excited state. However, the magnetic moment matrix element computed for a quantum tunnelling mechanism between the two components of the first excited Kramers' doublet ($|1;\pm\rangle$) suggests that this is not the most likely process to occur. Indeed, from the first excited state both Orbach and thermally assisted QT processes are more probable; the former provides access to the second excited state whereas the latter would allow a reversal of the magnetisation. Based on the above considerations, a relaxation via the second excited state ($E_2 = 237$ cm^{-1}) seems to be more likely, in fairly good agreement with the phenomenological value of the above-reported value of the energy barrier of 230 cm^{-1}.

The use of transition moments to evaluate potential relaxation paths still provides only semi-quantitative indications,[14,52] despite being increasingly used to rationalise the spin dynamics. A more directly quantitative reproduction of the observed dynamics, by using the electronic structure derived by ab initio calculations, can be obtained by using a master-matrix-based approach.[45] This approach assumes a series of steps of the direct-process type promoted by a suitable spin phonon coupling Hamiltonian, assumed here to be of the Villain type[45] for the sake of simplicity. Indeed, in the low symmetry of our system the dynamic spin phonon coupling Hamiltonian proposed by Abragam and Bleaney[49] would require the calculation of a huge number of CF parameters corresponding to different distortions making it practically unfeasible.[53] Notwithstanding its simplicity, our approach allows us to extract the relaxation time by calculating the relaxation rate γ_q^p from a state $|q\rangle$ (eigenstate of the Hamiltonian that describes the system) to another state $|p\rangle$:

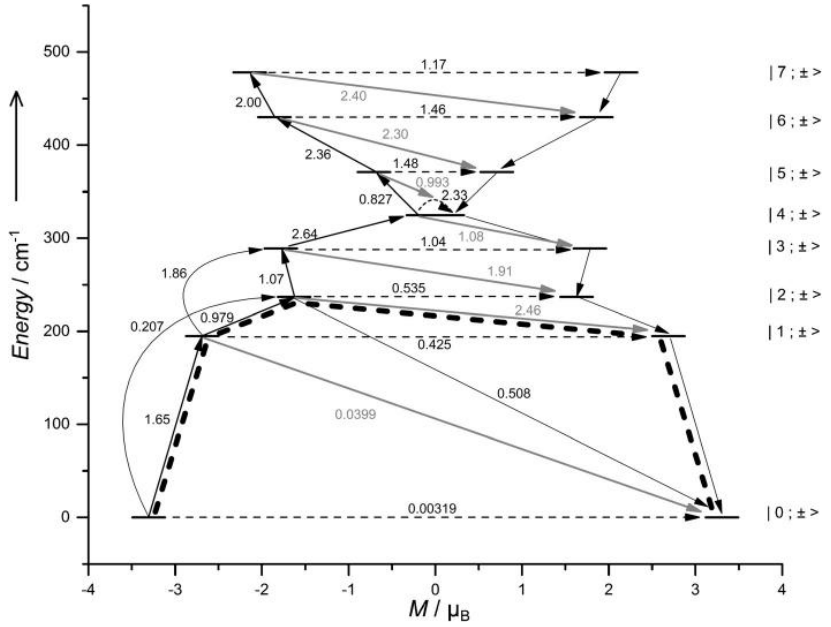

Figure 6. The ab initio computed magnetisation blocking barrier for **Dy**. The thick black horizontal lines indicate the Kramers' doublets as a function of the projection of the magnetic moment on the chosen quantisation axis (that of the ground multiplet). The light-grey arrows show the possible pathways of the Orbach process. The dotted black arrows represent the presence of (thermally assisted) quantum tunnelling between the connecting states. The numbers reported for each arrow are the mean absolute value for the corresponding matrix element of the transition magnetic moment. The thick dotted black lines show the most probable relaxation pathways for the reversal of magnetisation.

$$\gamma_q^p = \frac{3v}{\pi\hbar^4 m c_s^5} \cdot \frac{(E_p - E_q)^3}{\exp[\beta(E_p - E_q)] - 1} \cdot \{\left|\tilde{D}_a\right|^2 \cdot [|\langle p|\boldsymbol{J}_+^2|q\rangle|^2 + |\langle p|\boldsymbol{J}_-^2|q\rangle|^2] + \left|\tilde{D}_b\right|^2 \cdot [|\langle p|\{\boldsymbol{J}_+, \boldsymbol{J}_z\}|q\rangle|^2 + |\langle p|\{\boldsymbol{J}_-, \boldsymbol{J}_z\}|q\rangle|^2]\} \quad (4)$$

in which β is $1/k_BT$, v and m are the volume and the mass of the unit cell, $\tilde{D}_a$ and $\tilde{D}_b$ are the spin-phonon coupling parameters. If the energy levels and the eigenstates are known, the only parameters that need to be adjusted are the spin-phonon coupling parameters and $v/(mc_s^5)$. In our case, the CF eigenfunctions of the ground J multiplet and the corresponding eigenvalues in zero applied field obtained by using the ab initio calculations were used to obtain the CF matrix as $\mathbf{R}^T\mathbf{VR}$ (in which **R** is the eigenfunctions matrix and **V** is the diagonal matrix of the corresponding eigenvalues). The complete Hamiltonian (CF + static magnetic field) was then obtained by adding the Zeeman interactions in the $|M_J\rangle$ basis. This provided, after diagonalisation, new eigenvalues and eigenfunctions by which it was possible to calculate the master matrix (Γ) for all the investigated temperatures. Diagonalisation of the master matrix allowed us to extract the relaxation time as $\tau = -1/\lambda_1$, in which λ_1 is the first non-vanishing eigenvalue of the master matrix. The result, obtained by adjusting both the spin-phonon coupling parameter to 0.05 and the pre-factor $(3v/\pi\hbar^4 mc_s^5)$ to 3000, is shown in Figure 5b.

It is evident that although this approach reproduces the linear high-temperature region above 15 K, which is consistent with an energy barrier of about 230 K, it overestimates the relaxation time at lower temperature. This is a common feature for many lanthanide-based molecular magnets and is usually attributed to the higher effectiveness of the Raman process at lower temperatures. This process is, however, quite elusive because the corresponding parameters are usually considered to be phenomenological.[13,19,46,47,54–56] Indeed, to the best of our knowledge, no available reports relate the values of the Raman parameters (C and n) obtained by fitting the dynamic data to the structure of the investigated molecule. This is a severe drawback in the search for increased relaxation times for potential applications because this process, which provides a channel for relatively fast relaxation even at quite low temperature, is currently beyond our control. However, we stress that, despite the phenomenological fit of the temperature dependence of the relaxation rate that indicates the existence of a T^n contribution, we cannot be sure that this is associated with a real Raman process. Indeed, interactions that are not taken into account by the model, such as hyperfine and residual dipolar intermolecular interactions, may open the possibility of relaxation through quantum tunnelling and might also change the expected field- and temperature-dependence of direct processes.[57]

Conclusion

We have presented a comprehensive experimental and theoretical investigation of the anisotropy and dynamic behaviour of a novel mononuclear lanthanide-based single-molecule magnet. We showed that detailed cantilever torque magnetometry, which can be used more generally in terms of crystal symmetry and size than single-crystal magnetometry, can provide independent confirmation of the results of ab initio calculations in the absence of further spectroscopic information. This is particularly relevant for systems that are EPR silent and for which no detailed luminescent data are available. In turn, this allowed us to analyse the observed dynamics of the magnetisation on the basis of the calculated electronic structure of the lanthanide centre. For the studied complex, the experimental and theoretical results indicate a strong axiality of both the ground doublet and the first excited state; the ab initio prediction of an almost complete collinearity of the ground and first excited doublet is mirrored by the low-temperature slow relaxation of the magnetisation of the complex, which could be phenomenologically modelled by using a combination of an Orbach and a Raman process. The observed behaviour could be qualitatively rationalised by using the commonly used transition probabilities provided by the ab initio suite.[9,50] In addition to this, we showed that the relaxation behaviour at the higher temperature range can be correctly reproduced by using the ab initio computed electronic structure in a statistical analysis based on the master matrix approach. Conversely, further processes are clearly contributing at low temperature, resulting in an experimental relaxation rate that is much faster than predicted by this approach. This might be due either to a true Raman process or to the unaccounted-for hyperfine and dipolar intermolecular interactions, the latter reduced but not completely quenched by the doping level used herein. As a whole, these results outline the necessity of a virtuous interplay between detailed single-crystal studies and ab initio calculations. This process allowed us to obtain a detailed understanding of the relation between the electronic structure and the rich low-temperature magnetisation dynamics in this system, a point of crucial importance for rationally improving the properties of lanthanide-based single-molecule magnets.

Experimental Section

Synthesis

$Dy(NO_3)_3{\cdot}5H_2O$, $Y(NO_3)_3{\cdot}5H_2O$, pyridine carboxaldehyde and piperidine (Aldrich) were used as purchased. 2-Hydroxybenzohydrazide was prepared as previously described.[58] High-grade solvents (diethyl ether, dimethylformamide, methanol) were used for the syntheses of ligands and complexes.

2-Hydroxy-*N*′-[(*E*)-(2-hydroxy-3-methoxyphenyl)methylidene]benzhydrazide

Addition of pyridine carboxaldehyde (1.07 g, 1.0×10^{-3} mol) to a stirred solution of 2-hydroxybenzhydrazide (1.52 g,1.0×10^{-3} mol) in MeOH (30 mL) followed by heating for 30 min induced formation of a bulky white precipitate that was filtered off after cooling, washed with MeOH and diethyl ether and dried (yield: 2.7 g, 95%). ^{1}H NMR (400 MHz, [D_6]-DMSO): $\delta=6.99$ (t + d, $J=7$ Hz, 2H; CH-3 + CH-5), 7.45 (t + d, $J=7.5$ Hz, 5H; CH-4 + CH-4′), 7.89 (t + d, $J=7.5$ Hz, 2H; CH-5′ + CH-6′), 8.00 (d, $J=7$ Hz,1H; CH-6), 8.49 (s, 1H;HC- -N), 8.64 (d, $J=7$ Hz, 1H;CH-3′), 11.71 (s, 1H; NH), 12.1 ppm (s, 1H; OH); ^{13}C NMR (100.63 MHz, [D_6]-DMSO): $\delta=116.65$ (s, ArC-1), 117.71 (s, ArC-3), 119.44 (s, ArC-5), 120.53 (s, ArC-6′), 125.01 (s, ArC-4′), 129.14 (s, ArC-6), 134.36 (s, ArC-4), 137.37 (s, ArC-5′), 120.53 (s, ArC-6′), 149.16 (s, ArC-3′), 150.02 (s, NC- -N), 153.54 (s, ArC-6′), 165.44 ppm (s, OCNH); elemental analysis calcd (%) for $C_{13}H_{11}N_3O_2$ (241.2 g mol^{-1}): C 64.7, H 4.6, N 17.4; found: C 64.4, H 4.5, N 17.2.

$Dy(LH)_3$ (Dy)

Addition of piperidine (0.17 g,2.0×10^{-3} mol) to a stirred solution of the above ligand (0.27 g, 1.0×10^{-3} mol) and $Dy(NO_3)_3{\cdot}5H_2O$ (0.43 g, 1.0×10^{-3} mol) in DMF (10 mL) induced the appearance of a more intense yellow solution. The solution was filtered off and set aside. The crystals that appeared after 12 d were isolated by filtration and dried (yield: 0.16 g, 50.5%). IR (ATR): $\tilde{\nu}=$ 3448l, 3065 w, 2991 w, 2925 w, 2875 w, 2792 w, 2705 w, 2610 w, 1681 w, 1667 m, 1599 m, 1586 m, 1561 m, 1520 m, 1488 m, 1474 m, 1452 m, 1417 w, 1357 s, 1346 s, 1302 m,1252 m, 1230 w, 1147 m, 1090 w, 1065 m, 1008 w, 926 w, 866 w, 830 w, 760 m, 740 w, 702 w, 689 w, 658 w, 632 cm^{-1} w; elemental analysis calcd (%) for $C_{42}H_{37}DyN_{10}O_7$ (956.32 g mol^{-1}): C 52.75, H 3.90, N 14.65; found: C 52.45, H 3.78, N 14.43.

$YDy(LH)_3$

Use of the same experimental process described above with $Y(NO_3)_3{\cdot}5H_2O$ (0.36 g, 2.0×10^{-3} mol) with $Dy(NO_3)_3{\cdot}5H_2O$ (30 mg) gave crystals that were isolated by filtration and dried (yield: 0.19 g, 64.7%). IR (ATR): $\tilde{\nu}=$ 3440l, 3068 w, 2929 w, 2775 w, 2718 w, 2612 w, 1663 w, 1598 m, 1584 m, 1562 m, 1519 m, 1484 m, 1472 m, 1454 m, 1426 w, 1362 s, 1349 s, 1297 m, 1246 m, 1227 w, 1156 m, 1146 m, 1100 w, 1066 m, 1042 w, 1028 w, 1008 w, 921 w, 866 w, 830 w, 757 m, 741 w, 703 w, 689 w, 680 w, 633 cm^{-1} w; elemental analysis was carried out at the Laboratoire de Chimie de Coordination Microanalytical Laboratory in Toulouse, France, for C, H and N. IR spectra were recorded by using a Spectrum 100 FT-IR Perkin-Elmer spectrophotometer in the ATR mode.

Crystallographic data collection and structure determination

Crystals of **Dy** were kept in the mother liquor until they were removed and dipped in oil. The chosen crystals were mounted on a Mitegen micromount and quickly cooled to 180 K. The selected crystals of **Dy** (yellow, ($0.18\times0.10\times0.04$ mm^3) were mounted on an Oxford Diffraction Xcalibur diffractometer that used graphite-monochromated $Mo_{K\alpha}$ radiation ($\lambda=0.71073$ Å) and equipped with an Oxford Instrument Cooler Device. Data were collected at low temperature (180 K). The final unit cell parameters were obtained by using least-squares refinements. The structures were solved by using direct methods in SIR92,[59] and refined by using a least-squares procedures on F^2 with the program SHELXL97[60] included in the software package WinGX version 1.63.[61] The atomic scattering factors were taken from the International Tables for X-Ray Crystallography.[62] All non-hydrogen atoms were anisotropically refined, and in the last cycles of refinement a weighting scheme was used, in which weights were calculated from the following formula: $w=1/[\sigma^2(F_o^2)+(aP)^2+bP]$ in which $P=(F_o^2+2F_c^2)/3$. CCDC 1433866 (**Dy**) contains the supplementary crystallographic

data for this paper. These data are provided free of charge by The Cambridge Crystallographic Data Centre.

Crystal data for Dy

$C_{42}H_7DyN_{10}O_7$; $M_r = 956.32\ g\,mol^{-1}$; monoclinic $P2_1/n$; $Z=4$; $a=9.8585(3)$, $b=22.1870(6)$, $c=19.1215(5)$ Å; $\alpha=\gamma=90$, $\beta=94.160(3)^\circ$; $V=4171.3(2)$ Å^3; 35 087 collected reflections, 8511 unique reflections ($R_{int}=0.0416$); R factor = 0. 0368, weighted R factor = 0.0921 for 6996 contributing reflections [$I>2\sigma(I)$].

Magnetic characterisation

The purity of the polycrystalline powders of **Dy** used for magnetic characterisation was checked by using a Bruker D8 Advance powder diffractometer equipped with a Cu source ($Cu_{K\alpha}$, $\lambda = 1.54$ Å; see Figure S19 in the Supporting Information). The isomorphicity of diluted compound **YDy** compared with the pure **Dy** compound was checked by using a Xcalibur3 single-crystal diffractometer equipped with a $Mo_{K\alpha}$ source ($\lambda = 0.71073$ Å). Xcalibur3 is a four-cycle kappa geometry diffractometer equipped with a Sapphire 3 CCD detector. dc magnetic measurements were performed by using a Quantum Design MPMS SQUID magnetometer on powders pressed in a pellet to avoid field-induced orientation of the crystallites. The concentration of Dy^{III} in **YDy** was estimated to be 10.5% by the scaling factor between the isothermal magnetisation curves at low temperature of the pure and diluted compounds. ac susceptibility was measured by using a Quantum Design PPMS in ac mode for the frequency range of 10–10^4 Hz. The Quantum Design MPMS SQUID magnetometer was used for low frequencies (0.02–10^3 Hz). EPR spectra (not shown) were recorded at 3 and 5 K by using a E500 Bruker spectrometer for the X band ($\nu \approx 9.4$ GHz). The CTM measurements were performed by using a home-built two-legged CuBe cantilever separated by 0.1 mm from a gold plate. The cantilever was inserted into an Oxford Instruments MAGLAB2000 platform with automated rotation of the cantilever chip in a vertical magnet. The capacitance of the cantilever was detected by using a Andeen-Hegerling2500A Ultra Precision Capacitance Bridge. The faces of the measured crystal were indexed by using X-ray diffraction in the above-described setup, then fixed on the cantilever with glue. This procedure resulted in an estimated uncertainty of the actual orientation of the crystal of about 5°.

Ab initio calculations

The quantum chemistry package MOLCAS 8.0[63] was employed for all the calculations. The X-ray structure resolved from the diffraction pattern recorded at 180 K was used throughout the study. All atoms were described by using the standard all-electrons ANO-RCC basis set. The TZP basis set was employed for dysprosium, nitrogen and oxygen atoms (see Table S8 in the Supporting Information) and DZP and DZ were used for carbon and hydrogen atoms, respectively. The default contraction scheme was not altered. The Douglass–Kroll–Hess Hamiltonian was employed to take into account scalar relativistic effects. The spin-free wave functions were obtained by using the complete active space self-consistent field (CASSCF) method for a state-average calculation of all roots that arise from the considered active space. The active space consisted of nine electrons in the seven f orbitals of the lanthanide atom [CASSCF(9,7)]. The spin-orbit interaction was considered in the following restricted active space state interaction (RASSI) calculation by mixing all the state-averaged obtained 21 sextuplets. The g tensor for every Kramers doublet and its orientation in the molecular frame, the CF parameters and their decomposition in wavefunctions with definite projection of the total moment $|J, M_J\rangle$ were computed by using the SINGLE_ANISO package. The quantisation axis was chosen to be the main magnetic axis of the ground doublet.

Acknowledgements

We acknowledge the financial support from MIUR through the project Futuro in Ricerca 2012 (RBFR12RPD1), from the European Research Council through the Advanced Grant MolNanoMas (grant no. 267746). We also acknowledge the computational facilities at the National High-Performance Computing Center in Sao Paulo (Centro Nacional de Processamento de Alto Desempenho em São Paulo-CENAPAD-SP) for the awarded computational time (proj627).

Keywords: ab initio calculations · cantilever torque magnetometry · lanthanides · magnetisation relaxation · single-molecule magnets

[1] N. Ishikawa, M. Sugita, T. Ishikawa, S.-y. Koshihara, Y. Kaizu, *J. Am. Chem. Soc.* **2003**, *125*, 8694 – 8695.
[2] R. A. Layfield, M. Murugesu, *Lanthanides and Actinides in Molecular Magnetism*, Wiley, Hoboken, **2015**.
[3] C. Benelli, D. Gatteschi, *Introduction to Molecular Magnetism: From Transition Metals to Lanthanides*, Wiley, Hoboken, **2015**.
[4] R. Vincent, S. Klyatskaya, M. Ruben, W. Wernsdorfer, F. Balestro, *Nature* **2012**, *488*, 357 – 360.
[5] F. Habib, M. Murugesu, *Chem. Soc. Rev.* **2013**, *42*, 3278 – 3288.
[6] G. Aromí, D. Aguila, P. Gamez, F. Luis, O. Roubeau, *Chem. Soc. Rev.* **2012**, *41*, 537 – 546.
[7] J. D. Rinehart, J. R. Long, *Chem. Sci.* **2011**, *2*, 2078 – 2085.
[8] L. Sorace, D. Gatteschi, in *Lanthanides and Actinides in Molecular Magnetism* (Eds.: R. A. Layfield, M. Murugesu), Wiley, Hoboken, **2015**, pp. 1 – 25.
[9] L. Ungur, L. F. Chibotaru, *Phys. Chem. Chem. Phys.* **2011**, *13*, 20086 – 20090.
[10] G. Cucinotta, M. Perfetti, J. Luzon, M. Etienne, P.-E. Car, A. Caneschi, G. Calvez, K. Bernot, R. Sessoli, *Angew. Chem. Int. Ed.* **2012**, *51*, 1606 – 1610; *Angew. Chem.* **2012**, *124*, 1638 – 1642.
[11] N. F. Chilton, S. K. Langley, B. Moubaraki, A. Soncini, S. R. Batten, K. S. Murray, *Chem. Sci.* **2013**, *4*, 1719 – 1730.
[12] D. Aravena, E. Ruiz, *Inorg. Chem.* **2013**, *52*, 13770 – 13778.
[13] E. Lucaccini, L. Sorace, M. Perfetti, J.-P. Costes, R. Sessoli, *Chem. Commun.* **2014**, *50*, 1648 – 1651.
[14] R. J. Blagg, L. Ungur, F. Tuna, J. Speak, P. Comar, D. Collison, W. Wernsdorfer, E. J. McInnes, L. F. Chibotaru, R. E. Winpenny, *Nat. Chem.* **2013**, *5*, 673 – 678.
[15] J.-L. Liu, K. Yuan, J.-D. Leng, L. Ungur, W. Wernsdorfer, F.-S. Guo, L. F. Chibotaru, M.-L. Tong, *Inorg. Chem.* **2012**, *51*, 8538 – 8544.
[16] L. Tesi, E. Lucaccini, I. Cimatti, M. Perfetti, M. Mannini, M. Atzori, E. Morra, M. Chiesa, A. Caneschi, L. Sorace, R. Sessoli, *Chem. Sci.* **2016**, *7*, 2074 – 2083
[17] T. Fukuda, N. Shigeyoshi, T. Yamamura, N. Ishikawa, *Inorg. Chem.* **2014**, *53*, 9080 – 9086.
[18] R. Marx, F. Moro, M. Dorfel, L. Ungur, M. Waters, S. D. Jiang, M. Orlita, J. Taylor, W. Frey, L. F. Chibotaru, J. van Slageren, *Chem. Sci.* **2014**, *5*, 3287 – 3293.
[19] Y. Rechkemmer, J. E. Fischer, R. Marx, M. Dörfel, P. Neugebauer, S. Horvath, M. Gysler, T. Brock-Nannestad, W. Frey, M. F. Reid, J. van Slageren, *J. Am. Chem. Soc.* **2015**, *137*, 13114 – 13120.
[20] S. I. Klokishner, S. M. Ostrovsky, O. S. Reu, A. V. Palii, P. L. Tregenna-Piggott, T. Brock-Nannestad, J. Bendix, H. Mutka, *J. Phys. Chem. C* **2009**, *113*, 8573 – 8582.

[21] J. Long, J. Rouquette, J.-M. Thibaud, R. A. Ferreira, L. D. Carlos, B. Donnadieu, V. Vieru, L. F. Chibotaru, L. Konczewicz, J. Haines, Y. Guari, J. Larionova, *Angew. Chem. Int. Ed.* **2015**, *54*, 2236 – 2240; *Angew. Chem.* **2015**, *127*, 2264 – 2268.
[22] E. M. Pineda, N. F. Chilton, R. Marx, M. Dörfel, D. O. Sells, P. Neugebauer, S.-D. Jiang, D. Collison, J. van Slageren, E. J. McInnes, R. E. Winpenny, *Nat. Commun.* **2014**, *5*, 5243.
[23] L. Sorace, C. Sangregorio, A. Figuerola, C. Benelli, D. Gatteschi, *Chem. Eur. J.* **2009**, *15*, 1377 – 1388.
[24] J. J. Baldoví, J. M. Clemente-Juan, E. Coronado, A. Gaita-Ariño, *Inorg. Chem.* **2014**, *53*, 11323 – 11327.
[25] J. Jung, F. C. Le Natur, O. Cador, F. Pointillart, G. Calvez, C. Daiguebonne, O. Guillou, T. Guizouarn, B. Le Guennic, K. Bernot, *Chem. Commun.* **2014**, *50*, 13346 – 13348.
[26] K. Bernot, J. Luzon, L. Bogani, M. Etienne, C. Sangregorio, M. Shanmugam, A. Caneschi, R. Sessoli, D. Gatteschi, *J. Am. Chem. Soc.* **2009**, *131*, 5573 – 5579.
[27] M.-E. Boulon, G. Cucinotta, J. Luzon, C. Degl'Innocenti, M. Perfetti, K. Bernot, G. Calvez, A. Caneschi, R. Sessoli, *Angew. Chem. Int. Ed.* **2013**, *52*, 350 – 354; *Angew. Chem.* **2013**, *125*, 368 – 372.
[28] A. Cornia, D. Gatteschi, R. Sessoli, *Coord. Chem. Rev.* **2001**, *219*, 573 – 604.
[29] M. Perfetti, G. Cucinotta, M.-E. Boulon, F. El Hallak, S. Gao, R. Sessoli, *Chem. Eur. J.* **2014**, *20*, 14051 – 14056.
[30] M. Perfetti, E. Lucaccini, L. Sorace, J.-P. Costes, R. Sessoli, *Inorg. Chem.* **2015**, *54*, 3090 – 3092.
[31] X. Yi, K. Bernot, F. Pointillart, G. Poneti, G. Calvez, C. Daiguebonne, O. Guillou, R. Sessoli, *Chem. Eur. J.* **2012**, *18*, 11379 – 11387.
[32] P. Zhou, Y.-G. Zhao, Y. Bai, K.-L. Pang, C. He, *Inorg. Chim. Acta* **2007**, *360*, 3965 – 3970.
[33] S. Alvarez, P. Alemany, D. Casanova, J. Cirera, M. Llunell, D. Avnir, *Coord. Chem. Rev.* **2005**, *249*, 1693 – 1708.
[34] C. Janiak, *J. Chem. Soc. Dalton Trans.* **2000**, 3885 – 3896.
[35] P.-E. Car, M. Perfetti, M. Mannini, A. Favre, A. Caneschi, R. Sessoli, *Chem. Commun.* **2011**, *47*, 3751 – 3753.
[36] D.-P. Li, X.-P. Zhang, T.-W. Wang, B.-B. Ma, C.-H. Li, Y.-Z. Li, X.-Z. You, *Chem. Commun.* **2011**, *47*, 6867 – 6869.
[37] L. Rigamonti, A. Cornia, A. Nava, M. Perfetti, M.-E. Boulon, A.-L. Barra, X. Zhong, K. Park, R. Sessoli, *Phys. Chem. Chem. Phys.* **2014**, *16*, 17220 – 17230.
[38] N. F. Chilton, D. Collison, E. J. McInnes, R. E. Winpenny, A. Soncini, *Nat. Commun.* **2013**, *4*, 2551.
[39] L. F. Chibotaru, L. Ungur, *J. Chem. Phys.* **2012**, *137*, 064112.
[40] S. Xue, L. Ungur, Y.-N. Guo, J. Tang, L. F. Chibotaru, *Inorg. Chem.* **2014**, *53*, 12658 – 12663.
[41] G. Cosquer, F. Pointillart, S. Golhen, O. Cador, L. Ouahab, *Chem. Eur. J.* **2013**, *19*, 7895 – 7903.
[42] E. Bartolomé, J. Bartolomé, S. Melnic, D. Prodius, S. Shova, A. Arauzo, J. Luzón, F. Luis, C. Turta, *Dalton Trans.* **2013**, *42*, 10153 – 10171.
[43] L. Norel, K. Bernot, M. Feng, T. Roisnel, A. Caneschi, R. Sessoli, S. Rigaut, *Chem. Commun.* **2012**, *48*, 3948 – 3950.
[44] H. B. G. Casimir, F. K. Du Pré, *Physica* **1938**, *5*, 507 – 511.
[45] D. Gatteschi, R. Sessoli, J. Villain, *Molecular Nanomagnets*, Oxford University Press, Oxford, **2006**.
[46] M. Gregson, N. F. Chilton, A.-M. Ariciu, F. Tuna, I. F. Crowe, W. Lewis, A. J. Blake, D. Collison, E. J. McInnes, R. E. Winpenny, S. T. Liddle, *Chem. Sci.* **2016**, *7*, 155 – 165.
[47] J. M. Zadrozny, M. Atanasov, A. M. Bryan, C.-Y. Lin, B. D. Rekken, P. P. Power, F. Neese, J. R. Long, *Chem. Sci.* **2013**, *4*, 125 – 138.
[48] S. Demir, J. M. Zadrozny, J. R. Long, *Chem. Eur. J.* **2014**, *20*, 9524 – 9529.
[49] A. Abragam, B. Bleaney, *Electron Paramagnetic Resonance of Transition Ions*, Oxford University Press, Oxford, **1970**.
[50] L. Ungur, M. Thewissen, J.-P. Costes, W. Wernsdorfer, L. F. Chibotaru, *Inorg. Chem.* **2013**, *52*, 6328 – 6337.
[51] F. Pointillart, K. Bernot, S. Golhen, B. Le Guennic, T. Guizouarn, L. Ouahab, O. Cador, *Angew. Chem. Int. Ed.* **2015**, *54*, 1504 – 1507; *Angew. Chem.* **2015**, *127*, 1524 – 1527.
[52] C. Das, A. Upadhyay, S. Vaidya, S. K. Singh, G. Rajaraman, M. Shanmugam, *Chem. Commun.* **2015**, *51*, 6137 – 6140.
[53] N. F. Chilton, C. A. Goodwin, D. P. Mills, R. E. Winpenny, *Chem. Commun.* **2015**, *51*, 101 – 103.
[54] K. S. Pedersen, L. Ungur, M. Sigrist, A. Sundt, M. Schau-Magnussen, V. Vieru, H. Mutka, S. Rols, H. Weihe, O. Waldmann, L. F. Chibotaru, J. Bendix, J. Dreiser, *Chem. Sci.* **2014**, *5*, 1650 – 1660.
[55] Q.-W. Li, J.-L. Liu, J.-H. Jia, J.-D. Leng, W.-Q. Lin, Y.-C. Chen, M.-L. Tong, *Dalton Trans.* **2013**, *42*, 11262 – 11270.
[56] J. Ruiz, G. Lorusso, M. Evangelisti, E. K. Brechin, S. J. Pope, E. Colacio, *Inorg. Chem.* **2014**, *53*, 3586 – 3594.
[57] S. Gómez-Coca, A. Urtizberea, E. Cremades, P. J. Alonso, A. Camón, E. Ruiz, F. Luis, *Nat. Commun.* **2014**, *5*, 4300.
[58] J.-P. Costes, C. Duhayon, L. Vendier, *Inorg. Chem.* **2014**, *53*, 2181 – 2187.
[59] A. Altomare, G. Cascarano, C. Giacovazzo, A. Guagliardi, *J. Appl. Crystallogr.* **1993**, *26*, 343 – 350.
[60] G. Sheldrick, University of Göttingen, Germany, **1997**.
[61] L. J. Farrugia, *J. Appl. Crystallogr.* **1999**, *32*, 837 – 838.
[62] D. Moss, *Acta Crystallogr. Sect. A* **1975**, *31*, 877 – 878.
[63] F. Aquilante, L. De Vico, N. Ferré, G. Ghigo, P.-a. Malmqvist, P. Neogrády, T. B. Pedersen, M. Pitovnák, M. Reiher, B. O. Roos, L. Serrano-Andrés, M. Urban, R. Lindh, *J. Comput. Chem.* **2010**, *31*, 224 – 247.

Received: December 30, 2015
Published online on March 9, 2016

CHEMISTRY
A European Journal

Supporting Information

Relaxation Dynamics and Magnetic Anisotropy in a Low-Symmetry Dy^{III} Complex

Eva Lucaccini,[a] Matteo Briganti,[a, b] Mauro Perfetti,[a, c] Laure Vendier,[d] Jean-Pierre Costes,[d] Federico Totti,*[a] Roberta Sessoli,[a] and Lorenzo Sorace*[a]

chem_201505211_sm_miscellaneous_information.pdf

ELECTRONIC SUPPLEMENTARY INFORMATION

List of Figures

List of Tables

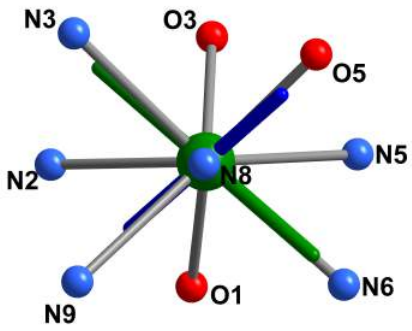

(a) Capped square antirprism view along C_4.

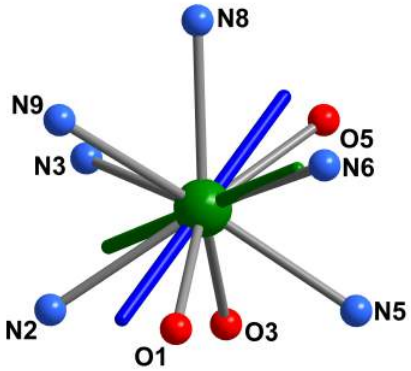

(b) Capped square antiprism equatorial plane view.

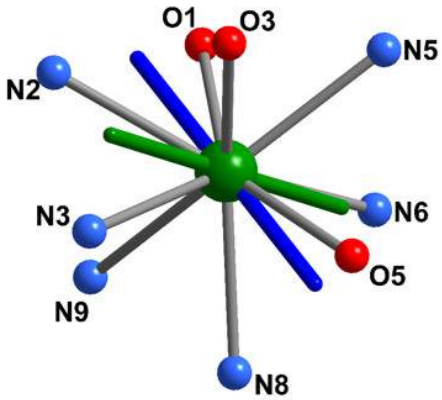

(c) Tricapped trigonal prism view along C_3.

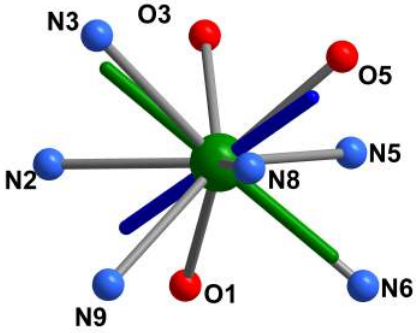

(d) Tricapped trigonal prism equatorial plane view.

Figure S1: View of the first coordination sphere of **Dy** emphasizing the similarity with capped square antiprism (top) and tricapped trigonal prism (bottom), as obtained by SHAPE calculation (see also Table S2). On the left the view is along the pseudo-symmetry axis (C_4 or C_3), on the right perpendicular to it. Blue and green sticks represent the two possible orientations after experimental CTM investigation, the blue one being essentially coincident with the *ab initio* calculated direction of the easy axis anisotropy.

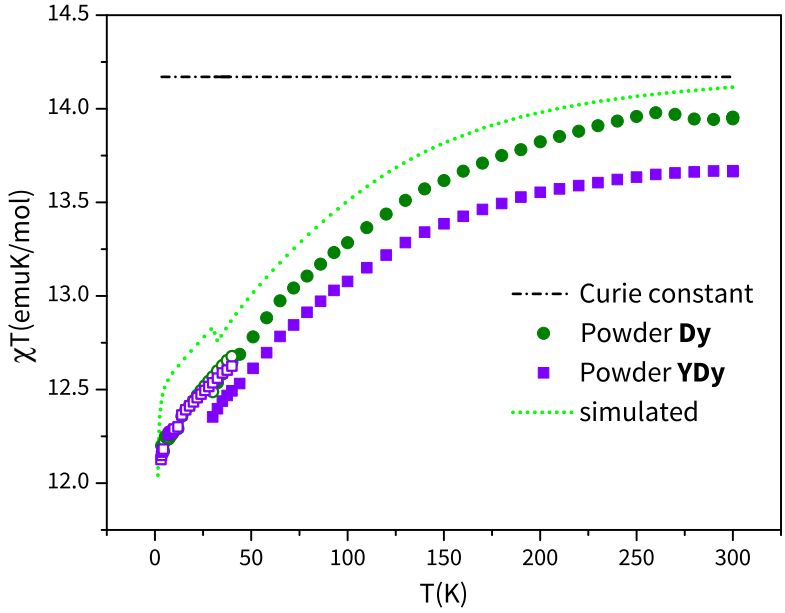

Figure S2: Temperature dependence of χT of **Dy** (circles)and **YDy** (squares) along with theoretical curves (dotted line) calculated by using CF parameters derived from ab initio calculations. The dashed line corresponds to the expected free-ion χT value. The empty circles and squares correspond to an applied static field H of 1000 Oe while the full ones to a field of 10 000 Oe. The difference observed for the two fields is to be attributed to saturation effects which are well reproduced by the theoretical prediction.

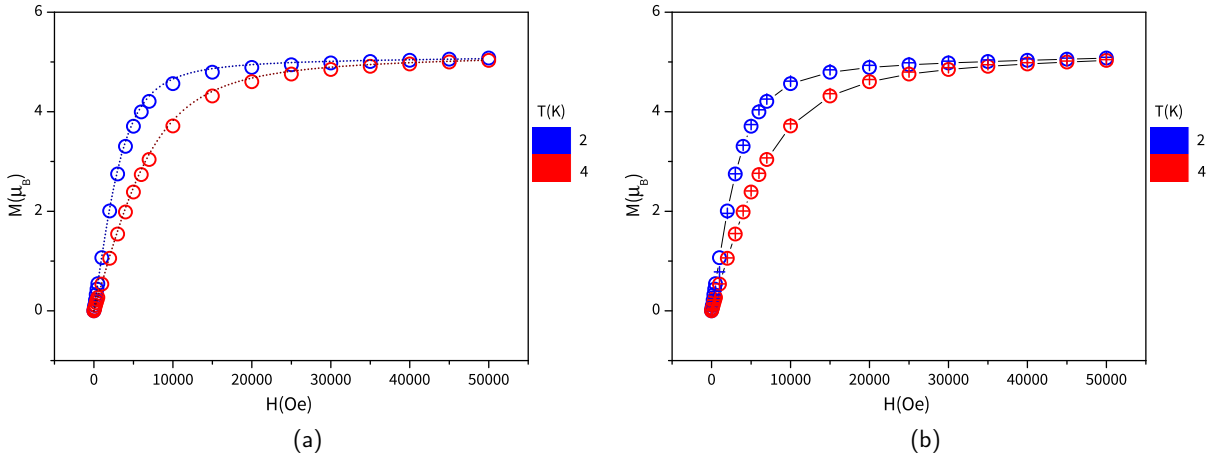

Figure S3: Left panel: empty circles represents the behavior of magnetization versus field at 2 K and 4 K for **Dy**, while the dotted lines are the simulation calculated with the CF parameters extracted from *ab initio* calculations. Right panel: the concentration of Dy in Y was estimated by superimposing the magnetization curve of pure (**Dy** - empty circles) and diluted sample (**YDy** - cross), resulting in a 10 % of dilution.

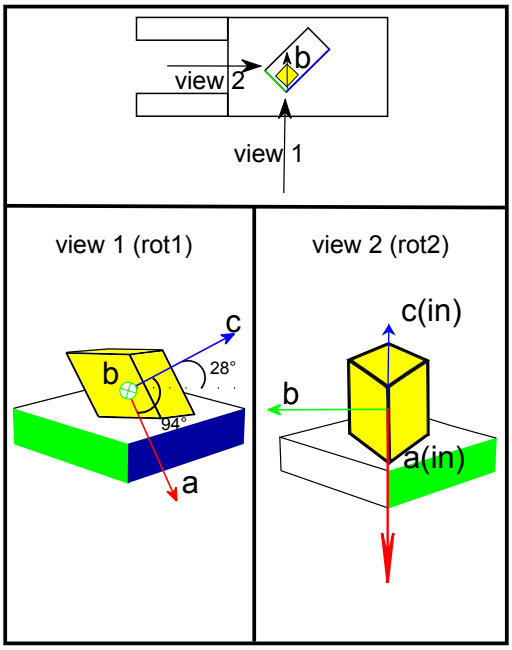

(a)

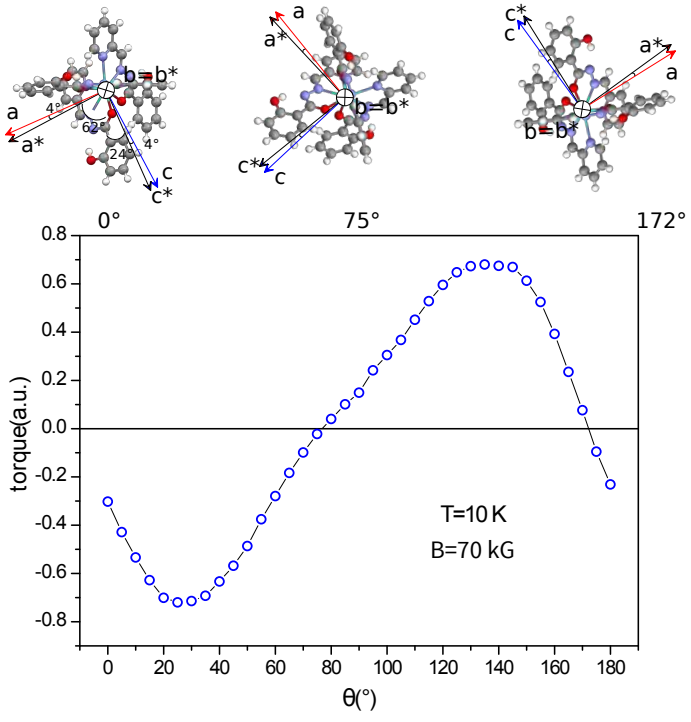

(b)

Figure S4: Upper panel: position of crystal on the cantilever for the two rotation. The orientation for view 1 and view 2 is for the rotation angle $\theta = 270°$. Lower panel: experimental curve recorded at 10 K and 70 kG for Rot1.

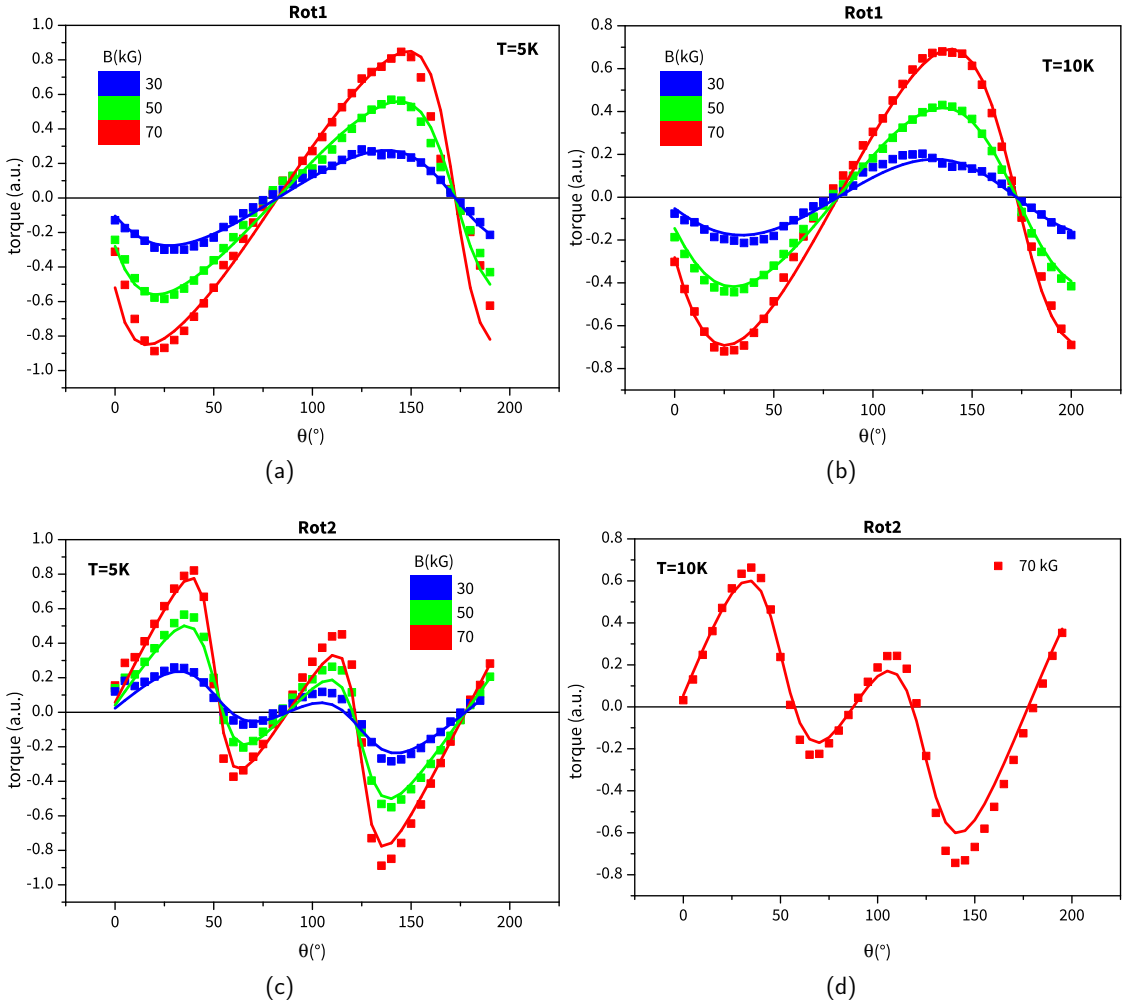

Figure S5: Upper panel: Torque curves for Rot1 recorded at 5 K and 10 K for various magnetic fields. The solid lines were obtained using the best fit parameters (see text). Lower panel: torque curves for Rot2 recorded at 5 K and 10 K for various magnetic fields. The solid lines were obtained using the best fit parameters (see text).

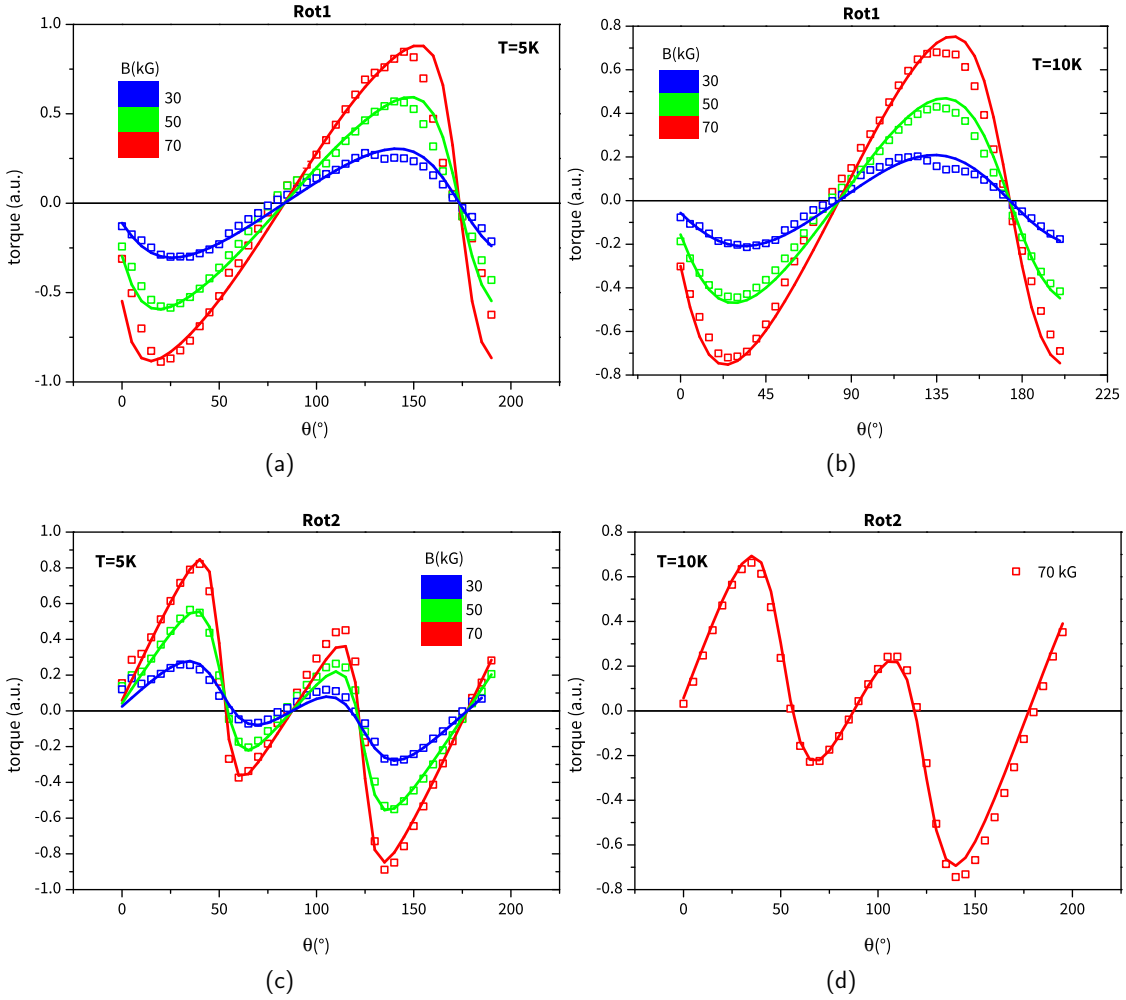

Figure S6: Torque curves for Rot1 and Rot2 along with the fit obtained fixing $g_z = 20$, $g_x = g_y = 0$.

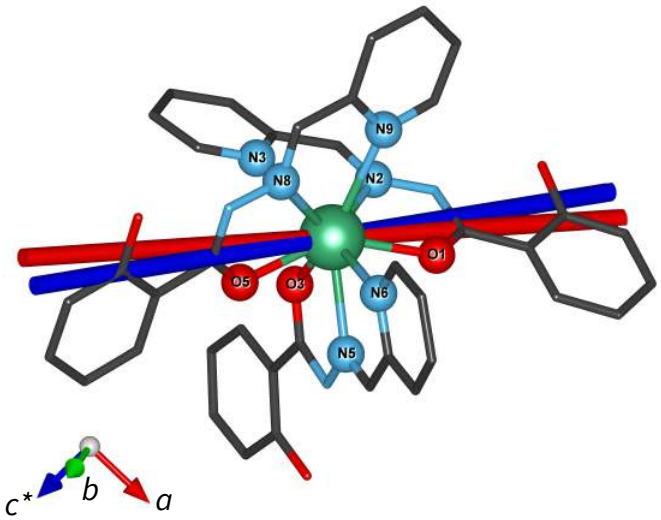

Figure S7: Orientation of the experimental easy axis (blue) and the one calculated with Magellan (red) [1] considering Option 2, see also table S4.

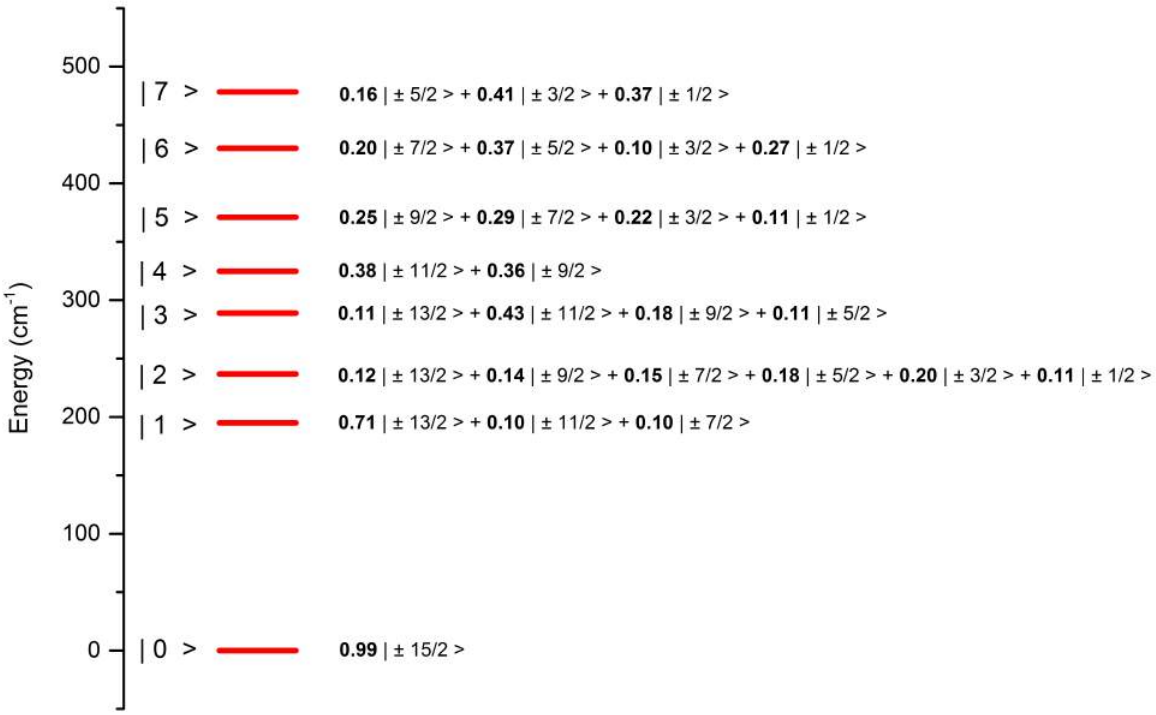

Figure S8: Energy levels and eigenstates for Dy extracted from *ab initio* calculations. The ground state is set at the origin.

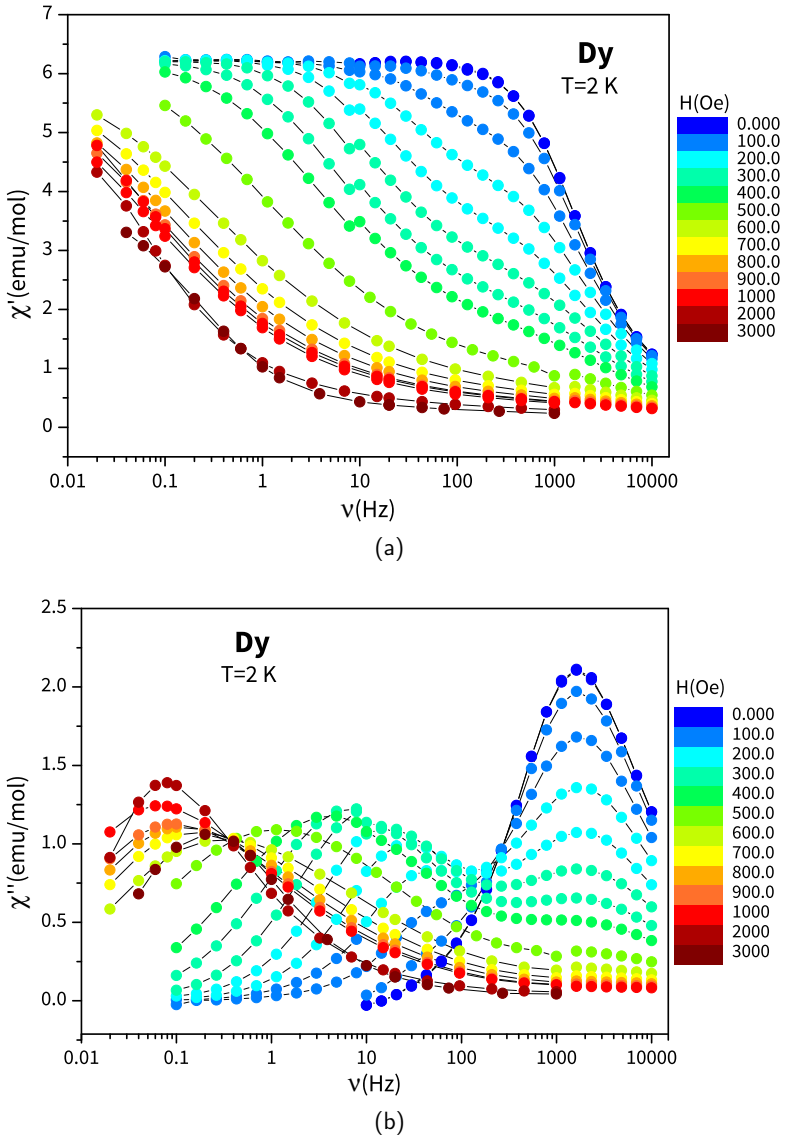

Figure S9: Real (upper) and imaginary susceptibility (lower)of **Dy** as a function of frequency at 2 K. The figure is a collage of measurements performed with different instrumentation: a Quantum Design MPMS SQUID magnetometer was used for low frequencies (0.02 to 10^3 Hz) and a Quantum Design PPMS for the frequency range 10 to 10^4 Hz.

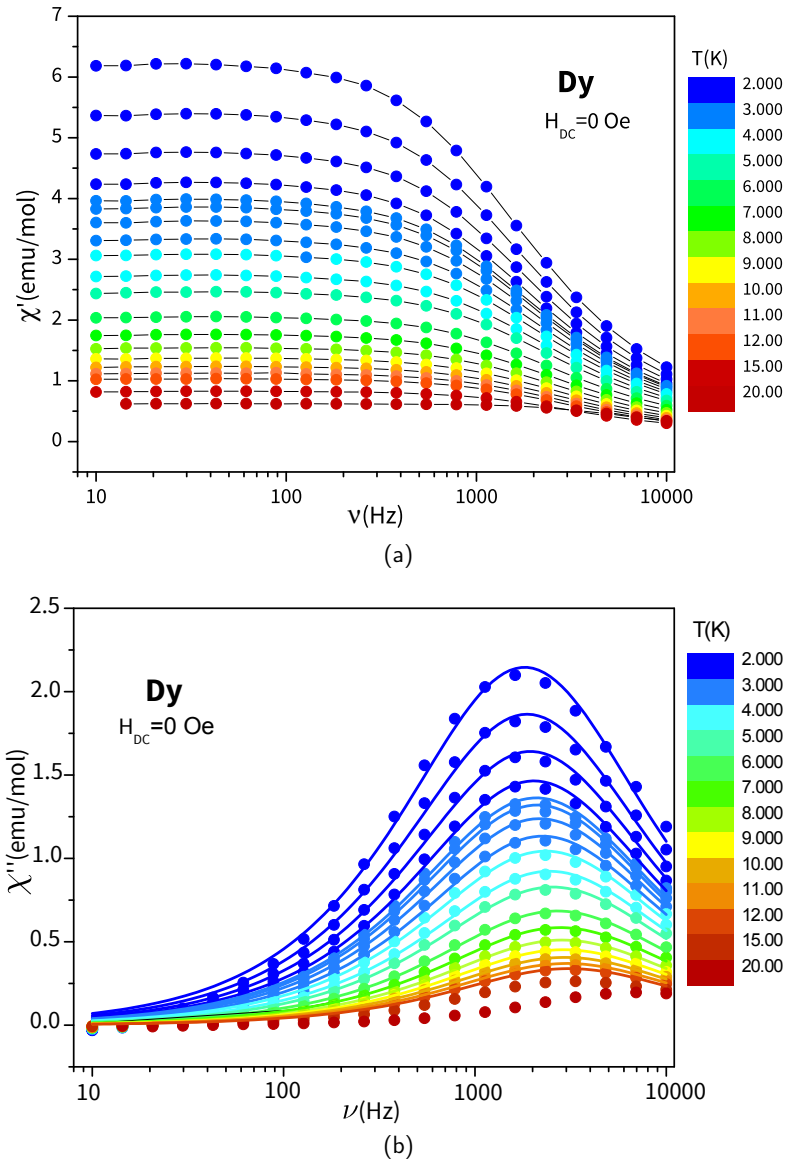

Figure S10: Upper panel: real susceptibility of **Dy** as a function of frequency for a temperature range 2 K to 20 K in zero applied field. Lower panel: imaginary susceptibility and fitting curves (solid lines) of **Dy** for a temperature range 2 K to 20 K.

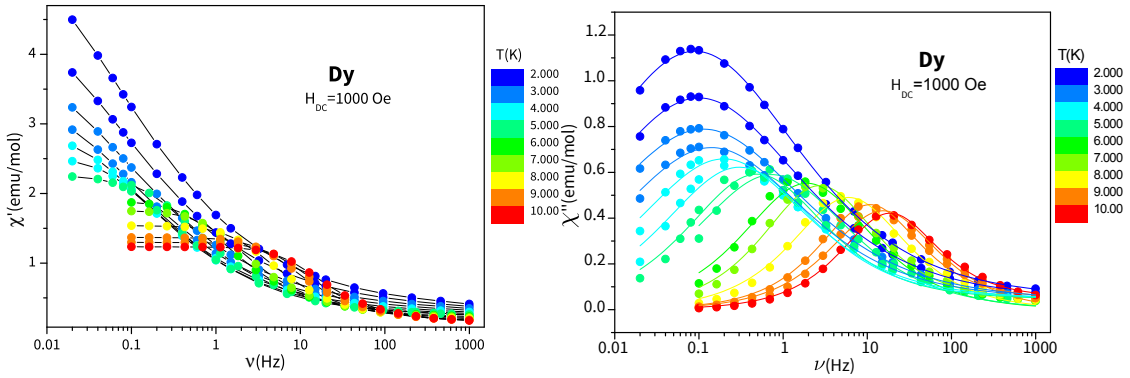

Figure S11: Upper panel: real susceptibility of **Dy** as a function of frequency for a temperature range 2 K to 10 K with an applied field of 1000 Oe. Lower panel: imaginary susceptibility and fitting curves (solid lines) of **Dy** for a temperature range 2 K to 10 K.

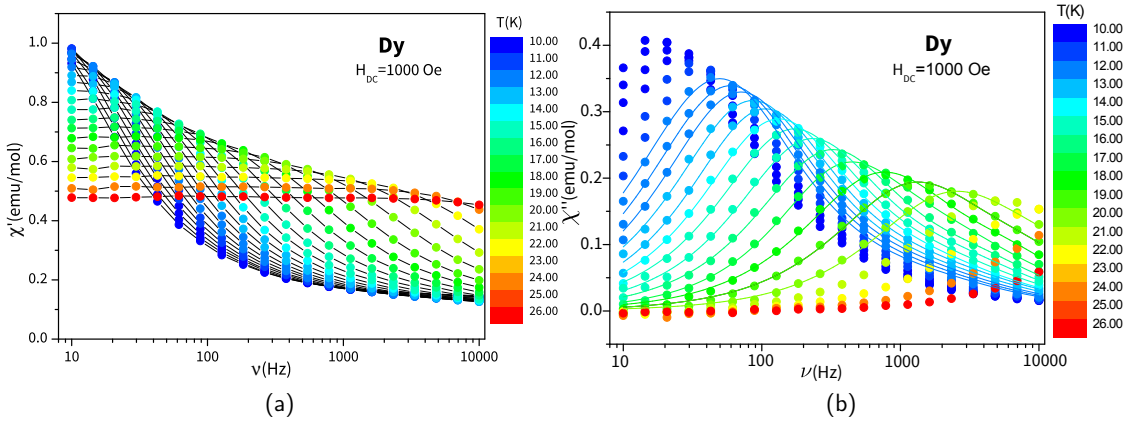

Figure S12: Upper panel: real susceptibility of **Dy** as a function of frequency for a temperature range 10 K to 20 K with an applied field of 1000 Oe. Lower panel: imaginary susceptibility and fitting curves (solid lines) of **Dy** for a temperature range 10 K to 20 K..

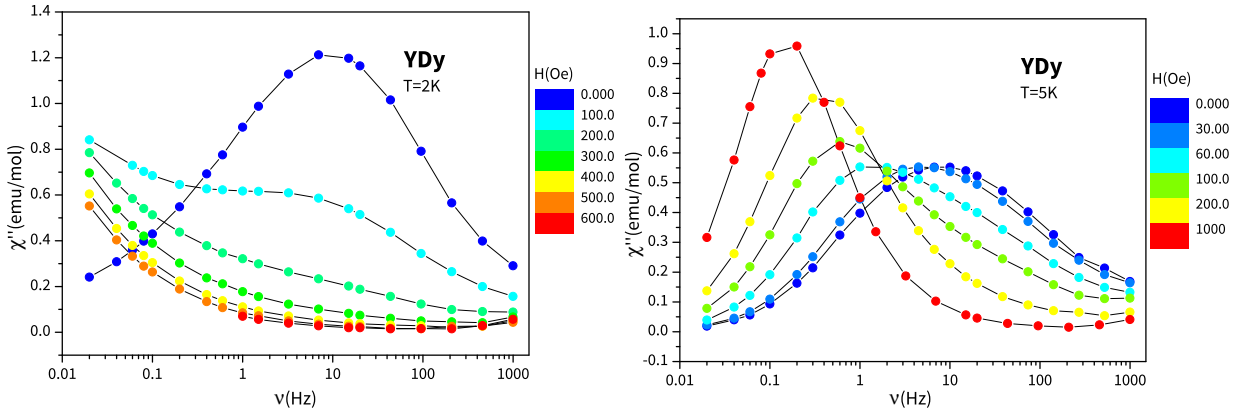

Figure S13: Left panel: imaginary susceptibility at 2 K for various applied field. The process in field could be recorded down to 0.02 Hz. Right panel: imaginary susceptibility at 5 K, the transition from the relaxation channel in zero field to the one in field is more rapid for the diluted compound compared to that of the pure one, see also fig. S9b.

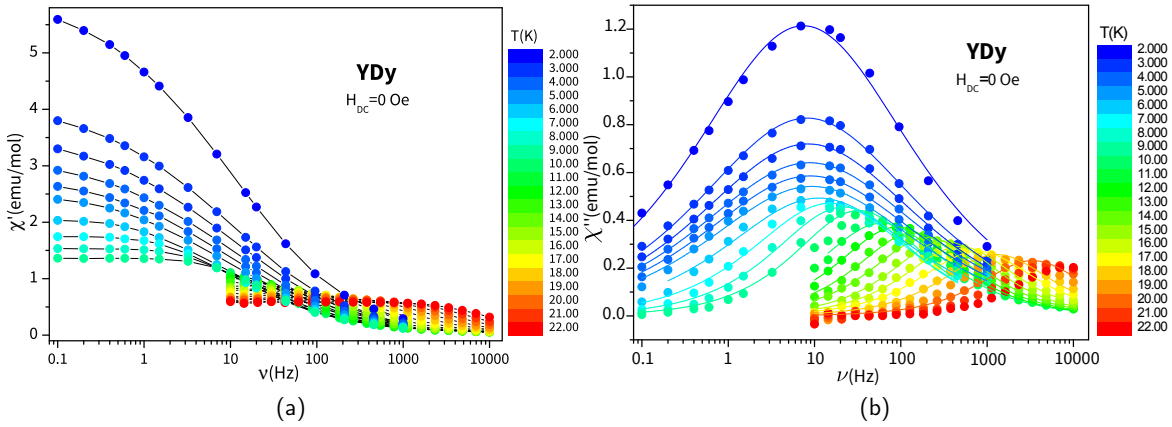

Figure S14: Upper panel: real susceptibility of **YDy** as a function of frequency for a temperature range 2 K to 22 K in zero applied field. Lower panel: imaginary susceptibility and fitting curves (solid lines) of **Dy** for a temperature range 2 K to 20 K.

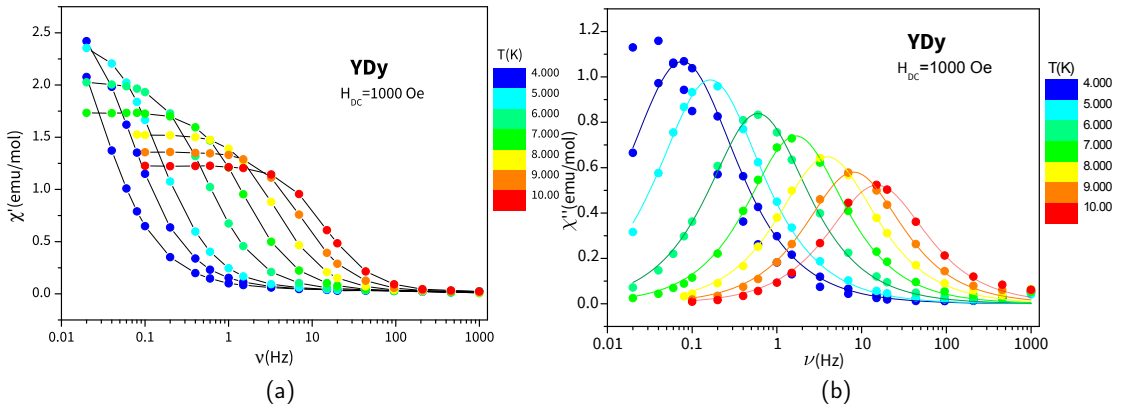

Figure S15: Left panel: real susceptibility of **YDy** as a function of frequency for a temperature range 2 K to 10 K with an applied field of 1000 Oe. Right panel: imaginary susceptibility and fitting curves (solid lines) of **YDy** for a temperature range 2 K to 10 K.

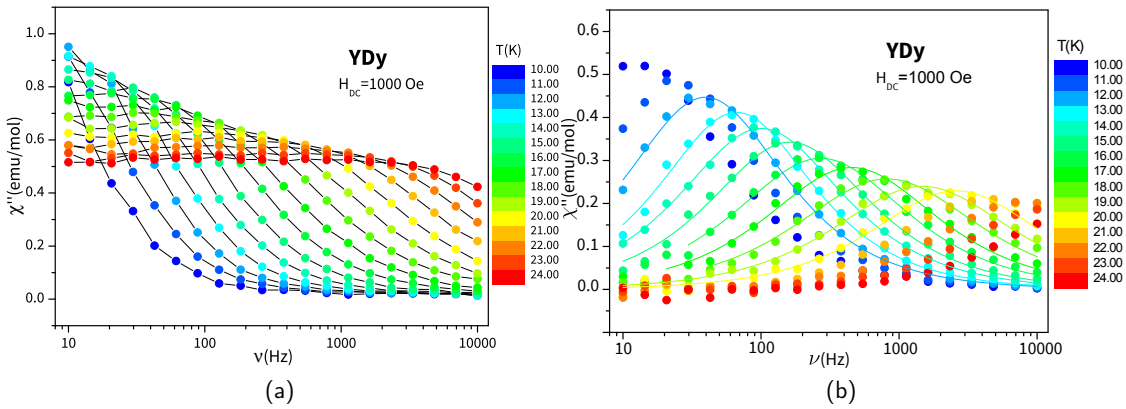

Figure S16: Left panel: real susceptibility of **YDy** as a function of frequency for a temperature range 10 K to 24 K with an applied field of 1000 Oe. Right panel: imaginary susceptibility and fitting curves (solid lines) of **YDy** for a temperature range 10 K to 20 K.

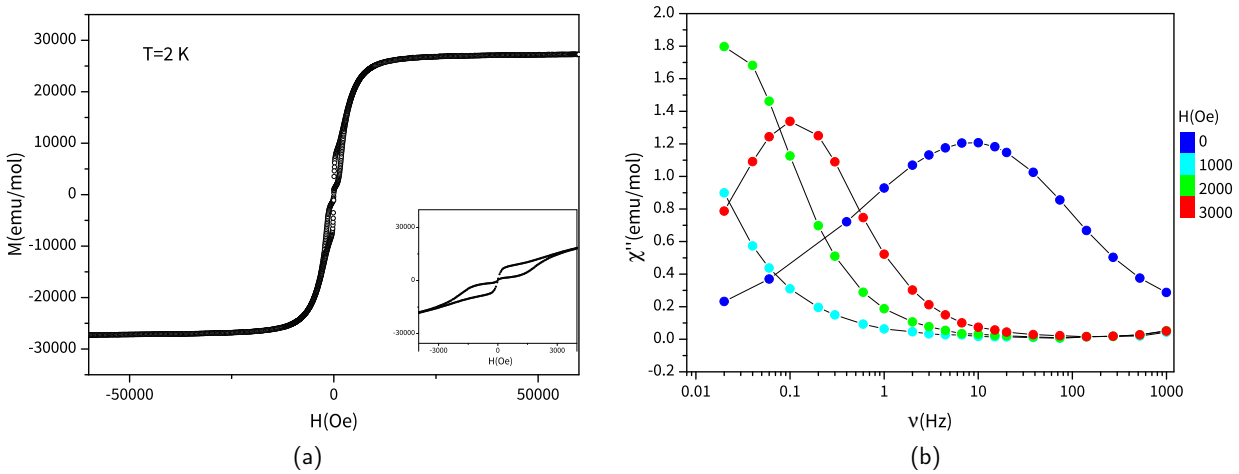

Figure S17: Left panel: compound **YDy** exhibits a butterfly shaped hysteresis at 2 K that is not longer visible above 4 K. Right panel: at 2 K the peak of imaginary susceptibility moves from higher frequencies in zero applied field to lower frequency when the field is applied up to a maximum of 1000 Oe. Afterwards the relaxation restarts to be faster.

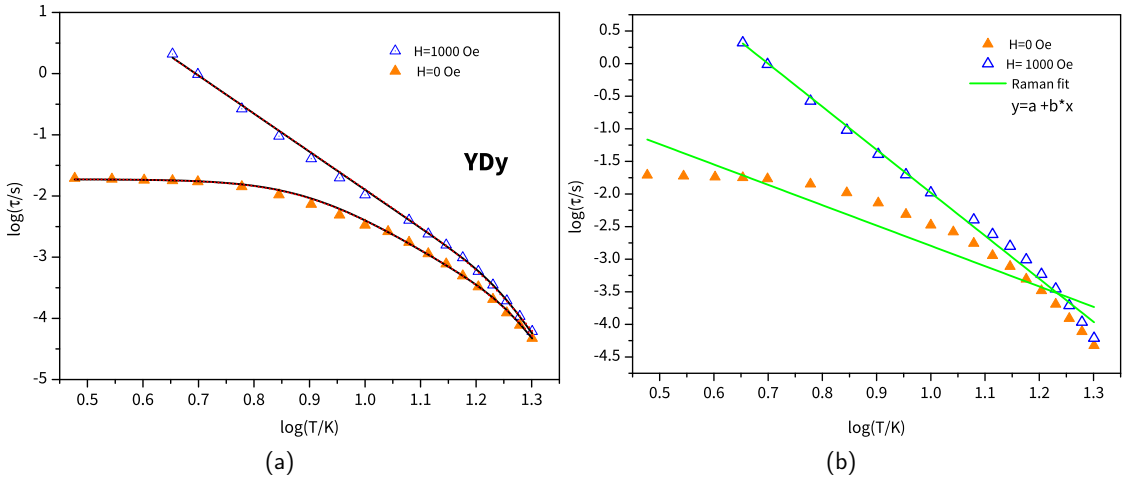

Figure S18: Left panel: log-log plot of the experimental relaxation time (symbols) for **YDy** along with the fitting curves (see eq. 3 in the main text): the black solid lines are the curves with $\Delta = 270$ K while for the red dotted ones the Δ parameter was left free to vary. Right panel: log-log plot of the experimental relaxation time (symbols) and the fits performed considering only a Raman contribution to relaxation. The value for the Raman exponent n is around 6.5 for the relaxation in field and around 3 for the relaxation in zero field.

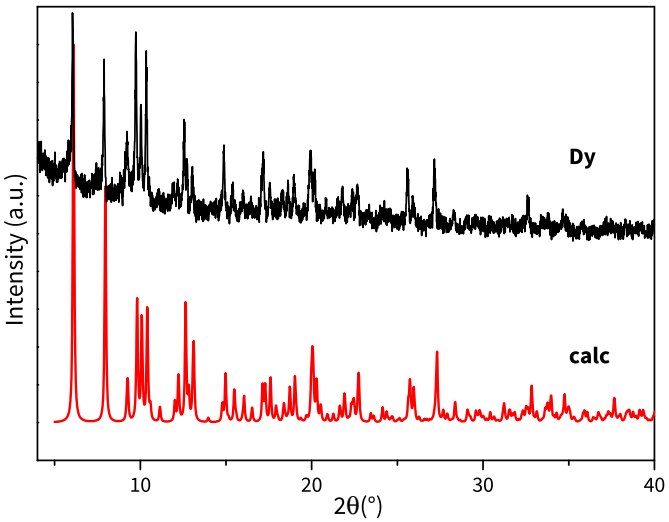

Figure S19: X-ray diffraction spectra of Dy(LH) · 3 dmf, the red line represents the calculated diffraction pattern for the reported molecular structure.

Bond	Å	Angle	\°
Dy1−N2	2.496(3)	O1 Dy1 N2	63.36(10)
Dy1−N3	2.574(3)	O3 Dy1 N5	63.08(10)
Dy1−N5	2.504(3)	O5 Dy1 N8	62.53(11)
Dy1−N6	2.577(3)	N2 Dy1 N3	63.97(11)
Dy1−N8	2.538(4)	N5 Dy1 N6	64.00(11)
Dy1−N9	2.696(4)	N8 Dy1 N9	61.13(12)
Dy1−O1	2.322(3)	O1 Dy1 O3	93.12(10)
Dy1−O3	2.344(3)	O1 Dy1 O5	145.17(10)
Dy1−O5	2.368(3)	O3 Dy1 O5	82.33(10)
		N2 Dy1 N5	112.69(10)
		N2 Dy1 N8	122.10(11)
		N5 Dy1 N8	125.20(11)
		N3 Dy1 N9	80.77(11)
		N6 Dy1 N9	88.30(11)

Table S1: Selected bond lengths and angles for **Dy**.

Capped square antiprism J10	Spherical capped square antiprism	Tricapped trigonal prism J51	Spherical tricapped trigonal prism	Muffin
2.693	1.370	2.755	2.131	1.988
C_{4v}	C_{4v}	D_{3h}	D_{3h}	Cs

Table S2: Agreement factors for different nine coordination polyhedra as obtained by SHAPE [2].

	Director Cosines		
	a	b	c^*
Option 1	−0.607	0.538	0.585
Option 2	−0.603	0.740	0.298
Option 3	−0.607	0.654	0.452
Option 4	−0.609	0.446	0.656
Option 5	−0.608	0.657	0.446

Table S3: Director cosines of the orientation of the easy axis calculated with Magellan [1] for different choices of charge distributions for ligand atoms, see also table S4.

	Charge				
Options	1	2	3	4	5
O1, O3, O5	−1	−0.5	−0.5	−0.75	−0.75
N1, N4, N7	0	−0.25	0	0	0
N2, N5, N8	0	−0.25	−0.25	0	−0.25
N3, N6, N9	0	0	−0.25	−0.25	0

Table S4: Different choice of charge distributions for ligand atoms used as input for Magellan: N1,N4 and N7 are the nitrogen which do not participate to the metal coordination; N2, N5 and N8 are the nitrogen coordinated to Dy and N3, N6 and N9 are pyridinic nitrogens.

Stevens' parameter					
	cm^{-1}		cm^{-1}		cm^{-1}
B_2^0	314.1	B_4^0	57.3	B_6^0	−21.7
B_2^1	−24.9	B_4^1	59.8	B_6^1	31.5
C_2^1	−24.9	C_4^1	−39.2	C_6^1	−23.2
B_2^2	−103.0	B_4^2	21.6	B_6^2	1.2
		B_4^3	13.5	B_6^3	33.9
		C_4^3	5.1	C_6^3	33.9
		B_4^4	−24.6	B_6^4	−8.2
				B_6^5	2.2
				C_6^5	−13.8
				B_6^6	−16.2
				C_6^6	32.3

Table S5: Crystal field parameters of the Crystal field Hamiltonian $\mathcal{H}_{CF} = \sum_{n,m} \alpha_n [B_n^m O_n^m + C_n^m W_n^m]$, where the operator O_n^m and W_n^m are defined in [3] and the α_n are the Stevens' coefficient for the lanthanide.

Energy Levels		(cm^{-1})
$^6H_{\frac{15}{2}}$	E_0	0
	E_1	195
	E_2	237
	E_3	289
	E_4	324
	E_5	371
	E_6	430
	E_7	478
$^6H_{\frac{13}{2}}$	E_8	3082
	E_9	3159
	E_{10}	3240
	E_{11}	3294
	E_{12}	3320
	E_{13}	3355
	E_{14}	3382

Table S6: Results of the calculations with RCC basis sets for $Dy(LH)_3$: energy splitting of the $^6H_{\frac{15}{2}}$ (ground) and the $^6H_{\frac{13}{2}}$ multiplets.

Principal g-values		a	b	c^*
			Ground Doublet	
g_x	0.0	0.505 440	0.587 959	−0.631 533
g_y	0.0	−0.679 770	−0.179 466	−0.711 130
g_z	19.8	−0.531 454	0.788 731	0.308 967
			First Excited Doublet	
g_x	0.5	0.655 910	0.696 041	−0.292 076
g_y	1.8	−0.460 955	0.062 932	−0.885 189
g_z	14.9	−0.597 747	0.715 239	0.362 121
			Second Excited Doublet	
g_x	0.1	0.390 680	−0.551 943	−0.736 701
g_y	2.2	0.651 787	0.731 000	−0.202 023
g_z	14.3	0.650 033	−0.401 246	0.645 336
			Third Excited Doublet	
g_x	1.5	−0.859 388	0.048 208	−0.509 047
g_y	3.7	−0.497 180	−0.311 322	0.809 871
g_z	12.1	−0.119 435	0.949 081	0.291 514
			Fourth Excited Doublet	
g_x	0.6	0.913 581	0.226 644	0.337 642
g_y	2.8	−0.374 290	0.144 034	0.916 057
g_z	13.8	0.158 987	−0.963 269	0.216 418
			Fifth Excited Doublet	
g_x	2.6	0.897 009	0.315 330	−0.309 745
g_y	4.5	0.047 565	0.627 828	0.776 897
g_z	8.8	0.439 446	−0.711 617	0.548 169
			Sixth Excited Doublet	
g_x	3.4	−0.369 322	−0.878 165	0.304 018
g_y	4.1	0.873 695	−0.439 584	−0.208 384
g_z	7.4	0.316 637	0.188 658	0.929 596
			Seventh Excited Doublet	
g_x	1.1	0.549 731	−0.830 355	−0.091 138
g_y	4.7	0.423 687	0.183 132	0.887 103
g_z	15.9	−0.719 920	−0.526 282	0.452 484

Table S7: Results of the calculations with RCC basis sets for $Dy(LH)_3$: value of the main magnetic axis of the eight doublets of the ground multiplet and their orientation in the crystalline frame.

	Basis set	
Atom	Label	Contraction
Dy	VTZP	[8s7p5d3f2g1h]
N	VTZP	[4s3p2d1f]
O	VTZP	[4s3p2d1f]
C	VDZP	[3s2p1d]
H	VDZ	[2s]

Table S8: Contractions of the ANO-RCC basis set used for *ab initio* calculations of $Dy(LH)_3$.

References

[1] N. F. Chilton, D. Collison, E. J. McInnes, R. E. Winpenny, A. Soncini, *Nat. Commun.* **2013**, *4*.

[2] M Llunell, D Casanova, J Cirera, J. Bofill, P Alemany, S Alvarez, M Pinsky, D Avnir, **2003**.

[3] L. F. Chibotaru, L. Ungur, *J. Chem. Phys.* **2012**, *137*, 064112.

C. $VO(dmp)_2$ paper

Chemical Science

EDGE ARTICLE

View Article Online
View Journal | View Issue

Cite this: *Chem. Sci.*, 2016, **7**, 2074

Quantum coherence in a processable vanadyl complex: new tools for the search of molecular spin qubits†

Lorenzo Tesi,[a] Eva Lucaccini,[a] Irene Cimatti,[a] Mauro Perfetti,[a] Matteo Mannini,[a] Matteo Atzori,[a] Elena Morra,[b] Mario Chiesa,[b] Andrea Caneschi,[a] Lorenzo Sorace*[a] and Roberta Sessoli*[a]

Electronic spins in different environments are currently investigated as potential qubits, *i.e.* the logic units of quantum computers. These have to retain memory of their quantum state for a sufficiently long time (phase memory time, T_m) allowing quantum operations to be performed. For molecular based spin qubits, strategies to increase phase coherence by removing nuclear spins are rather well developed, but it is now crucial to address the problem of the rapid increase of the spin–lattice relaxation rate, T_1^{-1}, with increasing temperature that hampers their use at room-temperature. Herein, thanks to the combination of pulsed EPR spectroscopy and AC susceptometry we evidence that an evaporable vanadyl complex of formula $VO(dpm)_2$, where dpm^- is the anion of dipivaloylmethane, presents a combination of very promising features for potential application as molecular spin-qubit. The spin–lattice relaxation time, T_1, studied in detail through AC susceptometry, decreases slowly with increasing temperature and, more surprisingly, it is not accelerated by the application of an external field up to several Teslas. State-of-the art phase memory times for molecular spin systems in protiated environment are detected by pulsed EPR also in moderate dilution, with values of 2.7 μs at 5 K and 2.1 μs at 80 K. Low temperature scanning tunnel microscopy and X-ray photoelectron spectroscopy *in situ* investigations reveal that intact molecules sublimated in ultra-high vacuum spontaneously form an ordered monolayer on Au(111), opening the perspective of electric access to the quantum memory of ensembles of spin qubits that can be scaled down to the single molecule.

Received 10th November 2015
Accepted 11th December 2015

DOI: 10.1039/c5sc04295j

www.rsc.org/chemicalscience

Introduction

The realization of a quantum computer is expected to trigger a second revolution in information and communication technology,[1–4] allowing for unequalled computation capabilities in disparate fields, ranging from structural biology[5] to quantum physics.[3] Quantum bits, or qubits, are at the basis of quantum computation, and different strategies to realize them are currently explored,[6] including ionic traps,[7] quantum dots in semiconductors,[8,9] photons,[10] and superconducting nanostructures.[11] Spins, either nuclear[12–14] or electronic,[15–19] are among the most efficiently addressable targets to build these logical units, as their initialization and read-out can be performed by well-established magnetic resonance techniques. The parameters to be optimized in the design of these qubits are: i) the longitudinal relaxation time, T_1, which corresponds to the lifetime of a classical bit that can assume either the $|0\rangle$ or the $|1\rangle$ value; ii) the characteristic time in which the spin loses the memory of the phase of the superposition state in which it has been prepared. A lower estimation of this decoherence time, T_2, can be extracted by the memory time, T_m, which is commonly measured with pulsed EPR or NMR: the ratio of T_m over the time necessary for an individual quantum operation has to be larger than 10^4 to allow for fault tolerant quantum computing.

In the field of electron spin-based qubits nitrogen vacancies in diamond[20,21] and impurities in silicon and silicon carbide[22] exhibit long-lived quantum coherence but present major challenges in the control of their organization and coupling to perform quantum logic operations. Molecular spin based qubits, on the contrary, can be organized on surfaces and the interaction between them tuned at will through a rational synthetic design. After an extensive research on polynuclear transition metal complexes[16,23,24] optimized to exhibit a long T_m, the research in this field has recently focused back on the

[a]*Department of Chemistry "Ugo Schiff", University of Florence & INSTM RU of Florence, Via della Lastruccia 3-13, 50019 Sesto Fiorentino, Italy*
[b]*Department of Chemistry, University of Turin & NIS Centre, via P. Giuria 7, 10125, Torino, Italy. E-mail: roberta.sessoli@unifi.it; lorenzo.sorace@unifi.it*

† Electronic supplementary information (ESI) available: Full experimental section and methods. Additional characterization including: AC susceptibility data (Fig. S1–S5); CW- and pulsed EPR results (Fig. S6–S11); STM and XPS of the UHV deposition (Fig. S12–S14); calculated field dependence of the eigenvectors composition (Fig. S15). See DOI: 10.1039/c5sc04295j

simplest spin $S = 1/2$ systems constituted either by organic radicals[25] or by 3d transition metal ions.[26–28] These have relatively long T_m, in particular at high temperature, because there are no excited spin levels that can foster the magnetic relaxation when thermally populated. In these systems the interaction of the electronic spin with the nuclear spins is the most relevant source of decoherence. Outstanding results have very recently been obtained with vanadium(IV) ions assembled with nuclear spin-free ligands.[27] When magnetic dilution is made in a nuclear spin-free solvent, such as CS_2, T_m approaches one millisecond at low temperature,[29] showing that molecular spin systems can be as performant as extended inorganic structures. Unfortunately this remarkable long coherence is rapidly lost on increasing temperature because the spin–lattice relaxation acts as a limiting factor for T_2.[30] A recent investigation has clearly evidenced that solid crystalline solutions can enhance T_1, thus resulting in enhanced coherence time at high temperature[26] but the mechanisms of relaxation, as well as strategies to enhance T_1, are still poorly investigated.

In this study we have investigated the magnetic relaxation of a simple mononuclear complex of vanadium(IV) by the combination of AC magnetic susceptometry to study spin–lattice relaxation with pulsed EPR spectroscopy to characterize the spin coherence. The two techniques can in fact shed light on different contributions to the relaxation but their association is unprecedented in the search for potential spin-based qubits.

The vanadyl complex $VO(dpm)_2$, where dpm^- is the anion of dipivaloylmethane, has been selected because the strong V=O bond is expected to increase the rigidity of the coordination sphere with a reduction of spin–lattice relaxation efficiency. The presence of β-diketonate ligands in a neutral complex imparts a high volatility that can be exploited to deposit the molecule on surfaces. An unexpected long T_1 over wide field and temperature ranges has been found to accompany T_m values that are among the longest ones observed in molecular species surrounded by spin active nuclei. The *in situ* morphological and spectroscopic characterization of a monolayer deposit of $VO_2(dpm)_2$ on Au(111) suggest that the molecules are intact on the surface, making these simple units potential candidates as molecular qubit individually addressable by scanning probe techniques.

Results and discussion

The synthesis of crystalline $VO(dpm)_2$ was achieved according to an earlier reported procedure,[31] operating under inert atmosphere to avoid oxidation. $VO(dpm)_2$, prepared in the crystalline form and characterized by X-ray diffractometry (see ESI†), presents a typical square pyramidal coordination (Fig. 1) with a short V=O double bond (1.59 Å *vs.* an average of 1.964 Å for the V–O single bonds). Deviations from tetragonal symmetry are already visible in the first coordination sphere in both bond lengths and bond angles. Given that the system crystallizes in the monoclinic $P2_1$ space group, two sets of molecules with the V=O directions forming an angle of 64.1° are present in the crystal lattice. The strongly axial ligand field produced by the short V=O bond removes orbital degeneracy with the d_{xy} orbital being the lowest in energy and the only one to be half occupied.

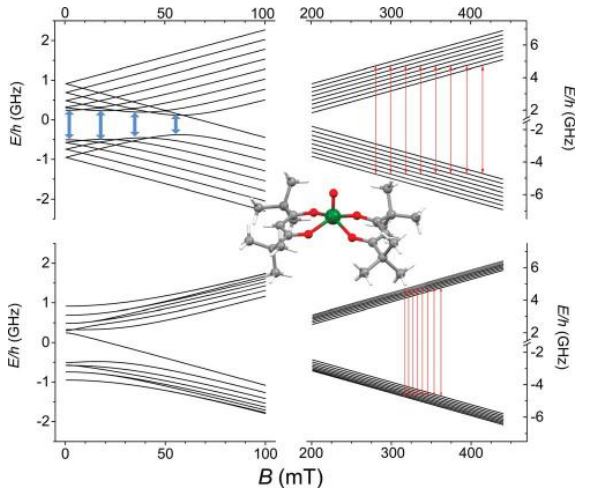

Fig. 1 Zeeman splitting of the $S = 1/2$, $I = 7/2$ manifold calculated with the field applied along the largest hyperfine coupling component (upper) and along the smallest (lower) (parameters in the text). Red lines correspond to the observed X-band (ν = 9.62 GHz) EPR transitions while in pale blue are drawn the potential low frequency transitions at the avoided level crossings. In the inset the molecular structure of $VO(dpm)_2$.

Vanadyl systems are therefore well described by a spin $S = 1/2$ with slightly anisotropic $\boldsymbol{g}$ tensor close to the free electron value. The most abundant isotope of vanadium, ^{51}V (99.75%), is characterized by $I = 7/2$ thus the $S = 1/2$ doublet is further split in 16 states by hyperfine interaction as schematized in Fig. 1.

Magnetization dynamics

The magnetization dynamics, investigated by AC-susceptometry (see ESI†), of a polycrystalline sample of $VO(dpm)_2$, hereafter **1**bulk, revealed no imaginary component of the susceptibility in zero static field down to the lowest investigated temperature (1.9 K). The application of a weak field induced however slow relaxation of the magnetization with the concomitant decrease of the real component χ' and the appearance of a peak in χ'' component (ESI Fig. S1†). In a field of 0.2 T the entire magnetization of the system relaxed slowly and this field was selected to investigate the temperature dependence of the relaxation time.

Maxima in χ'' were observed up to 80 K for frequencies lower than 10 kHz, as shown in Fig. 2a (ESI Fig. S2† for χ'), evidencing also a gradual increase in the width of the distribution on lowering the temperature (see ESI and Fig. S3†). Such a high temperature slow relaxation is usually observed in molecules exhibiting strong magnetic anisotropy known as Single-Molecule Magnet (SMMs), for instance in double-decker $TbPc_2$ complexes,[32] but clearly it has a different origin here. The data, reproduced with the Debye model,[33] allowed to extract the relaxation time of the susceptibility, τ, reported in Fig. 2b. It is evident that τ does not follow the Arrhenius behaviour, in agreement with the lack of electronic/magnetic states that can be thermally populated providing a path for the multiphonon

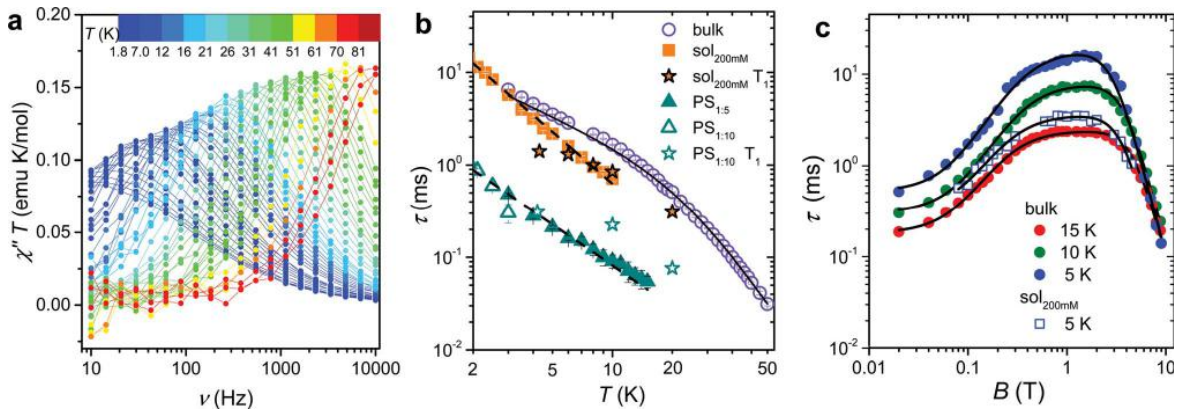

Fig. 2 (a) Frequency dependence of the imaginary component of the AC susceptibility of **1**bulk in $B_{dc} = 0.2$ T multiplied by temperature to be readable in the whole 2–80 K temperature range. (b) Temperature dependence of the relaxation time of the magnetic susceptibility measured in $B_{dc} = 0.2$ T for the pure and the diluted samples of **1**: two dispersions in polystyrene with 1 : 5 and 1 : 10 mass ratio and a 200 mM CH_2Cl_2 : toluene frozen solution (see legend). The black solid line corresponds to the best-fit of **1**bulk data using eqn (1), while the broken lines correspond to simulation with T^{-n} law. T_1 for the diluted sample, extracted from pulsed EPR spectra, are shown for comparison. (c) Field dependence of the relaxation time of the magnetic susceptibility of **1**bulk and **1**$sol_{200\ mM}$ frozen solution sample (see legend). The solid lines represent the best fit obtained with eqn (3). Best fit parameters are reported in Table 1.

Orbach mechanism of relaxation.[34,35] On the contrary the temperature dependence of τ can be reproduced by considering different contributions to the relaxation rate:

$$\tau^{-1} = aT + bT^n \quad (1)$$

where the first term ($a = 59 \pm 2\ s^{-1}\ K^{-1}$) corresponds to the direct mechanism, dominating at low temperature, and the second one ($b = 0.052\ s^{-1}\ K^{-n}$) to a Raman-like, *i.e.* a multi-phonon process involving virtual excited states.[34] Interestingly the exponent $n = 3.22 \pm 0.02$ is much smaller than the value of 9 or higher expected for the Raman process,[35] but approaches the value of 3 predicted in the case that both acoustic (lattice) and optical (molecular) vibrations are involved in the process.[34]

To shed light on the mechanisms of magnetic relaxation the AC susceptibility was investigated in a wide field range, *i.e.* up to 8.8 T, for three different temperatures, 5, 10, and 15 K. Notice that in this temperature range the direct process dominates as indicated by the almost linear dependence of τ^{-1} on T. The corresponding relaxation times are reported in Fig. 2c. The initial increase of τ for weak applied field is followed by an almost flat region that extends up to *ca.* 4 T, followed by a rapid decrease at higher fields. Data of Fig. 2c were reproduced considering different relaxation mechanisms that can be active in $S = 1/2$ systems. According to the seminal work done by de Vroomen *et al.* on the Cu^{2+} Tutton salt,[36] two contributions to the relaxation rate can be considered:

$$\tau^{-1} = {\tau_Z}^{-1} + {\tau_{int}}^{-1} \quad (2)$$

The first term represents the direct mechanism between the two states split by the Zeeman energy, which is expected to vanish in zero field as a result of the Kramers theorem.[37] In fact, a pure and isolated $S = 1/2$ should not be able to relax in zero field. The second term takes into account a sort of internal field whose origin can be either intramolecular (*i.e.* hyperfine interactions) or intermolecular (*i.e.* due to dipolar or exchange interactions). The latter is responsible for the efficient relaxation in zero field and presents, for the direct mechanism,[38] a field dependence that is similar to the Brons-van Vleck formula developed to describe the Raman process in concentrated systems.[39] Summing up the two contributions to the field dependence in eqn (2) the data of Fig. 2c have been reproduced according to:

$$\tau^{-1} = cB^4 + d\frac{1 + eB^2}{1 + fB^2} \quad (3)$$

The first term is the typical field dependence of the direct process for a $S = 1/2$ spin and reflects the fact that the larger is the Zeeman splitting between the states the higher is the density of phonons matching it. In the second one the d term represent the zero field relaxation rate, similar to the tunnelling rate in SMMs,[33] the f parameter takes into account the ability of the external field to suppress these mechanisms, while the e parameter, strongly dependent on the concentration of the spin centres, takes into account the field effects on the relaxation of interacting spins.[39] The best-fit values obtained with eqn (3) are summarized in Table 1. The c parameter for $T = 5$ K should be considered with caution because only a small fraction of the susceptibility is detected at such high fields. The field range where the relaxation remains slow is really remarkable, suggesting that the direct mechanism of relaxation is not very efficient.

In ESI Fig. S3 and S4† we also report the temperature and field dependence of the width of the distribution of relaxation rate, respectively. The width is correlated to the parameter α of the extended Debye formula (see ESI†). In general the

Table 1 Best-fit parameters of eqn (3) used to reproduce the field dependence of the magnetization relaxation rate of **1**bulk measured at the three investigated temperatures and of **1**sol$_{200\ mM}$ at 5 K (last row)

T (K)	c (T^{-4} s^{-1})	d (s^{-1})	e (T^{-2})	f (T^{-2})
5	0.96 ± 0.04	2060 ± 180	7.6 ± 0.7	240 ± 30
10	0.73 ± 0.01	3460 ± 150	7.6 ± 0.4	179 ± 12
15	0.97 ± 0.03	5740 ± 270	15.1 ± 0.9	190 ± 16
5	2.00 ± 0.11	3600 ± 550	13.7 ± 1.4	160 ± 40

distribution is quite narrow increasing up to 0.3 at the lowest temperature (ESI Fig. S3†). The decrease of α with increasing fields, see ESI Fig. S4,† is indicative that τ_{int}^{-1} is more sensitive to the local environment, as indeed expected. The non-monotonous trend at low temperature suggests the presence also in this powdered sample of a moderate phonon-bottleneck effect.[40]

The long spin–lattice relaxation time of VO(dpm)$_2$, above 10 ms at low temperatures, suggests that also decoherence times can be comparatively long. The latter are however accessible only by pulsed EPR techniques and require narrow lines that can be achieved in diluted systems. Unfortunately, extensive efforts to prepare the titanyl-based diamagnetic analogue failed due to the instability of the mononuclear species TiO(dpm)$_2$ in favour of the dimeric one [TiO(dpm)$_2$]$_2$,[41] thus precluding the preparation of isomorphous crystalline solid solutions. As an alternative, two dispersions of **1** in polystyrene with mass ratio 1 : 5, **1**PS$_{1:5}$, and 1 : 10, **1**PS$_{1:10}$, as well as a frozen 200 mM solution of **1** in a 2 : 3 CH_2Cl_2 : toluene mixture (**1**sol$_{200\ mM}$), were prepared and investigated by AC susceptometry (Fig. S5†). This was aimed at getting information on the relaxation time of the magnetic susceptibility to be compared to T_1 extracted from pulsed EPR data. Even if a reduced range of temperature and fields are accessible on the diluted samples for instrumental reasons, it is well evident that also diluted samples show slow relaxation of the magnetization (Fig. 2b): polymeric dispersions are characterized by a relaxation rate which is *ca.* 20 times faster than bulk sample, with minor difference between the two concentrations, suggesting that matrix effects to the relaxation dominate over those induced by dilutions. On the other hand, the low temperature relaxation rate of the frozen solution is comparable to the bulk phase but increases much faster on increasing temperatures. The almost linear temperature dependence in the log(τ) *vs.* log(T) plot of Fig. 2b allowed to analyse the data as $\tau^{-1} \propto T^n$, with n = 1.49 ± 0.04 for **1**PS$_{1:5}$ and n = 1.86 ± 0.04 for **1**sol$_{200\ mM}$. Exponents larger than one for the direct mechanism are generally attributed to spin–phonon bottleneck effects,[34] which are expected to be more relevant for these samples that have a small contact-surface with the helium bath than the ground microcrystalline powder of the bulk sample.[40] The field dependence of τ of **1**sol$_{200\ mM}$ was also investigated at T = 5 K (see Fig. 2c) and revealed the same wide plateau observed in the bulk phase, thus indicating that, despite some matrix effects, this interesting feature is an intrinsic property of the structure of the molecule. Unfortunately, a more direct comparison between the parameters reported in Table 1 for bulk and diluted samples would only be possible for a solid crystalline solution.

Continuous wave and pulsed EPR spectroscopy

The low temperature CW-EPR X-band spectrum of a frozen 1 mM solution of **1** (**1**sol$_{1\ mM}$) is shown in Fig. 3a. Similar features are observed for the other investigated samples (**1**bulk, **1**PS$_{1:5}$, **1**PS$_{1:10}$, and **1**sol$_{200\ mM}$ spectra available in ESI Fig. S6†), the effect of concentration being mirrored by the narrowing of the EPR lines when going from pure sample to dispersions and frozen solutions. On the other hand, the position of the lines is not varying, indicating that the spin Hamiltonian parameters, and then the electronic structure, are maintained in different environments.

The spectra clearly show the features due to the anisotropic hyperfine coupling of the electron spin to the I = 7/2 nuclear spin of ^{51}V: at the high and low field extreme region, peaks due to the parallel components of the hyperfine structure are observed, whereas in the centre the closely spaced perpendicular ones are evident, as schematized by the resonant fields in Fig. 1.

Spectral simulations were performed[42] on the basis of the following spin Hamiltonian:

$$\mathcal{H} = \hat{I}\cdot\boldsymbol{A}\cdot\hat{S} + \mu_B\hat{S}\cdot\boldsymbol{g}\cdot B \quad (4)$$

providing as best-fit parameters: g_x = 1.9880(2); g_y = 1.9815(3); g_z = 1.9490(2) and A_x = 0.0056(1) cm^{-1} (167.9 MHz); A_y =

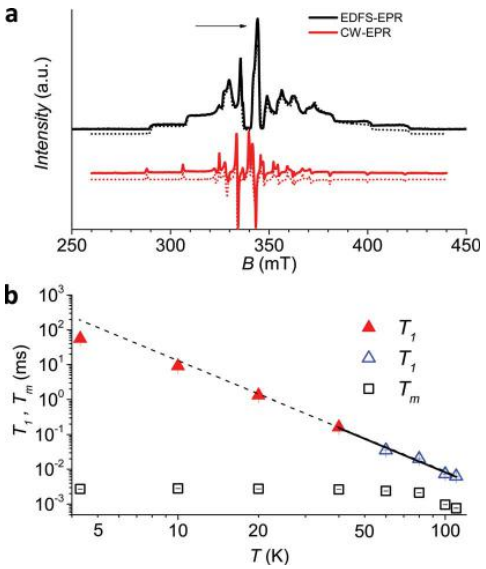

Fig. 3 (a) Echo detected (black trace) and CW (red trace) experimental EPR spectra of **1**sol$_{1\ mM}$, measured at 5 K, and best simulations (dotted traces). The arrow marks the field position of T_1 and T_m determination. (b) Temperature dependence of T_1 and T_m for **1**sol$_{1\ mM}$ sample. Full symbols refer to experiments of echo saturation by fast repetition, empty ones to inversion recovery experiments (see ESI† for details). The solid line corresponds to the best-fit of the high temperature data with $T_1 \propto T^{-n}$.

0.0063(3) cm^{-1} (190.4 MHz); $A_z = 0.0170(2)$ cm^{-1} (509.6 MHz). These parameters are in the range previously reported for VO^{2+} β-diketonate-type derivatives[43,44] and are consistent with the slight structural rhombicity observed by X-ray diffractometry. These spin Hamiltonian parameters have been employed to draw the Zeeman diagrams reported in Fig. 1.

An echo-detected field-swept EPR spectrum (EDFS) was recorded using the standard Hahn sequence (see ESI†) for $\mathbf{1}sol_{200\ mM}$, $\mathbf{1}sol_{1\ mM}$, and $\mathbf{1}PS_{1:10}$ diluted samples (Fig. 3a and ESI Fig. S7†). The observation of a spin-echo is a first indication that quantum coherence is observed in these samples. Further, the same spin Hamiltonian parameters used for the simulation of the CW spectrum yielded good simulations of the EDFS spectrum, confirming that the entire $VO(dpm)_2$ sample is experiencing the detected coherence.

Determination of the potential applicability of diluted samples of **1** as molecular qubit was performed by measuring the coherence time, T_m, as a function of temperature and field position for $\mathbf{1}sol_{1\ mM}$ to reduce spin–spin interactions. To maximize the observed echo the temperature dependence of T_m has been investigated on the so-called powder like line evidenced by an arrow in Fig. 3a.

The echo decay traces (Fig. 4a) were then fitted using a stretched-exponential equation:

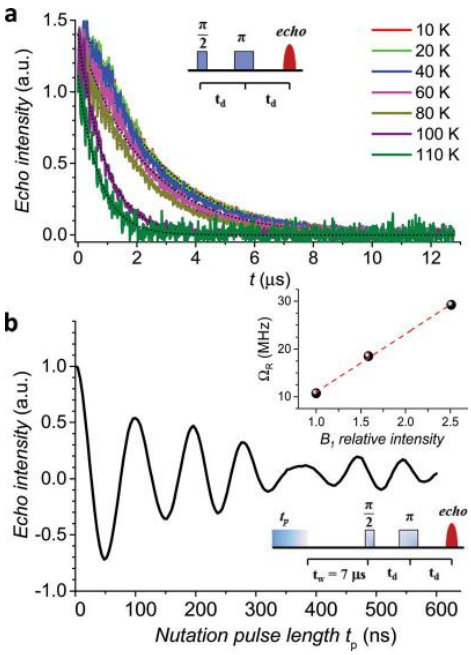

Fig. 4 (a) Pulsed EPR Hahn echo decay traces for $\mathbf{1}sol_{1\ mM}$ at different temperatures recorded at 343 mT. In the inset the employed pulse sequence. (b) Rabi oscillations for $\mathbf{1}sol_{1\ mM}$ recorded at 4.3 K at 10 dB microwave attenuation. The change in oscillations observed at t_p > 400 ns is due to the interaction between the electron spin and surrounding protons.[48] In the inset the Rabi frequency (Ω_R) *vs.* oscillating field intensity superimposed to the linear best-fit.

$$y = y_0 + k_m \exp[-(2t/T_m)^{\beta_m}] \quad (5)$$

It is evident that between 4 K and 80 K the resulting T_m values (Fig. 3b) are almost temperature independent (varying from 2.7 μs to 2.1 μs). Above 80 K the softening of the solvent glassy matrix, and consequently of the *tert*-butyl groups of the ligands, opens new relaxation pathways leading to the loss of echo above 110 K. The temperature dependence of β_m parameter essentially follows the same pattern, being slightly larger than 1 at 5 K and approaching a mono-exponential decay above 80 K (Fig. S8†). This behaviour suggests that decoherence is essentially dominated by physical motions of the magnetic nuclei.[45]

In agreement with the long coherence time observed at low temperature, Rabi-like oscillations of the echo intensity were observed for $\mathbf{1}sol_{1\ mM}$ in nutation experiments performed at different microwave powers as shown in Fig. 4b, where the observed linear dependence of the Rabi oscillation on the intensity of the oscillating field is reported in the inset. This indicates the possibility of creating any arbitrary superposition of states, thus fulfilling one of the two main requirements for creating universal quantum gates.[46]

Since earlier studies revealed strong correlation between the spin–lattice relaxation time T_1 and T_m for some molecular species candidate for quantum information processing (QIP),[26,30] we determined the temperature dependence of T_1 between 5 K and 110 K in $\mathbf{1}sol_{1\ mM}$, for which the AC susceptibility technique does not have the necessary sensitivity.

Given the large range of relaxation times two different experimental procedures were applied: at low temperature (5–60 K) the echo saturation by fast repetition, suitable for long relaxation times[47] was used, whereas at higher temperature the standard inversion recovery procedure was applied (see ESI† for details). Saturation recovery traces have been fitted using the following equation:

$$y = y_0 + k_1 \exp(-t/T_1)^{\beta_1} \quad (6)$$

with best-fit stretched parameter β_1 being in the range 0.6–0.9 in the investigated temperature range (ESI Fig. S9†). The results (Fig. 3b), consistent with those previously reported by Eaton *et al.* for $VO(acac)_2$ in H_2O:glycerol solution,[43] indicate that quite long values of T_1 are observed at low temperature (50 ms at 4 K) and on heating T_1 tends toward T_m (6 μs at 110 K). Interestingly, a T^{-n} dependence with $n = 3.2 \pm 0.2$ is observed above 40 K, with a gradual decrease of n at lower temperatures, in agreement with AC susceptibility results.

To have a more quantitative comparison we also measured the temperature dependence of the spin–lattice relaxation time for $\mathbf{1}sol_{200\ mM}$ by pulsed EPR: the obtained results are consistent with those obtained by AC susceptibility (Fig. 2b), confirming that the two techniques are actually probing the same process.

As a final test to establish whether this molecule maintains its long decoherence time in a solid matrix not affected by the melting of the frozen solution we measured the temperature dependence of relaxation times for $\mathbf{1}PS_{1:10}$. Remarkably, for

this relatively concentrated sample it is possible to observe an echo and measure T_m up to 220 K (Fig. S10†). In particular while T_m is 0.36 μs at 4.3 K, *i.e.* about one order of magnitude faster than for **1**sol$_{1\ mM}$, at the highest measured temperature a T_m value of 0.1 μs could be determined.

Deposition on Au(111) and *in situ* characterization

The high volatility of VO(dpm)$_2$ was here exploited to obtain thick films as well as sub-monolayer (ML) deposit assembled on the Au(111) surface. A complete *in situ* X-ray photoelectron spectroscopy (XPS) and low temperature scanning tunnelling microscopy (STM) characterization was carried out, while the stability of the sample toward oxidation was investigated by exposing a thick film to air. Fig. 5 reports the STM topography obtained at $T = 30$ K for sub-ML coverage. As observed for other complexes with dpm$^-$ ligands,[49,50] the molecules weakly interact with the substrate and form patches of variable size constituted by regularly packed molecules. The islands present regular boundaries maintaining the herringbone modulation of the gold substrate. Sub-molecular resolution was hard to achieve inside the patches, though isolated features were visible at the kinks of the herringbone structure.

The height of the molecular layer is 0.27 ± 0.02 nm (ESI Fig. S12†), in good agreement with similar deposits obtained with iron β-diketonate complex,[49] though no reports are available on VO(dpm)$_2$. By increasing the deposition time full coverage was achieved: regularly packed molecules still revealing the herringbone structure underneath were found (ESI Fig. S13†). Interestingly, as in the case of Fe(dpm)$_3$,[49] no additional molecular layer can be deposited at the employed low deposition rates (see ESI†).

In order to check if the complex is intact on the surface, the full monolayer deposit was investigated by XPS, revealing the presence of the expected elements (see Fig. 6).

The observed broad O 1s peak around 532 eV was reproduced by considering two components. The smaller one at 531.3 eV was attributed to the oxygen of the vanadyl group ($O_{V=O}$), in good agreement with what observed for vanadyl phthalocyanine, VOPc, on Ag(111),[51,52] while the larger one at 532.1 eV, was

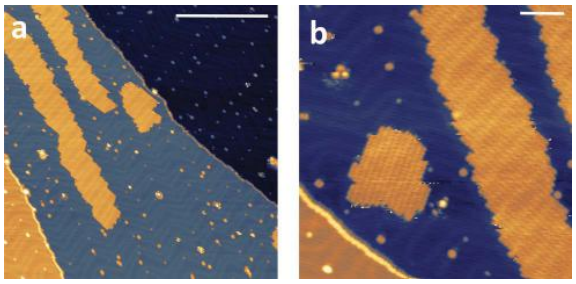

Fig. 5 STM images of a sub-monolayer deposition of VO(dpm)$_2$ measured at 30 K. Bias voltage = −2 V (empty states), tunnelling current = 5 pA. The scanned regions are 150 × 150 nm^2 in (a) and 60 × 60 nm^2 in (b) and the bars correspond to 50 nm and 10 nm, respectively.

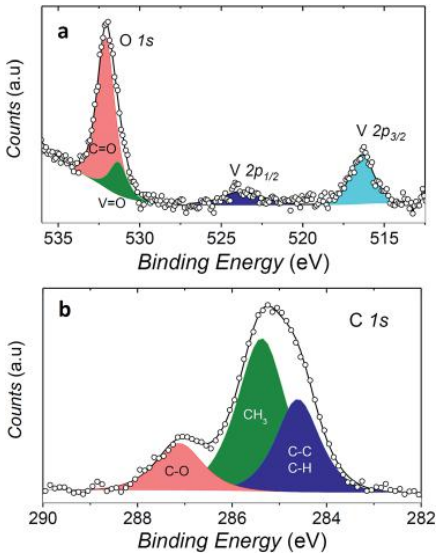

Fig. 6 XPS spectra of a monolayer coverage of **1** on Au(111). The O 1s and V 2p regions are shown in (a) while the C 1s region in (b). Filled area and lines represent the best fit components and resulting spectra, respectively.

associated to the oxygen atoms of the two dpm$^-$ ligands ($O_{C=O}$). The ratio of the area of the two peaks is close to 1 : 4, as expected for the stoichiometry of the molecule, thus confirming the integrity of the complex on surface. An analogous analysis allows to distinguish three components contributing to the C 1s region: the carbonylic carbon (287.2 eV), methyl carbon (285.4 eV) and the third one regrouping the remaining carbons (CH, CC, at 284.6 eV).

Even more interestingly the vanadium photoelectron peaks allowed to provide specific hints on the oxidation state of this element and thus on possible interaction with the metal surface. The V 2p$_{3/2}$ was observed at 516.4 eV, showing a distance to the oxygen peak $\Delta E(O_{V=O}\ 1s - V\ 2p_{3/2})$ of 14.9 eV which well compares with that observed in VOPc monolayer and multilayers ($\Delta E(O_{V=O}\ 1s - V\ 2p_{3/2}) = 14.6$ eV).[51] A semi-quantitative analysis of the composition according to the integrated peak signals gave for the three investigated elements the molar composition C = 81 ± 4%, O = 16 ± 1%, V = 2.6 ± 0.6% that well compares with the theoretical one (C = 78.6%, O = 17.9%, V = 3.6%).

These observations indicate that the VO(dpm)$_2$ molecules can be deposited intact on the surface and features a weak interaction with the gold substrate as the only occupied d orbital, d_{xy}, is expected to lie flat with limited overlap with the substrate orbitals. A similar scenario was observed for copper(II) phthalocyanine molecules that are known to retain their unpaired electron in the $d_{x^2-y^2}$ orbital.[53] In the vanadyl derivative VOPc the metal atom is slightly above the plane of the equatorial oxygen atoms; the distance of the metal ion from the surface is therefore further increased thus reducing the interaction with the substrate. It is thus not surprising that

synchrotron-based experiments on monolayers of VOPc on Ag(111)[51] detected a substantially unchanged magnetism of the $S = 1/2$ of V^{IV} compared to thicker films. It is therefore reasonable to envisage that $VO(dpm)_2$ molecules retain their paramagnetic nature when in contact with the gold substrate. This system represents therefore an appealing alternative to the use of N-donors phthalocyanine- and porphyrin-based systems for deposition on surfaces, though $VO(dpm)_2$ films resulted somehow instable in air: *ex situ* prepared thick films of about 150 nm showed a partial surface oxidation as suggested by the decrease in the ($\Delta E(O_{V=O}\ 1s - V\ 2p_{3/2})$) value accompanied by a progressive shift of the V 2p peak (ESI Fig. S14†).

Comparison with other molecular spin qubits

AC-susceptometry is currently widely employed to evidence slow relaxation in SMMs characterized by easy axis anisotropy and large magnetic moments; however, Luis *et al.*[54] have recently used this technique to characterize in detail the dynamics of a pseudo spin-doublet resulting from the large easy plane anisotropy of the $S = 3/2$ of Co^{II} in $Co(acac)_2(H_2O)_2$.[54] The role of hyperfine interaction and of the coupling of the nuclear spins with the phonon bath has been found to contribute to the opening of relaxation pathways otherwise forbidden in zero field for a pure $S = 1/2$ due to time reversal symmetry. $VO(dpm)_2$ corresponds exactly to the hyperfine-split $S = 1/2$ model recently developed[54] and indeed analogies in the magnetic behaviour of the two molecular systems are observed. In zero static field the hyperfine interaction with the $I = 7/2$ gives origin to two sets of states characterized by $F = |S \pm I|$ with multiplicity 9 and 7, respectively, as can be observed in Fig. 1. The isotropic hyperfine coupling is responsible for the gap between $F = 4$ and $F = 3$ states, which are however further split by the anisotropic components of the hyperfine tensor (see eqn (4)). The application of a weak static field has a different effect when applied along the molecular z direction, the one of largest hyperfine interaction corresponding to the V=O bond direction, or perpendicular to it, as also indicated in the eigenvectors composition (ESI Fig. S15†).

If similar features were already observed in the $Co(acac)_2(H_2O)_2$ *pseudo*-spin $S = 1/2$ system, some striking quantitative differences are evident. The first one is that the relaxation time remains long over a wide field range, *ca.* 30 times larger in $VO(dpm)_2$ compared to the Co^{II} derivative. At 5 K, where the relaxation is still governed by the direct mechanism, the relaxation rate starts to grow above 3 T, to be compared to the drastic 0.1 T upturn observed for Co^{II} at 1.8 K.[54] The comparison with early works on the dynamics of Cu^{II} spins[36] confirms that the field stability of slow relaxation of $VO(dpm)_2$ is unprecedented. This is extremely appealing for technological applications as it allows to exploit higher frequencies to coherently manipulate the spins, *e.g.* at W-band, corresponding to 95 GHz, with significant improvement of sensitivity. Moreover, working at W-band was also shown to increase T_m in samples of Yb^{3+} diluted in $CaWO_4$, though at the same time the larger field was found to reduce T_1. This serious drawback of the use of high frequencies is not expected for $VO(dpm)_2$.[55]

The origin of the striking difference between the two compounds can be associated to the reduced efficiency of the direct mechanism of relaxation, which relies on the spin–phonon coupling. The latter is mediated by the spin–orbit coupling, which is significantly lower for such a light transition metal as vanadium. As a result, T_1 of $VO(dpm)_2$ remains long over a wide temperature range. For instance, a relaxation time of 2 ms is observed at 6 K for diluted $Co(acac)_2(H_2O)_2$ but at temperatures as high as 40 K in concentrated $VO(dpm)_2$. The anomaly arises from the small exponent of the T^n dependence of the Raman-like mechanism of relaxation. Such low exponents are relatively common for $S = 1/2$ states with small orbital contributions comprising light elements and have been associated to the soft character of the molecular lattices.[35,56]

It is also interesting to compare the measured decoherence times with those of other molecules proposed as potential molecular qubits. Among similarly investigated electron spin-qubits of vanadium, we note that the T_m values observed for a frozen solution of $VO(dpm)_2$ are slightly longer – in the whole investigated temperature range – than those reported for a dispersion in protiated solvents at the same concentration of a vanadium complex with nuclear-spin free ligands:[27] this is of particular interest, since in our case an evaporable system containing a large number of protons has been chosen without optimizing the ligand to reduce the number of nuclear spins. We have in fact confirmed that the ligand hydrogen magnetic nuclei play the dominant role in the relaxation by investigating the coherence time of $VO(dpm)_2$ diluted in deuterated solvents. A substantially unchanged T_m was detected (Fig. S11†), in contrast to the improvement of at least an order of magnitude of T_m[45,47] expected upon solvent deuteration when nuclei flip-flops of the latter dominate the decoherence process.

The observed decoherence times for $VO(dpm)_2$ are also comparable, despite the higher concentration of our samples, to those reported by Warner *et al.*[28] for a 0.1% diluted film of CuPc (2.1 *vs.* 1 μs at 80 K, if one consider the frozen solution $\mathbf{1}sol_{1\ mM}$, 0.16 *vs.* 1 μs if one consider the $\mathbf{1}PS_{1:10}$). We must stress that the processability and the surface stability of this β-diketonate complex are comparable to those of metal porphyrins, without the drawback of introducing ^{14}N magnetic nuclei. This is not only relevant for reducing the efficiency of decoherence; as suggested by Freedman *et al.*,[27] the well-defined hyperfine states of vanadium ions coordinated by non-magnetic nuclei can be used to investigate multiple quantum coherence. It is interesting to notice that in the Zeeman diagram of Fig. 1 pronounced level anti-crossings with gaps of the order of 0.5–1 GHz are observed at low longitudinal magnetic field. These transitions (in pale blue in Fig. 1), also known as clock transitions, are inherently robust to external perturbations because their effective g is practically zero and therefore are weakly affected by changes in the local field. Enhanced coherence time for these clock transitions have been recently observed in Bi doped silicon enriched in ^{29}Si nuclei.[57] Similar effects should be observable at the molecular level in $VO(dpm)_2$ for which clock transitions are expected at fields where the magnetization dynamics is already rather slow.

On the other hand, when T_m of $VO(dpm)_2$ is compared with relaxation times for a copper dithiolate complex with deuterated PPh_4^+ cation reported by van Slageren *et al.*[26] it is found to be an order of magnitude shorter: this might be attributed both to the larger concentration of the electronic spins in our system as well as to the large number of mobile protons present on the ligand. Further, the use of Q-band frequency, as done by van Slageren *et al.*, is expected to increase T_m of $VO(dpm)_2$ as well as its T_1.

Conclusions

We have shown here that a more rational search for potential qubits can significantly benefit from the combination of AC susceptometry with pulsed EPR techniques. This multi-technique approach is of particular relevance to define synthetic strategies because the optimization of T_1, in terms of both temperature and field dependence, is mandatory for the realization of molecular spin qubits that can be operated at room temperature. AC susceptibility gives easily access to the field dependence of T_1, in contrast to EPR, which relies on the resonance condition. Though T_1 extracted with the two techniques are exactly the same only in the case of a $S = 1/2$ with no hyperfine splitting, a close relation exists also for systems with more than two levels. The simple molecule we have picked up with this approach, though not yet optimized for coherent manipulation of the spin state, presents state-of-the-art phase memory times combined with additional interesting features. The spin–lattice relaxation remains slow even in strong fields, allowing the use of higher frequencies for coherent spin manipulation without losses in performances.

A particularly low efficient spin–phonon coupling appears to be at the basis of this behaviour and the potentially positive role played by the strong V=O bond needs to be further investigated by extending the approach developed here to other and more promising systems.[27,29] *Ab initio* modellization of the spin relaxation could also help to identify which structural features can favour long T_1, and consequently long T_m, at high temperature.

Even if the crucial aspect of qubits entanglement has not been addressed in this work it can be easily achieved through connection of β-diketonate pockets in more complex architectures.[58,59] This approach has already been successfully employed to couple different spin centers[60] and to address them individually in resonance experiments in particular in lanthanide polynuclear complexes thanks to their significantly different ***g***-factors.[61]

Of great relevance is the possibility to obtain monolayers of ordered arrays of intact $VO(dpm)_2$ molecules, retaining their paramagnetic nature thanks to the reduced interaction of the orbital carrying the unpaired electron with the substrate. Metallic nanostructures can be easily decorated with a monolayer of ordered $VO(dpm)_2$ molecules, allowing to investigate the response of an ensemble of identical molecular qubits, whose size can be easily controlled by lithographic exposure of the metallic substrate. Thin films of $VO(dpm)_2$ could be evaporated directly on a μ-SQUID to detect by AC susceptometry the effects of surface confinement on the dynamics of the magnetization, as already done on SMMs.[62] Our low temperature STM investigation suggests that $VO(dpm)_2$ could be also a good candidate to investigate quantum coherence at the single molecule level thanks to the recently developed approach based on spin-polarized scanning tunnelling microscopy, employed at very low temperature on single Fe atoms deposited on a MgO surface.[63]

Combining the optimization of T_2 in nuclear spin free environments with the possibility to control the spin–lattice relaxation through a rational synthetic design is foreseen to boost the interest for molecular spin systems as potential qubits.

Acknowledgements

The support of ERC through AdG MolNanoMaS (267746), of Italian MIUR through the project Futuro in Ricerca 2012 (RBFR12RPD1) and of Fondazione Ente Cassa di Risparmio di Firenze is acknowledged. Brunetto Cortigiani and Dr Shengwei Shi are acknowledged for the assistance in the XPS characterization. This paper is dedicated to Prof. Dante Gatteschi on the occasion of his retirement.

Notes and references

1 R. P. Feynman, *Found. Phys.*, 1986, **16**, 507–531.
2 P. W. Shor, *35th Annual Symposium on Foundations of Computer Science*, 1994.
3 A. M. Steane, *Rep. Prog. Phys.*, 1998, **61**, 117–173.
4 D. Deutsch, *Proc. R. Soc. London, Ser. A*, 1985, **400**, 97–117.
5 P. Ball, *Nature*, 2011, **474**, 272–274.
6 T. D. Ladd, F. Jelezko, R. Laflamme, Y. Nakamura, C. Monroe and J. L. O'Brien, *Nature*, 2010, **464**, 45–53.
7 R. Blatt and D. Wineland, *Nature*, 2008, **453**, 1008–1015.
8 R. Hanson and D. D. Awschalom, *Nature*, 2008, **453**, 1043–1049.
9 J. T. Muhonen, J. P. Dehollain, A. Laucht, F. E. Hudson, R. Kalra, T. Sekiguchi, K. M. Itoh, D. N. Jamieson, J. C. McCallum, A. S. Dzurak and A. Morello, *Nat. Nanotechnol.*, 2014, **9**, 986–991.
10 E. Knill, R. Laflamme and G. J. Milburn, *Nature*, 2001, **409**, 46–52.
11 J. Clarke and F. K. Wilhelm, *Nature*, 2008, **453**, 1031–1042.
12 I. L. Chuang, L. M. K. Vandersypen, X. Zhou, D. W. Leung and S. Lloyd, *Nature*, 1998, **393**, 143–146.
13 S. Thiele, F. Balestro, R. Ballou, S. Klyatskaya, M. Ruben and W. Wernsdorfer, *Science*, 2014, **344**, 1135–1138.
14 J. J. Pla, K. Y. Tan, J. P. Dehollain, W. H. Lim, J. J. L. Morton, F. A. Zwanenburg, D. N. Jamieson, A. S. Dzurak and A. Morello, *Nature*, 2013, **496**, 334–338.
15 F. Troiani and M. Affronte, *Chem. Soc. Rev.*, 2011, **40**, 3119–3129.
16 G. Aromi, D. Aguila, P. Gamez, F. Luis and O. Roubeau, *Chem. Soc. Rev.*, 2012, **41**, 537–546.
17 A. Morello, J. J. Pla, F. A. Zwanenburg, K. W. Chan, K. Y. Tan, H. Huebl, M. Mottonen, C. D. Nugroho, C. Yang, J. A. van

Donkelaar, A. D. C. Alves, D. N. Jamieson, C. C. Escott, L. C. L. Hollenberg, R. G. Clark and A. S. Dzurak, *Nature*, 2010, **467**, 687–691.
18 J. J. Pla, K. Y. Tan, J. P. Dehollain, W. H. Lim, J. J. L. Morton, D. N. Jamieson, A. S. Dzurak and A. Morello, *Nature*, 2012, **489**, 541–545.
19 K. Sato, S. Nakazawa, R. Rahimi, T. Ise, S. Nishida, T. Yoshino, N. Mori, K. Toyota, D. Shiomi, Y. Yakiyama, Y. Morita, M. Kitagawa, K. Nakasuji, M. Nakahara, H. Hara, P. Carl, P. Hofer and T. Takui, *J. Mater. Chem.*, 2009, **19**, 3739–3754.
20 S. Takahashi, R. Hanson, J. van Tol, M. S. Sherwin and D. D. Awschalom, *Phys. Rev. Lett.*, 2008, **101**, 047601.
21 G. Balasubramanian, P. Neumann, D. Twitchen, M. Markham, R. Kolesov, N. Mizuochi, J. Isoya, J. Achard, J. Beck, J. Tissler, V. Jacques, P. R. Hemmer, F. Jelezko and J. Wrachtrup, *Nat. Mater.*, 2009, **8**, 383–387.
22 A. M. Tyryshkin, S. Tojo, J. J. L. Morton, H. Riemann, N. V. Abrosimov, P. Becker, H.-J. Pohl, T. Schenkel, M. L. W. Thewalt, K. M. Itoh and S. A. Lyon, *Nat. Mater.*, 2011, **11**, 143–147.
23 A. Ardavan, O. Rival, J. J. L. Morton, S. J. Blundell, A. M. Tyryshkin, G. A. Timco and R. E. P. Winpenny, *Phys. Rev. Lett.*, 2007, **98**, 057201.
24 C. J. Wedge, G. A. Timco, E. T. Spielberg, R. E. George, F. Tuna, S. Rigby, E. J. L. McInnes, R. E. P. Winpenny, S. J. Blundell and A. Ardavan, *Phys. Rev. Lett.*, 2012, **108**, 107204.
25 A. Collauto, M. Mannini, L. Sorace, A. Barbon, M. Brustolon and D. Gatteschi, *J. Mater. Chem.*, 2012, **22**, 22272–22281.
26 K. Bader, D. Dengler, S. Lenz, B. Endeward, S.-D. Jiang, P. Neugebauer and J. van Slageren, *Nat. Commun.*, 2014, **5**, 5304.
27 J. M. Zadrozny, J. Niklas, O. G. Poluektov and D. E. Freedman, *J. Am. Chem. Soc.*, 2014, **136**, 15841–15844.
28 M. Warner, S. Din, I. S. Tupitsyn, G. W. Morley, A. M. Stoneham, J. A. Gardener, Z. Wu, A. J. Fisher, S. Heutz, C. W. M. Kay and G. Aeppli, *Nature*, 2013, **503**, 504–508.
29 J. M. Zadrozny, J. Niklas, O. G. Poluektov and D. E. Freedman, *ACS Cent. Sci.*, 2015, **1**, 488.
30 C. Schlegel, J. van Slageren, M. Manoli, E. K. Brechin and M. Dressel, *Phys. Rev. Lett.*, 2008, **101**, 147203.
31 M. A. K. Ahmed, H. Fjellvåg, A. Kjekshus and B. Klewe, *Z. Anorg. Allg. Chem.*, 2004, **630**, 2311–2318.
32 N. Ishikawa, M. Sugita, T. Ishikawa, S. Koshihara and Y. Kaizu, *J. Am. Chem. Soc.*, 2003, **125**, 8694–8695.
33 D. Gatteschi, R. Sessoli and J. Villain, *Molecular nanomagnets*, Oxford University Press, Oxford, UK, 2006.
34 K. N. Shrivastava, *Phys. Status Solidi B*, 1983, **117**, 437–458.
35 A. Abragam and B. Bleaney, *Electron Paramagnetic Resonance of Transition Ions*, Dover, New York, 1986.
36 A. C. de Vroomen, E. E. Lijphart and N. J. Poulis, *Physica*, 1970, **47**, 458–484.
37 H. A. Kramers, *Proc. Acad. Sci. Amsterdam*, 1930, **33**, 959.
38 J. Soeteman, L. Bevaart and A. J. van Duyneveldt, *Physica*, 1974, **74**, 126–134.
39 J. H. van Vleck, *Phys. Rev.*, 1940, **57**, 426–447.
40 J. Soeteman, A. J. van Duyneveldt, C. L. M. Pouw and W. Breur, *Physica*, 1973, **66**, 63–69.
41 N. B. Morozova, A. E. Turgambaeva, I. A. Baidina, V. V. Krysyuk and I. K. Igumenov, *J. Struct. Chem.*, 2005, **46**, 1047–1051.
42 S. Stoll and A. Schweiger, *J. Magn. Reson.*, 2006, **178**, 42–55.
43 A. J. Fielding, D. B. Back, M. Engler, B. Baruah, D. C. Crans, G. R. Eaton and S. S. Eaton, *ACS Symp. Ser.*, 2007, **974**, 364–375.
44 J. P. Fackler, J. D. Levy and J. A. Smith, *J. Am. Chem. Soc.*, 1972, **94**, 2436–2445.
45 G. R. Eaton and S. S. Eaton, *J. Magn. Reson.*, 1999, **136**, 63–68.
46 M. A. Nielsen and I. L. Chuang, *Quantum Computation and Quantum Information: 10th Anniversary Edition*, Cambridge University Press, 2011.
47 A. Schweiger and G. Jeschke, *Principles of Pulse Electron Paramagnetic Resonance*, Oxford University Press, 2001.
48 S. R. Hartmann and E. L. Hahn, *Phys. Rev.*, 1962, **128**, 2042–2053.
49 I. Cimatti, S. Ninova, V. Lanzilotto, L. Malavolti, L. Rigamonti, B. Cortigiani, M. Mannini, E. Magnano, F. Bondino, F. Totti, A. Cornia and R. Sessoli, *Beilstein J. Nanotechnol.*, 2014, **5**, 2139–2148.
50 L. Malavolti, V. Lanzilotto, S. Ninova, L. Poggini, I. Cimatti, B. Cortigiani, L. Margheriti, D. Chiappe, E. Otero, P. Sainctavit, F. Totti, A. Cornia, M. Mannini and R. Sessoli, *Nano Lett.*, 2015, **15**, 535–541.
51 K. Eguchi, Y. Takagi, T. Nakagawa and T. Yokoyama, *J. Phys. Chem. C*, 2013, **117**, 22843–22851.
52 K. Eguchi, T. Nakagawa, Y. Takagi and T. Yokoyama, *J. Phys. Chem. C*, 2015, **119**, 9805–9815.
53 S. Stepanow, A. Mugarza, G. Ceballos, P. Moras, J. C. Cezar, C. Carbone and P. Gambardella, *Phys. Rev. B: Condens. Matter Mater. Phys.*, 2010, **82**, 014405.
54 S. Gómez-Coca, A. Urtizberea, E. Cremades, P. J. Alonso, A. Camón, E. Ruiz and F. Luis, *Nat. Commun.*, 2014, **5**, 4300.
55 R. M. Rakhmatullin, I. N. Kurkin, G. V. Mamin, S. B. Orlinskii, M. R. Gafurov, E. I. Baibekov, B. Z. Malkin, S. Gambarelli, S. Bertaina and B. Barbara, *Phys. Rev. B: Condens. Matter Mater. Phys.*, 2009, **79**, 172408.
56 J.-L. Du, G. R. Eaton and S. S. Eaton, *J. Magn. Reson., Ser. A*, 1996, **119**, 240–246.
57 G. Wolfowicz, A. M. Tyryshkin, R. E. George, H. Riemann, N. V. Abrosimov, P. Becker, H.-J. Pohl, M. L. W. Thewalt, S. A. Lyon and J. J. L. Morton, *Nat. Nanotechnol.*, 2013, **8**, 561–564.
58 C. Pariya, C. R. Sparrow, C.-K. Back, G. Sandí, F. R. Fronczek and A. W. Maverick, *Angew. Chem.,Int. Ed.*, 2007, **46**, 6305–6308.
59 J. K. Clegg, F. Li, K. A. Jolliffe, L. F. Lindoy, G. V. Meehan, S. Parsons, P. A. Tasker and F. J. White, *Dalton Trans.*, 2013, **42**, 14315–14323.
60 L. A. Barrios, D. Aguilà, O. Roubeau, P. Gamez, J. Ribas-Ariño, S. J. Teat and G. Aromí, *Chem.–Eur. J.*, 2009, **15**, 11235–11243.

61 D. Aguila, L. A. Barrios, V. Velasco, O. Roubeau, A. Repolles, P. J. Alonso, J. Sese, S. J. Teat, F. Luis and G. Aromi, *J. Am. Chem. Soc.*, 2014, **136**, 14215–14222.
62 E. Bellido, P. Gonzalez-Monje, A. Repollés, M. Jenkins, J. Sesé, D. Drung, T. Schurig, K. Awaga, F. Luis and D. Ruiz-Molina, *Nanoscale*, 2013, **5**, 12565–12573.
63 S. Baumann, W. Paul, T. Choi, C. P. Lutz, A. Ardavan and A. J. Heinrich, *Science*, 2015, **350**, 417–420.

Electronic Supplementary Information

Quantum Coherence in a processable vanadyl complex: new tools for the search of molecular spin qubits

Lorenzo Tesi[1], Eva Lucaccini[1], Irene Cimatti[1], Mauro Perfetti[1], Matteo Mannini[1], Matteo Atzori[1], Elena Morra[2], Mario Chiesa[2], Andrea Caneschi[1], Lorenzo Sorace[1], Roberta Sessoli[1*]*

1) Department of Chemistry "Ugo Schiff", University of Florence & INSTM RU of Florence, via della Lastruccia 3-13, 50019 Sesto Fiorentino, Italy

2) Department of Chemistry, University of Turin & NIS Centre, via P. Giuria 7, 10125, Torino, Italy

* Correspondence: lorenzo.sorace@unifi.it, roberta.sessoli@unifi.it

Synthesis and samples preparation. The whole synthesis was performed in inert atmosphere following a reported procedure.[1] Vanadium sulphate tetrahydrate (0.5 g, 2.13 mmol) was dissolved in 4 ml of H_2O milliQ and 8 ml of EtOH with magnetic stirring. Hdpm (1 g, 5.45 mmol) was added and the solution quickly became dark green. Finally, 3 ml of sodium carbonate 0.1 M was mixed with the solution and a solid appeared immediately. The latter was filtered out and washed with water. The powder was purified by sublimation thanks to which we obtained long green crystals. Anal. Calcd. (found) for [$C_{22}H_{38}O_5V$]: C, 60.96 (61.07); H 8.84 (9.00). Crystals were checked by X-ray diffraction and resulted to correspond to the structure available in the Cambridge Structural Database record CCDC 230339.[1]

Diluted samples were also prepared to evaluate the effect of intermolecular interactions on magnetization dynamics. Glassy dispersions were obtained by dissolving $VO(dpm)_2$ in a 2:3 toluene:CH_2Cl_2 solution to obtained a glass at low temperature or by dispersing the complex in polystyrene films.

AC susceptometry. A Quantum Design PPMS equipped with AC susceptibility probe (working in the range 10 Hz- 10 kHz) and a Quantum Design MPMS SQUID magnetometer (0.1 Hz - 1 kHz), have been used to measure the magnetic susceptibility over an extended frequency. The higher sensitivity of the latter set-up allowed to characterize the diluted samples. A variable static field was applied parallel to the oscillating field.

Through the Debye model (equation 1) we extrapolated the relaxation time, τ, and the width of the distribution of the relaxation time, α.

$$\chi''(\omega) = (\chi_T - \chi_S)\frac{(\omega\tau)^{1-\alpha}\cos\left(\frac{\pi\alpha}{2}\right)}{1 + 2(\omega\tau)^{1-\alpha}\sin\left(\frac{\pi\alpha}{2}\right) + (\omega\tau)^{2-2\alpha}} \qquad \text{(eq.1)}$$

where $\chi''(\omega)$ is the imaginary susceptibility, ω the angular frequency, χ_T the isothermal susceptibility and χ_S the adiabatic susceptibility.

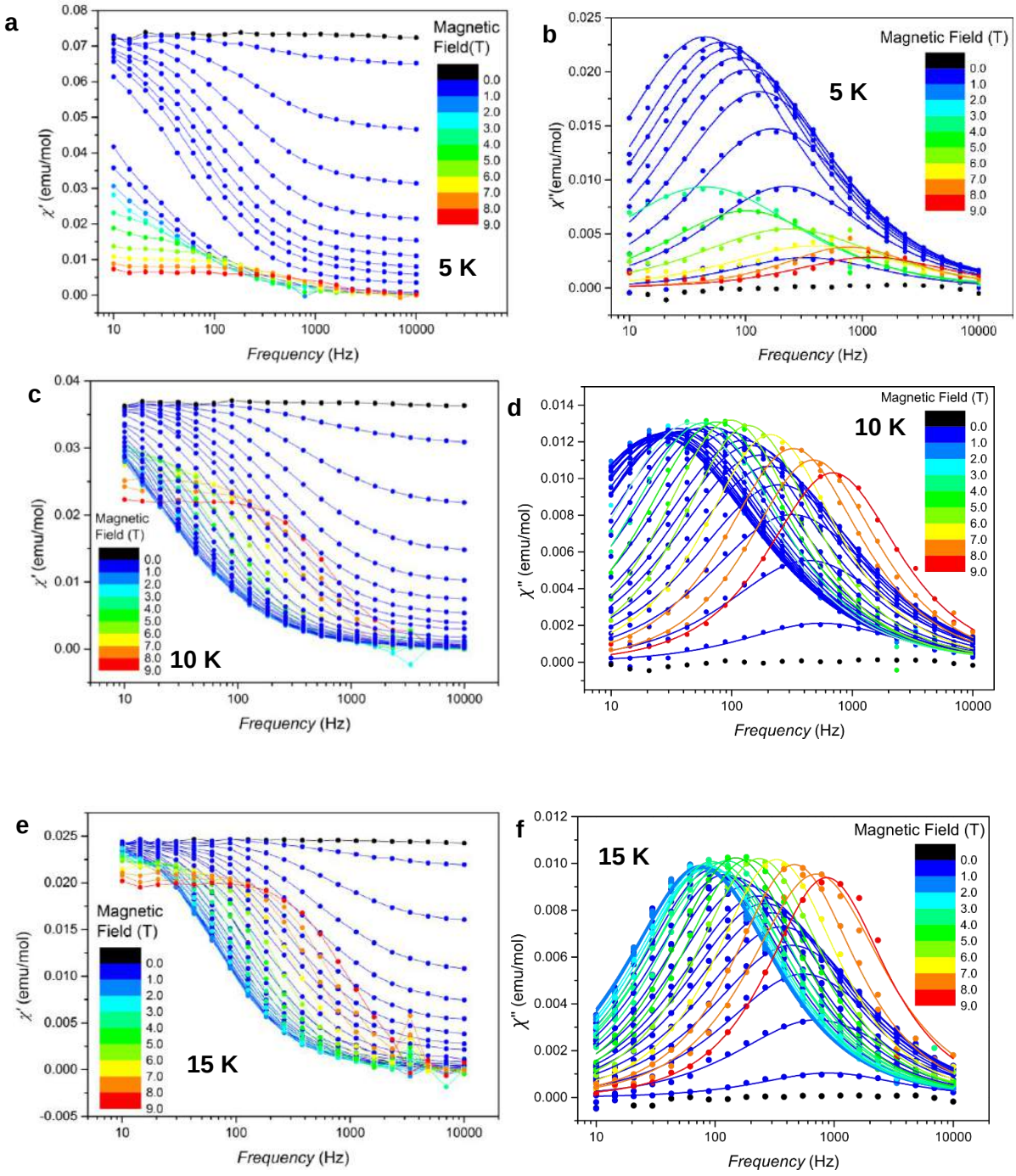

Figure S1. *Frequency dependence of the real (χ') and imaginary (χ'') susceptibility of $VO(dpm)_2$ bulk with static magnetic fields varying between 0 and 8.8 T. (a) and (b): at 5 K; (c) and (d): at 10 K; (e) and (f): at 15 K.*

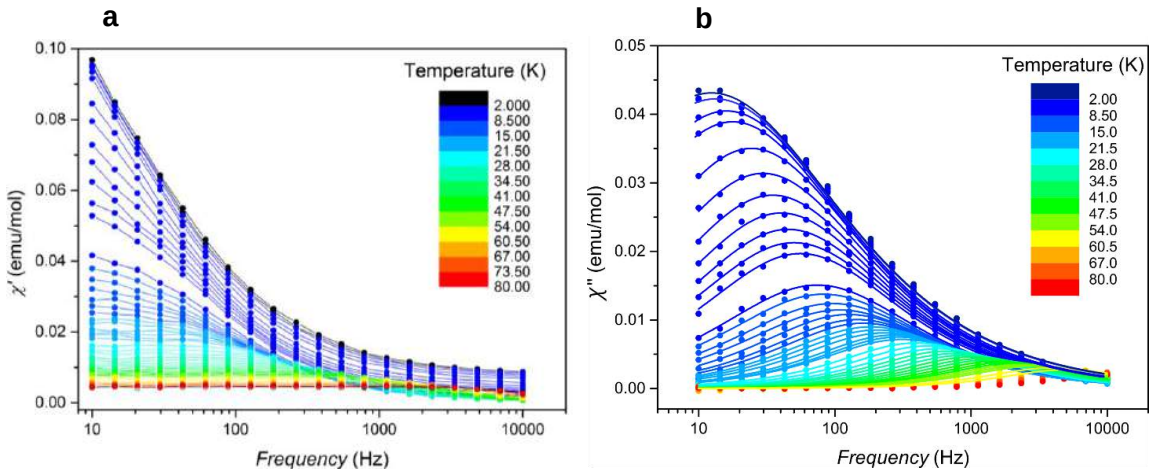

Figure S2. *Frequency dependence of the real susceptibility χ' (a) and of imaginary susceptibility χ'' (b) of $VO(dpm)_2$ bulk as a function of temperature between 1.8 and 80 K in a static applied field of 0.2 T.*

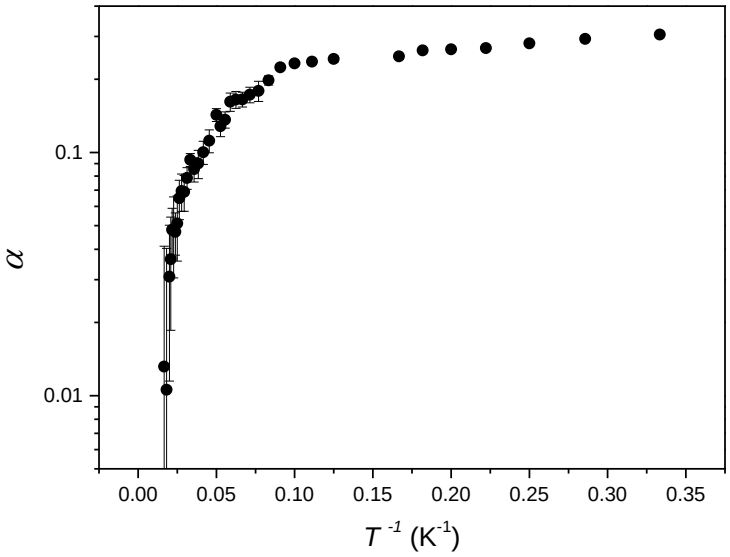

Figure S3. *Width of the distribution of the relaxation time for $VO(dpm)_2$ bulk, extrapolated by the Debye model through the α parameter, as a function of the reciprocal temperature in B_{dc}=0.2 T.*

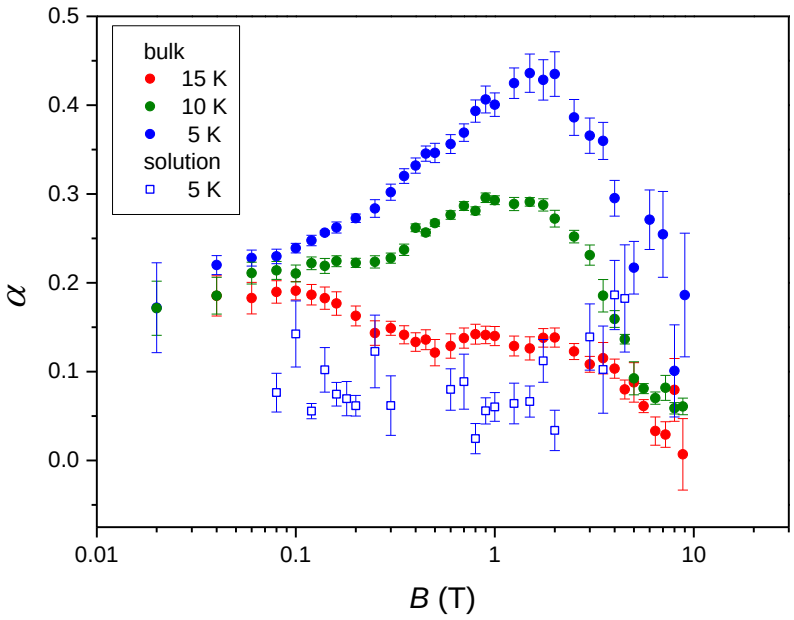

Figure S4. *Width of the distribution of the relaxation time, extrapolated by the Debye model through the α parameter, as a function of the magnetic field, both for the bulk at 5, 10, 15 K, and for the 200 mM solution of VO(dpm)₂ at 5 K.*

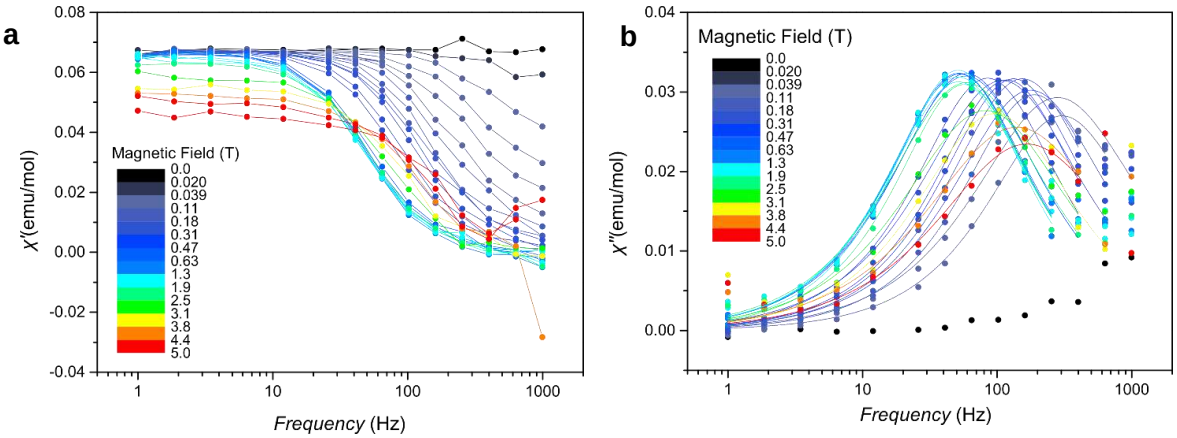

Figure S5. *Frequency dependence of the real susceptibility χ' (a) and of imaginary susceptibility χ'' (b) of a 200 mM VO(dpm)₂ solution in CH_2Cl_2-toluene 1:2 as a function of the magnetic field between 0 and 5 T at 5 K.*

EPR Spectroscopy. CW X-Band EPR spectra of all samples were recorded on a Bruker Elexsys E500 spectrometer equipped with a SHQ cavity (ν = 9.47 GHz, Florence). Low temperature measurements were obtained using an Oxford Instruments ESR900 continuous flow helium cryostat. Pulsed EPR measurements (**1**$PS_{1:10}$, **1**$sol_{200mM,}$ **1**$sol_{1mM,}$ **1**sol_{1mM}^{D}) were performed with a Bruker Elexsys E580 at X-band (Turin, ν = 9.75 GHz) equipped with a flexline dielectric ring ENDOR resonator (Bruker EN 4118X-MD4). Temperatures between 4 and 200 K were obtained with an Oxford Instruments CF935 continuous flow helium cryostat. Typical pulse lengths were 16 ns ($\pi/2$) and 32 ns (π). For Echo detected field swept EPR spectra, the Hahn Echo pulse sequence ($\pi/2$—t_d—π— t_d—echo), with fixed interpulse delay time t_d=200 ns, was applied while sweeping the magnetic field.

Phase memory times measurements were obtained by measuring the primary echo decay with varying interpulse delay starting from t_d=98 ns at a fixed magnetic field. Spin–lattice-relaxation times were measured using the standard inversion recovery sequence (π—t_w—$\pi/2$— t_d—π— t_d—echo) and by observing the variation of the amplitude of the primary echo as a function of the repetition rate (echo saturation by fast repetition). This second method was find to be more convenient at low temperature (T<40 K) due to the very long T_1 of the sample. Nutation measurements were performed with a nutation pulse (t_p) of variable length followed by a Hahn echo sequence (t_p-t_w—$\pi/2$— t_d—π— t_d—echo) with t_w =7 μs, t_d=200 ns and different pulse powers. The pulse length varied depending on the attenuation level of B_1. For 2 dB attenuation, the second and third pulses used were 10 and 20 ns in length. For 6 dB attenuation, 16 and 32 ns pulse lengths were used, and for 10 dB attenuation the second and third pulses were 26 and 52 ns in length respectively.

CW and Echo-detected spectra were simulated with Easy-Spin.[2] Errors of fit parameters (g and hyperfine values) were estimated by eye. T_m relaxation data were normalized to the first measurement point and fitted with Origin; indicated deviations correspond to the standard errors. Phase memory times (T_m) were extracted from fitting (stretched) exponentials, equation (4), to the Hahn echo decay curves. Experimental data of longitudinal relaxation times were fitted with a stretched exponential decay, equation (5).

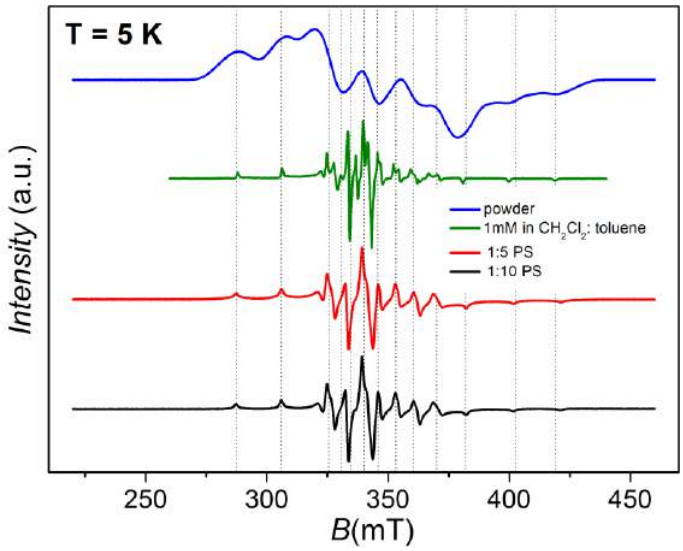

Figure S6. *CW-EPR X-band spectra at 5 K for the bulk sample, the PS dispersion (1:5 and 1:10) and the frozen 1mM solution of $VO(dpm)_2$. The dotted lines evidence the coincidence of the resonant fields in the different samples.*

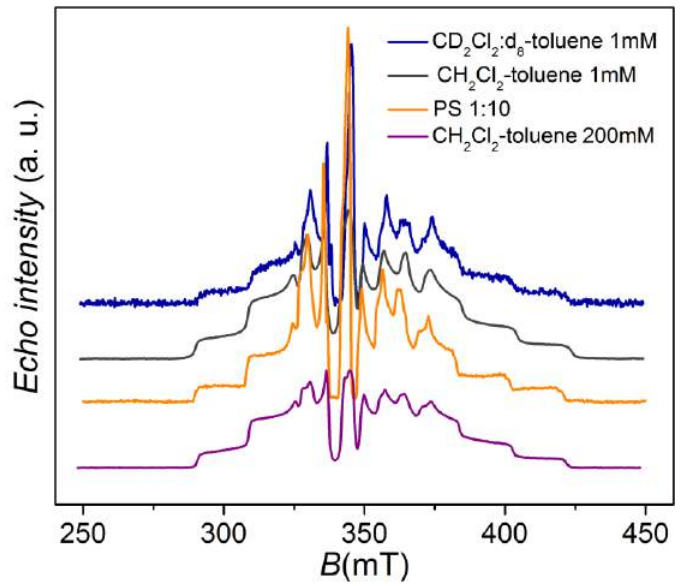

Figure S7. *Echo detected field swept EPR spectra of $VO(dpm)_2$ dispersed into PS (1:10), in a 1 mM deuterated solution, in a 1 mM protic solution and in a 200 mM protic solution. All the spectra were recorded at 5 K, except for the concentrated solution one, that was measured at 10 K due to receiver saturation at 5 K.*

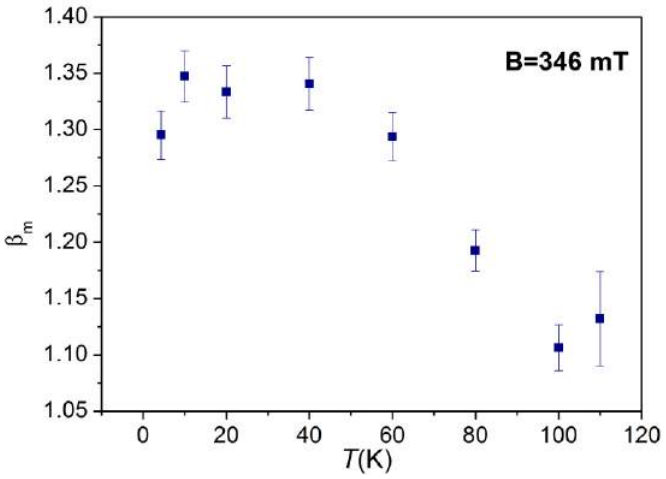

Figure S8. *Temperature dependence of the best fit values of the stretching parameter β_m for $VO(dpm)_2$ in a 1 mM CH_2Cl_2-toluene frozen solution.*

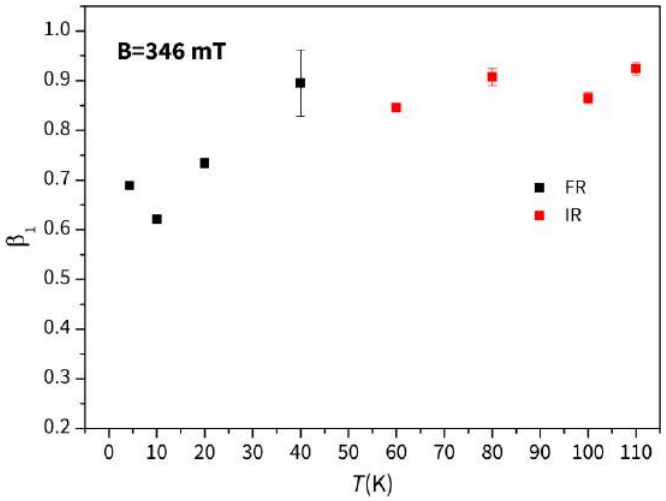

Figure S9. *Best fit values of the stretching parameter β_1, as a function of temperature for $VO(dpm)_2$ in a 1mM CH_2Cl_2-toluene frozen solution. The spin-lattice relaxation time was measured with echo saturation by fast repetition for low temperatures (black squares) and with inversion recovery mode for higher temperatures (red squares).*

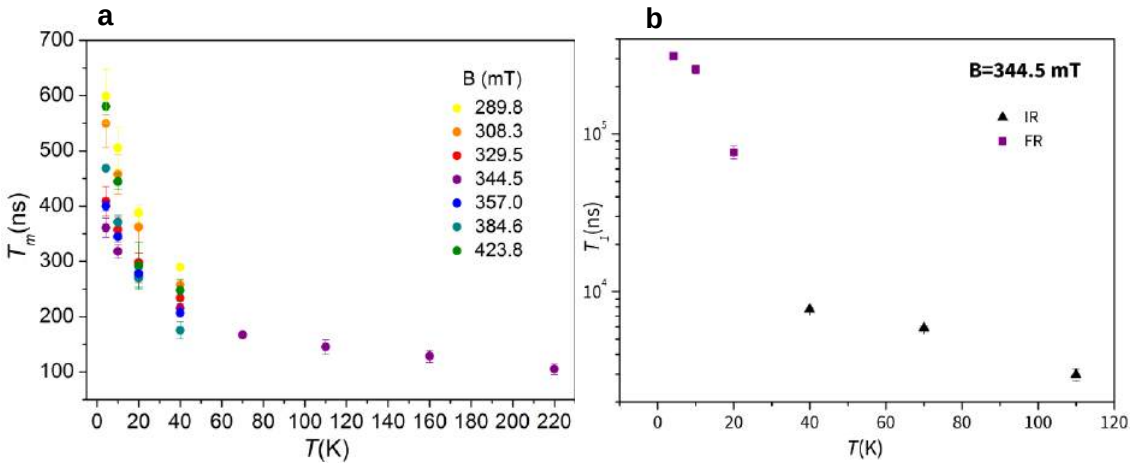

Figure S10. *a) Temperature dependence of T_m values for $VO(dpm)_2$ dispersed in PS (1:10), evaluated at resonant fields corresponding to parallel and perpendicular transitions between different hyperfine sublevels (B=289.8 mT: parallel, m_I=-7/2; B= 308.8 mT parallel m_I=-5/2; B=329.5 mT perpendicular m_I=-5/2; B=357.0 mT perpendicular m_I= 5/2; B=384.6 mT parallel m_I=3/2; B=423.8 mT parallel m_I=7/2). b) Comparison of T_1 values of the central line measured with echo saturation by fast repetition (purple squares) and inversion recovery mode (black triangles).*

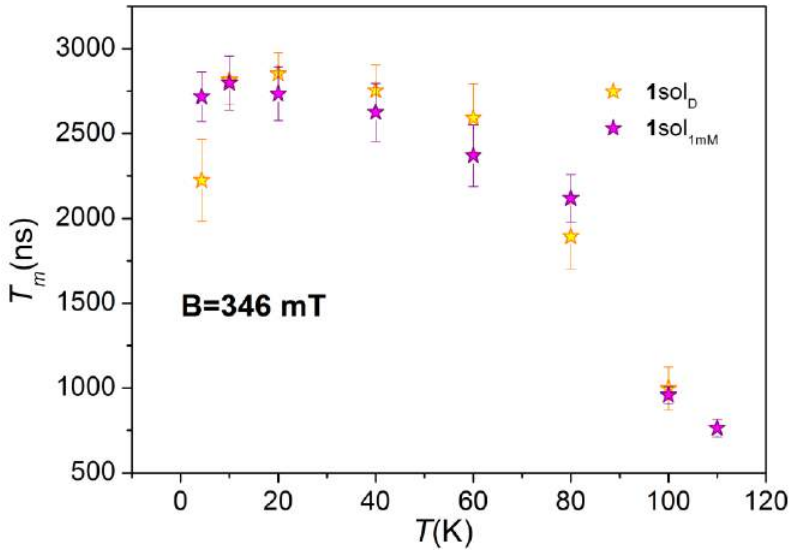

Figure S11. *Comparison of the phase memory time T_m measured at 346 mT for protic and deuterated 1mM solution of $VO(dpm)_2$.*

UHV deposition and characterization. The ML and sub-ML deposition and characterization of $VO(dpm)_2$ films were performed *in situ*. The substrate employed was an Au(111) single crystal. The surface was cleaned by repeated Ar^+ sputtering (2 μA, 1 keV) and annealing (720 K) cycles. Considering that $VO(dpm)_2$ like other β-diketonates shows high volatility,[3] the sublimation was performed in a dedicated preparation chamber with a base pressure of 1×10^{-7} mbar; this chamber is directly connected to the XPS and STM chambers. Low coverages were obtained by keeping the molecular powders, hosted in a quartz crucible, at room temperature. The comparison of the STM and XPS characterization of an *in situ* monolayer deposition performed by heating the powders (at 373 K, where a rate is observed by QCM) or leaving them at room temperature, proves that there is no difference between the two. During the sublimation, the substrate was kept at room temperature. A K-type thermocouple, buried into the molecular powder, allowed for temperature control.

The thick film was prepared in a home-made evaporation chamber, and transferred to the XPS chamber using a glove bag filled with nitrogen. The sublimation was performed on top of a polycrystalline Au film evaporated on Mica. Preliminarily to the sublimation a hydrogen flame-annealing procedure was adopted in order to clean the *ex situ* prepared substrate. The deposition was performed using the same evaporator as for the monolayer coverage but the powders were heated at 373 K.

The STM images were obtained by an UHV scanning tunneling microscope (Omicron VT-STM) operating at 30 K in the constant current mode with electrochemically-etched W tips. The applied tip bias voltage and the tunneling current of each image are given in the figure caption.

The height estimation of the $VO(dpm)_2$ molecules was carried out by plotting the height distribution of selected regions (see highlighted areas Figure S12). The measured heights of each region were then fit with two Gaussian functions, one for molecular domains and a second for the background. The height of the molecular domain is estimated as the difference between the peak positions of the two distributions. We then computed the mean height value averaging over the five considered areas. The error on the mean value, *s*, is then given by

$$s = \sqrt{\frac{\sum_{k=1}^{N} \sigma_k^2}{N-1}}$$

where σ_k is the standard deviation of height computed for the k-th area and N is the total number of the considered values.

XPS measurements were carried out in an UHV chamber with a base pressure in the low 10^{-10} mbar range. The chamber is equipped with a SPECS Phoibos 150 electron analyzer, a standard Al source

and a monochromatic Al X-ray source. The X-ray sources were assembled at 54.44° with respect to the analyzer. For the characterization of the monolayer deposition, we used the monochromatic Al source operating at a power of 100 W (13 kV and 7.7 mA). The characterization of the thick film was performed with a standard Al source with a power of 260 W (13 kV and 20 mA). The pass energy was set to 40 eV for all the experiments.

The monolayer was subjected to differential charging and the Au $4p_{3/2}$ peak present the same shift as the main ones of the molecule (O *1s*, V *2p*, C *1s*). Performing the calibration using the Au $4p_{3/2}$, the position of the main peak of C *1s* was 285.4 eV. In order to use the same calibration for the thin and the thick film, being the Au *4p 3/2* not visible, the methyl C *1s* at 285.4 eV signal has been used as a reference to correct the charging effect.

XPS data analysis have been performed by removing the inelastic background by means of the Shirley method[4] and then deconvoluting the experimental spectra using mixed Gaussian and Lorentzian line shapes for each component in the spectra. In the case of V *2p* component the adopted method resulted in line with previous literature reports.[5] The background for the O *1s* peak was obtained by subtracting also the contribution of the Au *4p 3/2* peak at 547 eV.

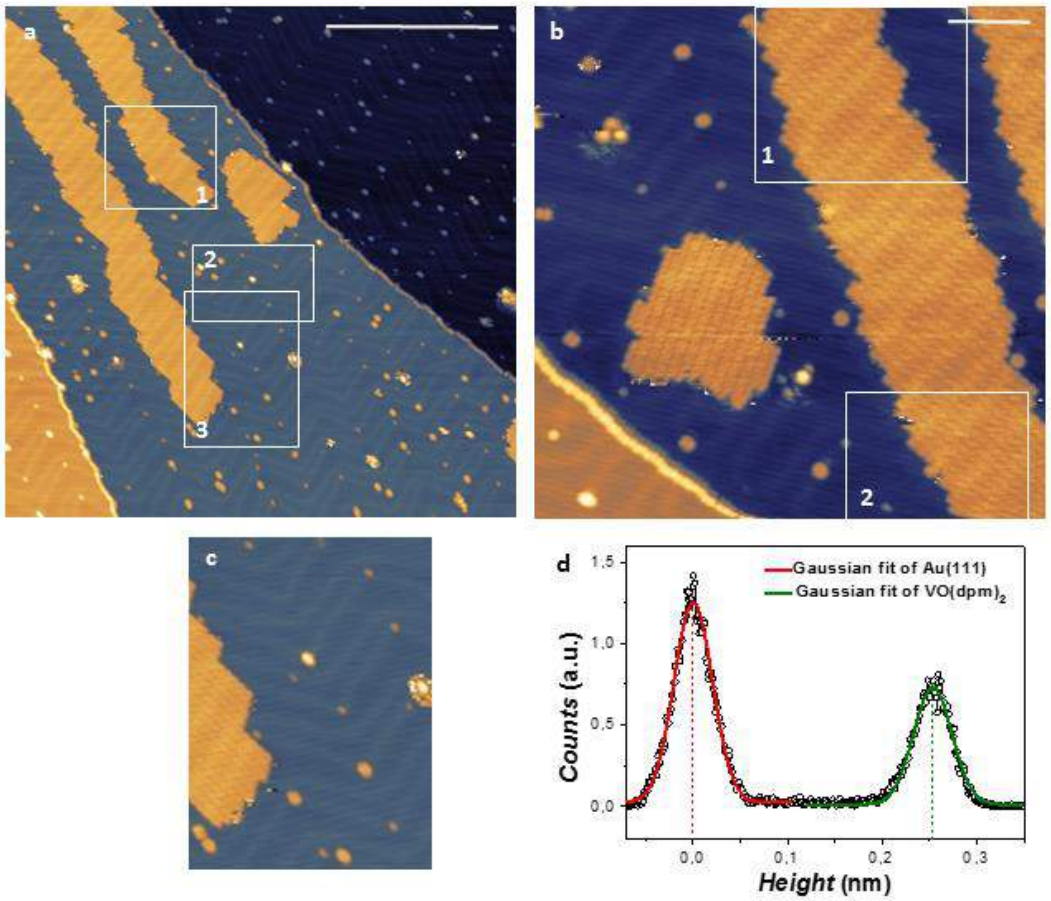

Figure S12. *a) and b) are STM images of a sub-monolayer deposition of $VO(dpm)_2$ measured at 30K, already reported in Fig. 5. The zones into the frames are the ones used for the evaluation of the height distribution. c) is the enlarged view of zone 3 in a), and d) is its height distribution.*

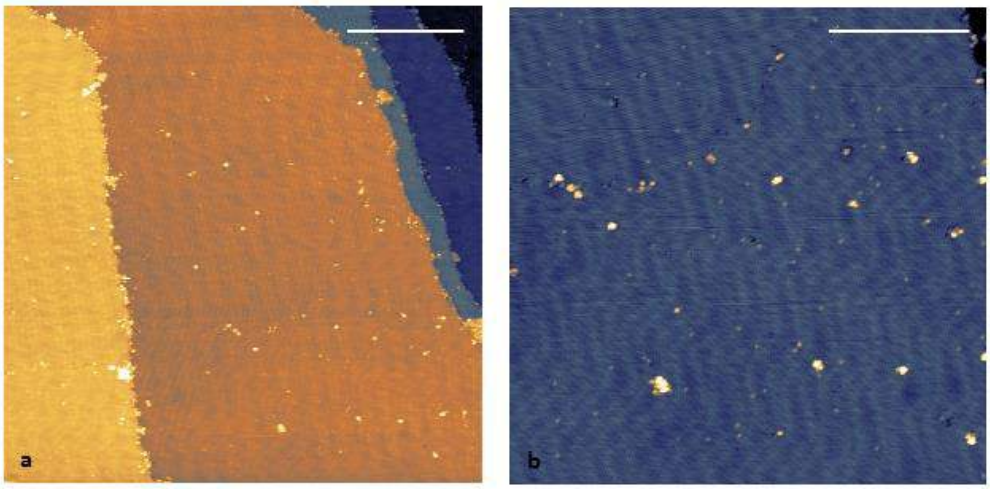

Figure S13. *STM image of a monolayer deposition of $VO(dpm)_2$ measured at 30 K. Bias = -2 V, current = 5 pA. a) 200x200 nm region. b) 100x100nm region, zoom of the precedent. The scale bar are 50 nm (a) and 30 nm (b).*

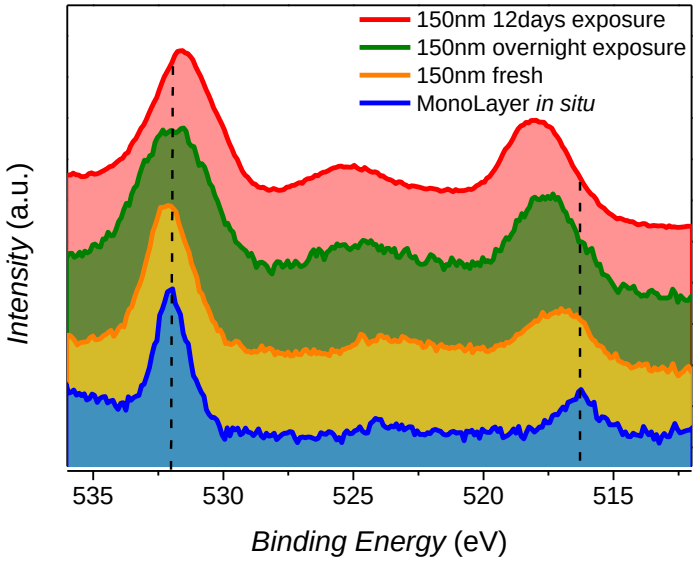

Figure S14. *Comparison of O 1s and V 2p XPS spectra of the monolayer and thick film. The thick film of 150 nm was prepared ex situ and transferred into the XPS chamber using a glove bag filled with nitrogen; the monolayer was prepared and kept in situ. The thick film was exposed to air for a variable time reported in the legend.*

Compositions of the eigenstates of the *S*=1/2, *I*=7/2 coupled system.

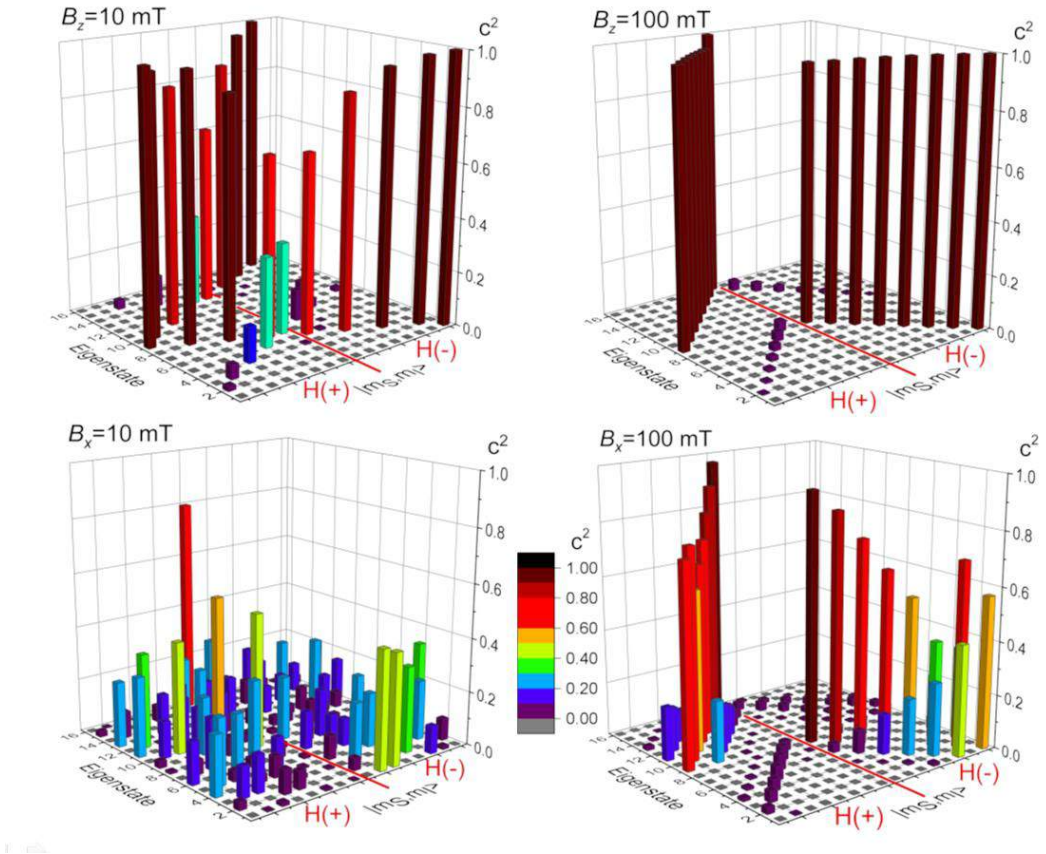

Figure S15. *Eigenstates composition at two different magnetic fields (10 and 100 mT) applied parallel and perpendicular to the largest hyperfine coupling component calculated with the spin Hamiltonian of eq. 3 of main text (see text for parameters). The basis has been selected as the projection along the field direction. The red lines separate basis-states with projection of the spin parallel (H+) and antiparallel (H-) to the external field.*

Bibliography

S1 Ahmed, M. A. K.; Fjellvåg, H.; Kjekshus, A.; Klewe, B. *Z. Anorg. Allg. Chem.* **2004**, 630, (13-14), 2311-2318.

S2 Stoll, S.; Schweiger, A. *J. Magn. Reson.* **2006**, 178, (1), 42-55.

S3 Evans, S.; Hamnett, A.; Orchard, A. F.; Lloyd, D. R. *Far. Disc. Chem. Soc.* **1972**, 54, 227-250.

S4 Shirley, D. *Phys. Rev. B* **1972**, 5, 4709-4714.

S5 Biesinger, M. C.; Lau, L. W. M.; Gerson, A. R.; Smart, R. S. C. *Appl. Surf. Sci.* **2010**, 257, 887-898.

List of publications

- L. Tesi, A. Lunghi, M. Atzori, E. Lucaccini, L. Sorace, F. Totti, and R. Sessoli. "Giant spin–phonon bottleneck effects in evaporable vanadyl-based molecules with long spin coherence". In: *Dalton Transactions* 45.42 (2016), pp. 16635–16643
- E. Lucaccini, M. Briganti, M. Perfetti, L. Vendier, J.-P. Costes, F. Totti, R. Sessoli, and L. Sorace. "Relaxation Dynamics and Magnetic Anisotropy in a Low-Symmetry Dy(III) Complex". In: *Chemistry–A European Journal* 22.16 (2016), pp. 5552–5562
- L. Tesi, E. Lucaccini, I. Cimatti, M. Perfetti, M. Mannini, M. Atzori, E. Morra, M. Chiesa, A. Caneschi, L. Sorace, et al. "Quantum coherence in a processable vanadyl complex: new tools for the search of molecular spin qubits". In: *Chemical Science* 7.3 (2016), pp. 2074–2083
- M. Perfetti, E. Lucaccini, L. Sorace, J.-P. Costes, and R. Sessoli. "Determination of Magnetic Anisotropy in the LnTRENSAL Complexes (Ln= Tb, Dy, Er) by Torque Magnetometry". In: *Inorganic Chemistry* 54.7 (2015), pp. 3090–3092
- E. Lucaccini, L. Sorace, M. Perfetti, J.-P. Costes, and R. Sessoli. "Beyond the anisotropy barrier: slow relaxation of the magnetization in both easy-axis and easy-plane Ln (trensal) complexes". In: *Chemical Communications* 50.14 (2014), pp. 1648–1651

Bibliography

[1] O. Kahn. *Molecular Magnetism*. New York: Wiley-VCH, 1993.

[2] R. Sessoli et al. "Magnetic bistability in a metal-ion cluster". In: *Nature* 365 (1993), pp. 141–143.

[3] D. Gatteschi, R. Sessoli, and J. Villain. *Molecular Nanomagnets*. Oxford University Press, 2006.

[4] A.-L. Barra et al. "Superparamagnetic-like behavior in an octanuclear iron cluster". In: *EPL (Europhysics Letters)* 35.2 (1996), p. 133.

[5] L. Thomas et al. "Macroscopic quantum tunnelling of magnetization in a single crystal of nanomagnets". In: *Nature* 383 (1996), pp. 145–147.

[6] J. R. Friedman et al. "Macroscopic measurement of resonant magnetization tunneling in high-spin molecules". In: *Physical review letters* 76.20 (1996), p. 3830.

[7] A. L. Barra, D. Gatteschi, and R. Sessoli. "High-frequency EPR spectra of a molecular nanomagnet: Understanding quantum tunneling of the magnetization". In: *Physical Review B* 56 (1997), pp. 8192–8198.

[8] P. Politi et al. "Tunneling in Mesoscopic Magnetic Molecules". In: *Physical Review Letters* 75 (1995), pp. 537–540.

[9] O. Waldmann. "A criterion for the anisotropy barrier in single-molecule magnets". In: *Inorganic chemistry* 46.24 (2007), pp. 10035–10037.

[10] C. J. Milios et al. "A record anisotropy barrier for a single-molecule magnet". In: *Journal of the American Chemical Society* 129.10 (2007), pp. 2754–2755.

[11] N. Ishikawa et al. "Lanthanide Double-Decker Complexes Functioning as Magnets at the Single-Molecular Level". In: *Journal of American Chemical Society* 125 (2003), pp. 8694–8695.

[12] D. N. Woodruff, R. E. Winpenny, and R. A. Layfield. "Lanthanide Single-Molecule Magnets". In: *Chemical Reviews* 113 (2013), pp. 5110–5148.

[13] Y.-S. Ding et al. "On Approaching the Limit of Molecular Magnetic Anisotropy: A Near-Perfect Pentagonal Bipyramidal Dysprosium (III) Single-Molecule Magnet". In: *Angewandte Chemie* 128.52 (2016), pp. 16305–16308.

[14] L. Bogani and W. Wernsdorfer. "Molecular spintronics using single-molecule magnets". In: *Nature Materials* 7 (2008), pp. 178–186.

[15] R. Vincent et al. "Electronic read-out of a single nuclear spin using a molecular spin transistor". In: *Nature* 488.7411 (2012), pp. 357–360.

[16] G. Aromí et al. "Design of magnetic coordination complexes for quantum computing". In: *Chemical Society Reviews* 41.2 (2012), pp. 537–546.

[17] J. Bartolomé, F. Luis, and J. F. Fernández, eds. *Molecular magnets*. Springer, 2014.

[18] E. Lucaccini et al. "Beyond the anisotropy barrier: slow relaxation of the magnetization in both easy-axis and easy-plane Ln (trensal) complexes". In: *Chemical Communications* 50.14 (2014), pp. 1648–1651.

[19] R. Orbach. "Spin-lattice relaxation in rare-earth salts". In: *Proceedings of the Royal Society of London A: Mathematical, Physical and Engineering Sciences*. Vol. 264. 1319. The Royal Society. 1961, pp. 458–484.

[20] N. W. Ashcroft and N. D. Mermin. *Solid State Physics*. Saunders College, 1976.

[21] Y. Rechkemmer et al. "Comprehensive spectroscopic determination of the crystal field splitting in an erbium single-ion magnet". In: *Journal of the American Chemical Society* 137.40 (2015), pp. 13114–13120.

[22] E. Lucaccini et al. "Relaxation Dynamics and Magnetic Anisotropy in a Low-Symmetry Dy(III) Complex". In: *Chemistry–A European Journal* 22.16 (2016), pp. 5552–5562.

[23] B. M. Flanagan et al. "A Ligand-Field Analysis of the trensal Ligand. An Application of Angular Overlap Model to Lanthanides". In: *Inorganic Chemistry* 41 (2002), pp. 5024–5033.

[24] L. Tesi et al. "Quantum coherence in a processable vanadyl complex: new tools for the search of molecular spin qubits". In: *Chemical Science* 7.3 (2016), pp. 2074–2083.

[25] H. A. Bethe. "Termaufspaltung in Kristallen". In: *Annalen der Physik* 395 (1929), pp. 133–208.

[26] B. H. Bransden and C. J. Joachain. *Physics of atoms and molecules*. Longman Scientific & Technical, 1983.

[27] B. N. Figgis. "Ligand field theory". In: *Comprehensive Coordination Chemistry* 1 (1987), pp. 213–279.

[28] R. L. Carlin and A. J. van Duyneveldt. *Magnetic properties of transition metal compounds*. Springer, 1977.

[29] C. Görller-Walrand and K. Binnemans. "Razionalization of Crystal Field Parametrization". In: *Handbook on the Physics and Chemistry of Rare Earths*. Ed. by K. A. Gscneidner jr. and L. Eyring. Vol. 23. Elsevier, 1996. Chap. 155, pp. 121–283.

[30] A. R. Edmonds. *Angular momentum in quantum mechanics*. Princeton University Press, 1996.

[31] R. Elliott and K. Stevens. "The theory of the magnetic properties of rare earth salts: cerium ethyl sulphate". In: *Proceedings of the Royal Society of London A: Mathematical, Physical and Engineering Sciences*. Vol. 215. 1123. 1952, pp. 437–453.

[32] J. R. Pilbrow. *Transition ion electron paramagnetic resonance*. Oxford University Press, 1990.

[33] A. Abragam and B. Bleaney. *Electron Paramagnetic Resonance of Transition Ions*. Oxford University Press, 1970.

[34] G. Stewart. "On the interpretation of nuclear quadrupole interaction data for rare-earth nuclei at low symmetry sites". In: *Hyperfine Interactions* 23.1 (1985), pp. 1–16.

[35] B. G. Wybourne. *Spectroscopic Properties of Rare Earths*. John Wiley and Sons, 1965.

[36] C. W. Nielson and J. F. Koster. *Spectroscopic Coefficients for the p^n, d^n f^n Configurations*. Cambridge: MIT Press, 1963.

[37] C. Rudowicz and J. Qin. "Can the low symmetry crystal (ligand) field parameters be considered compatible and reliable?" In: *Journal of luminescence* 110.1 (2004), pp. 39–64.

[38] S. T. Liddle and J. van Slageren. "Improving f-element single molecule magnets". In: *Chemical Society Reviews* 44.19 (2015), pp. 6655–6669.

[39] N. Ishikawa, T. Iino, and Y. Kaizu. "Determination of ligand-field parameters and f-electronic structures of hetero-dinuclear phthalocyanine complexes with a diamagnetic yttrium (III) and a paramagnetic trivalent lanthanide ion". In: *The Journal of Physical Chemistry A* 106.41 (2002), pp. 9543–9550.

[40] A. Stoneham. "The phonon bottleneck in paramagnetic crystals". In: *Proceedings of the Physical Society* 86.6 (1965), p. 1163.

[41] M. Novak et al. "Magnetic properties of a Mn cluster organic compound". In: *Journal of magnetism and magnetic materials* 146.1 (1995), pp. 211–213.

[42] M. Evangelisti et al. “Giant isotope effect in the incoherent tunneling specific heat of the molecular nanomagnet Fe 8”. In: *Physical review letters* 95.22 (2005), p. 227206.

[43] K. Shrivastava. “Theory of spin–lattice relaxation”. In: *physica status solidi (b)* 117.2 (1983), pp. 437–458.

[44] K. S. Cole and R. H. Cole. “Dispersion and absorption in dielectrics I. Alternating current characteristics”. In: *The Journal of chemical physics* 9.4 (1941), pp. 341–351.

[45] K. Salikhov and N. Zavoiskaya. “Zavoisky and the discovery of EPR”. In: *Resonance* 20.11 (2015), pp. 963–968.

[46] A. Schweiger. “Pulsed Electron Spin Resonance Spectroscopy: Basic Principles, Techniques, and Examples of Applications [New Analytical Methods (43)]”. In: *Angewandte Chemie International Edition in English* 30.3 (1991), pp. 265–292.

[47] S. K. Misra. *Multifrequency electron paramagnetic resonance: theory and applications*. John Wiley & Sons, 2011.

[48] K. S. Pedersen et al. “Toward Molecular 4f Single-Ion Magnet Qubits”. In: *Journal of the American Chemical Society* 138.18 (2016), pp. 5801–5804.

[49] C. P. Poole. *Electron spin resonance: a comprehensive treatise on experimental techniques*. Courier Corporation, 1996.

[50] F. Muller et al. “A high magnetic field EPR spectrometer”. In: *Review of scientific instruments* 60.12 (1989), pp. 3681–3684.

[51] A. Barra, L. Brunel, and J. Robert. “EPR spectroscopy at very high field”. In: *Chemical physics letters* 165.1 (1990), pp. 107–109.

[52] M. K. Bowman. “Pulsed electron paramagnetic resonance”. In: *Electron Paramagnetic Resonance: A Practitioner’s Toolkit*. Ed. by M. Brustolon and E. Giamello. John Wiley & Sons, 2009. Chap. 5.

[53] A. Schweiger and G. Jeschke. *Principles of pulse electron paramagnetic resonance*. Oxford University, 2001.

[54] R. T. Weber. *Pulsed EPR Primer*. Technical report. Bruker Instruments, Inc., 2000.

[55] G. Jeschke. *Introduction to electron paramagnetic resonance spectroscopy*. Lecture. ETH, 2008.

[56] G. Kalvius, D. Noakes, and O. Hartmann. “μSR studies of rare-earth and actinide magnetic materials”. In: *Handbook on the Physics and Chemistry of Rare Earths*. Vol. 32. Elsevier, 2001, pp. 55–451.

[57] P. Carretta and A. Lascialfari, eds. *NMR-MRI, μSR and Mössbauer Spectroscopies in Molecular Magnets*. Springer Science & Business Media, 2007.

[58] R. Kubo. "A stochastic theory of spin relaxation". In: *Hyperfine Interactions* 8.4 (1981), pp. 731–738.

[59] M. Kanesato and T. Yokoyama. "Synthesis and Structural Characterization of Ln (III) Complexes (Ln= Eu, Gd, Tb, Er, Tm, Lu) of Tripodal Tris (2-(salicylideneamino) ethyl) amine." In: *Chemistry Letters* 2 (1999), pp. 137–138.

[60] P. V. Bernhardt, B. M. Flanagan, and M. J. Riley. "Isomorphous lanthanide complexes of a tripodal N_4O_3 ligand". In: *Australian Journal of Chemistry* 53.3 (2000), pp. 229–231.

[61] K. S. Pedersen et al. "Modifying the properties of 4f single-ion magnets by peripheral ligand functionalisation". In: *Chemical Science* 5.4 (2014), pp. 1650–1660.

[62] K. S. Pedersen et al. "Design of single-molecule magnets: insufficiency of the anisotropy barrier as the sole criterion". In: *Inorganic Chemistry* 54.15 (2015), pp. 7600–7606.

[63] M. Perfetti et al. "Determination of Magnetic Anisotropy in the LnTRENSAL Complexes (Ln= Tb, Dy, Er) by Torque Magnetometry". In: *Inorganic Chemistry* 54.7 (2015), pp. 3090–3092.

[64] B. M. Flanagan et al. "Ligand-Field Analysis of an Er(III) Complex with a Heptadentate Tripodal N_4O_3 Ligand". In: *Inorganic Chemistry* 40 (2001), pp. 5401–5407.

[65] J. Sievers. "Asphericity of 4f-shells in their Hund's rule ground states". In: *Zeitschrift für Physik B Condensed Matter* 45.4 (1982), pp. 289–296.

[66] J. D. Rinehart and J. R. Long. "Exploiting single-ion anisotropy in the design of f-element single-molecule magnets". In: *Chemical Science* 2.11 (2011), pp. 2078–2085.

[67] M.-E. Boulon et al. "Magnetic Anisotropy and Spin-Parity Effect Along the Series of Lanthanide Complexes". In: *Angewandte Chemie-International Edition* 52 (2013), pp. 350–354.

[68] E. Morenzoni et al. "Low energy muons as probes of thin films and near surface regions". In: *Physica B: Condensed Matter* 326.1 (2003), pp. 196–204.

[69] J. Dreiser et al. "Exchange interaction of strongly anisotropic tripodal erbium single-ion magnets with metallic surfaces". In: *ACS nano* 8.5 (2014), pp. 4662–4671.

[70] *Dolly - Variox cryo + Beamline*. μSR facility, PSI. 2016.

[71] *GPS - User Guide*. μSR facility, PSI. 2015.

[72] *Mulab*. Università degli studi di Parma. URL: `http://www.fis.unipr.it/~derenzi/dispense/pmwiki.php?n=MuSR.Mulab`.

[73] D. Procissi et al. "Low-energy excitations in the $S = 1/2$ molecular nanomagnet $K_6[V_{15}(IV)\,As_6O_{42}(H_2O)] \cdot 8\,H_2O$ from proton NMR and μ SR". In: *Physical Review B* 73.18 (2006), p. 184417.

[74] F. Branzoli et al. "Spin dynamics in the neutral rare-earth single-molecule magnets $[TbPc_2]^0$ and $[DyPc_2]^0$ from μSR and NMR spectroscopies". In: *Physical Review B* 79.22 (2009), p. 220404.

[75] Z. Salman et al. "Dynamics at T$\rightarrow$ 0 in half-integer isotropic high-spin molecules". In: *Physical Review B* 65.13 (2002), p. 132403.

[76] D. Procissi et al. "Muon spin relaxation investigation of tetranuclear iron (III) $Fe_4(OCH_3)_6(dpm)_6$ molecular cluster". In: *Physical Review B* 80.9 (2009), p. 094421.

[77] N. Bloembergen, E. M. Purcell, and R. V. Pound. "Relaxation effects in nuclear magnetic resonance absorption". In: *Physical review* 73.7 (1948), p. 679.

[78] F. Aquilante et al. "MOLCAS 7: The next generation". In: *Journal of computational chemistry* 31.1 (2010), pp. 224–247.

[79] X. Yi et al. "A Luminescent and Sublimable DyIII-Based Single-Molecule Magnet". In: *Chemistry-A European Journal* 18.36 (2012), pp. 11379–11387.

[80] E. Lucaccini. "Correlation between magnetic properties and luminescence in lanthanide-based molecules". Master thesis. University of Florence, 2013.

[81] P.-E. Car et al. "Giant field dependence of the low temperature relaxation of the magnetization in a dysprosium(III)-DORA complex". In: *Chemical Communications* 47 (2011), pp. 3571–3573.

[82] D.-P. Li et al. "Distinct magnetic dynamic behavior for two polymorphs of the same Dy (III) complex". In: *Chemical Communications* 47.24 (2011), pp. 6867–6869.

[83] M. Perfetti et al. "Angular-Resolved Magnetometry Beyond Triclinic Crystals Part II: Torque Magnetometry of Cp* ErCOT Single-Molecule Magnets". In: *Chemistry-A European Journal* 20.43 (2014), pp. 14051–14056.

[84] L. Rigamonti et al. "Mapping of single-site magnetic anisotropy tensors in weakly coupled spin clusters by torque magnetometry". In: *Physical Chemistry Chemical Physics* 16.32 (2014), pp. 17220–17230.

[85] M. Perfetti. "Cantilever Torque Magnetometry: a powerful tool to investigate magnetic anisotropy in crystals and thin films". PhD Thesis. University of Florence, 2015.

[86] S. Xue et al. "Field-Induced Multiple Relaxation Mechanism of CoIII2DyIII Compound with the Dysprosium Ion in a Low-Symmetrical Environment". In: *Inorganic chemistry* 53.23 (2014), pp. 12658–12663.

[87] G. Cosquer et al. "Slow magnetic relaxation in condensed versus dispersed dysprosium (III) mononuclear complexes". In: *Chemistry-A European Journal* 19.24 (2013), pp. 7895–7903.

[88] E. Bartolomé et al. "$\{Dy(\alpha-fur)3\}_n$: from double relaxation single-ion magnet behavior to 3D ordering". In: *Dalton Transactions* 42.28 (2013), pp. 10153–10171.

[89] L. Norel et al. "A carbon-rich ruthenium decorated dysprosium single molecule magnet". In: *Chemical Communications* 48.33 (2012), pp. 3948–3950.

[90] H. B. G. Casimir and F. K. Du Pré. "Note on the thermodynamic interpretation of paramagnetic relaxation phenomena". In: *Physica* 5 (1938), pp. 507–511.

[91] M. Gregson et al. "A monometallic lanthanide bis (methanediide) single molecule magnet with a large energy barrier and complex spin relaxation behaviour". In: *Chem. Sci.* 7.1 (2016), pp. 155–165.

[92] J. M. Zadrozny et al. "Slow magnetization dynamics in a series of two-coordinate iron (II) complexes". In: *Chem. Sci.* 4.1 (2013), pp. 125–138.

[93] S. Demir, J. M. Zadrozny, and J. R. Long. "Large Spin-Relaxation Barriers for the Low-Symmetry Organolanthanide Complexes $[Cp *_2 Ln(BPh_4)]$ (Cp*= pentamethylcyclopentadienyl; Ln= Tb, Dy)". In: *Chem. Eur. J.* 20.31 (2014), pp. 9524–9529.

[94] L. Ungur and L. F. Chibotaru. "Magnetic anisotropy in the excited states of low symmetry lanthanide complexes". In: *Physical Chemistry Chemical Physics* 13.45 (2011), pp. 20086–20090.

[95] L. Ungur et al. "Interplay of strongly anisotropic metal ions in magnetic blocking of complexes". In: *Inorganic chemistry* 52.11 (2013), pp. 6328–6337.

[96] F. Pointillart et al. "Magnetic Memory in an Isotopically Enriched and Magnetically Isolated Mononuclear Dysprosium Complex". In: *Angew. Chem.* 127.5 (2015), pp. 1524–1527.

[97] R. J. Blagg et al. "Magnetic relaxation pathways in lanthanide single-molecule magnets". In: *Nature chemistry* 5.8 (2013), pp. 673–678.

[98] C. Das et al. “Origin of SMM behaviour in an asymmetric Er (III) Schiff base complex: a combined experimental and theoretical study”. In: *Chemical Communications* 51.28 (2015), pp. 6137–6140.

[99] N. F. Chilton et al. “The first near-linear bis (amide) f-block complex: a blueprint for a high temperature single molecule magnet”. In: *Chem. Comm.* 51.1 (2015), pp. 101–103.

[100] S. Gómez-Coca et al. “Origin of slow magnetic relaxation in Kramers ions with non-uniaxial anisotropy”. In: *Nature communications* 5 (2014).

[101] M. Speldrich et al. “A Computational Framework for Magnetic Polyoxometalates and Molecular Spin Structrures: CONDON 2.0”. In: *Israel Journal of Chemistry* 51 (2011), pp. 215–227.

[102] J.-P. Costes, F. Dahan, and F. Nicodeme. “Structure-based description of a step-by-step synthesis of homo-and heterodinuclear (4f, 4f’) lanthanide complexes”. In: *Inorganic chemistry* 42.20 (2003), pp. 6556–6563.

[103] A. Altomare et al. “EXPO2013: a kit of tools for phasing crystal structures from powder data”. In: *Journal of Applied Crystallography* 46.4 (2013), pp. 1231–1235.

[104] S. Stoll and A. Schweiger. “EasySpin, a comprehensive software package for spectral simulation and analysis in EPR”. In: *Journal of Magnetic Resonance* 178.1 (2006), pp. 42–55.

[105] M. Martínez-Pérez et al. “Gd-based single-ion magnets with tunable magnetic anisotropy: molecular design of spin qubits”. In: *Physical review letters* 108.24 (2012), p. 247213.

[106] A. Caneschi et al. “Evaluating the magnetic anisotropy in molecular rare earth compounds. Gadolinium derivatives with semiquinone radical and diamagnetic analogues”. In: *Chemical physics letters* 371.5 (2003), pp. 694–699.

[107] T. D. Ladd et al. “Quantum computers”. In: *Nature* 464.7285 (2010), pp. 45–53.

[108] R. Blatt and D. Wineland. “Entangled states of trapped atomic ions”. In: *Nature* 453.7198 (2008), pp. 1008–1015.

[109] E. Knill, R. Laflamme, and G. J. Milburn. “A scheme for efficient quantum computation with linear optics”. In: *nature* 409.6816 (2001), pp. 46–52.

[110] J. T. Muhonen et al. “Storing quantum information for 30 seconds in a nanoelectronic device”. In: *Nature nanotechnology* 9.12 (2014), pp. 986–991.

[111] I. L. Chuang et al. “Experimental realization of a quantum algorithm”. In: *Nature* 393.6681 (1998), pp. 143–146.

[112] S. Thiele et al. “Electrically driven nuclear spin resonance in single-molecule magnets”. In: *Science* 344.6188 (2014), pp. 1135–1138.

[113] J. J. Pla et al. "High-fidelity readout and control of a nuclear spin qubit in silicon". In: *Nature* 496.7445 (2013), pp. 334–338.

[114] F. Troiani and M. Affronte. "Molecular spins for quantum information technologies". In: *Chemical Society Reviews* 40.6 (2011), pp. 3119–3129.

[115] A. Morello et al. "Single-shot readout of an electron spin in silicon". In: *Nature* 467.7316 (2010), pp. 687–691.

[116] J. J. Pla et al. "A single-atom electron spin qubit in silicon". In: *Nature* 489.7417 (2012), pp. 541–545.

[117] K. Sato et al. "Molecular electron-spin quantum computers and quantum information processing: pulse-based electron magnetic resonance spin technology applied to matter spin-qubits". In: *Journal of Materials Chemistry* 19.22 (2009), pp. 3739–3754.

[118] L. Berliner, S. S. Eaton, and G. R. Eaton. *Distance measurements in biological systems by EPR*. Vol. 19. Springer Science & Business Media, 2006.

[119] A. Ardavan et al. "Will spin-relaxation times in molecular magnets permit quantum information processing?" In: *Physical review letters* 98.5 (2007), p. 057201.

[120] A. Collauto et al. "A slow relaxing species for molecular spin devices: EPR characterization of static and dynamic magnetic properties of a nitronyl nitroxide radical". In: *Journal of Materials Chemistry* 22.41 (2012), pp. 22272–22281.

[121] Y.-S. Ding, Y.-F. Deng, and Y.-Z. Zheng. "The Rise of Single-Ion Magnets as Spin Qubits". In: *Magnetochemistry* 2.4 (2016), p. 40.

[122] J. M. Zadrozny et al. "Multiple quantum coherences from hyperfine transitions in a vanadium (IV) complex". In: *Journal of the American Chemical Society* 136.45 (2014), pp. 15841–15844.

[123] J. M. Zadrozny et al. "Millisecond Coherence Time in a Tunable Molecular Electronic Spin Qubit". In: *ACS central science* 1.9 (2015), pp. 488–492.

[124] M. Ahmed et al. "New Oxovanadium (IV) Complexes with Mixed Ligands-Synthesis, Thermal Stability, and Crystal Structure of $(VO)_2(acac)_2(\mu - OEt)_2$ and $(VO)_2(thd)_2(\mu - OEt)_2$". In: *Zeitschrift für anorganische und allgemeine Chemie* 630.13-14 (2004), pp. 2311–2318.

[125] J. Van Vleck. "Paramagnetic relaxation times for titanium and chrome alum". In: *Physical Review* 57.5 (1940), p. 426.

[126] N. Morozova et al. "Crystal structure of oxotitanium (IV) 2, 2, 6, 6-tetramethyl-3, 5-heptanedionate". In: *Journal of Structural Chemistry* 46.6 (2005), pp. 1047–1051.

[127] L. Tesi et al. "Giant spin–phonon bottleneck effects in evaporable vanadyl-based molecules with long spin coherence". In: *Dalton Transactions* 45.42 (2016), pp. 16635–16643.

[128] M. A. Nielsen and I. L. Chuang. *Quantum computation and quantum information*. Cambridge university press, 2010.

[129] K. Bader et al. "Room temperature quantum coherence in a potential molecular qubit". In: *Nature communications* 5 (2014).

Acknowledgements

This thesis, and above all, my PhD student experience would not have been the same without the collaboration of several people, both colleagues and friends. First of all, I would like to thank my supervisor Lorenzo, for being always helpful in giving advice for my research activity and also for having answered tons of scientific doubts in these three years. I have to thank also Mauro, for the beautiful years that I spent in the LAMM group. We shared science and fun together and I can safely say that he will always be may favorite deskmate. All the people of the LAMM group deserve a special thanks: Claudia, Michele P., Roberta, Federico, Lorenzo T., Beppe, Matteo M., Matteo B., Irene, Elisabetta, Martin, Claudio, Andrea C., Andrea G... they all made these three years wonderful both for the science and the human relations.

I would like to thank my parents, Francesco and Elisabetta, my aunt Lucia and my siblings Tommaso, Ester and Elisa. My family gave me the chance to study and to achieve my personal goals. As regards this, I think that one of the most important things in life is friendship, because it helps sharing both good and bad moments, so I would like to start thanking my longtime friends Giulia and Giulia and also all the people I met at the university: Virginia, Giacomo, Fra, Ricca, Davide, Barbara, Tommaso and many other that now I forget to mention, but you will forgive me, I hope. A special thanks goes to my apartment mates Paola and Silvia. Silvia ran the Florence marathon few days ago, and that was inspiring to finish writing my PhD dissertation.

Last but not least, Lore, my friend and sweetheart. He has been always supportive even when he was writing its own PhD thesis. I am looking forward to organizing the next journey together and I think that many other adventures are waiting for us.

Eva